



HAL
open science

Experimental and numerical characterization of the rheological behavior of a complex fluid: application to a wet foam flow through a horizontal straight duct with and without flow disruption devices (FDD)

Rogelio Chovet

► **To cite this version:**

Rogelio Chovet. Experimental and numerical characterization of the rheological behavior of a complex fluid: application to a wet foam flow through a horizontal straight duct with and without flow disruption devices (FDD). Fluids mechanics [physics.class-ph]. Université de Valenciennes et du Hainaut-Cambresis, 2015. English. NNT : 2015VALE0021 . tel-03461497

HAL Id: tel-03461497

<https://theses.hal.science/tel-03461497>

Submitted on 1 Dec 2021

HAL is a multi-disciplinary open access archive for the deposit and dissemination of scientific research documents, whether they are published or not. The documents may come from teaching and research institutions in France or abroad, or from public or private research centers.

L'archive ouverte pluridisciplinaire **HAL**, est destinée au dépôt et à la diffusion de documents scientifiques de niveau recherche, publiés ou non, émanant des établissements d'enseignement et de recherche français ou étrangers, des laboratoires publics ou privés.

Présentée à

L'Université de Valenciennes et du Hainaut-Cambrésis

Pour obtenir le grade de Docteur

Discipline, spécialité selon la liste des spécialités pour lesquelles l'Ecole Doctorale est accréditée :
Mécanique

Présentée et soutenue par Rogelio CHOVET

Soutenance prévue le 17/07/2015 à 10h00, à l'UVHC (Valenciennes)

Ecole doctorale :

Sciences Pour l'Ingénieur (SPI)

Laboratoire, Equipe de recherche :

Laboratoire d'Automatique, de Mécanique et d'Informatique Industrielles et Humaines (LAMIH
CNRS UMR 8201), Département de Mécanique

**CARACTERISATION EXPERIMENTALE ET NUMERIQUE DU
COMPORTEMENT RHEOLOGIQUE D'UN FLUIDE COMPLEXE :
APPLICATION A UNE MOUSSE EN ECOULEMENT DANS UN CANAL
HORIZONTAL DROIT AVEC ET SANS SINGULARITES**

Composition du jury :

Président du jury

M. François MONNOYER : *Professeur à l'UVHC Valenciennes (LAMIH, CNRS UMR 8201)*

Rapporteurs

M. Jack LEGRAND : *Professeur à l'Univ. de Nantes (GEPEA, CNRS UMR 6144)*

M. Hassan PEERHOSSAINI : *Professeur à l'Univ. de Paris Diderot (LIED, CNRS UMR 8236)*

Examineurs

M. Mohamed SOUHAR : *Professeur à l'Univ. de Lorraine, INPL, Nancy (LEMTA, CNRS UMR 7563)*

M. Abdelkader MOJTABI : *Professeur à l'Univ. de Paul Sabatier, Toulouse (IMFT, CNRS UMR 5502)*

M. Abdelhak AMBARI : *Professeur à l'ENSAM ParisTech CER d'Angers (LAMPA)*

M. Laurent DUBAR : *Professeur à l'UVHC Valenciennes (LAMIH, CNRS UMR 8201)*

Invité

M. Daniel PIERRAT : *Ingénieur de Recherche, Expert en CFD (CETIM, Nantes)*

Directeur de thèse

M. Fethi ALOUI : *Professeur à l'UVHC Valenciennes (LAMIH, CNRS UMR 8201)*

ACKNOWLEDGEMENTS

I was fortunate from the beginning of my Ph.D. study to be part of the Department of Mechanics (team MFVSI) at the LAMIH, full of excellent researchers, professionals and above all people.

Fethi ALOUI, Professor at the University of Valenciennes and Hainaut-Cambrésis (Advanced Engineering School ENSIAME) and supervisor of this thesis, believed in me, gave me access to all the equipment and previous researches necessary to undertake and develop this one. He exposed new points of view, kept an open mind, solved constantly all sort of problems, and always looked for my well-being and the accomplishment of my Ph.D. studies.

Professor Larbi LABRAGA, who is no longer with us after a battle against sickness, may he rest in peace.

Professors Thierry-Marie GUERRA and Laurent DUBAR, respectively Director and Deputy Director of the LAMIH UMR CNRS 8201, welcomed me in their laboratory and were open in all the steps of this work.

The jury selected for this Ph.D. thesis will contribute by giving a critical and constructive review of my research work. I would like to thank especially, Professor Jack LEGRAND and Professor Hassan PEERHOSSAINI who gave me the honor to accept the evaluation of this Ph.D. thesis. As external examiners, their remarks and suggestions will allow me the improvement and critical extent of this work.

Professors Abdelkader MOJTABI, François MONNOYER, Mohamed SOUHAR, Laurent DUBAR, and Abdelhak AMBARI are acknowledged for their acceptance to be among the jury members. They will give me the honor to examine, enrich and improve my work by giving their constructive remarks. They are a part of the jury as examiners.

I would like to thank Daniel PIERRAT, Research Engineer and Expert in CFD for his acceptance to participate to this jury as an invited member. His comments and critical extent, especially on the CFD simulations study, will be very important for this research work.

The Deputy Director of the Mechanical Department at the LAMIH, Laurent KEIRSBULCK, a great person that guided me through many difficulties. His total dedication to his family, friends and work is a testimony of a balance professional that inspires everyone around him.

The secretary of the LAMIH, Sabine GUILAIN, had the hard work of helping me adapt to this life change. Always helpful, open and creative, she assisted me when I ran into bureaucratic difficulties, even personal matters.

Hadrien BAUDIN, post-doctoral researcher, was one of my most valuable aide; able, resourceful, humble and patient. He gave me all kind of advices, in the most detailed and clear way, and helped me to understand pertinent problems that came across my work.

Jon SAN JUAN, an old family friend, went through all my drafts, reviewing and correcting them. He has always given me the best counseling on my professional projection with kindness and concern.

Old colleagues and friends, including Fawzi FADLA, Marc LIPPERT, Jesse SCHIFFLER, Hervé WALKOWIAK Jean Michel DAILLIET, Anthony GRAZIANI, and Denis CORNU, gave me technical assistance, but most importantly their human support and empathy during the three years of developing the thesis project.

My family, my future wife, her family, and all my friends, supported and loved me unconditionally. They provided me with strength when mine was fading away.

I am indebted and grateful to all of them.

CONTENTS

ACKNOWLEDGEMENTS	<i>i</i>
FIGURES INDEX	<i>vii</i>
TABLES INDEX	<i>xiii</i>
NOMENCLATURE	<i>xv</i>
INTRODUCTION	1
CHAPTER 1	5
1. FOAM STRUCTURE	6
1.1 BUBBLE	6
1.2 SURFACE TENSION.....	6
1.3 VOID FRACTION AND FOAM QUALITY	7
1.4 FOAMS, WET AND DRY	7
1.4.1 THE DRY LIMIT.....	7
1.4.2 THE WET LIMIT	7
1.4.3 BETWEEN THE TWO LIMITS	8
1.5 FOAM DENSITY	8
1.6 THIN LIQUID FILM	8
2. LOCAL EQUILIBRIUM RULES.....	8
2.1 THE LAW OF LAPLACE.....	8
2.2 THE LAWS OF PLATEAU.....	9
2.3 BUBBLE-BUBBLE INTERACTION.....	10
3. MAKING FOAMS	11
3.1 SURFACTANTS	11
3.1.1 CRITICAL MICELLE CONCENTRATION (CMC).....	12
3.2 FOAM CREATION	13
3.2.1 NUCLEATION	13
3.2.2 ENTRAINMENT OF GAS OCCLUSIONS	13
3.2.3 INJECTION	14
3.3 PRACTICAL APPLICATION	14
4. IMAGING AND PROBING FOAM STRUCTURE	15
4.1 THE PRINCIPLE OF ARCHIMEDES	15
4.2 THE PRESSURE OUTLETS METHOD.....	16
4.3 THE CONDUCTIMETRY TECHNIQUE.....	17
4.4 THE AC CAPACITANCE MEASUREMENT (ACM).....	17
4.5 THE ELECTRICAL IMPEDANCE TOMOGRAPHY (EIT).....	18
4.6 THE FLUORESCENCE METHOD	18
4.7 THE SPEED OF SOUND METHOD	18
4.8 THE TRANSMISSION AND REFLECTION OF LIGHT.....	19

4.9	THE OPTICAL GLASS FIBER PROBE METHOD.....	19
4.10	THE PHOTOGRAPHIC METHOD.....	20
4.11	THE MAGNETIC RESONANCE IMAGING (MRI).....	21
4.12	OTHER FOAM MEASUREMENT TECHNIQUES.....	21
5.	FOAM RHEOLOGY.....	21
5.1	LINEAR ELASTICITY.....	23
5.2	NON-LINEAR ELASTICITY.....	24
5.3	YIELDING.....	24
5.4	PLASTIC FLOW.....	25
5.5	FOAM-WALL VISCOUS FRICTION.....	25
5.6	RHEOLOGICAL PARAMETERS.....	26
6.	FOAM EVOLUTION.....	26
6.1	DRAINAGE.....	27
6.1.1	DRAINAGE CHARACTERIZATION.....	27
6.1.2	THE CONTINUITY EQUATION.....	28
6.2	COARSENING.....	28
6.3	GIBBS-MARANGONI MECHANISM.....	29
6.4	THE DISJUNCTION PRESSURE.....	30
6.5	FOAM COLLAPSE.....	30
6.5.1	THE COALESCENCE.....	30
6.5.2	T1 AND T2 REARRANGEMENTS.....	31
7.	FOAM FLOW.....	32
7.1	FOAM VISCOSITY.....	32
7.2	NON-NEWTONIAN FLOW MODELS.....	33
7.3	HORIZONTAL FLOW REGIMES.....	35
7.4	WALL-SLIP LIQUID LAYER.....	36
7.4.1	WALL-SLIP VELOCITY.....	36
7.4.2	CORRECTION METHODS.....	36
7.4.3	THICKNESS.....	37
7.4.4	SHEAR RATE INFLUENCE.....	38
7.5	COMPRESSIBILITY INFLUENCE.....	39
7.6	THEORETICAL FOAM FLOW MODELS.....	39
8.	CFD CODE FOR COMPLEX FLUID SIMULATIONS: ANSYS-CFX.....	40
8.1	ANSYS CFX DESCRIPTION.....	40
8.2	INTRODUCTION TO ANSYS CFX.....	40
8.3	CFX-PRE.....	41
8.3.1	DOMAINS.....	41
8.3.2	PHYSICAL MODELS.....	41
8.4	CFX-SOLVER.....	42
8.4.1	LINEAR EQUATION SOLUTION.....	42
8.4.2	ALGEBRAIC MULTIGRID.....	43
8.5	CFX-SOLVER MANAGER.....	43
8.6	CFD-POST.....	43
8.7	GEOMETRY GENERATION.....	43
8.8	MESHING.....	44
8.9	NUMERICAL MODEL.....	44
8.9.1	GOVERNING EQUATIONS.....	44
8.10	SHEAR STRAIN RATE.....	45

8.11	NON-NEWTONIAN MODELS.....	45
9.	CONCLUSIONS	46
CHAPTER 2		49
1.	EXPERIMENTAL FACILITY	50
1.1	RECIRCULATION PUMP.....	51
1.2	RECUPERATION TANK.....	51
1.3	CHARGE TANK	51
1.4	FOAM GENERATORS.....	51
1.5	TEST SECTION	52
1.5.1	FLOW DISRUPTION DEVICES (FDD).....	53
1.6	CALIBRATION SECTION.....	54
2.	MEASUREMENT TECHNIQUES.....	54
2.1	LIQUID FLOWMETER	54
2.2	GAS FLOWMETER.....	54
2.3	PRESSURE OUTLETS	55
2.4	PARTICLE IMAGING VELOCIMETRY (PIV).....	55
2.5	POLAROGRAPHIC METHOD (OR ELECTROCHEMICAL METHOD)	56
2.5.1	METHOD PRINCIPLE	57
2.5.2	MASS TRANSFER COEFFICIENT	58
2.5.3	CONVECTION-DIFFUSION EQUATION FOR A SIMPLE PROBE IN STEADY STATE	58
2.5.4	FREQUENCY RESPONSE OF THE MICROELECTRODES	60
2.6	CONDUCTIMETRY METHOD.....	63
3.	EXPERIMENTAL ARRANGEMENTS.....	64
3.1	SURFACTANT CHOICE AND QUALITY	64
3.2	FOAM FLOW CHARACTERIZATION	64
3.3	FOAM GENERATORS CALIBRATION.....	65
3.4	PARTICLE IMAGING VELOCIMETRY.....	66
3.5	POLAROGRAPHIC METHOD	67
3.5.1	CHOICE OF AN ELECTROCHEMICAL REACTIVE	67
3.5.2	MEASUREMENT PROBES	67
3.5.3	MEASUREMENT SYSTEM.....	68
3.5.4	PROBES CALIBRATION	69
3.6	CONDUCTIMETRY METHOD	72
3.6.1	CALIBRATION PROCEDURE	73
3.7	ANALOG DATA ACQUISITION SYSTEM	74
4.	CONCLUSIONS	74
CHAPTER 3		75
1.	FOAM FLOW ALONG A STRAIGHT CHANNEL WITH NO FDD	76
1.1	PRESSURE LOSSES AND GRADIENT.....	76
1.2	VELOCITY PROFILES	77
1.3	LIQUID FILM THICKNESS	78
1.3.1	BOTTOM WALL.....	78
1.3.2	LATERAL WALL	80
1.3.3	TOP WALL	85

1.3.4	STATISTICAL DESCRIPTION OF THE CONDUCTIMETRY SIGNAL	89
1.4	POLAROGRAPHIC SIGNALS.....	92
1.5	STATISTICAL DESCRIPTION OF THE MICRO-TURBULENCE	119
1.6	WALL SHEAR STRESS	123
1.7	CONCLUSIONS.....	129
2.	FOAM FLOW ALONG A HORIZONTAL STRAIGHT CHANNEL WITH FDD.....	131
2.1	VALIDATION OF THE VELOCITY PROFILE UPSTREAM THE DISRUPTION DEVICES.....	131
2.2	PRESSURE LOSSES AND PRESSURE GRADIENT.....	132
2.3	LOCAL AVERAGE VELOCITY FIELDS	135
2.3.1	HALF SUDDEN EXPANSION.....	135
2.3.2	FENCE	143
2.3.3	CYLINDER	151
2.4	CONCLUSIONS.....	159
3.	NUMERICAL CFD SIMULATIONS OF AQUEOUS FOAM OVER DIFFERENT FDD	160
3.1	GEOMETRY AND NUMERICAL PARAMETERS	160
3.2	VALIDATION OF THE VELOCITY PROFILES UPSTREAM OF THE FDD	163
3.3	STATIC PRESSURE LOSSES.....	164
3.4	AVERAGED AXIAL AND VERTICAL VELOCITY FIELDS.....	164
3.5	AVERAGED AXIAL AND VERTICAL VELOCITY PROFILES.....	168
3.6	CONCLUSIONS.....	172
	GENERAL CONCLUSIONS	175
	REFERENCES	179

FIGURES INDEX

INTRODUCTION	1
FIGURE I.1 DRY AND WET LIMIT [2].....	2
FIGURE I.2 PLATEAU BORDER: LIQUID FILM LOCATED BETWEEN BUBBLES.....	2
FIGURE I.3 FOAM COARSENING. AIR DIFFUSION TROUGH THE LIQUID FILMS [1].....	2
FIGURE I.4 CHARACTERISTICS LENGTH OF THE FOAM.....	3
CHAPTER 1	5
FIGURE 1.1 LORD KELVIN CELL OR TETRAKAIDECAHEDRON [10].....	6
FIGURE 1.2 DISJOINING PRESSURE: PRESENCE OF A REPULSION FORCE INSIDE THE LIQUID FILMS [1].	9
FIGURE 1.3 PLATEAU BORDERS ARE SMOOTHLY JOINED TO THE ADJACENT FILM [1].	10
FIGURE 1.4 SODIUM STEARATE, THE MOST COMMON COMPONENT OF MOST SOAP, MAKES ABOUT 50% OF COMMERCIAL SURFACTANTS.....	11
FIGURE 1.5 SURFACTANT GROUPS ACCORDINGLY TO ITS HEAD CHARGE.....	12
FIGURE 1.6 SURFACE TENSION VS. SURFACTANT CONCENTRATIONS AND THE CRITICAL MICELLE CONCENTRATION (CMC).....	12
FIGURE 1.7 FOAM FLOWING THROUGH A PRESSURE CANISTER AND ITS NUCLEATION.	13
FIGURE 1.8 ARCHIMEDES PRINCIPLE MAY BE USED TO ESTIMATE THE (AVERAGE) LIQUID FRACTION OF A FOAM COLUMN [1].	15
FIGURE 1.9 THE PRESSURE OUTLETS LOCATED AT THE WALLS ALLOW US TO MEASURE THE PRESSURE LOSSES [32].	16
FIGURE 1.10 CAPACITANCE MEASUREMENTS USING SEGMENTED ELECTRODES TO OBTAIN A VERTICAL PROFILE OF LIQUID FRACTION [36].....	17
FIGURE 1.11 BUBBLES DEFORMATION AT THE CHANNEL WALL [51].....	20
FIGURE 1.12 SCHEMATIC REPRESENTATION OF THE RELATIONSHIP BETWEEN THE SHEAR AND THE STRAIN FOR AQUEOUS FOAM.....	22
FIGURE 1.13 SCHEMATIC PRESENTATION OF THE ORIGIN OF ELASTIC RESPONSE OF FOAM, SUBJECT TO SHEAR STRESS LOWER THAN THE FOAM YIELD STRESS CLOSE TO THE A CHANNEL WALL [2].	22
FIGURE 1.14 FOAM YIELDING AND PLASTIC DEFORMATION, UNDER APPLIED SHEAR STRESS, INCREASING FROM (A) TO (C). THIS STRUCTURE CAN RELAX EITHER ELASTICALLY, BY RETURNING TO STRUCTURE (A), OR BY A BUBBLE REARRANGEMENT, LEADING TO STRUCTURE (D) [59,58].....	23
FIGURE 1.15 A CUBE OF FOAM IS SHEARED IN THE X1 DIRECTION. THE ARROWS ILLUSTRATE THE COMPONENTS OF THE INDUCED STRESS [62].	24
FIGURE 1.16 SCHEMATIC PRESENTATION OF THE ZONE OF BUBBLE–WALL CONTACT WITH THE PROFILE OF THE FLUID VELOCITY: A) IN THE CASE OF TANGENTIALLY MOBILE BUBBLE SURFACE, THERE IS NO VELOCITY GRADIENT IN THE WETTING FILM, SO THAT THE BUBBLE–WALL FRICTION ORIGINATES IN THE MENISCUS ZONES AROUND THE FILM ONLY; (B) IN THE CASE OF TANGENTIALLY IMMOBILE BUBBLE SURFACE, THE FRICTION OCCURS IN BOTH ZONES – OF THE FILM AND IN THE SURROUNDING MENISCUS REGIONS. [72].	25
FIGURE 1.17 RIPENING OF A WET BUBBLY SYSTEM.	28
FIGURE 1.18 SCHEMATIC REPRESENTATION OF 2D DRY FOAM. THE BUBBLE NOTED BY I HAS $n = 7$ SIDES OF LENGTH l_{ij} . THE TOTAL ANGLE COVERED BY FILMS' CURVATURES ALONG THE PERIMETER OF BUBBLE I IS EQUAL TO $\sum_j = 1/n \phi_{ij} = \sum_j = 1/n l_{ij}/R_{ij} = \pi (6 - n)/3$. ARROWS ILLUSTRATE THE EXCHANGE OF GAS BETWEEN n -SIDES BUBBLES [83].	29
FIGURE 1.19 T1 AND T2 REARRANGEMENT.	31
FIGURE 1.20 VELOCITY FIELD OF A LAMINAR FLOW WITH A WALL-SLIP VELOCITY [51].	36
FIGURE 1.21 VELOCITY PROFILE OF A FOAM FLOW INSIDE A ROTAMETER [108].	37
FIGURE 1.22 ANSYS CFX MODULES.	41

CHAPTER 2	49
FIGURE 2.1 PHOTOGRAPHY AND SCHEMATIC VIEW OF THE EXPERIMENTAL FACILITY	50
FIGURE 2.2 DIAGRAM AND PHOTOGRAPHY OF A FOAM GENERATOR	51
FIGURE 2.3 EXAMPLE OF FOAM FLOW OVER THE LATERAL WALL FOR THE THREE MECHANIC FLOW RESTRICTIONS (FENCE, HALF-SUDDEN EXPANSION AND CYLINDER)	52
FIGURE 2.4 TOP VIEW OF THE FOAM GENERATORS	52
FIGURE 2.5 DIAGRAM OF THE CROSS SECTION	52
FIGURE 2.6 IMAGE AND DIAGRAM OF THE TEST SECTION	53
FIGURE 2.7 LATERAL SCHEMATIC REPRESENTATION OF THE THREE FLOW DISRUPTION DEVICES: (A) FENCE, (B) CIRCLE AND (C) HALF-SUDDEN EXPANSION (DIMENSIONS IN MM).....	53
FIGURE 2.8 DIAGRAM OF THE CALIBRATION CHANNEL	54
FIGURE 2.9 DIAGRAM OF THE CALIBRATION CHANNEL CROSS SECTION	54
FIGURE 2.10 DIAGRAM OF THE PRESSURE OUTLETS ARRANGEMENT	55
FIGURE 2.11 OVERVIEW OF THE PARTICLE IMAGING VELOCIMETRY (PIV) SYSTEM.....	56
FIGURE 2.12 MEASUREMENT ELECTRODE.....	57
FIGURE 2.13 CURRENT/VOLTAGE CURVE AND ITS DIFFUSION PLATEAU	58
FIGURE 2.14 POLAROGRAPHIC METHOD PRINCIPLE.....	59
FIGURE 2.15 PRESSURE LOSSES INSIDE THE TEST SECTION WITH A HALF-SUDDEN AS FLOW DISRUPTION, A FOAM VELOCITY OF 2 CM/S AND QUALITY 70% FOR THE THREE GENERATORS.	65
FIGURE 2.16 SCHEMATIC REPRESENTATION OF THE PIV BEHAVIOR ON THE FOAM FLOW	66
FIGURE 2.17 SETTING ARRANGEMENT OF THE THREE POLAROGRAPHIC BLOCKS.....	68
FIGURE 2.18 POLAROGRAPHIC PROBES.....	68
FIGURE 2.19 SIMPLIFIED REPRESENTATION OF THE POLAROGRAPHIC MEASUREMENT SYSTEM	69
FIGURE 2.20 POLAROGRAMS OF THE THREE ELECTROCHEMICAL BLOCKS: (A) TOP, (B) LATERAL AND (C) BOTTOM.....	69
FIGURE 2.21 THEORETICAL DIMENSIONLESS VELOCITY PROFILE INSIDE THE CALIBRATION CHANNEL.....	70
FIGURE 2.22 EXPERIMENTAL PRESSURE LOSSES VS. DARCY-WEISBACH EQUATION ALONG THE CALIBRATION DUCT	71
FIGURE 2.23 SIMPLIFIED DIAGRAM OF THE CONDUCTIMETRY SYSTEM.....	72
FIGURE 2.24 POSITIONING OF THE CONDUCTIMETRY PROBES OVER THE EXCHANGEABLE BLOCKS	73
FIGURE 2.25 CALIBRATION ARRANGEMENT FOR THE CONDUCTIMETRY BLOCKS	73
FIGURE 2.26 CALIBRATION CURVES FOR THE TWO CONDUCTIMETRY BLOCKS (A) AND (B).	74
CHAPTER 3	75
FIGURE 3.1 STATIC PRESSURE LOSSES ALONG THE SQUARE CHANNEL WITHOUT FLOW RESTRICTIONS: (A) CASE I; (B) CASE II AND (C) CASE III.....	76
FIGURE 3.2 PRESSURE GRADIENT FOR A FOAM FLOW INSIDE A STRAIGHT CHANNEL WITH NO FDD FOR DIFFERENT FOAM QUALITIES AND VELOCITIES.	76
FIGURE 3.3 AVERAGED AXIAL VELOCITY PROFILES AT THE LATERAL WALL OF THE FOAM FLOWING THROUGH A STRAIGHT CHANNEL WITH DIFFERENT QUALITIES FOR: CASE I (A), CASE II (B) AND CASE III (C).	77
FIGURE 3.4 AXIAL VELOCITY PROFILES AT THE TOP WALL OF THE FOAM FLOWING THROUGH A STRAIGHT CHANNEL WITH DIFFERENT QUALITIES FOR: CASE I (A), CASE II (B) AND CASE III (C).	77
FIGURE 3.5 AXIAL VELOCITY PROFILES AT THE LIQUID/FOAM INTERPHASE OF THE FOAM FLOWING THROUGH A STRAIGHT CHANNEL WITH DIFFERENT QUALITIES FOR: CASE I (A), CASE II (B) AND CASE III (C).	78
FIGURE 3.6 CONDUCTIMETRY SIGNAL OF THE LIQUID FILM THICKNESS OVER THE BOTTOM WALL FOR ALL FOAM QUALITIES (B) AND CASES: CASE I; (B) CASE II AND (C) CASE III.	79
FIGURE 3.7 MEAN LIQUID FILM THICKNESS AT THE BOTTOM OF THE CHANNEL FOR ALL CASES STUDIED AND QUALITIES.	80
FIGURE 3.8 CONDUCTIMETRY SIGNAL OVER THE LATERAL WALL FOR A FOAM VELOCITY OF 2 CM/S AT:.....	81
FIGURE 3.9 CONDUCTIMETRY SIGNAL OVER THE LATERAL WALL FOR A FOAM VELOCITY OF 4 CM/S AT:.....	82
FIGURE 3.10 CONDUCTIMETRY SIGNAL OVER THE LATERAL WALL FOR A FOAM VELOCITY OF 6 CM/S AT:.....	83
FIGURE 3.11 SCHEMATIC REPRESENTATION OF THE FLUCTUATIONS OF THE CONDUCTIMETRY SIGNAL [51].	84
FIGURE 3.12 EVOLUTION OF THE MEAN LIQUID FILM THICKNESS VALUE OVER THE LATERAL WALL FOR ALL FOAM QUALITIES AND THE THREE CASES: (A) CASE I; (B) CASE II AND (C) CASE III.	84

FIGURE 3.13 MEAN LIQUID FILM THICKNESS AT THE BOTTOM OF THE CHANNEL FOR ALL CASES AND QUALITIES. .	85
FIGURE 3.14 CONDUCTIMETRY SIGNAL OVER THE TOP WALL FOR THE CASE I AT: (A) $Z = -9$ MM; (B) $Z = 0$ MM AND $Z = 9$ MM FOR ALL FOAM QUALITIES (B).....	86
FIGURE 3.15 CONDUCTIMETRY SIGNAL OVER THE TOP WALL FOR THE CASE II AT: (A) $Z = -9$ MM; (B) $Z = 0$ MM AND $Z = 9$ MM FOR ALL FOAM QUALITIES (B).....	87
FIGURE 3.16 CONDUCTIMETRY SIGNAL OVER THE TOP WALL FOR THE CASE III AT: (A) $Z = -9$ MM; (B) $Z = 0$ MM AND $Z = 9$ MM FOR ALL FOAM QUALITIES (B).....	88
FIGURE 3.17 SIGNAL WITH A POSITIVE SKEWNESS FACTOR J.	89
FIGURE 3.18 SIGNALS WITH SMALL AND LARGE KURTOSIS FACTOR (F).....	90
FIGURE 3.19 STANDARD DEVIATIONS OF THE CONDUCTIMETRY THICKNESSES OVER THE LATERAL WALL FOR ALL FOAM QUALITIES AND VELOCITIES: (A) CASE I; (B) CASE II AND (C) CASE III.	90
FIGURE 3.20 STANDARD DEVIATIONS OF THE CONDUCTIMETRY THICKNESSES OVER THE TOP WALL FOR ALL FOAM QUALITIES (B) AND VELOCITIES: (A) CASE I; (B) CASE II AND (C) CASE III.....	91
FIGURE 3.21 SKEWNESS FACTORS OF THE CONDUCTIMETRY THICKNESSES OVER THE TOP WALL FOR ALL FOAM QUALITIES (B) AND VELOCITIES: (A) CASE I; (B) CASE II AND (C) CASE III.....	91
FIGURE 3.22 SKEWNESS FACTOR OF THE CONDUCTIMETRY THICKNESSES OVER THE TOP WALL FOR ALL FOAM QUALITIES (B) AND VELOCITIES: (A) CASE I; (B) CASE II AND (C) CASE III.....	91
FIGURE 3.23 FLATNESS FACTOR OF THE CONDUCTIMETRY THICKNESSES OVER THE LATERAL WALL FOR ALL FOAM QUALITIES (B) AND VELOCITIES: (A) CASE I; (B) CASE II AND (C) CASE III.....	92
FIGURE 3.24 FLATNESS FACTORS OF THE CONDUCTIMETRY THICKNESSES OVER THE LATERAL WALL FOR ALL FOAM QUALITIES (B) AND VELOCITIES: (A) CASE I; (B) CASE II AND (C) CASE III.....	92
FIGURE 3.25 POLAROGRAPHIC SIGNALS OVER THREE WALLS: (A) BOTTOM; (B) LATERAL AND (C) TOP; FOR A FOAM QUALITY OF 55% AT A FOAM VELOCITY OF 2 CM/S.....	93
FIGURE 3.26 POLAROGRAPHIC SIGNALS OVER THREE WALLS: (A) BOTTOM; (B) LATERAL AND (C) TOP; FOR A FOAM QUALITY OF 60% AT A FOAM VELOCITY OF 2 CM/S.....	94
FIGURE 3.27 POLAROGRAPHIC SIGNALS OVER THREE WALLS: (A) BOTTOM; (B) LATERAL AND (C) TOP; FOR A FOAM QUALITY OF 65% AT A FOAM VELOCITY OF 2 CM/S.....	95
FIGURE 3.28 POLAROGRAPHIC SIGNALS OVER THREE WALLS: (A) BOTTOM; (B) LATERAL AND (C) TOP; FOR A FOAM QUALITY OF 70% AT A FOAM VELOCITY OF 2 CM/S.....	96
FIGURE 3.29 POLAROGRAPHIC SIGNALS OVER THREE WALLS: (A) BOTTOM; (B) LATERAL AND (C) TOP; FOR A FOAM QUALITY OF 75% AT A FOAM VELOCITY OF 2 CM/S.....	97
FIGURE 3.30 POLAROGRAPHIC SIGNALS OVER THREE WALLS: (A) BOTTOM; (B) LATERAL AND (C) TOP; FOR A FOAM QUALITY OF 80% AT A FOAM VELOCITY OF 2 CM/S.....	98
FIGURE 3.31 POLAROGRAPHIC SIGNALS OVER THREE WALLS: (A) BOTTOM; (B) LATERAL AND (C) TOP; FOR A FOAM QUALITY OF 85% AT A FOAM VELOCITY OF 2 CM/S.....	99
FIGURE 3.32 SYNCHRONIZATION BETWEEN THE BUBBLES PASSAGE OVER THE POLAROGRAPHIC PROBE AND THE MEASURED CURRENT.....	100
FIGURE 3.33 POLAROGRAPHIC SIGNALS OVER THREE WALLS: (A) BOTTOM; (B) LATERAL AND (C) TOP; FOR A FOAM QUALITY OF 55% AT A FOAM VELOCITY OF 4 CM/S.....	101
FIGURE 3.34 POLAROGRAPHIC SIGNALS OVER THREE WALLS: (A) BOTTOM; (B) LATERAL AND (C) TOP; FOR A FOAM QUALITY OF 60% AT A FOAM VELOCITY OF 4 CM/S.....	102
FIGURE 3.35 POLAROGRAPHIC SIGNALS OVER THREE WALLS: (A) BOTTOM; (B) LATERAL AND (C) TOP; FOR A FOAM QUALITY OF 65% AT A FOAM VELOCITY OF 4 CM/S.....	103
FIGURE 3.36 POLAROGRAPHIC SIGNALS OVER THREE WALLS: (A) BOTTOM; (B) LATERAL AND (C) TOP; FOR A FOAM QUALITY OF 70% AT A FOAM VELOCITY OF 4 CM/S.....	104
FIGURE 3.37 POLAROGRAPHIC SIGNALS OVER THREE WALLS: (A) BOTTOM; (B) LATERAL AND (C) TOP; FOR A FOAM QUALITY OF 75% AT A FOAM VELOCITY OF 4 CM/S.....	105
FIGURE 3.38 POLAROGRAPHIC SIGNALS OVER THREE WALLS: (A) BOTTOM; (B) LATERAL AND (C) TOP; FOR A FOAM QUALITY OF 80% AT A FOAM VELOCITY OF 4 CM/S.....	106
FIGURE 3.39 POLAROGRAPHIC SIGNALS OVER THREE WALLS: (A) BOTTOM; (B) LATERAL AND (C) TOP; FOR A FOAM QUALITY OF 85% AT A FOAM VELOCITY OF 4 CM/S.....	107
FIGURE 3.40 BOUNDARIES OF THE NUMERICAL SOLUTION.....	109
FIGURE 3.41 ISOCONCENTRATION LINES.....	109
FIGURE 3.42 EVOLUTION OF THE CONCENTRATION "C" IN A THREE-DIMENSIONAL DOMAIN.....	109

FIGURE 3.43 $01 \partial C \partial YY = 0 \partial X$ EVOLUTION FOR $Pe = 115771$ 110

FIGURE 3.44 MEAN SHERWOOD NUMBER EVOLUTION VERSUS THE PECLLET NUMBER ACCORDING TO THE NUMERICAL SOLUTION AND THE LEVÊQUE EQUATION. 110

FIGURE 3.45 MEAN SHERWOOD NUMBER EVOLUTION AS A FUNCTION OF THE LIQUID FILM THICKNESS FOR DIFFERENT VALUES OF THE WALL SHEAR STRESS T_0 111

FIGURE 3.46 CURVE LIMITING THE REGION WHERE THE POLAROGRAPHIC SIGNAL DOES NOT DEPEND ON THE LIQUID FILM THICKNESS OBTAINED NUMERICALLY 111

FIGURE 3.47 POLAROGRAPHIC SIGNALS OVER THREE WALLS: (A) BOTTOM; (B) LATERAL AND (C) TOP; FOR A FOAM QUALITY OF 55% AT A FOAM VELOCITY OF 6 CM/S..... 112

FIGURE 3.48 POLAROGRAPHIC SIGNALS OVER THREE WALLS: (A) BOTTOM; (B) LATERAL AND (C) TOP; FOR A FOAM QUALITY OF 60% AT A FOAM VELOCITY OF 6 CM/S..... 113

FIGURE 3.49 POLAROGRAPHIC SIGNALS OVER THREE WALLS: (A) BOTTOM; (B) LATERAL AND (C) TOP; FOR A FOAM QUALITY OF 65% AT A FOAM VELOCITY OF 6 CM/S..... 114

FIGURE 3.50 POLAROGRAPHIC SIGNALS OVER THREE WALLS: (A) BOTTOM; (B) LATERAL AND (C) TOP; FOR A FOAM QUALITY OF 70% AT A FOAM VELOCITY OF 6 CM/S..... 115

FIGURE 3.51 POLAROGRAPHIC SIGNALS OVER THREE WALLS: (A) BOTTOM; (B) LATERAL AND (C) TOP; FOR A FOAM QUALITY OF 75% AT A FOAM VELOCITY OF 6 CM/S..... 116

FIGURE 3.52 POLAROGRAPHIC SIGNALS OVER THREE WALLS: (A) BOTTOM; (B) LATERAL AND (C) TOP; FOR A FOAM QUALITY OF 80% AT A FOAM VELOCITY OF 6 CM/S..... 117

FIGURE 3.53 POLAROGRAPHIC SIGNALS OVER THREE WALLS: (A) BOTTOM; (B) LATERAL AND (C) TOP; FOR A FOAM QUALITY OF 85% AT A FOAM VELOCITY OF 6 CM/S..... 118

FIGURE 3.54 PROBABILITY DENSITY FUNCTION OF THE VELOCITY GRADIENT OBTAINED WITH THREE POLAROGRAPHIC PROBES OVER THE TOP WALL FOR: (A) CASE I; (B) CASE II AND (C) CASE III..... 120

FIGURE 3.55 PROBABILITY DENSITY FUNCTION OF THE VELOCITY GRADIENT OBTAINED WITH THREE POLAROGRAPHIC PROBES OVER THE LATERAL WALL FOR: (A) CASE I; (B) CASE II AND (C) CASE III. 120

FIGURE 3.56 STANDARD DEVIATIONS OF THE VELOCITY GRADIENTS OBTAINED WITH THE POLAROGRAPHIC PROBES OVER THE LATERAL WALL FOR ALL FOAM QUALITIES AND VELOCITIES: (A) CASE I; (B) CASE II AND (C) CASE III..... 121

FIGURE 3.57 STANDARD DEVIATIONS OF THE VELOCITY GRADIENTS OBTAINED WITH THE POLAROGRAPHIC PROBES OVER THE TOP WALL FOR ALL FOAM QUALITIES AND VELOCITIES: (A) CASE I; (B) CASE II AND (C) CASE III. 121

FIGURE 3.58 SKEWNESS COEFFICIENTS OF THE VELOCITY GRADIENTS OBTAINED WITH THE POLAROGRAPHIC PROBES OVER THE LATERAL WALL FOR ALL FOAM QUALITIES AND VELOCITIES: (A) CASE I; (B) CASE II AND (C) CASE III..... 122

FIGURE 3.59 SKEWNESS COEFFICIENTS OF THE VELOCITY GRADIENTS OBTAINED WITH THE POLAROGRAPHIC PROBES OVER THE TOP WALL FOR ALL FOAM QUALITIES AND VELOCITIES: (A) CASE I; (B) CASE II AND (C) CASE III. 122

FIGURE 3.60 FLATNESS FACTORS OF THE WALL VELOCITY GRADIENTS OBTAINED WITH THE POLAROGRAPHIC PROBES OVER THE LATERAL WALL FOR ALL FOAM QUALITIES AND VELOCITIES: (A) CASE I; (B) CASE II AND (C) CASE III..... 123

FIGURE 3.61 FLATNESS FACTORS OF THE VELOCITY GRADIENTS OBTAINED WITH THE POLAROGRAPHIC PROBES OVER THE LATERAL WALL FOR ALL FOAM QUALITIES AND VELOCITIES: (A) CASE I; (B) CASE II AND (C) CASE III..... 123

FIGURE 3.62 WALL SHEAR STRESS OBTAINED OVER THE LATERAL WALL WITH THE VELOCITY PROFILES AND THE LIQUID FILM THICKNESSES FOR ALL FOAM QUALITIES AND VELOCITIES: (A) CASE I; (B) CASE II AND (C) CASE III..... 124

FIGURE 3.63 WALL SHEAR STRESS OBTAINED OVER THE TOP WALL WITH THE VELOCITY PROFILES AND THE LIQUID FILM THICKNESSES FOR ALL FOAM QUALITIES AND VELOCITIES: (A) CASE I; (B) CASE II AND (C) CASE III. 124

FIGURE 3.64 WALL SHEAR STRESS OBTAINED OVER THE BOTTOM WALL WITH THE VELOCITY PROFILES AND THE LIQUID FILM THICKNESSES FOR ALL FOAM QUALITIES AND VELOCITIES: (A) CASE I; (B) CASE II AND (C) CASE III..... 125

FIGURE 3.65 WALL SHEAR STRESS OBTAINED OVER THE LATERAL WALL WITH THE POLAROGRAPHIC PROBES FOR ALL FOAM QUALITIES AND VELOCITIES: (A) CASE I; (B) CASE II AND (C) CASE III. 125

FIGURE 3.66 WALL SHEAR STRESS OBTAINED OVER THE BOTTOM WALL WITH THE POLAROGRAPHIC PROBES FOR ALL FOAM QUALITIES AND VELOCITIES: (A) CASE I; (B) CASE II AND (C) CASE III.	126
FIGURE 3.67 WALL SHEAR STRESS OBTAINED OVER THE TOP WALL WITH THE POLAROGRAPHIC PROBES FOR ALL FOAM QUALITIES AND VELOCITIES: (A) CASE I; (B) CASE II AND (C) CASE III.	126
FIGURE 3.68 MEAN WALL SHEAR STRESS ALONG THE SQUARE CHANNEL’S SURFACE FOR ALL FOAM QUALITIES AND VELOCITIES: (A) CASE I; (B) CASE II AND (C) CASE III.	127
FIGURE 3.69 INFLUENCE OF THE BUBBLES PASSAGE OVER THE ISOCONCENTRATION LINES ON THE ELECTROCHEMICAL ELECTRODES.....	128
FIGURE 3.70 ISOCONCENTRATION LINES FOR $Y=2.5$	129
FIGURE 3.71 EVOLUTION OF THE CONCENTRATION “C” IN THREE-DIMENSIONS FOR $Y=2.5$ (OBTAINED NUMERICALLY)	129
FIGURE 3.72 LATERAL SCHEMATIC REPRESENTATIONS OF THE THREE FDD: (A) FENCE; (B) CYLINDER AND (C) HALF-SUDDEN EXPANSION (DIMENSIONS IN MM)	131
FIGURE 3.73 AXIAL VELOCITY PROFILES UPSTREAM OF THE THREE FDD FOR ALL QUALITIES AND CASES:	132
FIGURE 3.74 EVOLUTION OF THE STATIC PRESSURE ALONG THE TEST CHANNEL WITH A “HALF-SUDDEN EXPANSION” FOR ALL FOAM QUALITIES AND CASES: (A) CASE I; (B) CASE II AND (C) CASE III.	132
FIGURE 3.75 EVOLUTION OF THE STATIC PRESSURE ALONG THE TEST CHANNEL WITH A FENCE FOR ALL FOAM QUALITIES AND CASES: (A) CASE I; (B) CASE II AND (C) CASE III.	133
FIGURE 3.76 EVOLUTION OF THE STATIC PRESSURE ALONG THE TEST CHANNEL WITH A FENCE FOR ALL FOAM QUALITIES AND CASES: (A) CASE I; (B) CASE II AND (C) CASE III.	133
FIGURE 3.77 PRESSURE GRADIENT FOR ALL FOAM QUALITIES AND CASES: (A) UPSTREAM AND (B) DOWNSTREAM OF THE HALF-SUDDEN EXPANSION	133
FIGURE 3.78 PRESSURE GRADIENT FOR ALL FOAM QUALITIES AND CASES: (A) UPSTREAM AND (B) DOWNSTREAM OF THE FENCE.....	134
FIGURE 3.79 PRESSURE GRADIENT FOR ALL FOAM QUALITIES AND CASES: (A) UPSTREAM AND (B) DOWNSTREAM OF THE CYLINDER.....	134
FIGURE 3.80 AVERAGED AXIAL AND VERTICAL MEAN VELOCITY FIELDS FOR ALL QUALITIES AND THE CASE I OVER THE HALF-SUDDEN EXPANSION.	136
FIGURE 3.81 AVERAGED AXIAL AND VERTICAL MEAN VELOCITY FIELDS FOR ALL QUALITIES AND THE CASE II OVER THE HALF-SUDDEN EXPANSION.	137
FIGURE 3.82 AVERAGED AXIAL AND VERTICAL MEAN VELOCITY FIELDS FOR ALL QUALITIES AND THE CASE III OVER THE HALF-SUDDEN EXPANSION.	138
FIGURE 3.83 AVERAGED AXIAL AND VERTICAL MEAN VELOCITY PROFILES FOR ALL QUALITIES, THE CASE I AND DIFFERENT DISTANCES OVER THE HALF-SUDDEN EXPANSION.	140
FIGURE 3.84 AVERAGED AXIAL AND VERTICAL MEAN VELOCITY PROFILES FOR ALL QUALITIES, THE CASE II AND DIFFERENT DISTANCES OVER THE HALF-SUDDEN EXPANSION.	141
FIGURE 3.85 AVERAGED AXIAL AND VERTICAL MEAN VELOCITY PROFILES FOR ALL QUALITIES, THE CASE III AND DIFFERENT DISTANCES OVER THE HALF-SUDDEN EXPANSION.	142
FIGURE 3.86 AVERAGED AXIAL AND VERTICAL MEAN VELOCITY FIELDS FOR ALL QUALITIES AND THE CASE I OVER THE FENCE.....	144
FIGURE 3.87 AVERAGED AXIAL AND VERTICAL MEAN VELOCITY FIELDS FOR ALL QUALITIES AND THE CASE II OVER THE FENCE.....	145
FIGURE 3.88 AVERAGED AXIAL AND VERTICAL MEAN VELOCITY FIELDS FOR ALL QUALITIES AND THE CASE III OVER THE FENCE.	146
FIGURE 3.89 AVERAGED AXIAL AND VERTICAL MEAN VELOCITY PROFILES FOR ALL QUALITIES, THE CASE I AND DIFFERENT DISTANCES OVER THE FENCE.	148
FIGURE 3.90 AVERAGED AXIAL AND VERTICAL MEAN VELOCITY PROFILES FOR ALL QUALITIES, THE CASE II AND DIFFERENT DISTANCES OVER THE FENCE.	149
FIGURE 3.91 AVERAGED AXIAL AND VERTICAL MEAN VELOCITY PROFILES FOR ALL QUALITIES, THE CASE III AND DIFFERENT DISTANCES OVER THE FENCE.	150
FIGURE 3.92 AVERAGED AXIAL AND VERTICAL MEAN VELOCITY FIELDS FOR ALL QUALITIES AND THE CASE I OVER THE CIRCLE	152
FIGURE 3.93 AVERAGED AXIAL AND VERTICAL MEAN VELOCITY FIELDS FOR ALL QUALITIES AND THE CASE II OVER THE CIRCLE.	153

FIGURE 3.94 AVERAGED AXIAL AND VERTICAL MEAN VELOCITY FIELDS FOR ALL QUALITIES AND THE CASE III OVER THE CIRCLE.	154
FIGURE 3.95 AVERAGED AXIAL AND VERTICAL MEAN VELOCITY PROFILES FOR ALL QUALITIES, THE CASE I AND DIFFERENT DISTANCES OVER THE CIRCLE.	156
FIGURE 3.96 AVERAGED AXIAL AND VERTICAL MEAN VELOCITY PROFILES FOR ALL QUALITIES, THE CASE II AND DIFFERENT DISTANCES OVER THE CIRCLE.	157
FIGURE 3.97 AVERAGED AXIAL AND VERTICAL MEAN VELOCITY PROFILES FOR ALL QUALITIES, THE CASE III AND DIFFERENT DISTANCES OVER THE FENCE.	158
FIGURE 3.98 AVERAGED AXIAL VELOCITY PROFILES FOR AN AQUEOUS FOAM AND A BINGHAM FLUID UPSTREAM OF THE THREE FDD AT X = -35 MM: (A) HALF-SUDDEN EXPANSION, (B) FENCE AND (C) CYLINDER.	163
FIGURE 3.99 EVOLUTION OF THE STATIC PRESSURE LOSSES FOR AN AQUEOUS FOAM AND A BINGHAM FLUID THROUGH THREE FDD: (A) HALF-SUDDEN EXPANSION, (B) FENCE AND (C) CYLINDER.	164
FIGURE 3.100 AVERAGED AXIAL VELOCITY FIELD OF AN (A) EXPERIMENTAL AQUEOUS FOAM AND A (B) CFD BINGHAM FLUID FLOWING TROUGH A HALF-SUDDEN EXPANSION.	165
FIGURE 3.101 AVERAGED VERTICAL VELOCITY FIELD OF AN (A) EXPERIMENTAL AQUEOUS FOAM AND A (B) CFD BINGHAM FLUID FLOWING TROUGH A HALF-SUDDEN EXPANSION.	165
FIGURE 3.102 AVERAGED AXIAL VELOCITY FIELD OF AN (A) EXPERIMENTAL AQUEOUS FOAM AND A (B) CFD BINGHAM FLUID FLOWING TROUGH A FENCE.	166
FIGURE 3.103 AVERAGED VERTICAL VELOCITY FIELD OF AN (A) EXPERIMENTAL AQUEOUS FOAM AND A (B) CFD BINGHAM FLUID FLOWING TROUGH A FENCE.	166
FIGURE 3.104 AVERAGED AXIAL VELOCITY FIELD OF AN (A) EXPERIMENTAL AQUEOUS FOAM AND A (B) CFD BINGHAM FLUID FLOWING TROUGH A CYLINDER.	167
FIGURE 3.105 AVERAGED VERTICAL VELOCITY FIELD OF AN (A) EXPERIMENTAL AQUEOUS FOAM AND A (B) CFD BINGHAM FLUID FLOWING TROUGH A CYLINDER.	168
FIGURE 3.106 AVERAGED AXIAL AND VERTICAL MEAN VELOCITY PROFILES FOR AQUEOUS FOAM AND A BINGHAM FLUID GOING THROUGH A HALF-SUDDEN EXPANSION.	169
FIGURE 3.107 AXIAL AND VERTICAL MEAN VELOCITY PROFILES FOR AQUEOUS FOAM AND A BINGHAM FLUID GOING THROUGH A FENCE.	170
FIGURE 3.108 AVERAGED AXIAL AND VERTICAL MEAN VELOCITY PROFILES FOR AQUEOUS FOAM AND A BINGHAM FLUID GOING THROUGH A CYLINDER.	171

TABLES INDEX

CHAPTER 1	5
TABLE 1.1 BUBBLE SIZE AND DENSITY IN DIFFERENT PRODUCTS [2].....	10
TABLE 1.2 NON-NEWTONIAN MODELS PRESENT INSIDE THE ANSYS CFX SOFTWARE.....	46
CHAPTER 2	49
TABLE 2.1 FOAM FLOW CHARACTERIZATION CASES	65
TABLE 2.2 SPATIAL CHARACTERISTICS FOR EACH FDD	66
TABLE 2.3 ACTIVE PROBES DIAMETERS [MM]	72
CHAPTER 3	75
TABLE 3.1 SENSITIVE STUDY OF THE PECLLET NUMBER AND CRITICAL THICKNESS OF THE MASS BOUNDARY LAYER IN ORDER TO ATTAIN A DIFFUSION LIMITING CURRENT.	129
TABLE 3.2 AVERAGED VERTICAL VELOCITY VALUES UPSTREAM AND DOWNSTREAM, AT THE UPPER AND LOWER PART OF THE CHANNEL, NEAR THE CYLINDER IN ALL CASES ($x = -5$ MM, $x = 0$ MM AND $x = 5$ MM).....	155
TABLE 3.3 MESH CHARACTERISTICS (CELL NUMBERS AND SMALLER CELL).....	161
TABLE 3.4 GCI RESULTS	162
TABLE 3.5 RHEOLOGICAL PROPERTIES OF BINGHAM FLUIDS FOR EACH FDD	163

NOMENCLATURE

ABBREVIATIONS

Symbol	Description
<i>sstrnr</i>	Shear strain rate
<i>FDD</i>	Flow Disruption Devices
<i>GCI</i>	Grid Convergence Index
<i>PDF</i>	Probability Density Function
<i>PIV</i>	Particle Imaging Velocimetry

ROMAN LETTERS

Symbol	Description	Units
<i>a</i>	Matrix coefficient	
<i>A</i>	Surface	m^2
<i>b</i>	Grid hand size	
<i>c</i>	Concentration	$mol.m^{-3}$
<i>C</i>	Carbone	
<i>Ca*</i>	Capillary number	
<i>Cp/Cv</i>	Isotropic expansion	
<i>CF</i>	Friction factor	
<i>d</i>	Diameter	m
<i>D</i>	Diffusion coefficient	$m^2.s^{-1}$
<i>Dg</i>	Gas density compared to the air at normal conditions	
<i>e</i>	Liquid Film Thickness	m
<i>e_x</i>	Unit vector in the x coordinate direction	
<i>e⁻</i>	Electron	$[-]$
<i>E</i>	Energy	J
<i>EF</i>	Expansion factor	
<i>f</i>	Frequency	Hz
<i>F</i>	Faraday number (96500 C)	C
<i>F(t)</i>	Normalized reducing function	
<i>Fe</i>	Iron	
<i>g</i>	Gravity	$m^2.s^{-1}$
<i>G</i>	Shear modulus	Pa
<i>h(s)</i>	Impulse response	$N.s$
<i>h₁, h₂</i>	Height of the liquid column out of the pressure outlets	m
<i>h</i>	Enthalpy	J
<i>H</i>	Total foam height	m
<i>H(f)</i>	Transfer function	
<i>i</i>	Electric current intensity	A
<i>k</i>	Consistency index	$Pa.s$

k_f	Film permeability	m^2
k_m	Mass coefficient transfer	$m.s^{-1}$
K	Potassium	
K	Gain	
\mathcal{F}	Kurtosis	
K_T	Gas compression modulus	Pa
l	Probe width	m
l_{ij}	Length of the films separating neighbor bubbles	m
L	Length	m
M	Momentum source	$N.s$
n	Power law index	
N	Nitrogen	
N_1, N_2	Normal Stress	Pa
O	Oxygen	
Ox	Oxidant	[+]
p	Depth to which foam extends beneath the liquid surface	m
P	Pressure	Pa
Pe	Peclet number	
P_m	Wetted perimeter	m
q	Flow rate	$m^3.s^{-1}$
Q	Flow	$m^3.s^{-1}$
r	Radius of curvature of the cross section of a Plateau border	m
r_1, r_2	Radii of curvature of a Plateau border	m
R	Duct region	m
R_{32}	Sauter mean radius	m
Re	Reducer	[-]
$s(t)$	Sinusoidal perturbations	
S	Sodium	
S	Wall velocity gradient	s^{-1}
Sc	Schmidt number	
\mathfrak{S}	Skewness	
Sh	Sherwood number	
S_{ij}	Strain rate tensor	s^{-1}
t	Time	s
T	Temperature	K
T_i	Intensity of the laser transmitted	$W.m^{-2}$
u	Axial velocity	$m.s^{-1}$
U	Velocity $f(x,y,z)$	$m.s^{-1}$
Up	Tension	V
v	Vertical velocity	$m.s^{-1}$
V	Volume	m^3
W_{ii}	Power spectral density of the limit intensity	$A^2.s$
W_{ss}	Power spectral density of the wall velocity gradient	s^{-1}
x, y, z	Coordinates	
X, Y, Z	Characteristic length scales	
z_e	Electron number	

GREEK LETTERS

Symbol	Description	Units
α_{sp}	Asymptotic curve of Cottrel	$A.s^{-2}$
β	Foam quality	
B	Oscillation amplitude	
γ	Yield strain	s^{-1}
Γ	Surface tension	N/m
δ	Slip layer thickness	m
Δ	Difference	
λ	Time constant	s
μ	Dynamic viscosity	$Pa.s$
ν	Kinematic viscosity	$m^2.s^{-1}$
Π	Osmotic pressure of the foam	Pa
ρ	Density	$Kg.m^{-3}$
σ	Conductivity	Ω
τ	Shear stress	Pa
φ	Solution vector	
ϕ	Void fraction	
ψ	Liquid flux	$m^3.m^{-2}.s$
ω	Real pulsations	s^{-1}
Ω	Oscillation pulsations	s^{-1}

SUBSCRIPTS

Symbol	Description
0	Characteristic
<i>a</i>	Atmospheric
<i>b</i>	Bubble
<i>c</i>	Corrected
<i>cp</i>	Close packing
<i>crit</i>	Close packing
<i>d</i>	Rectangular
<i>e</i>	Establishment
<i>f</i>	Foam
<i>g</i>	Gas
<i>gr</i>	Reference gas flow
<i>h</i>	Hydraulic
<i>in</i>	Foam generator inlet
<i>l</i>	Liquid
<i>lim</i>	Limit diffusion current
<i>loc</i>	Local
<i>out</i>	Foam generator outlet
<i>p</i>	Obtained through the polarographic technique
<i>q</i>	Quasi-stationary state
<i>r</i>	Relative
<i>s</i>	Electrode
<i>sf</i>	Speed of sound inside the foam
<i>slip</i>	Slip velocity
<i>t</i>	Total
<i>velocity</i>	Obtained through the velocity profiles

w	Foam-wall friction
γ_0	Capillary
τ	Friction velocity
∞	At the fluids core

SUPERSCRIPTS

Symbol	Description
*	Dimensionless value
\rightarrow	Vector
'	Fluctuating value
—	Mean
·	Rate

INTRODUCTION

A question not easy to answer is whether “foam” is a liquid or a solid. Different scientists, coming most of them with similar answers, have discussed this item. The main objective of this work has to do with this question; we approach it by studying the physical phenomena of this complex flow, in its structure, stability and hydrodynamic behavior. The resulting experimental database may be used to validate rheological models developed for this complex fluid.

For an excellent review of a foam experience, please consider the following”:

“For a bottle of beer. Restraining your thirst for the moment, admire its lively performance. One by one, bubbles of gas are nucleated, rise and crowd together at the surface. A foam, or froth is quickly formed. Most of the liquid drains away; leaving the bubbles packed closely together in the form of elegant polyhedral cells. This gradual change is punctuated by sudden local rearrangements. In most brands of beer it is quickly overtaken by the collapse of the foam, as its individual films burst. Drink it in time, and you can feel the foam is not a liquid. Paradoxically, it is a soft solid, creamy in texture if the bubbles are small. Cheers!” [1].

The above excerpt covers many relevant observations concerning foam behavior, its transformations and dependence on many elements and conditions. Besides following a detailed review of foam research publications, this doctoral work conducted experimental validations of foam parameters under complex conditions. Being of great importance for many industries the optimum availability and handling of special foams, this work should result on practical applications, but additionally be a base for further research projects on “Foam”.

The word “Foam” originates from the medieval German “Veim”. Foams form by trapping pockets of gas in a liquid or solid. In most of them, the volume of gas is larger than the liquid one, which forms thin films separating the gas. In practice, “froth” usually designates foam on top of a liquid. It never refers to solid foam. The closest analogue is the emulsions, in which two liquids combine, the same way as do liquid and gas in a foam. The same behavior also occurs in polymer gel (carbopol) and biological systems as cytoskeletal arrangements.

Foam may contain more or less liquid. Dry foam, for instance, has lesser liquid in thin films. The bubbles form polyhedral cells, which are not flat. The films meet in lines (edges of the polyhedral), and the lines meet at vertices. In two dimensions, the dry foam consists of polygonal cells (Figure I.1.a). The liquid is mainly to be found in Plateau borders, which are channels of finite width, replacing the lines in the dry foam (Figure I.2). As the fraction of liquid increases, the swelling of the plateau borders eventually leads to the extreme limit of a wet foam. The bubbles recover a spherical form and any further increase of liquid will make them to fall apart. Then, the foam losses its rigidity and it is replaced by a bubbly liquid. For a two-dimensional case, the bubbles become circular at the stability limit (Figure I.1.b)

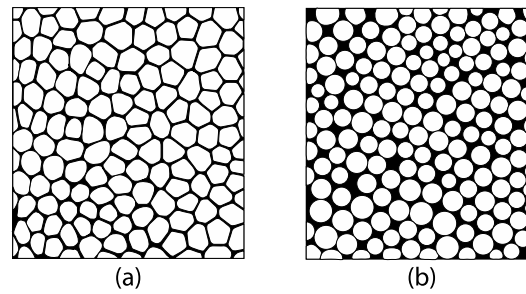


Figure I.1 Dry and Wet Limit [2]

Beating, shaking or nucleation may create foam. The bubbles have a wide size distribution, randomly mixed and arranged. If seen as a macroscopic system, its elements undergo no significant thermal fluctuations, exploring minimum energy alternatives. In this sense, foams are always in a metastable state, even if the bubbles do not coalesce. It continually evolves according to the coarsening process (Figure I.3).

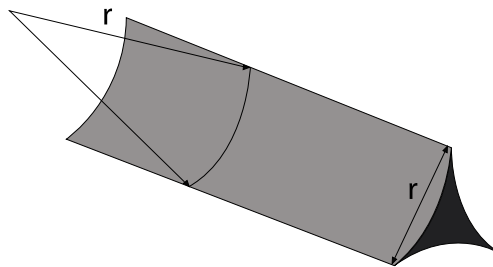


Figure I.2 Plateau Border: liquid film located between bubbles.

Foam has unusual rheology properties: they present low densities and an important interfacial surface. They are mainly composed of gas. But under low applied stress, foam behave as a solid; hence shaving foam adheres to the shaver's face, the weak force of gravity being incapable of letting it flow. This results from an elastic shear modulus, as occurs in isotropic solid materials. It depends only on bubble size and wetness. They can also behave as elastic solid or a plastic one. Beyond a certain yield stress foam flows, as topological changes are promoted indefinitely. This is the second most important parameter characterizing its rheological properties. Dry foams follow the same order as the shear modulus. Wet foams present the same behavior, but their yield stress presents a smaller value.

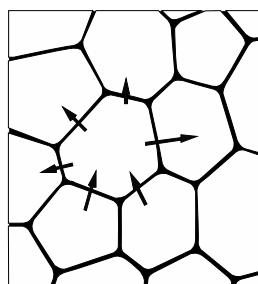


Figure I.3 Foam Coarsening. Air diffusion through the liquid films [1].

It is pertinent to indicate the sizing and scales considered in foams (Figure I.4). The smallest length-scales are that of the surfactant molecules, typically in the order of nanometers. The forces of repulsion (often expressed as a *disjoining pressure*) determine the thickness of the film, in the range 5nm to 10 nm in relative dry foam. There is a medium scale usually applied by physicists to the

relation between bubbles, and in topology transformations -usually in static mode-. The bubble diameter is widely variable, but is in the order of a few millimeters. The Plateau border width is typically a small fraction of this, i.e. a fraction of a millimeter. In an engineering approach, the air and liquid phases are taken as a continuum model. It is normally studied as a foam flow [3]. This author applied the PIV (Particle Image Velocimetry) to evaluate the behavior of aqueous foam along a channel.

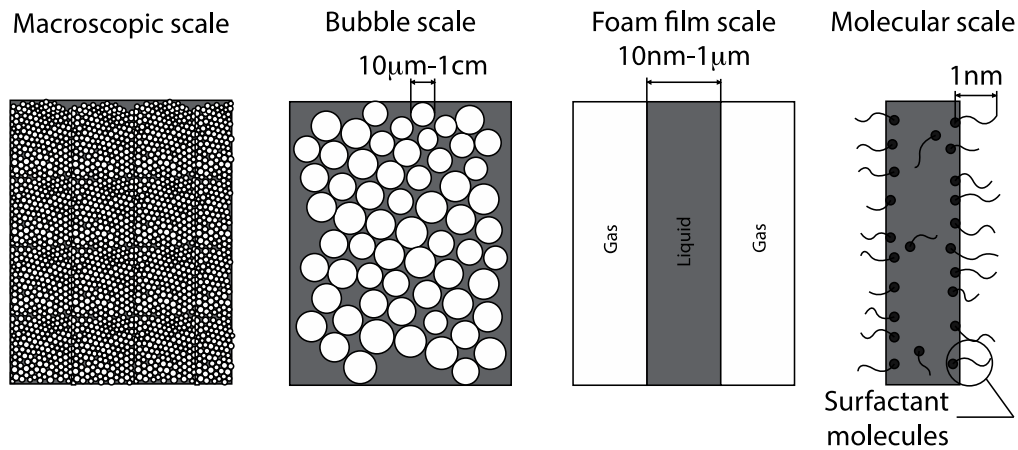


Figure I.4 Characteristics length of the foam.

Foam flow has become a mayor study subject for industries around the world. It is indispensable to better understand its main characteristics, especially the knowledge of the rheological behavior and of the foam stability. Most of the studies carried out focus on the geometry and topology of stationary foam and not on the flow itself, due to its complexity [1,4,5].

Blondin (1999), as we mentioned above, tried to set a rheological model for foam flow, taking into account pressure losses along a duct, but concluded that the losses alone did not allow building the model. Tisé (2003) added an innovative measurement method to combine the pressure losses with the wall shear stress. But at the end, he could not collect enough data to propose a model. The major problem is that a foam flow is influenced by an enormous quantity of parameters. Looking at the high interest shown for foam flow along the industries, it is indispensable to achieve the capacity to understand and evaluate all the variables concerning the hydraulic behavior: pressure losses, velocity distribution and wall shear stress.

Reviewing possible CFD (computational Fluid Mechanics) tools to assist us on this matter, we evaluated ANSYS ®. It is a computer program that can model mechanical processes like fluid flow, heat transfer, chemical reactions, yielding, stress, etc. ANSYS ® acquired other program, FLUENT®, creating an improved fluid simulator. Some other simulations have focused on foam generation [6], physical properties [7], complex rheological behavior [8] and heat exchanges [9]. But they have not compared numerical and experimental results, or have made an intensive study on foam flow.

This experimental work will be a database to validate rheological models, capable of predicting the behavior and reorganization of foam flow through a channel flow disruption devices (fdd) or singularities or obstacles. At the same time, a numerical simulation, using ANSYS-CFX® software will be undertake. Comparing this one with the experimental results, it will be able to test its aptitude to represent this kind of foam flow. Through this research, we will like to understand the behavior of foam flow: its physics, its stability and hydrodynamics. At the same time, establish some guideline to perform the characterization of any complex fluid.

Chapter 1 presents an introduction to the study of foam flow, the theoretical factors surrounding the study of such a complex fluids. It also contains a review of previous works, which talk about structure, stability, rheology, and other properties of flowing foams. These ones will allow a solid background in the study and identify the main concerns around it.

Chapter 2 describes the experimental devices used for the characterization and study of aqueous foam flowing horizontally inside a square channel with flow disruption devices. At the same time, the innovative measurement techniques used, and the setting arrangement for each one of them, especially for the polarographic technique, which allows obtaining the wall shear stress, without an influence over the flow behavior. The measurement chains and the treatments methods will also be specified.

Chapter 3 is dedicated to the experimental and numerical results. First for a square channel without fdd, they alter the rheology and properties of the foam. This allowed obtaining the static pressure losses, the surrounding liquid film thickness, and the wall shear stress, using different measurement techniques. Three different disruption devices, a half-sudden expansion, a fence, and a cylinder, were put inside the channel. They permitted the study of the foam behavior when faced against a change in its pattern. CFD simulations, using a Bingham fluid, reproduce the behavior of aqueous foam flow. The velocity fields and profiles are also presented in this part.

Finally, we conclude this work by summarizing the main obtained results during this research. We propose different aspects to improve the research over foam flow, and which should be the next studies for flowing aqueous foam.

“Great things are done by a series of small things brought together” Vincent Van Gogh

CHAPTER 1

BIBLIOGRAPHY

Aqueous foam is a structured fluid where the air bubbles are separated by a liquid film, generally thin. For an emulsion they are often called *disperse* and *continuous* phase, but this is not in a gas (liquid foam). When bubbles congregate to form foam, they create fascinating structures that evolve as they age. This chapter undertakes a general description of foam flow, its properties, characteristics, and aspects involved in its study. At the same time, a brief narrative is done for the software ANSYS-CFX, used to represent the numerical approximation of the flow behavior.

1. Foam Structure

To better understand the evolution of a foam structure along time, it is important to comprehend some basic parameters: the bubbles characteristics such as distribution, mean diameter, form, influence of the surface tension, the foam viscosity and the void fraction. Foams may be divided into closed-cell foams and open-cell foams. In closed-cell foam, the gas forms discrete pockets, each completely surrounded by the continuous phase. In open-cell foams, the continuous phase can easily flow through the entire structure, displacing the air. These concepts are also known as the dry and wet limit.

1.1 Bubble

Although real foams often have polydisperse disordered bubbles, they are metastable, and the mean size of them tends to increase with time. It is useful to simplify the structure of idealized monodisperse foam. The most conventional structure is the *bcc packing* of rectangular octahedral whose six corners are truncated and create square faces. A commonly used name for this shape is the Kelvin bubble in honor of Lord Kelvin.

According to Lord Kelvin (1887), a bubble is a tetrakaidecahedron (Figure 1.1) or Kelvin cell; six square faces and eight hexagonal ones compose it. Kelvin was inspired by Plateau studies and made a conjecture on the ideal structure of monodisperse foam. He started a chain of investigations and debates that continues today. For example, in 1994 Wearie and Phelan determined which is the optimal arrangement for dry foam composed only of same size bubbles. Applying the software “Surface evolver”, they established that a group of polyhedrons would be the perfect match. The most common cell was made out of fourteen faces: two hexagonal and 12 pentagonal.

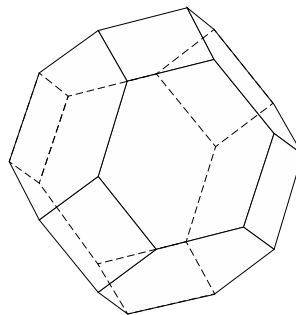


Figure 1.1 Lord Kelvin cell or tetrakaidecahedron [10].

1.2 Surface Tension

Surface Tension (ST) is defined as the quantity of energy needed to augment a liquids surface while maintaining constant entropy. It means that liquids have resilience to augment their surface. It is a manifestation of the intermolecular forces inside the liquids.

$$\Gamma = \left(\frac{\partial E}{\partial A} \right)_S \quad (1.1)$$

ST depends on numerous factors: the size of the hydrophobic and hydrophilic parts, their nature, and their dispersity. Indeed, the energy presented by a molecule can vary according to its location.

Energy is larger if it is located at the liquids surface, because being surrounded by a lower number of similar molecules.

1.3 Void Fraction and Foam Quality

For foam made out of a known gas volume V_g and a known liquid volume V_l , we can define the void fraction, as a measure of the empty spaces inside the foam.

$$\phi = \frac{V_g}{V_t} \quad (1.2)$$

where V_t corresponds to the total foam volume; such as $V_t = V_l + V_g$. For a foam flow, the foam quality expression is often used:

$$\beta = \frac{Q_g}{Q_t} \quad (1.3)$$

where Q_g represents the gas flow and $Q_t = Q_g + Q_l$, with Q_l as the liquid flow. Some authors prefer to apply the expansion factor term [11,12,13].

$$EF = \frac{1}{1 - \phi} \quad (1.4)$$

1.4 Foams, Wet and Dry

Foams may be classified as dry or wet according to liquid volume fraction. It ranges from less than 1% to about 30%. At each extreme (the dry and the wet limits) the bubbles come together to form a structure which resembles one of the classic idealized paradigms of nature's morphology: the division of cells in the dry limit, and the close-packing of spheres in the wet limit.

Bubble size is important in determining the resulting equilibrium under gravity. If the average bubble diameter is less than the capillary length l_0 , a thin layer of foam consisting of small bubbles will be wet (i.e. have liquid fraction larger than about 20%).

$$L_{\gamma 0}^2 = \frac{\Gamma}{\Delta\rho g} \quad (1.5)$$

where Γ is the surface tension of the liquid, g the acceleration due to gravity and $\Delta\rho$ is the density difference between the gas and liquid.

1.4.1 The Dry Limit

In the dry limit, the soap films that constitute the interface between bubbles may be idealized as infinitesimally thin curved surfaces, which are generally not simply spherical. These surfaces constitute the faces of polyhedral cells. Many varieties of polyhedral are found in equilibrated dry foams [14]. As showed before in 2D geometry, dry foam consists of polygonal cells. Since the vertices can only be threefold, it follows -from the Euler's theorem- that the average number of sides a cell is exactly six [1].

1.4.2 The Wet Limit

In the wet limit, only spherical bubbles form foam. There are restrictions on the possibilities for such packing of hard spheres, familiar in the idealized models used in the field of granular material. Each sphere must be in contact with at least three others. For a random compact stacking of the spheres, it has been proved that the sphere bubbles will occupy 63.5% of the volumetric fraction [15].

For the 2D case, the cells are touching circular disks. As in the 3D case, we make contact with close packed structures and hence with the theory of granular materials [16].

1.4.3 Between the Two Limits

A real foam must lie somewhere between these two idealized cases. Let us start from the dry end, first considering the addition of an amount of liquid that is large enough that we may neglect the liquid content of the films, but nevertheless still close to the dry limit. It is not obvious what happens in the intermediate regime. Some authors have established a value of 85% for the change of limit, but they also admit that it may seem a bit arbitrary [17].

The gas volume fraction changes constantly along the foams age (time that separates it from the instant of its generation). A humid foam losses progressively the liquid inside it, normally by drainage and becomes dry foam.

1.5 Foam Density

The density of aqueous foam is defined as its mass per unit volume. It is, essentially, a measurement of how tightly matter is crammed together. The Greek scientist Archimedes created the first principle of density as an innovative way to quantify the materials used to elaborate the king's crown. As foam is made out of gas and liquid, it can be usually calculated as [18]:

$$\rho_f = (1 - \beta)\rho_l + \beta\rho_g \quad (1.6)$$

where ρ_l and ρ_g are respectively the densities of water and air.

1.6 Thin liquid film

In foams, the liquid films between two adjacent gas bubbles are composed of two surfactant monolayers separated by a thin layer of water. The overlap of interaction between the two layers induces a force normal to the interfaces. The pressure can be either positive or negative, and its magnitude depends upon the thickness of the film.

This pressure has been measured experimentally by maintaining a balance between capillary and thin film forces [19]. In later experimental improvements, a single thin-liquid film is formed in a hole drilled through a solution saturated fritted glass disk fused to a capillary tube. The film holder is enclosed in a hermetically sealed Plexiglas cell with the capillary tube exposed to a constant reference pressure. The solution under investigation is placed in a glass container within the cell to prevent contact or any contamination with the Plexiglas chamber. Manipulation of the cell pressure with a precise screw-driven syringe pump alters the imposed capillary pressure, P_c , on the film and sets the disjoining pressure. Once equilibrium is established, the aqueous core film thickness, h , is measured using an optical interferometer [20].

2. Local Equilibrium Rules

2.1 The Law of Laplace

The surfaces that constitute the cell faces of any foam must normally conform to the law of Laplace-Young. It expresses the balance of forces on a small element of soap film, in terms of a pressure difference ΔP , and the force of surface tension.

$$\Delta P = \frac{2\Gamma}{r} \quad (1.7)$$

where r is the local radius of curvature of the surface. This one is the inverse *mean* local curvature, which is related to the two principal curvatures by:

$$\frac{2}{r} = \frac{1}{r_1} + \frac{1}{r_2} \quad (1.8)$$

In the general case of dry foams, r_1 differs from r_2 . For the case of a sphere $r_1 = r_2$. In an ordinary soap bubble in air, or in a film within foam, eqn. (1.1) must be adjusted on account of the surface involved, although γ_s is sometimes used in place of 2γ .

$$\Delta P = \frac{4\Gamma}{r} \quad (1.9)$$

The pressure within the films is the mean of the two gas pressures in the adjacent cells. This is inconsistent with the equality of pressure throughout the liquid, since a much lower pressure exists inside the Plateau borders. To resolve this discrepancy, we need to recognize that the thin film is prevented from shrinking to zero thickness, by the repulsive forces between its two surfaces. These forces per unit area may be represented as a pressure to be included in the equilibrium condition. This is the *disjoining pressure* (Figure 1.2).

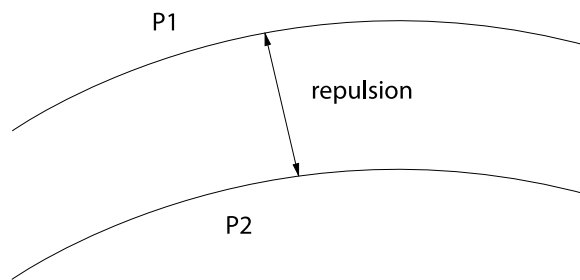


Figure 1.2 Disjoining Pressure: presence of a repulsion force inside the liquid films [1].

2.2 The Laws of Plateau

Plateau [21] developed some geometrical rules (“equilibrium rules”) for the foam structure. They define an equilibrium configuration, studying foams in the dry limit and also in the more general case.

Equilibrium rule A1. For dry foams, the films intersect only three at a time, that being at 120° . In two dimensions, this applies to the lines that define the cell boundaries. This union gives form to the *Plateau border*, or film liquid between bubbles. Results into the equilibrium of three equal surface tension force vectors acting at the intersection.

Equilibrium rule A2. Again for dry foams, no more than four of the intersection lines (or six of the surfaces) may meet at the vertices of the structure, and this tetrahedral vertex is perfectly symmetric. All the angles (Maraldi) have the value $\phi = \cos^{-1}(-1/3)$. This union is also called *Plateau junction*. For wet foams, the above rules must be reconsidered, and the film thickness may still be treated as infinitesimal. The thickness depends on the volume fraction and tensoactive quantity [15].

Equilibrium rule B. Where a Plateau border meets an adjacent film, the surface is joined smoothly, that is, the surface normal is the same on both sides of the intersection. This means that the Plateau borders terminate in sharp cusps, as in Figure 1.3 and in previous figures. There are however

no general stability rules for the multiplicity of the intersections at Plateau borders, or their intersections junctions.

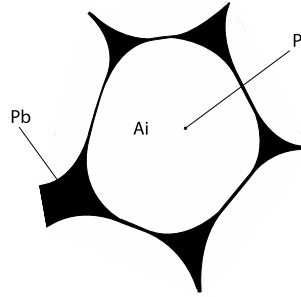


Figure 1.3 Plateau borders are smoothly joined to the adjacent film [1].

2.3 Bubble-bubble interaction

The bubbles in a flow with a high liquid content are spherical or nearly so. As the liquid drains out, due to gravity the individual bubbles are deformed into polyhedral shapes. The *osmotic pressure* is described as the average force per unit area necessary to counter the increasing bubble-bubble repulsion, as they are squeezed together.

$$\Pi = - \left(\frac{\partial E}{\partial V} \right)_{Vg} \quad (1.10)$$

where E is the total surface energy as $E = \gamma S$, and V the total foam volume. Regarding the bubbles as the primary constituents of wet foam, may lead to limiting views of their interactions.

Products	Bubble diameter (μm)	Estimated number density (cm^{-3})	Notes
Shaving foam	10-20	10^8	Aerosol generated with initial $\phi = 0.926$ [22].
Ice cream	15-40	10^7	For a 100% overrun ice cream $\phi = 0.926$ [23].
Microcellular starch foam	50-200	10^6	Continuous supercritical CO_2 fluid extrusion [24].
Bread	2500 area av. 600 number av.	10^3	Many small cells contribute to the foam, but the large cohort of the population dominates the visual appearance [25].
Hand dish washing-up detergent	3000	10^2	Shaking/tumbling/impinged jets, initial $\phi = 0.995$ [26].
Bubble bath	5000	10	Bubble size depends on generation method.

Table 1.1 Bubble size and density in different products [2]

3. Making Foams

Many foam production techniques are applied for the range of consumer products. This range from stable, monodisperse foams of micro-sized bubbles in shaving foam, to the transitory ones, up to a centimeter in bubble baths and laundry detergents. The location of creation also varies, from the production line, to the actual point of use. The range of foam creation requirements is illustrated in Table 1.1.

3.1 Surfactants

Liquids that are absolutely pure generally do not foam, as any gas bubble will immediately coalesce on contact or rupture at a surface. As foams last longer, they move from a *transient* (unstable) nature, in some applications, to a *persistent* (metastable), nature desired in most consumer products.

Even in aqueous foams, there is a vast choice of surfactants. They offer a wide range of properties, useful for specific industries areas: capability to foam and disperse, to lubricate, anti-static, softener, anti-corrosive and dampener.

Most surfactants are organic *amphiphilic* compounds, meaning they contain both *hydrophobic* (tails) and *hydrophilic* (heads) groups (Figure 1.4). A surfactant contains both water insoluble and water-soluble components. The insoluble hydrophobic group may extend, into the air, out of the bulk water phase while the water-soluble head group remains in the water phase.

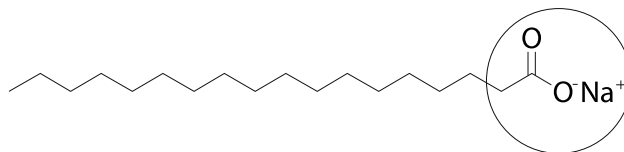


Figure 1.4 Sodium stearate, the most common component of most soap, makes about 50% of commercial surfactants.

The polar head part defines three groups of surfactants (Figure 1.5):

- **The ionic surfactants:** The hydrophilic head presents a positive or a negative charge. The *anionic* surfactants ionize themselves, in the aqueous solution, to give negative charged ions. They are normally used in the cosmetic and detergent industry, also in the assisted recovery of oil. In the *cationic* surfactants, the heads present positive charged ions. They are applied in the bituminous coal emulsion fabrication.
- **The amphoteric surfactant:** The heads have both, positive and negative, localized charges. They are biodegradable and are normally used in the cosmetics industry.
- **The non-ionic surfactants:** The polar group does not present any type of charge. They are commonly applied in the pharmaceutical applications.

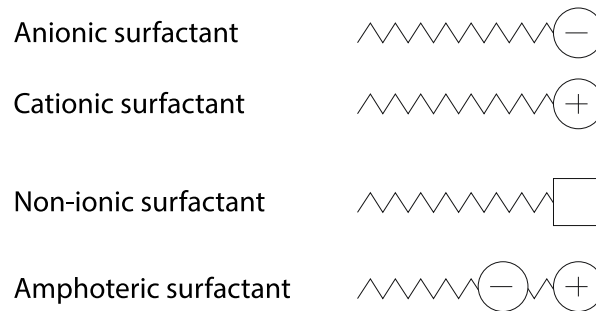


Figure 1.5 Surfactant Groups accordingly to its head charge

The size of a surfactant molecule affects its diffusivity in solution. While a larger molecule (for example, a protein) might have a high surface active, it may not diffuse quickly enough to stabilize a surface that only exists for a short period of time. This can be significant when the objective is to create very small daughter bubbles by break-up. It is not sufficient to make bubbles small enough; a surfactant layer must be adsorbed quickly enough to stabilize the bubble before it experiences a collision that risks coalescence [27].

The industrial application of these molecules is growing every day, because of their physicochemical properties. They attach to interphases and lower the surface tension of the solution and the liquid films energy, prompting foam formation.

3.1.1 Critical Micelle Concentration (CMC)

The surfactant properties of a foaming agent may include: effectiveness at reducing surface tension, diffusion ability, disjoining pressure properties in films, elastic properties given to films [28]. Generally, foaming characteristics increase up to the critical micelle concentration (CMC). As already established, the principal foam property is its surface tension. As the surfactant concentration increases, the superficial tension diminishes.

In colloidal and surface chemistry, CMC is defined as the concentration of surfactant above which micelles form, and all additional surfactants added to the system compose them. It is an important characteristic of a surfactant. Before reaching the CMC, the surface tension changes strongly with the concentration of the surfactant. After reaching the CMC, the surface tension remains relatively constant, or changes with a lower slope (Figure 1.6).

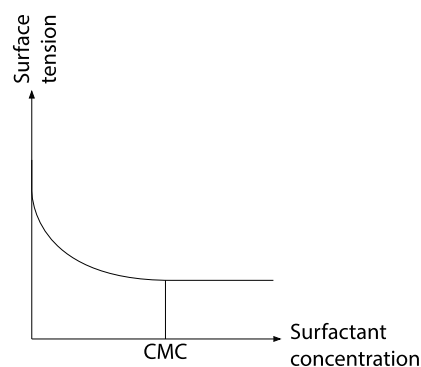


Figure 1.6 Surface Tension vs. Surfactant Concentrations and the Critical Micelle Concentration (CMC).

Solutions used to create foam present a surfactant concentration over the CMC (ten to one hundred times it). Higher than this point, the gas/liquid interphase is supersaturated and cannot accommodate more molecules.

3.2 Foam Creation

In foams, bubbles can develop in three different forms: by nucleation of a new small bubble, by the introduction of a gas into the liquid phase through entrainment or injection, or by break-up of smaller bubbles.

3.2.1 Nucleation

Nucleation means the creation of a supersaturated solution of a foaming gas in liquid, until gas spontaneously comes out of the solution to form a gas bubble. Often, a rapid pressure drop can achieve this; for instance, the passage of shaving foam flowing from a pressure canister (Figure 1.7). If the bubbles nucleate randomly within a continuous liquid phase, it is known as a homogeneous nucleation. It can be effective at producing large number of small bubbles quickly, but there is little control over the process. There is a risk that once formed, bubbles will grow rapidly, consuming the supersaturated gas from the solution, instead of propagating the growth of future bubbles. This leads to polydisperse bubble size and reduction in the total number of bubbles [29]. Nucleation agents are used for the production of polymeric foams by, continuous extrusion with a blowing agent.

3.2.2 Entrainment of gas occlusions

It is essentially the bringing together of liquid surfaces, trapping gas between them. An example of long agitation processes is massaging shampoo into hair with hands or laundry solution in a rotating drum. Another high agitation process is that of food whisking or rotor-stator structuring devices. Any newly created bubbles are likely to undergo further changes once incorporated into the fluid, most significantly of breaking-up during the processing stage. Experimental studies normally start with a liquid with little entrained gas, increasing the amount of entrained gas. The rate of disentrainment is typically a function of the quantity of gas entrained, and so plays a role with time. It has been found that in non-soluble gases, volumetric entrainment is largely independent of mixing pressure, and the rate of entrainment per impeller revolution is fairly constant, at typical operation conditions [30].

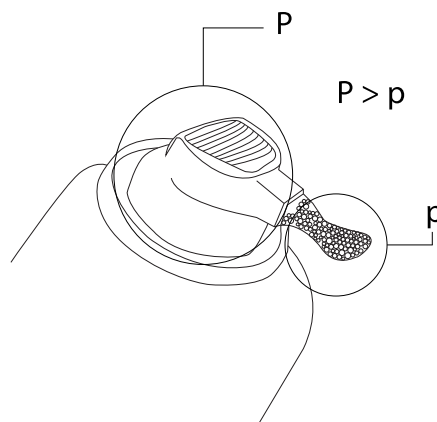


Figure 1.7 Foam flowing through a pressure canister and its nucleation.

3.2.3 Injection

The direct injection of gas into a liquid is other way of creating foams. The injected bubbles may act as seeds for further bubble growth, or more frequently, are the final bubbles of the foam. It is a method used for drinks, such as in beer can containers, which release a burst of nitrogen when the can is opened, or sparklers on bar taps, which avail small bubbles as a beer is pulled.

3.3 Practical application

In everyday life, liquid foam is present in *soaps, cleaning agents, shaving products and beverages*. In many cases, its appeal is largely psychological, as a factor in customer perception and satisfaction. What purpose the suds in a washing machine serve, other than to indicate that one has not forgotten to add the detergent? The foam properties of soaps and shampoos is often said to have no purpose. But the particular rheological properties, to be explained further, do have some value, in enabling the clearly visible foam to a vertical surface – being the face of a shaver, or the wall of a factory – before being washed off.

This ability to coat surfaces without immediately running off is also helpful when foams are used in *fire fighting*. For fire made out of petrol, the foam invades the fire triangle (oxygen, heat and combustion) excluding oxygen from the combustion zone, cooling the fuel below the ignition point, and trapping the fuel vapor of the liquid surface.

In chemical engineering, foams are used in *separation* of impurities through *foam filtration and flotation*. Here, the solute carries at the surface of bubbles created at the bottom of a fractionation column, by blowing air through a liquid pool. One well-known application is the segregation of ore.

Foam is a substitute of more violent means of *controlling civil disorders*. To be enveloped in foam is a relatively innocuous means of stopping violence. Indeed, it can be a positive pleasure; hence the popularity of the foam parties in children celebrations and other events. This same application of foams occurs in the decontamination of materials in nuclear reactors, to avoid contact with the hazardous zones.

In traditional “Secondary Recovery of Hydrocarbons”, water is injected in the reservoirs with surfactants, to displace and recover some of the residual oil and gas in-situ. Foams provide a more efficient mixing of the chemicals, optimizing water requirements. They are also used in the oil industry “air-drilling” and drilling of unbalanced formations, where it is necessary to maintain a lower density drilling-fluid column, so as not loose circulation.

Many products inside the agro alimentary industry are made out of foam, e.g. ice cream, chocolate mousse, beer, champagne. These ones suffer an important change in structure from the production to the packaging. This is mainly due to the transport of the product from one chain to another.

In many cases, the final foam structure is a combination of a nucleation or entrainment break-up process, followed by bubbles growth. This has particular applications in products where the foam is created at the point of use by an action of the user, but also finds applications in other processes.

Pressure gas expansion: The bubble size in an “aerated insoluble liquid” will change along with headspace pressure, applying Laplace equation principles to surface tension effects. However,

significant changes may occur when a highly soluble gas is used under pressure. This is applied in extrusion processing, carbonated drinks, and pressurized cans such as shaving gels. For example, sparkling wines bar will form foam when poured if the bottle CO₂ pressure reaches at least 3.5 bars [31].

Chemical gas creation: Foam is to be created on specific demand; for example cake-raising agents.

Biochemical gas creation: Fermentation processes in the wine, beer and bread industries have a significant role in the taste as well as rheology of the liquid phase.

Heat: Rapid heating of a liquid material results in the creation of a large volume of vapor. This is normally generated on the surface along with bubbles and foams in, baking and frying are both effective ways of inflating pre-existing bubbles in a liquid to create a foam product as the liquid phase sets.

4. Imaging and Probing Foam Structure

The measurement methods of a static foam structure, and its dynamic evolution (bubble scale), were mainly developed in the 80's. They essentially measured the liquid fraction and its granulometry distribution. The *granulometry* is the measurement of the size distribution in a collection of grains. These methods are normally optic, photographic or by ultrasound. Nevertheless, the high light diffusion of the foams at the test walls does not allow the direct visualization of their geometry, size, distribution or dynamics.

4.1 The Principle of Archimedes

In a foam liquid column (Figure 1.8), the application of the principle of Archimedes may be stated as follows, for the *average* liquid fraction $\overline{\Phi}_l$.

$$\overline{\Phi}_l = \frac{p}{H} \quad (1.11)$$

Where H is the total foam height, and p is the depth to which the foam extends beneath the liquid surface.

This formula has been frequently utilized in the study of forced drainage, in which the uniform drainage receives a continuous feed of light in the top. However, it is approximation that may include error.

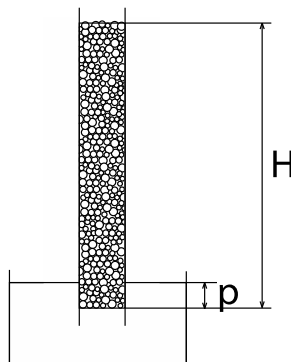


Figure 1.8 Archimedes principle may be used to estimate the (average) liquid fraction of a foam column [1].

4.2 The Pressure Outlets Method

This method (Figure 1.9) allows calculating the foam density inside the channel. To achieve this, at least two pressure outlets must be located at the test section wall.

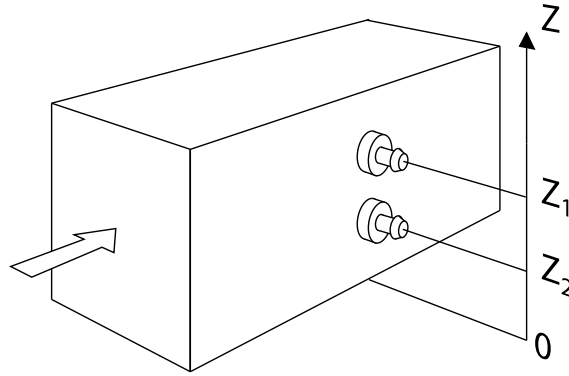


Figure 1.9 The pressure outlets located at the walls allow us to measure the pressure losses [32].

Being P_0 the atmospheric pressure, P_1 the pressure at the first outlet, P_2 the pressure at the second outlet and z_c the distance of the two outlets. It assumes that the foam fills the whole channel, and that the liquid of the foam is the same as the one inside the manometer.

$$P_1 = P_0 + \rho_f g z_1 + \rho_l g (z_c - z_1) \quad (1.12)$$

$$P_2 = P_0 + \rho_f g z_2 + \rho_l g (z_c - z_2) \quad (1.13)$$

where ρ_f is the foam density, and g is the gravity acceleration. The pressure difference ΔP between the two outlets can be expressed:

$$\Delta P = P_1 - P_2 = \rho_f g (z_1 - z_2) + \rho_l g (z_2 - z_1) = g (z_2 - z_1) (\rho_l - \rho_f) \quad (1.14)$$

The foam density ρ_f can be written:

$$\rho_f = \rho_l (1 - \phi_g) + \rho_g \phi_g \quad (1.15)$$

where:

$$\Delta P = g (z_2 - z_1) [\rho_l - \rho_l (1 - \phi_g) - \rho_g \phi_g] \quad (1.16)$$

where ρ_g is the gas density.

Thus:

$$\Delta P = g \phi_g (\rho_l - \rho_g) (z_2 - z_1) \quad (1.17)$$

And $\rho_g \ll \rho_l$, the difference of pressure between the two outlets can be defined as:

$$\Delta P \approx g \rho_l \phi_g (z_2 - z_1) \quad (1.18)$$

Knowing the foam density, the distance between the two outlets and the ΔP pressure “value”, the gas fraction of the foam flow can be determined.

When the pressure outlets are at the bottom of the test channel, they are useful to define the pressure losses along this one.

$$\Delta P \approx \rho_l g (h_2 - h_1) \quad (1.19)$$

where h is the height of the liquid column out of the pressure outlets. They are full of the same liquid filling the bottom of the channel.

4.3 The Conductimetry Technique

The electric conductance in a foam flow, σ_f , is an accurate method to determinate the liquid fraction. If divided by the liquid conductivity σ_l , the relative conductivity σ_r becomes a function of the liquid fraction ϕ_l :

$$\sigma_r = \frac{\sigma_f}{\sigma_l} = f(\phi_l) \quad (1.20)$$

A linear approximation of this equation occurs in a dry foam case ($\phi_l \rightarrow 0$) [33].

$$\sigma_r = \frac{\sigma_f}{\sigma_l} = \frac{1}{3} \phi_l \quad (1.21)$$

The surfactant choice (ionic or non-ionic), its concentration, and the bubbles form and shape don't have any major effect over the foams conductance; but as the bubbles become smaller, the conductance does the same. The gas phase is non-conductive. This means that the electric conduction only occurs at the Plateau's borders, which have higher liquid concentration, and have been defined as the main electrical drivers [34]. Small bubble dependency is related to the electric conductivity of a foam flow.

Nevertheless, it has been revealed [35] that for dry foams with a gas fraction over 96%, the linearity between the foams conductivity and its volume fraction does not apply any longer.

4.4 The AC capacitance measurement (ACM)

It is a measure technique related to the conductance method. The difference is that in the ACM, the electrodes are in contact with the foam flow (Figure 1.10), while in the conductance method they are not. To perform capacitance measurements, a non-ionic surfactant is needed. A capacitor segment is formed by transmit or excitation electrode and its projection on the opposite pick-up or detection electrode. An AC excitation signal at a frequency in the kHz range is sent to each of the excitation electrodes in sequence. By switching the corresponding pick-up electrode to a charge amplifier, the capacitance of each capacitor segment can be obtained.

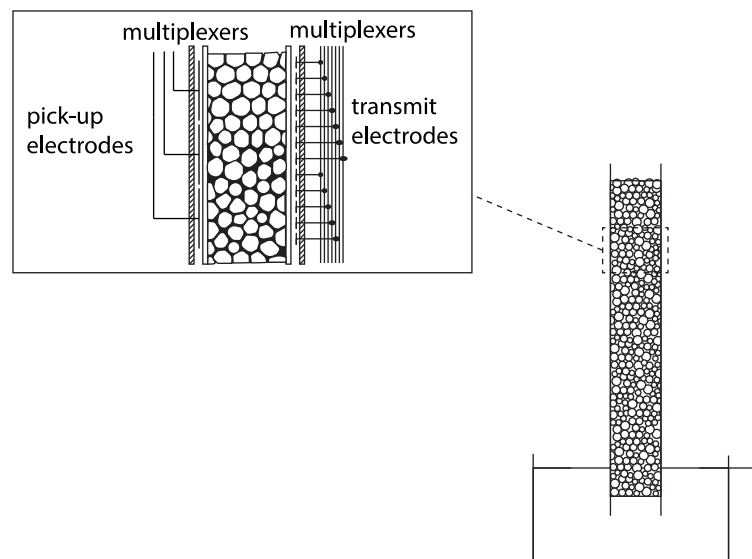


Figure 1.10 Capacitance measurements using segmented electrodes to obtain a vertical profile of liquid fraction [36].

The capacitance measurement offers an easy way to characterize the general properties of non-conductive foams. The relation between the measured capacitance and the observed liquid fraction, however, is not a simple one [36].

4.5 The Electrical Impedance Tomography (EIT)

The EIT is used to study the interstitial liquid at foams flow center, from electric measures at the periphery. As a known current passes through a pair of neighbor electrodes, the differential tension is measured. This is repeated for every pair of electrodes where the spatial electrical conductivity gradient can be measured.

The EIT has been used to detect local conductivity changes [37] and to control the conductivity inside channels [38]. One of its main advantages is the velocity of its measure: Only few milliseconds allow defining the liquid network at the center.

4.6 The Fluorescence Method

The addition of fluorescent dye, to be illuminated with ultraviolet light, has been used for demonstration purposes. It has been shown to be also useful in actual measurements [39]. It allows defining the spatial and temporal variations of the liquid fraction. The monitoring of fluorescence light allows extending measurements to very low liquid fractions.

The fluorescent dye presented in the liquid part of the foam flow is excited with a U.V. light. The small fluorescent quantity added to the solution absorbs this luminous radiation, and emits a visible light. The intensity of this light is registered allowing measuring the liquid content of the foam.

This technique assumes a linear relation between liquid fraction and fluorescent light intensity, which in cases may need adjustments for absorption and/or multiple scattering.

4.7 The Speed of Sound Method

By measuring the speed of sound inside the foam, this method allows calculating the liquid fraction of a foam column [40]. Two microphones and one speaker are submerged inside the foam. An oscilloscope quantifies the difference of a sound, emitted by the speaker and captured by the microphones.

The speed of sound inside foam, V_{sf} , is related to the liquid fraction ϕ_l by treating it like a mix of an ideal compressive gas and a non-compressive liquid [41]:

$$U_{sf} = \sqrt{\frac{C_P/C_V P_a}{\rho_f} \left(\frac{1}{\phi_l(1 - \phi_l)} \right)} \quad (1.22)$$

where C_P/C_V is the isotropic expansion of an ideal gas, P_a is the atmospheric pressure, and ρ_f is the density of the foam.

4.8 The Transmission and Reflection of Light

Unless foam is very dry, it is opaquely white, due to multiple scattering of light that reaches it. The individual scattering events are reflection/refraction of formed films and Plateau borders. This makes direct optical observation of structures and processes difficult or impossible within the bulk.

The observation of multiple scattered lights, in reflection and transmission, shows that useful information could be extracted from it [42]. A wavelength laser reaches the foam inside a glass column. The intensity of the laser transmitted, T_i , through the foam is measured. The light transmission is described as analogue to the diffusion phenomena (multiple light diffusion).

A relationship has been proposed for the light transmitted, the column thickness e_f , and the bubbles diameter d_b .

$$T_i \approx \frac{6d_b}{e_f} \quad (1.23)$$

This method allows an easy measurement of the mean bubbles diameter; it was made over static foam for a void fraction of 92%. However, it does not account for the diversity that can be encountered inside the existent foam samples.

4.9 The Optical Glass Fiber Probe Method

In this method, a thin glass fiber probe is immersed into the foam [43]. The diameter of the fiber can be under $50 \mu m$, and that of the tip only $20 \mu m$. It takes advantage of the difference between the gas and liquid refraction. Light is reflected at the end of the tip. When there is a mismatch of the refractive indices of the glass and the surrounding medium, thus light is reflected if the tip points into a gas bubble. There are hardly reflections if its points into the liquid cell walls, or Plateau borders.

The returning beam is received by a light-sensitive cell and converted into an electronic signal. The signal given by the light-sensitive cell is later amplified and transformed into a logic signal of level two, which represents the medium phase. By slowly introducing the glass fiber into the sample, it is possible to scan through the foam and detect gas or liquid as a function of the tip position. Some statistics are applied to transform the measured signal into a bubble size distribution.

This method has been used to obtain the bubble size distribution in beer foam, generated by bubbling nitrogen or carbon dioxide through a glass filter. Both foams had similar initial bubble size distributions in this test, but differences showed up after the foam had evolved for three minutes [44].

It has been said, that the interaction between foam and the fiber does not alter the foam structure. Because the bubbles contained inside the foam, do not collapse at the contact with the fiber. This hypothesis has never been corroborated, but it may be truth if the liquid wets well the fiber. Also, it leads to believe that some bubble, may slide aside the fiber, which will generate an error in the measures.

The use of the double-clad fibre (DCF) allows the acquisition of an optic signal with two levels (liquid and gas). It measures the void fraction, the bubble diameter and the local velocity of the foam. The void fraction is obtained with the average value of the two optic fibers. The axial velocity comes from the time that a bubble takes to pass through the two fibers, and the distance between these last

ones. The bubble size value is a function of the retention time in each fiber and of its local velocity [45].

From double-clad studies [46], the following relationship was obtained:

$$\bar{d}_b \approx 1.5 \bar{l}_d \quad (1.24)$$

where \bar{d}_b is the average bubble diameter and \bar{l}_d the length of the average interceptions.

4.10 The Photographic Method

There are two main ways of treating images of foam distribution: a) consider each bubble distributed along the foam; and b) a Fourier transform to analyze the texture of an image [47].

The main advantage of this method is it not being an intrusive method. Accordingly, the process of taking the measurements will not affect the foam flow itself, and the essays can be made without stopping. Nevertheless, it also means that the only data that can be acquired is that of the bubbles passing along the duct walls.

This type of wall measures present four types of error [48]:

- **The static derivative:** There is possibility of seeing the big bubbles than the smaller ones, which may require an adjustment [49]. This method presents an error of 1.8% [48].
- **Bubble deformation with the contact of the wall:** The bubble diameter observed at the wall is different from the actual bubble size, due to a deformation presented in the bubble film. This difference can be neglected, as experiment showed the bubble size did not change drastically at the contact of the wall [48].
- **Bubble segregation:** It brings the opposite effect of the static derivative. In this case, the small bubbles tend to stick to the duct walls, relegating the big bubbles to the interior. The same static derivative corrections may be applied.
- **Foam stability effect:** Occurs when the diffusion of gas and coalescence are weaker at the walls. It is normally neglected as being difficult to recognize.

The influence of the foam structure over the bubble deformation at the wall (Figure 1.11) was also studied by analyzing the photographic images [50]. The conclusion was that as the foam gets dryer, it is harder to deform it.

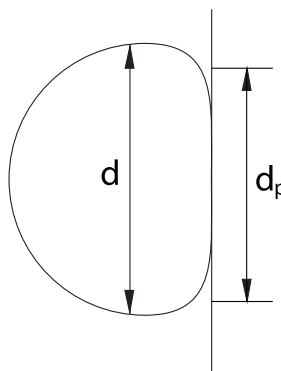


Figure 1.11 Bubbles deformation at the channel wall [51].

4.11 The Magnetic Resonance Imaging (MRI)

MRI can be used to determine the liquid density as a function of vertical position [52], and also to monitor the cross-sections of foams, to study the process of coarsening.

In nuclear magnetic resonance (NMR), the atomic nucleus with non-zero spin angular momentum absorbs radio frequency (RF) electromagnetic energy; they behave as magnetic dipoles in a strong magnetic field. Their precession frequency is given by the Larmor relationship. Measuring the dispersion of the frequency response in surrounding RF coil, gives information about structural and chemical features of the sample.

MRI extends the idea of NMR by adding to the applied homogeneous external magnetic field a pulsed linear magnetic field gradient. This alters the precession frequency and thus, linearly encodes the spatial position.

4.12 Other foam measurement techniques

- **Long-path infrared spectroscopy:** It was used to study the liquid films in foams. The infrared light absorption gives information about the quantity of liquid inside the foam films [53].
- **X-rays reflectivity:** It was also used for liquid films research inside the foams that presented big and uniform bubbles [54].
- **Interferometry:** It was used for the measurement of the microscopic liquid films [55].

These techniques remain too complex and their interpretations of measurements required making additional hypotheses concerning the films structure. As for the measurement techniques used during this investigation, they are explained in detail on Chapter 3.

5. Foam rheology

Rheological properties of foams, such as elasticity, plasticity, and viscosity, play a major role in foam production, transportation and application. Obvious examples are foam extrusion through nozzles and slits (used in cosmetic and food applications, and in plastic foam production), transportation through pipes (for compartment cleaning in nuclear plants and in foam-aided natural gas production), flow through permeable media (in enhanced oil recovery), foam perception in personal and home care application (shaving and styling foams, facial cleanser, shampoos), and many other applications.

If foam is subjected to small shear stress, it deforms like a soft solid (Figure 1.12). This response can be characterized with visco-elastic moduli. For applied low *yield stress*, visco-plastic flow sets in. In this regime, foams behave like shear-thinning fluids, being their effective viscosity a decreasing function of shear rate [56].

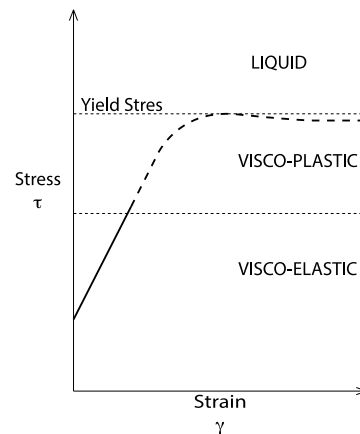


Figure 1.12 Schematic representation of the relationship between the shear and the strain for aqueous foam.

Additional rheological phenomena arise at the contact between foams and confining solid walls: If the surface of the solid wall is smooth, on the scale of the bubble size, the foam tends to slip on the wall (Figure 1.13). In this case, the velocity of the first layer of bubbles, in contact with the wall velocity does not match, in contrast to what is observed with simple liquids [57].

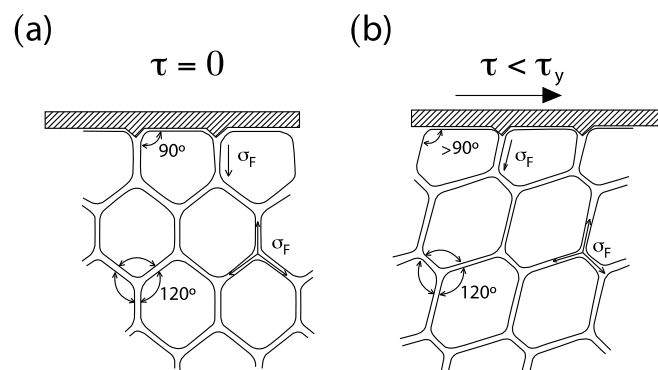


Figure 1.13 Schematic presentation of the origin of elastic response of foam, subject to shear stress lower than the foam yield stress close to a channel wall [2].

The rheological properties of foams are complex, not only because both elastic and viscous responses are nonlinear functions of the applied stress, but also because shear localization (coexistence of moving and non-moving regions) may occur under certain conditions.

The elastic response is due to surface tension effects: each foam film bears a mechanical tension, approximately equal to twice the surface tension of the liquid, from which the foam is generated [58]. If shear stress is applied externally, the bubbles are deformed (Figure 1.14). As a consequence, the average orientation of the film is biased in the direction of the applied stress. As long as the applied stress is smaller than the foam yield stress, the films meeting at the Plateau borders are in static mechanical equilibrium and the bubbles are trapped in a self-supporting structure.

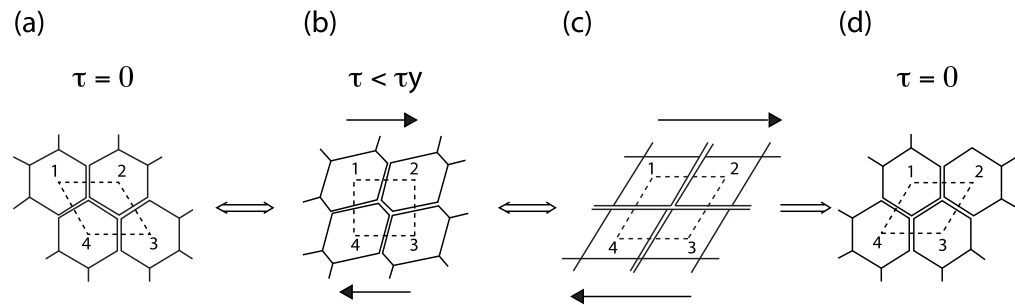


Figure 1.14 Foam yielding and plastic deformation, under applied shear stress, increasing from (a) to (c). This structure can relax either elastically, by returning to structure (a), or by a bubble rearrangement, leading to structure (d) [59,58].

If the applied stress is strong enough to separate neighboring bubbles, the foam structure yields, a steady shear flow sets in, and the bubbles slide along each other. The bubble rearrangement leads to local shear flow of the liquid inside the foam films, resulting in dissipation of energy and shear-rate dependent (viscous) contribution to the macroscopic stress. If the applied stress is decreased back to zero, the flow stops and the bubbles tend toward a new equilibrium (Figure 1.14) [59].

5.1 Linear Elasticity

Foam behaves like an elastic material when it is under a sufficiently small shear strain. In this case, the stress τ varies linearly with the strain γ . In this regime, the bubbles are deformed, but the applied strain is too small to modify the topology of their packing. The specific surface area of the foam increases with the applied strain, and so does the volume density of the bubble surface energy. Dimensional models have shown that the foam shear modulus, $G = \tau/\gamma$, scales as the surface energy density, multiplied by a prefactor, which depends on foam structure, polydispersity and liquid content [59].

For a given mean bubble size, wet foams are softer than dry ones; this is because the gas volume fraction ϕ decreases, the shear modulus G also decreases. The latter tends toward zero as the void fraction approaches the random close packing volume fraction ϕ_{CP} , which is a weakly increasing function of polydispersity. The loss of rigidity occurs when the packing reaches an isostatic mechanical equilibrium, where the bubbles are spherical and barely touch each other [60].

At $\phi = \phi_{CP}$, the foam can be sheared slowly without any interfacial energy cost. The following empirical relation [15] shows the dependence of the shear modulus of polydisperse foam on ϕ :

$$G = 1.4\phi(\phi - \phi_{CP})\frac{\gamma_l}{R_{32}} \quad (1.25)$$

Where $R_{32} = \langle R^3 \rangle / \langle R^2 \rangle$ is a characteristic length in foams known as the Sauter mean radius, which governs foam elasticity and $\phi_{CP} = 0.64$ [61].

Foams are much difficult to compress than to shear, and their Poisson ratio (relation between the transverse and the axial strain) is close to 0.5. Neglecting the water compressibility and the interfacial contribution, the foam compression modulus is given by the ratio K_T/ϕ , where K_T is the compression modulus of the gas confined in the bubbles. The magnitude of K_T is related to the gas pressure outside the foam. Taking realistic values, one obtains that $K_T/\phi \gg G$. Therefore, the bubble volume is constant to a good approximation in foam undergoing shear flow [61].

On the other hand, foam that flows under significant variations of the applied pressure may lead to significant changes of the bubble air volume fraction.

5.2 Non-Linear Elasticity

For larger strains, still too small to induce bubble rearrangements, foam film rotations and stretching lead to nonlinear mechanical response. For instance, shear deformation of a foam in the X_1 direction (Figure 1.15) induces the shear stress component τ_{12} (proportional to γ) and two normal stress differences, $N_1 = (\tau_{11} - \tau_{22})$ and $N_2 = (\tau_{22} - \tau_{33})$. These differences arise because, with increasing strain, the foam films become predominantly oriented perpendicularly to the direction X_2 . As a result, the surface tension of the foam films contributes more to the normal stresses τ_{11} and τ_{33} , and less to τ_{22} , thus leading to the normal stress difference N_1 and N_2 [62].

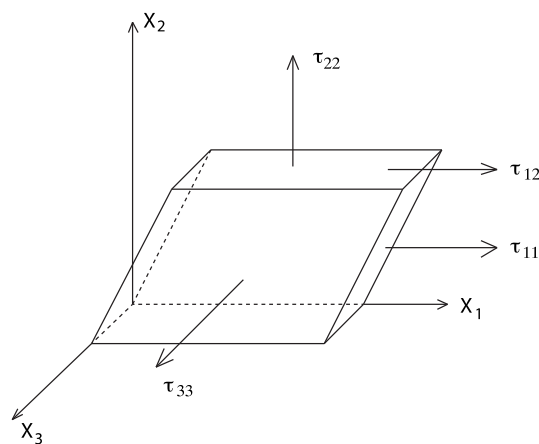


Figure 1.15 A cube of foam is sheared in the X_1 direction. The arrows illustrate the components of the induced stress [62].

Aqueous foams subject to mechanical stress, not only store elastic energy – they can also dissipate energy, via viscous friction in the liquid contained in foam films and Plateau borders, intrinsic viscous friction on the bubble surfaces and/or diffusive exchange of surfactant molecules between the solution and the air-water interface [63].

5.3 Yielding

Foams subjected to increasing shear stress or strain exhibit a transition from solid-like to fluid-like behavior, called *yielding* [64]. As described in the previous section, the stress first increases, as in elastic solid. Afterwards, the stress passes through a weak maximum and settles at a plateau. In this latter regime, the stress (height of the plateau) is in increasing function of the applied shear rate, $\dot{\gamma}$. The stress threshold, beyond which the flow sets in, is called *yield stress* and is denoted by τ_c . The corresponding strain threshold is the yield strain, denoted by $\dot{\gamma}_c$.

The foam yielding occurs at the scale of the individual bubbles when the applied macroscopic stress or strain is large enough to induce rearrangements in the bubble packing. For real polydisperse 3D foams, the bubble structure is more complex, but similar irreversible bubble rearrangements lead to yielding and plastic flow on the foam.

The experimental time scale, over which the mechanical response is probed, is another control parameter of the foam response. This time scale is set by the inverse frequency of an applied

oscillatory strain, or by the inverse strain rate for a steady flow. For sufficiently long time scales, so the bubble coarsening induces a significant number of bubbles rearrangements, foam flows like a highly viscous liquid, in spite of low stress $\tau < \tau_c$. Even if the experimental time scale is so short that coarsening is negligible, the time scale can still affect the yielding behavior [65].

5.4 Plastic Flow

Plastic Strain is defined as the irreversible deformation that takes place when material is sheared beyond its yield strain. In a slow plastic shear flow, one may expect the sample to relax almost instantaneously towards static equilibrium whenever the applied shear rate is released suddenly. Such behavior is called *quasi-static*. In practice, even slow foams flows may only approach quasi-static behavior, due to the slow viscoelastic relaxations.

As a first step towards a general constitutive law, relating stress and strain in rearrangement-driven plastic flow, the elementary plastic events have been modeled as forces dipoles acting on an elastic continuum [66]. This has shown a good agreement with numerical simulations [67]. In another approach, so far limited to 2D foams, the anisotropy of the foam microstructure is captured by a texture tensor related to the macroscopic stress [68].

5.5 Foam-Wall Viscous Friction

If foam is in contact with a smooth solid wall, the application of external stress leads to sliding of the boundary bubbles along the wall surface, violating the common *non-slip* boundary condition for fluid flow at solid surfaces [69]. This *foam-wall slip* phenomenon may affect the rheological measurements because the actual shear rate inside the foam cannot be directly deduced from the motion of the walls bounding the sample.

This “wall slipping” is studied by placing the foam in contact with a smooth surface inside the rheometer and applying a stress lower than the yield stress of that foam [57].

Most of the theorems [70,71,72] trying to model the viscous friction between the bubbles and the walls are based on calculations made over the fluid velocity profile in the wetting films formed in the contact zone (Figure 1.16). In these calculations, a *non-slip* boundary condition is applied for the liquid film flowing along the solid wall, whereas different conditions are considered for the gas-liquid interface. Two cases merit retrieving: The first one is that when exists a tangentially mobile bubble surface; there is no velocity gradient in the wetting film, so that the *bubble-wall* friction originates only in the zones around the film. The second case considers a tangentially immobile bubble surface where the friction occurs in both zones – of the film and in the surrounding meniscus regions [72].

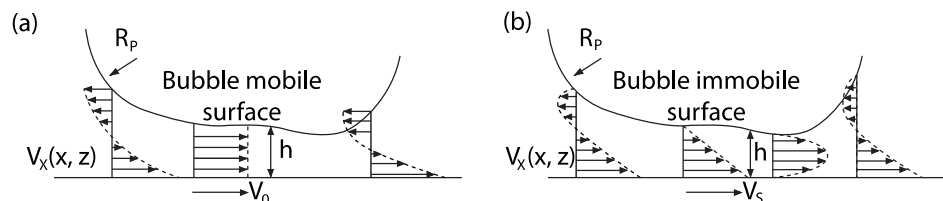


Figure 1.16 Schematic presentation of the zone of bubble–wall contact with the profile of the fluid velocity: a) In the case of tangentially mobile bubble surface, there is no velocity gradient in the wetting film (b) In the case of tangentially immobile bubble surface, the friction occurs in both zones – of the film and in the surrounding meniscus regions [72].

Theoretical models for the first case predict a foam-wall friction stress τ_w [73]:

$$\tau_w \propto (Ca^*)^{2/3} \quad (1.26)$$

where $Ca^* = \mu u_0/\Gamma$ is the capillary number, μ_l is the viscosity of the liquid, V_0 is the characteristic velocity and Γ is the surface tension.

In the second case where the bubble-wall friction is dominated by the viscous stress inside the wetting film and is only possible if the bubble surface is tangentially immobile [72], the foam-wall friction is a result of:

$$\tau_w \propto (Ca^*)^{1/2} \quad (1.27)$$

5.6 Rheological parameters

One of the objectives of this work is the use a rheological model that may be capable of representing the behavior of complex flows, such as the foam one. Accordingly to previous studies, it is indispensable for any rheological foam model to present the following parameters [74]:

- Relationship between the bubbles diameter and the conduct hydraulic diameter,
- Wall-slip layer thickness,
- Bubbles size distribution,
- Flows anisotropy due to the bubbles size distribution,
- Boundary effects: Slipping, absorption, shear, etc.,
- Geometry characteristics and flow rates,
- Gas volume fraction (Foam quality),
- Physicochemical properties of both phases,
- Absolute pressure (Gas compressibility),
- Surfactants and their properties,
- Rheological properties of the in-between bubbles liquid films and their stability

If the model does not consider any of these parameters, it will remain only an approximation.

6. Foam evolution

Despite the stabilizing influence of the surfactants, aqueous foam never reaches a steady state. As mentioned, foam will stay at a metastable state, and will exhibit a continuous evolution through time and space. From the thermodynamic point of view, foam will always try to diminish its interfaces to lower its inside energy. The foam evolution may be explained through a series of mechanisms.

Foam presents a simple composition: gas bubbles, highly concentrated in a fluid with small amounts of surfactants. To achieve present level of understanding on this matter, it has taken over a century of considerable effort by the scientific community. Still today most models that try to recreate the behavior of aqueous foam remain empirical, and several questions remain unanswered.

In foam evolution, we distinguish two main dynamic processes: the redistribution of liquid (foam drainage or syneresis) and the redistribution of gas between bubbles (coarsening or Ostwald ripening) [75,76]. We may recognize how the “normal” shrinking head on a beer freshly poured into a glass, is a complicated process that involves both processes.

6.1 Drainage

“Foam drainage” was described as the phenomena by which liquid flows out of foam [77]. It has had many applications like: cleaning services, mineral extraction, water purification, and many features of production of food and porous materials, among others. Consequently, foam drainage has received much more attention than fluid flowing between compressed bubbles.

Foam drainage may appear to be a relatively straightforward fluid problem dealing with the flow between bubbles, but it is rather a complex one, with length scales ranging from nanometers for surfactant molecules, micrometers for films, millimeters for bubbles, and centimeters for bulk foams.

Two main flow stages may be distinguished: the drainage of the films between the bubbles and the liquid flow to the center of the channels towards the Plateau junctions. The flow inside the liquid film is due to phenomena like: the gravity force, the capillarity force, and the pressure force between the Plateau regions and the film between the bubbles.

The drainage physics', physicochemical and geometrical parameters included the: liquid volume fraction, density, liquid viscosity, bubble size distribution, surface rigidity, surface tension and nature of the surfactants. If a constant input of liquid is applied to the top of the foam to achieve a constant flow, it is called *forced* drainage. The opposite of this, the *free* drainage, is in which no liquid is added.

Foams composed of larger bubbles have greater drainage pressure and so they tend to drain rapidly from their films. They also have larger Plateau border cross-sectional areas (for the same wetness of foam); accordingly they will drain more rapidly under gravity. Also, higher surface tension increases film drainage forces, so stability is enhanced with smaller bubbles or surfactants that further reduce surface tension.

6.1.1 Drainage Characterization

The stability of foam has been studied through volume phases. They are a function of temperature and the surface tension between them. A simple experiment can measure the time needed to reduce by half the foam contained in a column. It is the continuous phase (with a much higher density) that separates from the rest of the flow. Experiments have been conducted in static foam to determinate the liquid quantity drained through time by a column of known area [78]. However, this type of analysis only considers the global drained liquid. Other factors are the foam fabrication conditions, the column form, and surface.

More extensive methods allow evaluating the local properties in the column without affecting the foam structure. They measure the conductance, AC capacitance and electrical impedance. This way, not only we can evaluate the global drainage in a given static foam sample but also the local drainage, by measurement of the gas liquid fractions, even in foam flows.

Other non-destructive methods, like the MRI or the tomography method, have been used to characterize foam drainage [79]. Using the attenuation of the gamma rays, they were able to study the drainage inside static perfectly isotropic foam. Because of this particular necessity, this method is not suitable for foam flow.

6.1.2 The Continuity Equation

The equation for the drainage of foam describes the spatial-temporal evolution of the liquid fraction on the scale of several bubbles. It is based upon the continuity equation, a relationship between the foams volume fraction and its liquid velocity.

From the continuum point of view, the foam's liquid fraction is changed by the divergence of the liquid flux, ψ . Assuming that the foam is confined, the conservation of liquid requires:

$$\frac{\partial \varepsilon}{\partial t} = -\nabla \cdot \psi = -\nabla \cdot (\bar{u} \varepsilon) \quad (1.28)$$

where \bar{u} is the mean-axial velocity.

Once the average liquid velocity \bar{u} is determined, and applied in the continuity equation, it leads to a partial differential equation describing the spatial-temporal evolution of the liquid fraction, also known as the foam drainage equation. Before, the velocity had a simple dependence over the liquid gradient and its fraction [80]. However, the liquid velocity has a complex dependence on parameters not accounted for in the original formulation, such as surface viscosity. To date, there is no a theory covering foam drainage in its complexity and only exist semi-empirical approaches [81,82].

6.2 Coarsening

Also known as the Ostwald ripening, it expresses the gas lost through the bubbles film from a high-pressure bubble to a low-pressure one. Through gas diffusion occurs this exchange is associated to a decrease in the small bubbles size at expenses of the big ones (Figure 1.17). It is an important phenomenon by which, liquid foam evolves toward a thermodynamic equilibrium. This process is strongly coupled with drainage, and other rheological phenomena. It is mainly due to the increase of the average bubble size, but also that ripening induces dynamics that are central in the complex rheological behavior of foams.

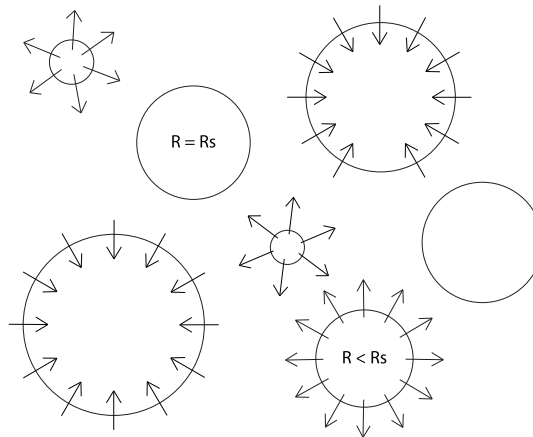


Figure 1.17 Ripening of a wet bubbly system.

Wet foam is considered to be a suspension of well-separated spherical bubbles with radius R , as shown in Figure 1.17. The concentration of gas $c = c(r, t)$ diffusing in the liquid surrounding each bubble is spherically symmetric and described by Fick's second law of diffusion:

$$\frac{\partial c}{\partial t} = D \cdot \Delta c \quad (1.29)$$

where D is the diffusion coefficient of the gas in the liquid.

Assuming that it takes a small time (in comparison to the bubbles radius evolution time) to reach a fully developed concentration profile i.e. $\partial c/\partial t \approx 0$, the expected concentration is:

$$c(r) = c_\infty + R(c(R) - c_\infty)/r \quad (1.30)$$

where c_∞ and $c(R)$ are gas concentrations at $r \approx \infty$ and $r = R$

In *dry foam*, gas bubbles resemble closely packed polyhedra. So, the gas diffusion will take place through the thin liquid films separating neighboring bubbles. If we consider 2D dry foam that satisfies the Plateau's rules (Figure 1.18), where the length of the films separating the neighbor bubbles i and j is known as l_{ij} , with an angle of $2\pi/3$. The gas flow rate (per unit of length) is given by [83]:

$$q_{ij} = -k_f(P_i - P_j) \cdot l_{ij} \quad (1.31)$$

where k_f is the permeability of the complete film.

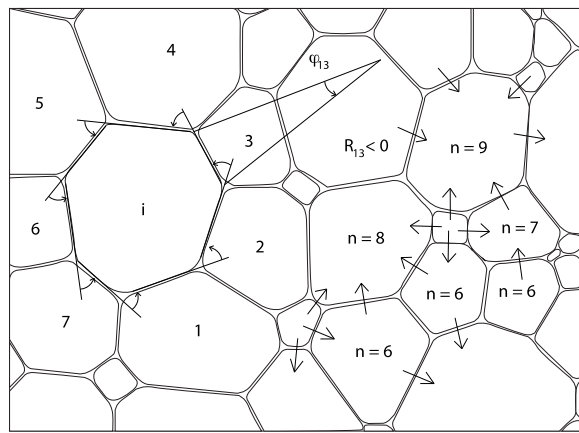


Figure 1.18 Schematic representation of 2D dry foam. The bubble noted by i has $n = 7$ sides of length l_{ij} . The total angle covered by films' curvatures along the perimeter of bubble i is equal to $\sum_{j=1}^n \varphi_{ij} = \sum_{j=1}^n l_{ij}/R_{ij} = \pi(6 - n)/3$. Arrows illustrate the exchange of gas between n -sides bubbles [83].

The Laplace law can be used to express the pressure difference as a function of the radius of curvature R_{ij} , which is counted positively, when the center of the circle lies inside the bubble:

$$P_i - P_j = 2\sigma/R_{ij} \quad (1.32)$$

Then, from the sum of q_{ij} over the n neighboring bubbles the von Neumann's law states:

$$\frac{\partial A_n}{\partial t} = \frac{2\pi}{3} \gamma k_f (n - 6) \quad (1.33)$$

6.3 Gibbs-Marangoni mechanism

The Gibbs-Marangoni mechanism explains the stability of the dilute aqueous surfactant solution. A surface tension difference may result from surfactant deficit, stretching or drainage. When the surface tension difference occurs, the surfactant from the neighbor cells will migrate to this weak zone. They will fill the hole by dragging with them (hydrophilic heads) a liquid part that is present in the film between bubbles. The entire zone will grow, and recover its meta-stable property by creating the double surfactant layer [84]. This phenomenon gives an extra elasticity by the surface tension effect. It will extend the foams life.

6.4 The disjunction pressure

Excess in chemical potential characterizes the liquid films. This quality creates extra pressure inside these areas, also known as disjunction pressure. It is normally a result of the repulsive electrostatic forces (from the ions to the gas-liquid interface), the Van der Waals attraction forces and the steric effect (intermolecular force).

The mutual electrostatic repulsion forces in the surfactants will eventually prevent the film rupture and the bubbles coalescence [85].

6.5 Foam collapse

Once a soap film is formed, either by itself or within foam, it will keep on thinning until equilibrium is reached. Most liquid foams do not last long, in comparison with other type of fluids. They tend to collapse by the rupture of exposed films. Many factors are related for this, singly or in combination. Drainage is one of the most important factors that reduce the film thickness, evaporation may also affect it, and the surfactant selection or the presence of dust may also impact on the films. Foam stability is a subject of great importance but offers many difficulties regarding its scientific framework and comprehension. Three reasons for this are: the immense variability of chemical composition; the large effect of small levels of additive and impurities; and the dynamic character of the instability mechanisms.

6.5.1 The coalescence

Coalescence is a limiting mechanism in the foam evolution. It mainly appears in the rupturing of the thin liquid film that separates two adjacent cells. In comparison to the drainage effect, coalescence takes more time to affect the foam behavior. Along with, the coarsening and the drainage are the principal phenomena of foam destabilization.

As a general principle, thin films break by spontaneous growth of thermal fluctuations of thickness. The fluctuations are controlled by two contributions to the free energy of the film. The first one is always positive, due to the increase film surface area (the surface energy is the product of the surface area by the surface tension), and the second contribution may be either positive or negative, depending on the sign of the disjoining pressure, and the film thickness [86].

In 2D foams, the bubbles of five or less sides shrink, and those of seven or more sides grow. Accordingly, mean cell area $\langle a \rangle$ grows along with time. Most significantly, in the case of Ostwald ripening after a transient regime, the evolution is characterized by a steady regime, where the normalized volume distribution is steady. The evolution of breaking foams is significantly different. The process of breaking includes three distinct phases [87]. At first, foam is generated in a cell by vigorous shaking of dodecyl sulphate solution. Removing some of the liquid regulates the liquid fraction. In these experiments, coalescence is induced by the effect of gentle induction of heat. It is noted that coalescence is a rapid process in comparison with Ostwald ripening. The destruction of the foam is completed in less than 10 min, whereas Ostwald ripening relaxation proceeds over 10h. This is one of many methods to study this mechanism, beside those of thermal induction with higher viscosities [88] and acoustic experiments [89].

The parameters in charge of the coalescence process include: the film size, the surfactant properties, the surfactant concentration, and the gas and liquid properties. Of them, the key one is the

liquid fraction. Its effects are enhanced below a critical liquid fraction, which does not depend on the size of the bubbles [90].

When the foam is left to coalesce and collapse freely, three successive regimes take place. First, the height of the foam remains constant; the liquid flows and the foam dries. Second, the foam continues to dry but the bubbles present at the air/foam interface break down. The rupture front propagates in the foam, and the height of the foam decreases. This discontinuous evolution evolves by avalanches separated by periods of stasis. Coalescence events only occur at the top of the foam. Finally, in the third regime at the end of the experiment, a residual height of bubbles persists at the lower part of the column.

The coalescence is a catastrophic process that takes place at critical liquid fractions. It is clearly related to the T1 events occurring when the foam is drying or ageing. Experiments at the level of a few bubbles in movement are required to better understand this point. Avoiding drainage will increase dramatically the lifetime of foam. Foams with small bubbles, surfactants with high surface viscosity, and jellified systems are thus more stable.

6.5.2 T1 and T2 Rearrangements

The topological structure of the foam may be brought to a configuration in which there is a violation of Plateau's rules by the introduction of a forbidden vertex. This dissociates rapidly and a new structure is formed.

In 2D, the possibilities are rather simple: The so-called T1 process eliminates a fourfold vertex and forms two threefold ones, while the T2 process is associated to the disappearance of a bubble and coalesce (Figure 1.19).

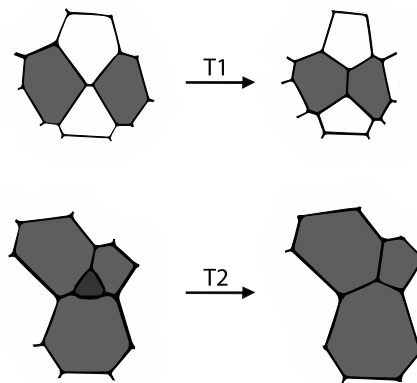


Figure 1.19 T1 and T2 Rearrangement.

In 3D, the most elementary possibility involves the disappearance of a triangular face, or the inverse process in which a line (Plateau border) is reduced to zero length. But the disappearance of one triangle generally causes a neighboring triangle to vanish too. The topological changes often come in cascades, particularly for wet foams [91].

For both dry and wet foams, the processes of phase change in ordered foams (for example, from *bcc* to *fcc*) are largely unexplored. This may be of little direct importance, but the close analogy with some metallurgical phase transformations could add interest.

7. Foam Flow

The study of foam flow has been encouraged by a desire to understand the flow of fire-fighting foams and the transport of cuttings in oil well drilling. As already explained, the foam is a non-Newtonian fluid that exhibits a slip boundary condition. This type of flow makes an important impact in the wall shear stress and contributes to the entire pressure gradient. Because of this characteristic, foam flow has been used for cleaning oil pipes and equipment like heat exchanger.

At glance, two different kinds of foam flow cases may be noted:

- **Micro-flow:** Is when the confinement space of the foam flow has a size close to the bubbles diameter (porous medium, capillarity tube)
- **Macro-flow:** In this case the confinement space of the foam has a size bigger than the bubbles diameter.

For the micro-flow, the bubbles take the form of the channel, or space surrounding it. As for the macro-flow, the bubbles can move freely and will interact between them. Another important aspect differencing them is the bubble diameter. For the smallest one, the bubbles can be bigger than the channel; in that case the important size is the porous medium and the predominant interaction is between the bubbles and the walls.

Basically, foam flow can be described as a perfect plug flow inside any tube. A liquid film is noted at the wall of an acrylic channel, its slip velocity is obtained using the Mooney's formalism [92]. Overall, it comprises two phenomena. The wall-slipping layer characterized by the slipping velocity and its thickness. The second is the shear at the foam core.

It is important to relate the foam rheology to its flowing. This is the only way that the velocity inferred by Lemlich can be explained. The observation of plug flow requires the existence of a yield stress. There are many factors that influence the behavior of the foam flow. Because of this, a rheological-equation that can describe it, is difficult to define. The foam flow study is at the border of multiple scientific domains: mechanical engineering, chemical engineering, rheology, and physics.

7.1 Foam viscosity

It is known that viscosity stands as the resistance exerted by a fluid that is being deformed by either shear stress or tensile stress. As the viscosity increases, the fluids capacity to flow diminishes. The most common types of fluid viscosity referred to the dynamic viscosity and the cinematic viscosity.

All along nature, most of the fluids present a Newtonian behavior. Non-Newtonian behavior means that there is no proportionality between the stress and the deformation rate. So, the viscosity is not constant over an extended shear velocity plateau. We can characterize this type of fluids with visco-elastic behavior laws.

Foam viscosity has been object of many studies by the scientific community. Many authors have proposed correlations between the viscosity and the structure. The most used model, based only in the volumetric gas fraction, is [93]:

$$\mu_f = \frac{\mu_l}{1 - \phi_G^{1/3}} \quad (1.34)$$

where μ_l is the liquid viscosity

It is based on a heuristic model for concentrate emulsions, and does not take into account the surface tension.

A viscometer can be used to measure the wall stress for different shear values inflict over foam. The apparent viscosity can be calculated with these two values. Another viscosity model was created, based on this tool [94]:

$$\mu_f = \mu_l e^{K\phi_G} \quad (1.35)$$

where K is a constant, function of the shear rate $\dot{\gamma}$:

$$K = 6.0 + 2.5e^{-5.3 \cdot 10^{-3} \dot{\gamma}} \quad (1.36)$$

Nevertheless, the physic value of K in this model is not clearly established. It seems to be related to the interaction between the bubbles.

Numerous experimental results have allowed adjusting the non-Newtonian model of Herschel-Bulkley. Then, the effective viscosity can be expressed as:

$$\frac{\partial \tau}{\partial \dot{\gamma}} = n \cdot k \cdot \dot{\gamma}^{n-1} \quad (1.37)$$

where τ is the stress, $\dot{\gamma}$ the shear rate, k the consistency index and n the Power Law index.

Other viscosity model was built considering Bingham's non-Newtonian model. Drainage and its viscous effects are taken into account. It is mainly based in the liquids viscosity and the gas volume fraction [95]:

$$k \approx 0.026 \cdot \phi \cdot \mu_l \quad (1.38)$$

This model remains restricted to monodisperse foams, where the gas fraction is extremely close to the unity.

In most of these models, the viscosity results from mathematical analysis where the physic approach is less taken into consideration.

7.2 Non-Newtonian flow models

Foam flows in a non-Newtonian way. Because of this property, a model with at least two parameters better explains the behavior of such complex flow. For all continuum models, mechanical properties, such as elastic and viscous moduli, effective viscosity and yield stress, are incorporated in laws and models that relate the stress, strain and rate of strain. In a general approach, the most common models are those that consider a shear at the middle of the foam. The continuum non-Newtonian models are:

- **Bingham:**

When the stress applied to the fluid is higher, or the same, as the *yield stress* τ_C is:

$$\tau = \tau_C + k\dot{\gamma} \quad (1.39)$$

where k is the consistency index and $\dot{\gamma}$ the shear rate. However, when the stress does not surpass the yield stress, $\dot{\gamma}=0$.

- **Ostwald de Weale:**

In this model, the stress can be specified as:

$$\tau = k\dot{\gamma}^n \quad (1.40)$$

where n is known as the Power Law index, k the consistency index and $\dot{\gamma}$ the shear rate.

- **Herschel-Bulkley:**

It is the model most applied for foam flows, in case the stress applied to the fluid is higher than the *yield stress*:

$$\tau = \tau_c + k\dot{\gamma}^n \quad (1.41)$$

where n is known as the Power Law index, k the consistency index, and $\dot{\gamma}$ the shear rate. In case the stress does not surpass the yield stress, $\dot{\gamma}=0$.

Although these mathematical approximations are useful, they only broadly describe the behavior of real non-Newtonian fluids. If n were less than one, the models will predict that the effective viscosity will decrease with increasing shear rate. All real fluids have both a minimum and a maximum effective viscosity, according to the physical-chemistry at the molecular level.

Power laws fluids cover three types of them, according to their flow behavior index n . For Power Law index values lower than 1, the fluid is called *Pseudoplastic*. When it is equal to 1, it is known as a *Newtonian* fluid. Finally, for values above 1 it is called *Dilatant*.

For foam and concentrated emulsions, the power-law index, n , is typically between 0.2 and 0.5, reflecting the strong shear-thinning behavior of these systems [57,96]. The dimension of the consistency index, k , is $(Pa.s)^n$ and it is, therefore dependent of the specific value of n .

The wall shear stress can also be obtained experimentally, with a Couette type rotational rheometer [97]. They put in evidence an Ostwald de Weale, or a Herschel-Bulkley, fluid behavior. For these studies, the important parameters are the foam quality and the bubbles diameter. The wall shear stress for a laminar regime, was established as:

$$\tau_P = \tau_c \left(\frac{d_h}{d_b}, \phi \right) + k \left(\frac{d_h}{d_b}, \phi \right) \cdot \dot{\gamma}^n \quad (1.42)$$

where τ_c is the yield stress, d_h the hydraulic diameter, \bar{d}_b the bubbles mean diameter, ϕ the gas volume fraction, k the consistency index, $\dot{\gamma}$ the shear and n the Power Law index.

The foam texture has less influence than the gas volume fraction, as long as it flows inside a conduct bigger than the bubbles size [98]. Because of this, some laws should be considered to relate the yield stress and consistency, to the gas volume fraction:

$$\tau_c = 7 \cdot 10^{-2} \phi \quad \text{if } \phi \leq 0.6 \quad (1.43)$$

$$\tau_c = 2 \cdot 10^{-4} \exp(9\phi) \quad \text{if } \phi > 0.6 \quad (1.44)$$

$$k = 2 \cdot 10^{-4} \exp(3.6\phi + 0.75\phi) \quad (1.45)$$

These results may be compared to the ones in other studies [15]. For polydisperse foams (bubbles diameter between 90 and 140 micrometers), it has been proven that the yield stress remains the same, as long as the gas volume fraction is greater than 63.5%. So, previous results showing the possibility of different values for yield stresses require further review.

A second branch of the yield stress, studies tried to relate this to the bubbles diameter. Using a rotational rheometer, it was shown that the yield stress increases while the bubbles diameter decrease. The relationship established is the following [99]:

$$\tau_c = 5.2 \bar{d}_b^{-0.648} \quad (1.46)$$

There have been different opinions concerning the causes of the foam flow. Some propose that it results from shear in the middle of the foam [11,94] and others suggested that the slipping liquid layer is a more relevant characteristic [99,100]. Probably, foam flow results from a mix of these two processes.

7.3 Horizontal flow regimes

There are two main ways to evaluate a horizontal foam flow inside a channel or a pipe. First, it can be studied by the void fraction. This type of flow can exhibit seven different flow regimes. They represent a detailed qualitative description, and provide an excellent platform to develop future mechanistic models [101]:

- **Pattern 1.** When the foam is very wet, with a liquid fraction above 27%, a liquid stratum forms at the bottom of the pipe, and the foam layer moves on top.
- **Pattern 2.** At a liquid fraction of 21-27%, the liquid layer becomes thinner and bubbles exhibit limited shear past one another. There is also some bubble size segregation, with the bigger bubbles tending to locate near the top of the pipe.
- **Pattern 3.** At a liquid fraction of 11-21%, the agitation of bubbles causes the size classification observed in pattern 2 to disappear. The visible liquid layer vanishes, and the foam exhibits a distinct velocity profile.
- **Pattern 4.** At a liquid fraction of 3-11%, the foam exhibits plug flow, which corresponds to Lemlich's observation in the Perspex Tube. The authors refer to the foam as a 'wispy solid'.
- **Pattern 5.** At a liquid fraction of 2-3%, the large bubbles start to segregate towards the top of the column once more.
- **Pattern 6.** At a liquid fraction of 1-2%, the foam forms into distinct plugs separated by pockets of gas.
- **Pattern 7.** The gas rate becomes so great that it can break through the foam plugs and the foam becomes incoherently dispersed in the tube. This resembles the phenomenon of 'gas pull-through' observed in gas-liquid oil flow lines.

The other way to evaluate horizontal foam flow inside a channel is through its global velocity. For foam quality of 70%, three different regimes can be observed [3]. They result from the interpolation of the velocity, measured at the ducts wall, over a straight section. The three different foam regimes are:

- **One-dimensional flow:** It is obtained when the established flow behaves as a whole. It moves in a block form, or as a piston. The velocity vectors have only one uniform axial direction:

$$\vec{u} = u \vec{e}_x = cte \vec{e}_x \quad (1.47)$$

- **Two-dimensional flow:** It is obtained when the established flow has an axial component velocity, which only depends of the y -coordinate (vertical coordinate):

$$\vec{u} = u(y) \vec{e}_x \quad (1.48)$$

- **Three-dimensional flow:** It is obtained when the established flow velocity has an axial component, which depends of the z (span wise) and y (vertical) coordinates:

$$\vec{u} = u(y, z) \vec{e}_x \quad (1.49)$$

These regimes depend on numerous factors: the gas velocity, the liquid velocity, the mean velocity in the test-section, and the channels geometry, already explained for the visual method to characterize foam flow.

7.4 Wall-Slip liquid layer

As foam flows, liquid segregates from the foam to form a thin liquid layer at the wall. This provides decreased resistance to shear, and can engender slip at the wall. The particle imaging Velocimetry has been used to determine the velocity profiles of a horizontal foam flow [3]. Normally this liquid film has a thickness in the order of millimeters, and presents a laminar regime. Because this slipping film is formed from a relation between the wall and the foam, it is a function of the wall roughness, channel dimensions, surfactant concentration, gas and liquid flow.

The wall liquid film was described using a rotational rotameter [99]. From this experience, the foam flow was supposed to be the cause of two different phenomena: the shear at its middle, and the subjacent liquid film. Considering the presence of liquid film in any foam flow, its behavior can be related to the Herschel-Bulkley for Non-Newtonian flows [102].

7.4.1 Wall-Slip Velocity

For a flow with a slipping film, the velocity field can be decomposed into two main components: the wall slip velocity u_{slip} , and the shear velocity u_{shear} (Figure 1.20).

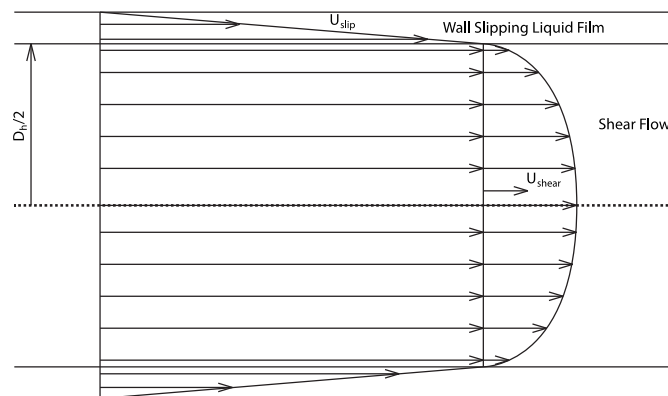


Figure 1.20 Velocity field of a laminar flow with a wall-slip velocity [51].

Inside the wall liquid film, the higher velocity corresponds to the wall slip velocity. It can be related to the bubbles velocity flowing over the foam flow, inside this film with a shear velocity. Inside this film, composed of liquid, a boundary layer might develop and increase the value of this gradient. The foam flow will always take into consideration both velocity and the contribution from the wall slip velocity [51]. The layer thickness, δ , and its velocity can be related through the following expression [103]:

$$\delta = \alpha u_{slip}^{1-\beta} \quad (1.50)$$

where $\alpha = 3.7 \cdot 10^{-4}$ and $\beta = 0.5$. The value of β was obtained at a study of the flow of simple bubbles through a capillary tube [104]. The layer thickness is directly related to the slip velocity. As the velocity increases, so does the layer thickness [102,100].

7.4.2 Correction methods

For a non-Newtonian fluid flowing in a tube, with a no-slip condition, the shear stress can be translated as a function of the strain rate through the Weissenberg-Rabinowitsh method. This method was adjusted to accommodate a slip velocity at the wall [92], and to obtain constitutive relationship for

foam [33]. Once the slip velocity, u_{slip} , has been estimated, the thickness of the liquid layer, δ , can be obtained as a function of the wall shear stress:

$$u_{slip} = \frac{\delta}{\mu_l} \tau_w \quad (1.51)$$

where μ_l is the liquid viscosity.

The flow of pastes through a capillarity tube did not produce linear Mooney plots, which was reconciled by suggesting that the slip velocity was inversely proportional to the capillary radius [105]. This suggestion has been adopted for the interpretation of foam data. However, the Tikhonov regularization is used to analyze capillary rheometry data, and have shown that Jastrzebski has limited support and that the Mooney formalism, with this regularization is successful for the interpretation of foam data [106,107].

7.4.3 Thickness

A foam flow inside a duct can be studied within three different zones (Figure 1.21). Inside these, the shear and the slipping phenomena are combined [108].

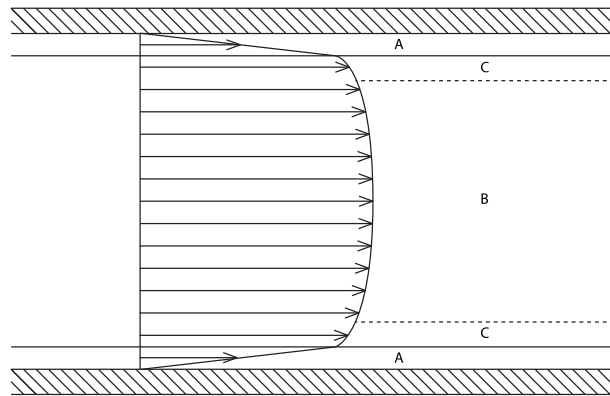


Figure 1.21 Velocity profile of a foam flow inside a rotameter [108].

- **Zone A:** It corresponds to the wall slipping liquid film and presents the characteristics of a Newtonian liquid. The gaseous phase is completely absent. The foam flows over this parietal liquid that is highly sheared. As for any other Newtonian fluid, the velocity at the wall is zero.
- **Zone B:** Inside this region, the foam behaves as a whole. All the bubbles flow together and the elasto-plastic properties attach one to the other. The shear stress is lower than the yield stress.
- **Zone C:** At this zone the foam shears. The shear stress is higher than the yield stress. If the foam velocity is not high enough to create a high shear, the foam will flow as a block (piston type).

The main characteristics of each zone are function of foam properties; such as the liquid fraction, the bubbles diameter, and the velocity. It can also be related to the wall and its state (slipping wall or rough wall).

The direct measure of the liquid film thickness is not an easy task with actual measurement techniques. An indirect measure method can be based on the modeling of the foams flow. From the modeling, the pressure losses can be obtain, and from these, the film thickness.

One hypothesis suggests that the shear is mainly located at the wall liquid film [100]. As long as the film thickness can be neglected in comparison to the channels dimensions, it is strictly attached to next relationship:

$$\delta = \mu_L \frac{u_f}{\tau_w} = \frac{16 L Q_t \mu_l}{\pi d_h^3 \Delta P} \quad (1.52)$$

where u_M is the foam mean velocity, Q_t is the total measured flow, d_h is the hydraulic diameter of the channel, μ_l is the liquid viscosity and L the distance between the two pressure outlets, for which ΔP is measured. For a Plexiglas tube, with a diameter of 44 mm, a liquid film of 3 to 8 μm can be observed.

A second hypothesis is for a shear at both, the liquid film and the foam core [108]. The proposed model is formed by: the liquid film thickness, the yield stress, the bubbles mean diameter and the foam gas fraction. For this model, the yield stress is not sensitive enough and the rheological properties at the foam core remain constant. From experimental results, the model was adjusted and a relationship was created. This one relates the liquid film thickness to the bubbles diameter, d , and the gas volume fraction ϕ [109]:

$$\delta = \frac{2d_b(1 - \phi)}{3\phi} \quad (1.53)$$

The relationship was constructed over a theoretical base, relating the slipping liquid film to the film between bubbles. It is restraint to bubbles diameter of 100 μm and a gas volume fraction lower than 86%. Accordingly to this model, the slipping liquid film can measure from 8 to 40 μm .

A third and final hypothesis was made out of the previous two ones [50]. It approached the characterization of the liquid slipping film of the following foam flow: a gas volume fraction between 95% and 97%, a foam velocity of 1 m/s, a channel hydraulic diameter between 20 mm and 40 mm. Assuming a shear caused only by the liquid layer, the thickness would be between 15 and 25 μm . These values highly differ from those expressed by the first model. Later on, the second model was tried. A thickness between 7 and 10 μm was obtained; it had a lower deviation than the other model. These results proved that the foam flow is affected by a shear at the foam core.

Accordingly to these authors and experiment, the wall-slip liquid layer thickness value is between 1 and 100 μm . There are different ways to approach its calculation.

7.4.4 Shear rate influence

The foam shear and its wall stress seem to have an important effect over the thickness of the liquid layer. Many authors also studied the stretch relationship between these phenomena. For a given gas volume fraction, between 98.5% and 99.5%, the liquid layer thickness diminishes as the stress rises [103]. The same behavior was observed for foam flows, with a gas volume fraction between 66% and 80% [102]. However, for the gap between these two limits, from 87.5% to 98%, a different relationship was noted, the thickness increases at the same time as the stress [100].

Close to 80% of gas volume fraction, the limit between dry and wet foam is achieved. In consequence, the bubbles will cease to be spheres and become polyhedral. The liquid layer will be created by the foam-wall contact and also from the liquid trapped in-between the bubbles, acting as reservoirs.

When stress, higher than the yield stress, is applied to the foam flow, the layer of bubbles closer to the wall will be sheared. The movement between bubbles will deform and break the in-between films. They will expel the liquid inside towards the wall and the slip liquid layer. So, for higher stresses, more liquid drained to the walls.

7.5 Compressibility influence

As foams are mainly composed of gas. They may be considered as pseudo-compressible fluids. There have been few studies that take into consideration the influence of the compressible characteristics of the air inside the foam flow. This is because most of the studies were made in conditions in which the gas compressibility did not make a relevant difference over the results obtained.

The compressibility phenomenon considers, so as predicting the pressure losses along a duct. This method can only be applied if the pressure difference between the entrance and the exit of the duct is neglected in regards to the mean pressure [110]. A theoretical foam flow model did consider upon the influence of the air compressibility over the foam dispersion [11].

7.6 Theoretical foam flow models

Several authors already tried to develop an equation capable of predicting the foam flow and some of its complex properties; such as the shear, the stress and the pressure losses. It is important to note that they are limited to certain conditions and duct geometries.

In order to develop an equation of a simple medium for polymer foams, a study of the foam flow through a vertical tube was carried [11]. It was assumed that the foam flow is only due to the foam shear at its core. Starting from theoretical considerations, the VEPL (Volume Equalized Power Law) was proposed. To be able to characterize gas volume fraction inside the foam, a specific volume expansion factor was added:

$$\tau = k EF^{1-n} |\dot{\gamma}|^{n-1} \dot{\gamma} \quad (1.54)$$

where τ is the local stress, EF the expansion factor, k the consistency index, n the Power Law index, and $\dot{\gamma}$ the shear rate. Adjusting this model to the pressure losses, will allow to determine the k and n parameters.

A theoretical study was undertaken for a block foam flow inside a cylindrical duct [111]. It took into consideration the drainage and the viscous effects present in foam. The pressure gradient caused by the redistribution of the liquid phase and the bubbles deformation will create a stress over the interfaces. From here, the values of the deformation components and interfacial shear were obtained.

After including the energetic factor of foam flow, it was established that the phase redistribution would be followed by energy loss. Also, the foam flow is joined by a volumetric, deformation giving origin to the wall-slip layer, which controls the gas phase compression.

For a piston foam flow, the core velocity depends on the liquid film thickness and the axial pressure gradient, B . Assuming that the velocity inside the wall-slip layer presents a linear slope, the interfacial shear and the wall shear are similar [100]. The foam flow is linked to the axial pressure gradient through the next relation:

$$Q_t = 0.857 \frac{B^2 R^5 e^{0.042K_0}}{\mu_l \rho_0 P_{\gamma 0}} \quad (1.55)$$

where R is the duct region, ρ_0 is the foam initial density, $P_{\gamma 0}$ is the capillarity pressure (Laplace pressure) and μ_l is the liquid viscosity.

Although this model considers the parameters of the foam structure, and how pressure losses relate to the foam flow, it disregards the variation of the wall-slip thickness.

8. CFD Code for Complex Fluid Simulations: ANSYS-CFX

8.1 ANSYS CFX Description

Computational Fluid Dynamics (CFD) uses algorithms and numerical methods to study fluid flow and carrying out the calculation and simulations of liquid and gases interacting with surfaces defined as boundary conditions. CFD often applies Navier-Stokes equations, which define any single-phase fluid flow. They can be simplified by removing terms describing viscous actions to yield the Euler equations and describing vorticity, giving place to the full potential equations. To attend small perturbations, they may be adjusted by many linearized potential equations.

Different solutions methods are used in CFD codes. The most common, on which CFX is based, is the finite volume technique, when the region of interest is divided into small sub-regions, the “control volumes”. The equations are discretized and solved iteratively for each control volume. As a result, an approximation of the value of each variable, at specific points throughout the domain, and a full picture of the flow obtained.

CFD has applications in a wide range of fields like: mixing vessels, chemical reactors, ventilation, fire and smoke, combustion modeling, car aerodynamics, heat transfer within and around circuit boards, dispersion of chemical pollutants in different media, optimization of combustion processes, blood flow through grafted material.

CFD can determine the performance of a component at the design state, or it can analyze difficulties with a particular design, leading to improvement. The first step is to identify the region of interest, and define its geometry. The mesh is created and applied in the pre-processor, together with other elements required in the simulation including the boundary conditions and fluids properties. The solver produces a file of results of the variables throughout the region of interest, providing the user a better understanding of the fluid behavior [112].

8.2 Introduction to ANSYS CFX

ANSYS-CFX is a general purpose CFD software that combines an advance solver with powerful pre- and post-processing capabilities. It includes an advance coupled solver reliable and robust, full integration of problem definition, analysis, and results presentation and an intuitive and interactive setup process, using menus and advanced graphics. It is capable of modeling fluid flow cases, but especially, laminar, turbulent, non-Newtonian, buoyant related and multiphase flow. ANSYS CFX includes four software modules for the required geometry and mesh information to perform a CFD analysis (Figure 1.22) [5]:

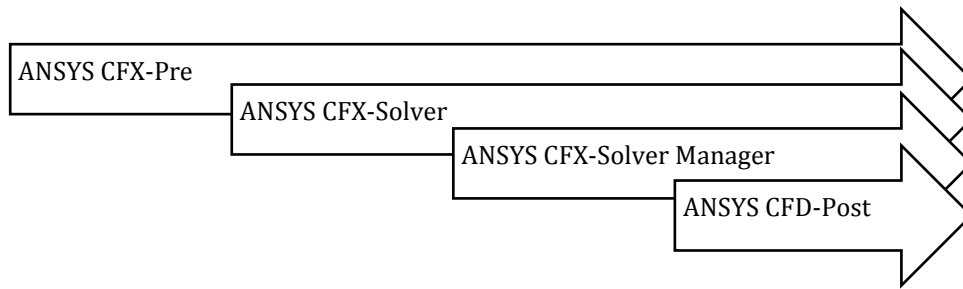


Figure 1.22 ANSYS CFX modules.

8.3 CFX-Pre

CFX-Pre is a next-generation physics pre-processor used in simulations. It allows importing data from multiple meshes; including the more appropriate, depending on the region configuration. Analyses, such as the flow physics, the boundary conditions, the initial values, and the solver parameters, may be carried out. A full range of boundary conditions are available including inlets, outlets and openings, together with boundary conditions for heat transfer models and periodicity.

Complex simulations can be assembled from one or more configurations; each one combines analysis definition with other related tasks. The control over the configuration execution order, and the inter-configuration solution dependence, facilitates the setup of common simulations, such as the initialization of a transient analysis using results from a steady-state analysis. It also facilitates the setup of increasing complex simulations. This characteristic allows evolving from simple Newtonian problems with apparent viscosity, to non-Newtonian setups capable of predicting the wall-shear stress, created by a foam flow.

8.3.1 Domains

The regions of fluid flow and/or heat transfer in CFX are called domains. *Fluid domains* define a region of fluid flow, while *solid domains* are regions occupied by conducting solids, in which volumetric sources of energy can be specified. To define a domain, three conditions are required:

- The domain must be formed from one or more 3D primitives. They constrain the fluid region.
- The physical nature of the flow
- The materials properties inside the region

Many domains may define the same model. Multidomain problems can be created from a single mesh, if it contains multiple 3D primitives or multiple meshes.

8.3.2 Physical models

For a reliable simulation, the physical model must be properly selected, and should be consistent with the type of simulation wanted. The physical models available at ANSYS CFX, of special interest for flow studies are:

- **Steady State and Transient Flows:** Specifies the time dependence of the flow characteristics. Steady state simulations are those whose characteristics do not change with time. While transient simulations require real time information to mark the time intervals at which the CFX-Solver calculates the flow field.

- **Laminar Flow:** A laminar flow is governed by the unsteady Navier-Stokes equations. It is normally applied at low Reynolds number flows ($Re < 1000$). The energy transfer in the fluid is accomplished by molecular interaction.
- **Turbulence Flow:** The turbulence models predict the effects of turbulence in fluid flows, without resolving all scales of the smallest turbulent fluctuations. Several models can be used to approximate turbulence based on the Reynolds Average Navier-Stokes (RANS) equations.
- **Non-Newtonian Flow:** A non-Newtonian fluid does not obey the simple linear relationship between shear stress and shear strain rate. ANSYS-CFX has several models for calculating viscosity based on shear strain rate.

Multiphase flow can also be modeled with ANSYS-CFX, but there is no CFD software in the market that can simulate our particular case, which presents elasto-plastic properties. Our approach relates the foam qualities to a Newtonian fluid with an apparent viscosity. Later, the results from the Newtonian model will be boundary conditions for a Non-Newtonian simulation, capable of predicting the relationship between the shear stress and the shear strain rate, taking into consideration the pressure losses.

8.4 CFX-Solver

The CFX-Solver processes the variables generated in CFX-Pre. One of its most important features is the use of a coupled solver, in which all the hydrodynamic equations are solved as a single system. This mechanism is faster than the traditional segregated solver, and less iteration are required to obtain a converged flow solution. This approach follows a fully implicit discretization of the equations at any given time step.

8.4.1 Linear Equation Solution

ANSYS CFX uses a Multigrid (MG) accelerated Incomplete Lower Upper (ILU) factorization technique for solving the discrete system of linearized equations. It is an iterative solver whereby the exact solution of the equations is approached during the course of several iterations.

The linearized system of discrete equations can be written in the general matrix form [5]:

$$[a] [\varphi] = [b] \quad (1.56)$$

where $[a]$ is the coefficient matrix, $[\varphi]$ the solution vector, and $[b]$ the grid hand side. The above equation can be solved iteratively by starting with an approximate solution, φ' , to yield a better solution, φ^{n+1} :

$$\varphi^{n+1} = \varphi^n + \varphi' \quad (1.57)$$

where φ' is the solution of:

$$A \varphi' = r^n \quad (1.58)$$

With r^n , the residual, obtained from:

$$r^n = b - A \varphi^n \quad (1.59)$$

Repeated application of this algorithm will yield a solution of the desired accuracy.

By themselves, iterative solvers, such as ILU, tend to rapidly decrease in performance, as the number of computational mesh elements increases. Performance also tends to diminish, if there are large elements aspects ratios present.

8.4.2 Algebraic Multigrid

The convergence behavior of our linear equation can be greatly enhanced by the use of this technique. It involves carrying out early iterations on a fine mesh, and later iterations on progressively coarser virtual ones. The results can be transferred from the coarser mesh to the original one.

For a given mesh size, iterative solvers are efficient at reducing errors that have a wavelength of the order of the mesh spacing. So, while shorter wavelength disappear quickly, errors with longer wavelengths, of the order of the domain size, can take an extremely long time to disappear. The Multigrid Method bypasses this problem by using a series of coarse meshes, such that longer wavelength errors appear as shorter wavelength errors related to the mesh spacing. It also prevents the need to mesh the geometry, using a series of different mesh spacing.

8.5 CFX-Solver Manager

It is a graphical user interface that enables the setting of the CFD calculation, control the CFX-Solver interactively and view information about emerging solutions. This interface is generally used to view the plotted data during problem solving. The convergence history plot is also displayed.

Its major functions are specifying the input files to the CFX-Solver, star/stop the CFX-Solver, monitor the progress of the solution, and set up the CFX-Solver for a parallel calculation. This manager is an easy and reliable way to control and supervise the solution convergence and criteria. It will help detecting problems and anomalies in the problem, before the results are even showed.

8.6 CFD-Post

It provides a state of the art interactive post-processing graphics tools to analyze and present the ANSYS CFX simulation results. Important features include quantitative post-processing, user-defined variables, a variety of graphical objects where visibility transparency, color, and line/face rendering can be controlled, and a power syntax allowing a fully programmable session files.

It includes a vast range of functionalities that support transient data, including moving mesh. Node locations are repositioned based on the position for the current timestep. It is feasible to import or export ANSYS data, generic data and generic geometries. CFD-Post also supports macros through an embedded user interface. Outputs to PostScript, JPEG, PNG, as well as various animations (key frame) can be created within this part of the software.

8.7 Geometry generation

Every engineering simulation starts with a geometry that represents the design. The problem geometry can go -from a solid component for structural analysis- to the air volume for a fluid one. Geometries are normally reproduced with a Computer-Aided Design (CAD) system. This software is called ANSYS Design Modeler; it is a gateway to geometry handling for a later analysis with other ANSYS software.

The ANSYS Design Modeler has connection to all major CAD systems, allowing seamless transfer of data including parameters. They can be adjusted or updated without affecting the main geometries imported, or disrupting the model. This permits application of design changes and updates.

A proper conception of the geometry is fundamental; errors in the CAD model may bring simulations with incoherent results. ANSYS Design Modeler holds powerful geometry construction tools from the ground up. A complex model can be obtained by simple modeling operations. Two-dimensional sketches can be extruded into 3-D solids and be modified with other operation. A construction history is recorded during the creation of the geometry, allowing the user to make changes and the update the design.

8.8 Meshing

The mesh generation is one of the most critical aspects of an engineering simulation. Too few cells may lead to inaccurate results, and too many may require more CPU calculation time. The ANSYS meshing software provides a way to balance these requirements, in the most automated way possible. Furthermore, the time it takes to create and mesh a model is often a significant portion of the time it takes to get results from a CAE solution.

From easy and automatic meshing to a highly crafted mesh, ANSYS provides an optimal solution. Powerful automation capabilities ease the initial meshing of a new geometry by keying physics preferences and using smart defaults, so a mesh can be obtained upon first try. Additionally, a user can update immediately to a parameter change, making the handoff from CAD to CAE seamless and aiding upfront design.

The highly automated meshing system allows generating different mesh types: tetrahedral, hexahedral, prismatic inflation layer, hexahedral inflation layer, hexahedral core, body fitted Cartesian, and cut cell Cartesian. Consistent user controls make switching methods straightforward and multiple methods can be used within the same model. Mesh connectivity is maintained automatically.

It is important to note that different physical problems require different meshing approaches. Multiphase models and non-Newtonian simulations require high-quality meshes in both element shapes and smoothness of size changes. ANSYS Meshing has shown to offer the right meshes for each simulation.

8.9 Numerical Model

The group of equations that describe the processes of momentum, heat and mass transfer are known as the Navier-Stokes equations. These partial differential equations were derived in the early nineteenth century and have no general analytical solution, but can be discretized and solved numerically. Equations describing other processes, such as the non-relationship between the shear and the stress, can also be solved in conjunction with the Navier-Stokes equations. Often, an approximating model is used to derive these additional equations, turbulence models being a particularly important example [5].

8.9.1 Governing Equations

The set of equations solved by ANSYS CFX are the unsteady Navier-Stokes equations in their conservation form. For all the following equations, static (thermodynamic) quantities are given unless otherwise stated. The instantaneous equation of mass, momentum, and energy conservation are presented. Given the low velocities presented in our problem can be considered as a laminar flow.

8.9.1.1 The Continuity Equation

$$\frac{\partial \rho}{\partial t} + \nabla(\rho U) = 0 \quad (1.60)$$

where U is the vector of velocity $U_{x,y,z}$, ρ is the density and t is the time.

8.9.1.2 The Momentum Equation

$$\frac{\partial(\rho U)}{\partial t} + \nabla(\rho U \times U) = -\nabla p + \nabla \cdot \tau + M \quad (1.61)$$

where p is the static pressure, M is the momentum source, the stress tensor, τ , will be detailed later.

8.9.1.3 The Total Energy Equation

$$\frac{\partial(\rho h_t)}{\partial t} - \frac{\partial p}{\partial t} + \nabla(\rho U h_t) = \nabla(\lambda \nabla T) + \nabla(U \cdot \tau) + U \cdot M + E \quad (1.62)$$

where E is the energy source and h_t is the total is the total enthalpy, related to the static enthalpy $h(T, p)$ by:

$$h_t = h + \frac{1}{2}U^2 \quad (1.63)$$

The term $\nabla(U \cdot \tau)$ represents the work due to viscous stresses and is referred to the viscous term. It reflects the internal heating by viscosity in the fluid, and is negligible in most flows. The term $U \cdot M$ represents the work due to external momentum sources, and is currently neglected.

8.10 Shear Strain Rate

The viscosity of non-Newtonian fluids is often expressed as a function of the shear strain rate scalar. The strain rate tensor is defined as:

$$S_{ij} = \frac{1}{2} \left(\frac{\partial U_i}{\partial x_j} + \frac{\partial U_j}{\partial x_i} \right) \quad (1.64)$$

This tensor has three scalar invariants, one of which is simply called the shear strain rate:

$$sstrnr = \left[2 \frac{\partial U_i}{\partial x_j} S_{ij} \right]^{\frac{1}{2}} \quad (1.65)$$

With the velocity components, this expands to:

$$\begin{aligned} sstrnr = & \left[2 \left\{ \left(\frac{\partial U_x}{\partial x} \right)^2 + \left(\frac{\partial U_y}{\partial y} \right)^2 + \left(\frac{\partial U_z}{\partial z} \right)^2 \right\} + \left(\frac{\partial U_x}{\partial y} + \frac{\partial U_y}{\partial x} \right)^2 \right. \\ & \left. + \left(\frac{\partial U_x}{\partial z} + \frac{\partial U_z}{\partial x} \right)^2 + \left(\frac{\partial U_y}{\partial z} + \frac{\partial U_z}{\partial y} \right)^2 \right]^{\frac{1}{2}} \quad (1.66) \end{aligned}$$

8.11 Non-Newtonian Models

The first step in our foam flow simulations was to consider the general physics of the problem. This meant reviewing several factors: A two-phase model, the wall-slipping layer, the drainage, the drag and the elasto-plastic properties created by the bubble to bubble interaction. Reviewing results concluded that the ANSYS CFX software was not able to reproduce such a complex flow. The results disagree with the actual behavior of the foam flow. With this experience, we decided to simplify the problem. Foam flow behavior was compared against some non-Newtonian models such as, Bingham,

Bird Carreau, Ostwald de Waele and Herschel-Bulkley. ANSYS CFX has several models for calculating viscosity based on shear strain rate, where μ is the dynamic viscosity, and $\dot{\gamma}$ is the shear strain rate (Table 1.2) [5].

Model	Description	Settings
Bingham	<p>A model for viscoplastic fluids.</p> $\mu = \frac{\tau_c}{\dot{\gamma}} + k$ <p>Examples of viscoplastic fluids include tomato paste and tooth paste. A few electro-rheological fluids can be modeled as Bingham fluids, with the yield stress as a function of the intensity of the electric field, or the electric current.</p>	<p>Yield Stress: τ_c</p> <p>Viscosity Consistency: k</p> <p>Minimum Shear Strain Rate</p> <p>Maximum Shear Strain Rate</p>
Bird Carreau	<p>A model intended for shear-thinning fluids.</p> $\mu = \mu_\infty + \frac{(\mu_0 - \mu_\infty)}{(1 + (\lambda\dot{\gamma})^2)^{\frac{1-n}{2}}}$ <p>The model reverts to a Newtonian behavior of $\mu = \mu_0$ for $n = 1$, or $\lambda = 0$.</p> <p>Examples of shear-thinning fluids include applesauce, banana puree, and orange juice concentrate.</p>	<p>Low Shear Viscosity: μ_0</p> <p>High Shear Viscosity: μ_∞</p> <p>Time Constant: λ</p> <p>Power Law Index: n</p>
Ostwald de Waele	<p>The most popular viscosity model because of its simplicity. However, it does not have bounded either on the low or high shear limits, unlike Carreau's models.</p> $\mu = k(\lambda\dot{\gamma})^{n-1}$	<p>Minimum Shear Strain Rate</p> <p>Maximum Shear Strain Rate</p> <p>Time Constant: λ</p> <p>Power Law Index: n</p> <p>Yield Stress: τ_c</p>
Herschel Bulkley	<p>A model for viscoplastic fluids that, after yield, exhibits a power law behavior in shear stress versus shear strain rate.</p> $\mu = \frac{\tau_c}{\lambda\dot{\gamma}} + k(\lambda\dot{\gamma})^{n-1}$	<p>Viscosity Consistency: k</p> <p>Minimum Shear Strain Rate</p> <p>Maximum Shear Strain Rate</p> <p>Time Constant: λ</p> <p>Power Law Index: n</p>

Table 1.2 Non-Newtonian models present inside the ANSYS CFX software.

9. Conclusions

The vast majority of industrial foams are located within the wet limit, and that the foam quality remains under 84%. However, most of the theoretical and experimental studies done so far have been focused on dry foams, with gas volume fraction near the unity. Foams are primarily formed by nucleation, entrainment or injection of gas into a liquid mixed with surfactants and other possible compounds. They lower the surface tension of the solution, and liquid films energy, facilitating the foam formation.

To better understand foam rheology, many parameters must be considered, like the foam quality, the bubble diameter, the fabrication process used, the wall-slipping layer and the

compressibility. A relationship with existent non-Newtonian models allows predicting the foam capacity to shear against a given stress.

When foam flows through horizontal ducts, the two phases separation is evident. The denser phase will tend to occupy the bottom of the duct, in our case the mix between water and surfactant, while the second one, the air, will remain trapped inside the pockets formed by the liquid films at the rest of the duct. This liquid layer, located close to the walls, proceeds from the drainage inside foam flow and the density difference between the two phases present. It originates the wall-slip layer. This phenomenon, along with the shear inside the foam core are include in numerous models studying the foam flow behavior.

Foam flow studies include experimental results interpreted under empiric or semi-empiric models. However, they lack local data, important to better comprehend the foam flow inside a duct, like the local velocity fields, void fraction, bubble size, the liquid film thickness and the wall shear stress. In this work we'll consider the foam rheology in a duct. The following measurement techniques will be applied:

- Particle Imaging Velocimetry Method,
- Conductimetry Method,
- Polarographic Method

In this work, we will extend the experimental studies done by Blondin [3], Tisné [51] and Madani [113] for a foam flow though a horizontal duct and flow disruption devices (fdd). We added obstacles geometry and generate a database for foam flow inside ducts.

As explained, a foam flow is influenced by numerous parameters, and a proper database requires a coherent study methodology. Our experimental arrangement is capable of generating a foam flow with different qualities and velocities. The velocities based on Blondin studies are 2 cm/s, 4 cm/s and 6 cm/s. They allow evaluating the different regimes of horizontal foam flow [3]. Previous studied one particular foam quality, trying to simulate the industrial uses of foam flow. The industrial foams, however, change widely depending on their utilization, and their value may be different for each case. This work, covers a wide range of values, going from the very wet limit, 55%, to the wet/dry limit, 85%. The bubbles diameter remains constant along the experiments by the use of a uniform glass porous media.

The first step in our work will be to measure the static pressure losses along a square channel without fdd or obstacles for all velocities and qualities, with the help of pressure outlets located along the length of the bottom of the channel. We will, then, obtain the foam velocity profile using the PIV method over the entire square section of the channel. The mean local wall-shear stress will be calculated through three different methods. The static pressure measurements will relate the pressure gradient with an average wall shear stress. The velocity fields and the liquid film thickness, will be obtained along the square channel surface with the conductimetry method, they will be use to assume a velocity gradient that will lead to a wall shear stress. Finally, the polarographic method will acquire the velocity gradient through an electrochemical reaction that occurs over the channel's walls.

For the flow disruption devices, pressure outlets will be also located along the length of the bottom of the channel; they allow measuring the static pressure losses. The PIV will be applied in the near vicinity of the half-sudden expansion, the fence and the cylinder. Therefore, the rheological and physical behavior will be determined. The pressure losses and velocity fields will be compared to numerical simulations obtained by th ANSYS-CFX software for all fdd.

The experimental work will provide a database that can be used to validate rheological models, capable of predicting the behavior and reorganization of foam flow through a channel, and obstacles. At the same time, a numerical simulation, using ANSYS-CFX® software will be carried. Comparing it with the experimental results, it will allow testing its aptitude to represent this type of flow.

Through this research, we will try to further understand the behavior of foam flow: its physics, its stability and hydrodynamics. At the same time, establish some guideline concerning the characterization of any complex fluid.

All these facts have been described in an easy to understand statement:

“A meringue is really nothing but a foam. And what is foam after all, but a big collection of bubbles? And what's a bubble? It's basically a very flimsy little latticework of proteins draped with water. We add sugar to this structure, which strengthens it. But things can, and do, go wrong.” **Alton Brown**

CHAPTER 2

EXPERIMENTAL FACILITY AND MEASUREMENT TECHNIQUES

This experimental study constitutes the continuity of the works of Blondin [3], Tisné [51], Madani [113] and earlier studies concerning horizontal foam flow. One of the main goals is to facilitate data suitable for numerical models simulating rheological conditions of such complex flow. Our work is to complete the foam flow characterization over a different range of void fraction and flow disruption devices. The experimental facility is based on the one of Tisné [51]. It allows creating stable foam that does not depend on the flow variation, or the channel geometry. This chapter presents the detailed description of the experimental facility, and the measurement techniques used. These latest are, pressure outlets, PIV method, polarographic method and conductimetry method.

1. Experimental facility

The experimental facility was designed to handle the different requirements of foam flow. Its geometry is capable of making studies for a horizontal flow. It presents plane walls making it suitable for the experimental measurements undertaken. Thus, the plane walls allowed the easy placement of polarographic probes along its surface. They are required in the Particle Imaging Velocimetry. The use of circular pipes would create important refraction problems making nearly impossible the use of this method.

A schematic view of the experimental facility appears in Figure 2.1. It includes two adjacent ducts; the test section covers a close liquid circuit and an open gas one. It takes care of the data acquisition; its section can adapt to different channels and fdd. Inside the second duct is where the polarographic method calibration takes place; additional details are described in the following sections.

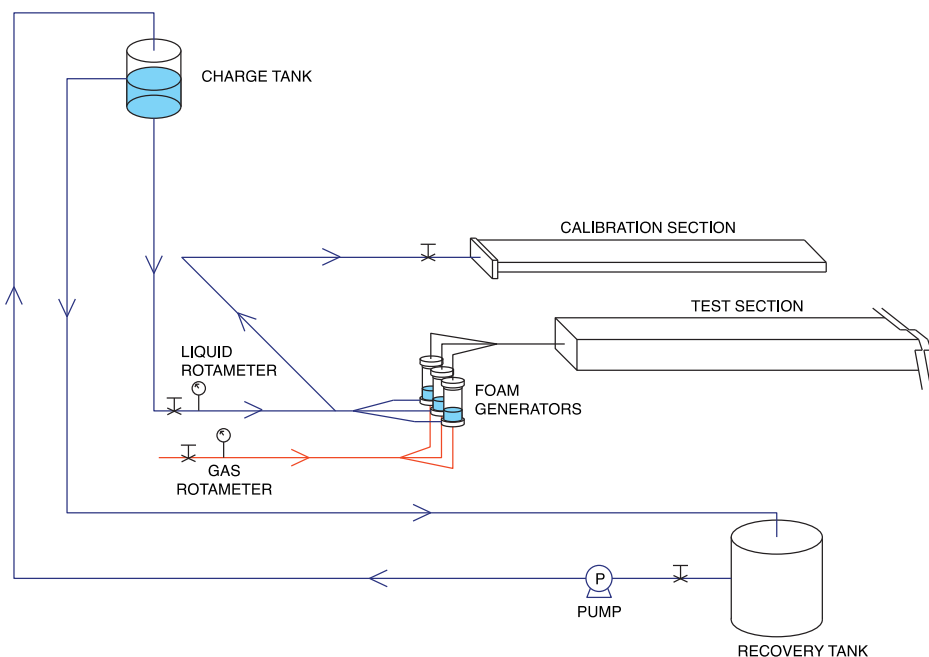
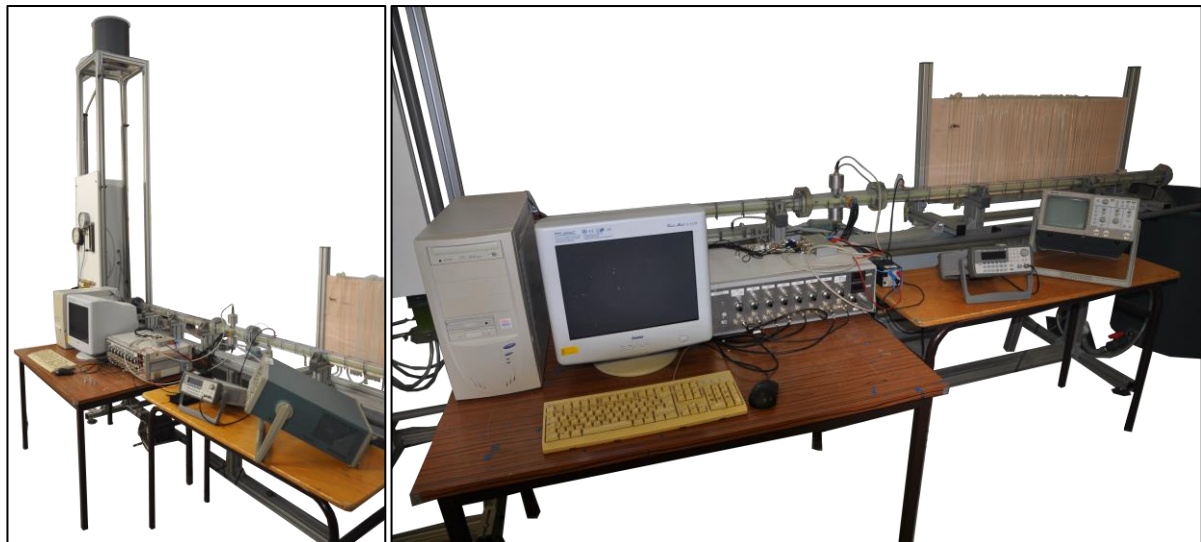


Figure 2.1 Photography and schematic view of the experimental facility

1.1 Recirculation pump

A centrifugal pump is in charge of pumping the liquid (water and surfactants) from the bottom recovery tank to the top charge one. Its maximum flow rate is about $1 \text{ m}^3/\text{h}$ and can deliver a head of 7 m.

1.2 Recuperation tank

The recuperation tank has a 300 liters capacity and is connected to the test section and the calibration channel outlets. It recovers the liquid through the drainage of the foam. Its capacity allows that a highly stable foam be created and later completely drain, as it stays in the tank. This way, the liquid can be used again.

1.3 Charge tank

It is located 2 m above the experimental facility, assuring a constant charge of liquid inside the foam generators, avoiding the flow fluctuations that a centrifugal pump may create.

1.4 Foam generators

The foam is created injecting pressured air, through a permeable media inside cylindrical containers filled with liquid, which act as foam generators. The water contains surfactants, described further ahead (Figure 2.2).

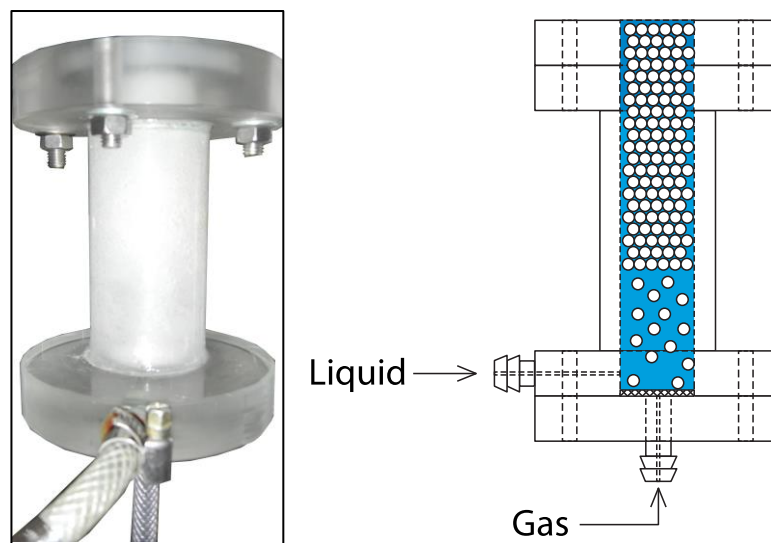


Figure 2.2 Diagram and photography of a foam generator

The presence of three generators, parallels and independents, allow us to modify the foam flow and bulk velocity (one generator for 2 cm/s, two generators for 4 cm/s and three generators for 6 cm/s) without altercating the foam structure. Previously, other authors [3] used only one generator with bypasses at its exit. This method creates a change of the foam structure and texture as it passes trough the bypass, meaning that the foam inside the test duct is not the same as the one created by the generator. Each generator presents an interior diameter of 40 mm and a height of 120 mm.

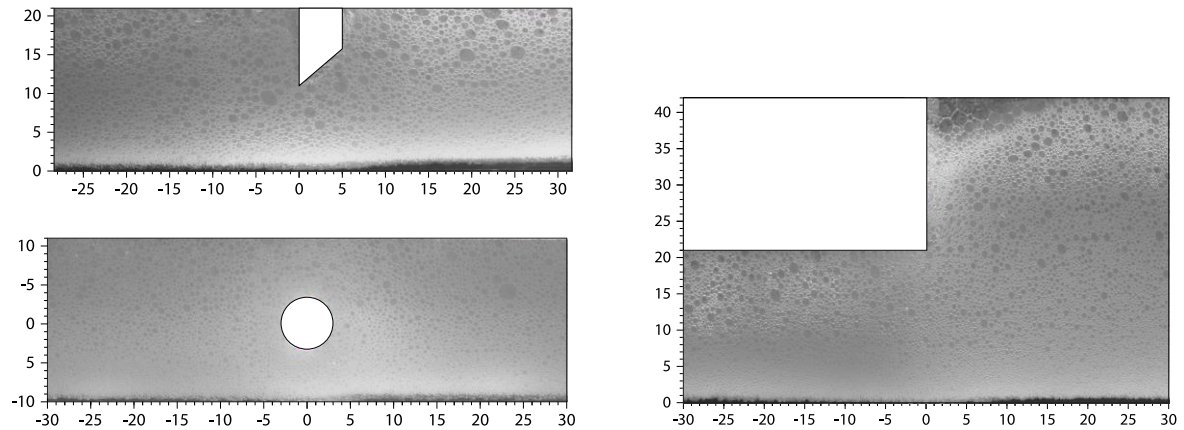


Figure 2.3 Example of foam flow over the lateral wall for the three mechanic flow restrictions (fence, half-sudden expansion and cylinder)

Injecting the air through a glass permeable media, with porosity between 10 and 15 μm , creates the bubbles. The bubbles diameter is around 0.5 mm with a maximum size of 1 mm (the foam quality makes the diameter vary). The porosity of the permeable media and the surfactants are the most important factors that condition the bubbles size [43]. Because of the deviation that the permeable media presents it is impossible to create all the bubbles with the same size.

Normally, the foam qualities or void fraction will be between 55% and 85%. In these ranges we contemplate both limits of foam, wet and dry. Figure 2.3 shows an example the foam flowing through three different mechanics' restrictions: fence, half-sudden expansion and cylinder. It indicates how the bubble size deviation is not relevant and that almost every bubble presents a similar diameter.

1.5 Test section

The test duct has a length of approximately 3.2 m. It is made of Plexiglas with a 21x21 mm² square section. The channel is located on permanent supports that assure its horizontality. At the middle, there is an exchangeable section that allows us to adjust the restrictions through which the foam will flow. The exit of the test section is open to the atmosphere (Figure 2.4, Figure 2.5 and Figure 2.6).

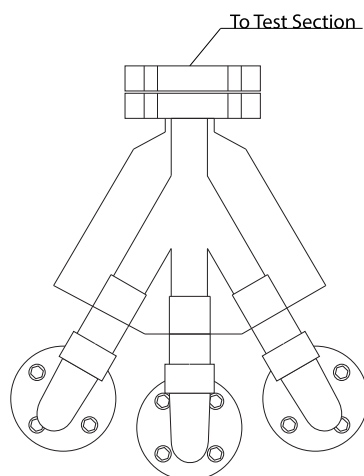


Figure 2.4 Top view of the foam generators

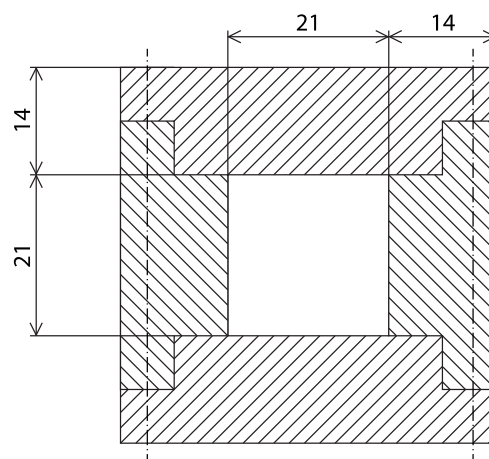


Figure 2.5 Diagram of the cross section

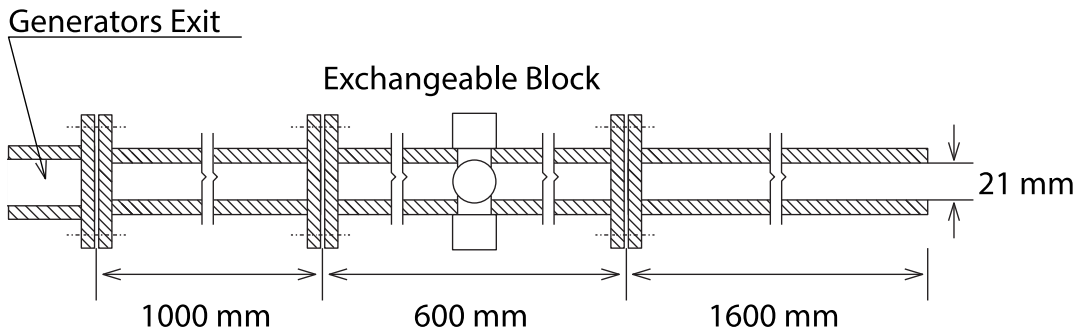
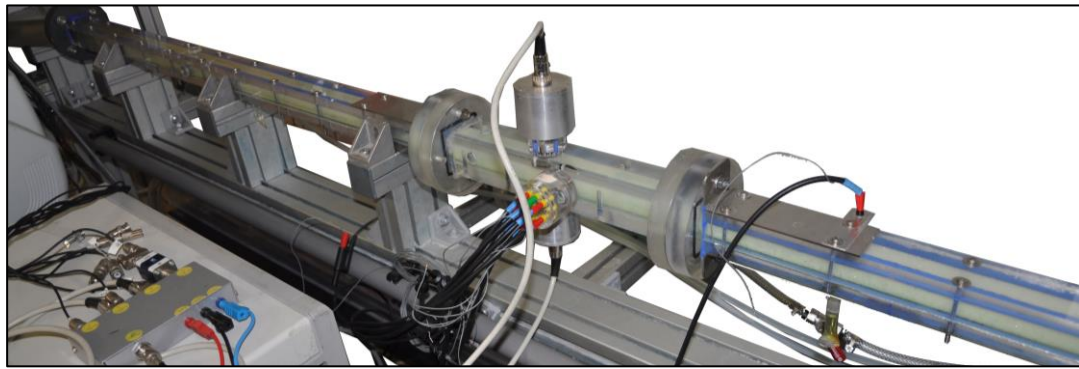


Figure 2.6 Image and diagram of the test section

The exchangeable sections were modified to allow the use of the polarographic method and the conductimetric method. Along this section, a series of interchangeable blocks can be added or removed to allow the measurements.

The test section should be located at least 20 times the hydraulic diameter from the duct entrance [114]. For our experiment, we located the test section 60 times the hydraulic diameter. This way, the influence of the inlet and the outlet can be neglected.

1.5.1 Flow Disruption Devices (FDD)

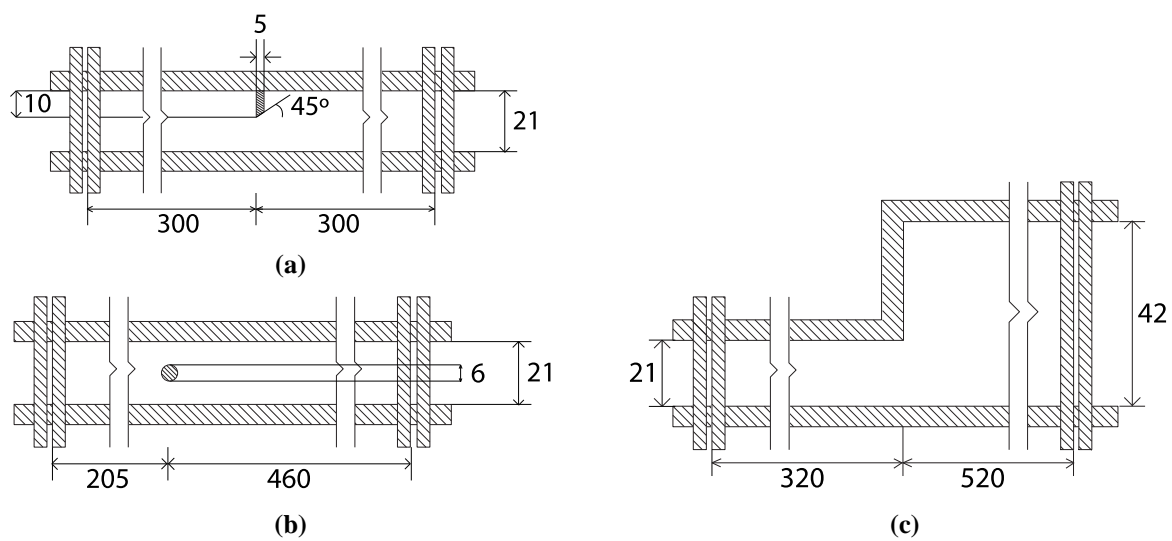


Figure 2.7 Lateral schematic representation of the three flow disruption devices: (a) fence, (b) circle and (c) half-sudden expansion (dimensions in mm)

Figure 2.7 represents a scheme with the dimensions of the three flow disruption devices used to study the foam behavior, and reorganization after facing a sudden change in its flow pattern. These mechanisms include: a fence (a), a cylinder (b), and a half-sudden expansion (c). As the foam passes through each one of them, they induce a forced drainage, coalescence and coarsening, due to bubbles reorganization and energy loss. It is important to note that after the half-sudden expansion, the duct changes its square section for a rectangular one (21x42 mm²) all the way to the outlet into the recovery tank.

1.6 Calibration section

The calibration duct (Hele-Shaw channel) is shown on Figure 2.8, and its section on Figure 2.9. It is parallel to the test section, as showed before. It has a length of 1 m with a rectangular section of 1x21 mm². Its design creates a dissipative flow. This section is used to calibrate the polarographic probes that can be placed over the channel, inside a removable block. The pressure losses along this duct are measured by two pressure outlets located at both sides of the polarographic block. The wall shear that may be determined inside this section, presents similar values to those obtained in our experiments inside the test section.

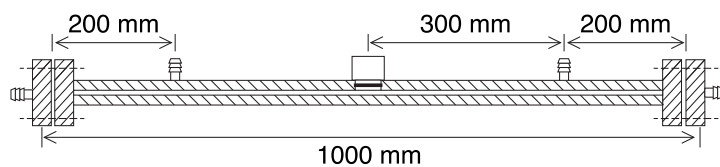


Figure 2.8 Diagram of the calibration channel

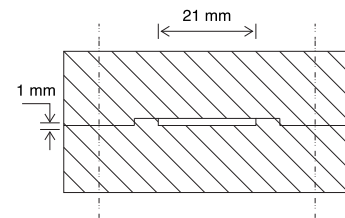


Figure 2.9 Diagram of the calibration channel cross section

2. Measurement techniques

This section describes the measurement techniques used in this work to define the pressure losses, velocity fields, local velocity, wall-slip liquid layer, and wall shear stress.

2.1 Liquid flowmeter

The liquid flow is regulated by three liquid flowmeters (Sho-Rate series, model 1350 Inox VD2), parallel to the foam generators. This configuration allows a precise foam generation with no foam quality oscillations or variation.

The flowmeters elements show heavy-walls, precision bore, borosilicate glass metering tubes, a wide range of scales on the metering tube -with contrasting background for easy readability- and interchangeable floats. Because they are in direct contact with the liquid, must avoid any chemical reaction with the polarographic substances. Therefore, the components are made of stainless steel and glass. They may cover a flow range from 0 to 20 l/h.

2.2 Gas flowmeter

The gas flow is regulated by two parallel Brooks flowmeters (Sho-rate series) with similar features to the water flowmeter. The first one (R2-15-A) has a spherical float of sapphire, while the second flowmeter's float (R2-15-B) is made of tantalum. They can span a flow range from 0 to 52 l/h

and 0 to 48.9 l/h, respectively, with a reproducibility of 0.5%. The curves provided by the manufacturer had to be corrected. The following relationship was applied, from a mass balance and perfect gas equation:

$$Q_{gr} = Q_{gmes} \cdot \frac{P_{in}}{P_{out}} \cdot \sqrt{\frac{D_G}{1} \cdot \frac{T_a}{294} \cdot \frac{1.013 \cdot 10^5}{P_S}} \quad (2.1)$$

where Q_{gmes} is the gas flow measured from the calibration curves, D_G is the gas density compared to the air at normal conditions (air = 1), T_a is the condition temperature [K], P_{in} is the absolute pressure [Pa] at the foam generator inlet and P_{out} is the absolute pressure [Pa] at the foams generator outlet. The absolute Temperature is near 291 K. The absolute pressure was measured inside the foam generator with the use of a ‘‘Bourdon’’ manometer.

2.3 Pressure outlets

The static pressure along each test section (fence, half-sudden expansion and cylinder) is measured by pressure outlets located at the bottom of the channel, at the middle vertical plane. These pressure outlets are attached, through silicon hoses, to a series of manifold tubes placed over a scaled plate (Figure 2.10). The misreading of the manifolds pipes is estimated at a maximum of 1mm water column. The measured static pressure value at the wall is determined using the hydrostatic equation:

$$P = P_a + \rho g \Delta z \quad (2.2)$$

where P_a is the atmospheric pressure, Δz is the height difference between the water column height measured at the pressure outlet and the one measured for the atmospheric pressure, ρ is the liquid density and g is the gravity acceleration.

Near the fence, there are 23 pressure outlets; eight of them are located upstream of the flow restriction mechanism and the other 15 downstream of it. The enlargement holds 38 pressure outlets, 14 being upstream, and 24 downstream. And the cylinder has 27 pressure outlets, 10 upstream of the fence and 14 behind. The static pressure outlets allow measuring the pressure drop along the channel, before and after the singularity. This way we quantify the effect that bubble restructuring, coalescence and foam quality have on the pressure loss curve.

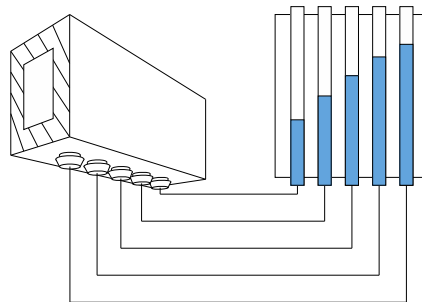


Figure 2.10 Diagram of the pressure outlets arrangement

2.4 Particle Imaging Velocimetry (PIV)

It's a non-intrusive optic method able to measure the displacement of particles in a plane. Its principle is based on the comparison between two instantaneous position fields of particles in the flow. It is possible to calculate and instantaneous mean velocity fields by this particle displacement.

The PIV is widely used as a technique in aerodynamics and hydrodynamics, for low and supersonic velocities, depending on the technical characteristics of the equipment used [115,116]. The PIV measurement process includes (Figure 2.11):

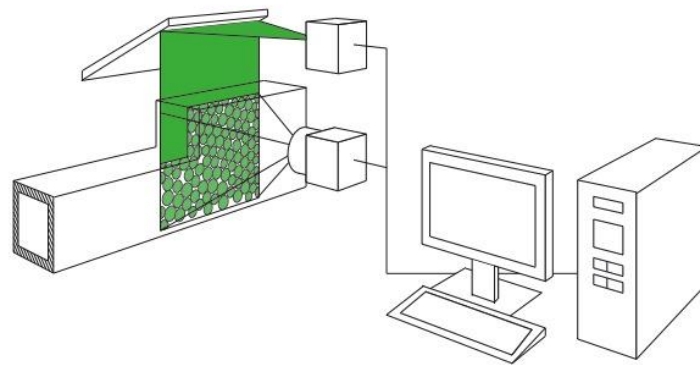


Figure 2.11 Overview of the Particle Imaging Velocimetry (PIV) system

- **Tracking particles:** Normally, fine particles are added to the flow for seeding. The quantity of particles should not affect the density of the liquid. It has been shown how, others particles will later reflect the light reflected by one particle. This phenomena can increase the signal to noise ratio.
- **Illumination:** When a zone from the flow goes through the plane created by the laser, the particles reflect the light. The light reflections are captured with a camera (CCD) placed perpendicular to the laser plane. The time difference between laser pulses is known (frequency of the pulse laser).
- **Capturing the images:** The first laser pulse fixes the particles over an image. Later, the second pulse fixes a second image that detects the movement difference due to the flow.
- **Image treatment:** The two images are treated to find the velocity fields at the area of interest; the plane is divided in several interrogation zones. The particle displacement between images is studied in each zone. The interrogation zones can have a size of: 16x16, 32x32, 64x64 or 128x128 pixels. Using a correlation technique, the measurements provide the velocity vectors inside the flow zone. They consider the scale factor (between the real image and the pixel size) and the timestep between the two pulses.

2.5 Polarographic method (or electrochemical method)

The evaluation of any hydrodynamic phenomenon requires learning many aspects related to the wall shear stress: “the force applied over the cross sectional area of the wall”. However, the techniques able to measure this feature are few. The most commonly used are, the hot film anemometry (inside the viscous boundary layer) and the polarographic technique (at the wall). They work in similar ways being based on a heat transfer or mass exchange, respectively. This work, we chose the polarographic method, capable of measuring the wall velocity gradient and wall shear stress in aqueous foam flow.

A study of the ions transport mechanism allowed developing a polarographic technique as an analogy of heat and mass transfer. It is based on the diffusion properties of chemical components; the oxy-reduction couples [117]. Later, it was used to describe the mass transfer of a fluid in two coaxial fixed cylinders. These played the role of the anode and the cathode of an oxy-reduction reaction controlled by the ionic diffusion [118]. Recently, this method applied in the study of aqueous foam flow. Many authors have used it to estimate wall intensity turbulence, energy dissipation, energy production, mass transfer, wall velocity gradient, and wall shear stress [119,51,113].

2.5.1 Method principle

The polarographic or electrochemical or electrodiffusional, method is based on a fast oxy-reduction reaction controlled by convection and diffusion phenomena. It occurs over an electrode surrounded by an aqueous solution containing the oxy-reduction couple:



where Ox is the oxidant, Red the reducer and z_e the electron number involved in the reaction.

After adding the oxy-reduction couple in the solution, the electrodes will reach equilibrium potential. When the reaction is balanced, there is no current in the circuit. As we impose a potential, the reaction starts. A charge transfer occurs between the cathode and the ions present inside the solution. This electrons migration will generate an electric current over the external circuit. This current, can be caused by four different phenomena:

- Mass diffusion at the electrode vicinity, due to a concentration difference,
- Ions exchange between the cathode and anode, due to an existent electric field. It can be easily removed by adding in excess an indifferent electrolyte,
- Ions transfer, due to the forced convection,
- Natural ions convection under the influence of the mass volume gradients, linked to the concentration gradients. This convection can be neglected, as long as the transport due to the hydrodynamic convection predominates.

The polarographic method can be used in two-phase problems only if there is a liquid film at the walls. In fact, the ions diffusion layer must be smaller than the shear liquid film. For these conditions, the mass conservation equation (or convection-diffusion equation) can be reduced to:

$$\frac{\partial c}{\partial t} + U \cdot grad(c) = D \Delta c \quad (2.4)$$

where c is the local instantaneous concentration of the oxidant (mol/m^3), D is the molecular diffusion coefficient and U the instantaneous velocity.

In two-dimensional cases the imposed boundary conditions are given in an axial coordinate system over the electrodes surface (Figure 2.12):

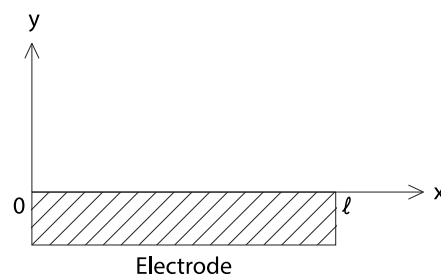


Figure 2.12 Measurement electrode

- $c = 0$ for $y = 0$; there is no concentration over the electrode surface,
- $\left(\frac{\partial c}{\partial t}\right)_{y=0} = 0$; there is no mass transfer at the channel wall,
- $c = c_\infty$ for $y = \infty$; there is a constant concentration at the flow core.

The reactive flux over the electrode and the current generated by this one are given by:

$$\phi_R = \iint_0^{elec} -D \left(\frac{\partial c}{\partial y} \right) dA_s \quad (2.5)$$

$$I = z_e \cdot F \cdot \phi_R \quad (2.6)$$

where F is the Faraday's number (= 96500 Coulombs).

The concentration field and the current depend of the hydrodynamic conditions.

Microelectrodes with particular geometry and size can be used to simplify even more, the convection-diffusion equation. This simplification relates the current to the parietal gradient. If the fluid presents Newtonian properties, then the wall shear stress can be deduced from the wall velocity gradient.

2.5.2 Mass transfer coefficient

The polarographic technique is based upon the capacity to occur a limited diffusion at the electrode surface. The measured current is related to the ions' transfer at the vicinity of the electrode, normally known as diffusion limiting current, I_{lim} . As long as $I = I_{lim}$, the diffusional plateau is achieved, and the maximal concentration gradient. This means that the reactive concentration can be neglected at the electrode surface and the cathode reaction is complete. In this case, the limit diffusion current only depends on the hydrodynamics and physics properties of the studied flow.

A plot of the current intensity recovered at the electrode versus the applied voltage (Figure 2.13), will make appear the diffusional plateau. Its height is proportional to the reactive concentration, c_∞ , and to the mass transfer coefficient, k_m .

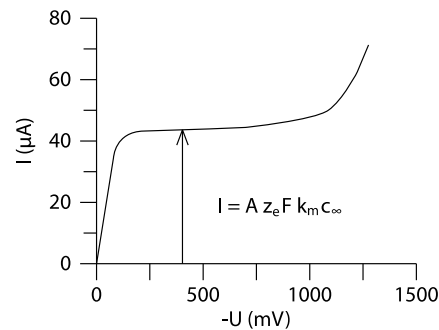


Figure 2.13 Current/voltage curve and its diffusion plateau

The mass transfer coefficient relates to the current density trough the following equation:

$$I/A_s = z_e \cdot F \cdot k_m \cdot c_\infty \quad (2.7)$$

where S is the electrode surface.

In our case, with the couple ferricyanide-ferrocyanide (fast electrochemical reaction), only one electron occurs for the exchange. The chart of current intensity vs. voltage shows that for values below the plateau of diffusion the cathode reaction is not complete. While for values higher than the diffusion plateau water electrolysis occurs.

2.5.3 Convection-diffusion equation for a simple probe in steady state

The instantaneous mass transfer relates to the velocity field by the convection-diffusion equation, is governed by:

$$\frac{\partial c}{\partial t} + U \cdot \text{grad}(c) = D \Delta c \quad (2.8)$$

It was first solved for a rectangular probe, where its length L_s was sufficiently large, compared to its width l . The following settings were proposed [120]:

- The flow is permanent, two dimensional and uniform over the width of the electrode (small electrode surface). The equation of the mass balance can then be written as:

$$u \frac{\partial c}{\partial x} + v \frac{\partial c}{\partial y} = D \left(\frac{\partial^2 c}{\partial x^2} + \frac{\partial^2 c}{\partial y^2} \right) \quad (2.9)$$

where x is the mean flow direction, y is the wall distance, u the velocity component in the x direction, and v the velocity component in the y direction (Figure 2.14).

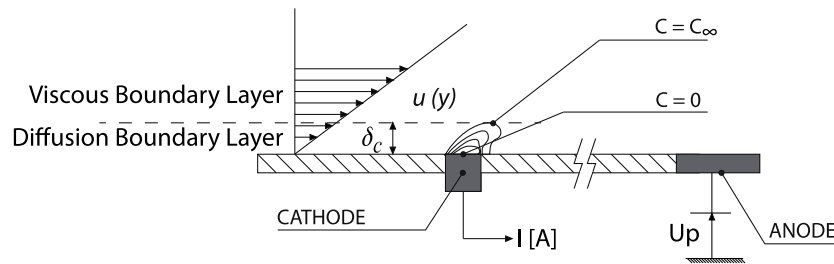


Figure 2.14 Polarographic method principle

- The mass boundary layer is small enough when compared against the viscous sub-layer (Schmidt number $Sc = \nu/D \gg 1$). Therefore, the velocity profile near the wall has a linear behavior over the whole study domain:

$$u = S_0 \cdot y \text{ and } v = 0 \quad (2.10)$$

This also means that the concentration only varies significantly at the immediate vicinity of the wall, where the viscosity forces prevail. The linearity inside the viscous sub-layer also allows the velocity component to be a function of the wall distance y , from the velocity gradient at the vicinity of the wall S_0 .

With these settings, the equation evolves into:

$$S_0 y \frac{\partial c}{\partial x} = D \left(\frac{\partial^2 c}{\partial x^2} + \frac{\partial^2 c}{\partial y^2} \right) \quad (2.11)$$

The axial diffusion can be neglected before the normal diffusion ($\partial^2 c / \partial x^2 \ll \partial^2 c / \partial y^2$) when the transversal length of the electrode is:

$$Pe = \frac{S_0}{D} l^2 \geq 5000 \quad (2.12)$$

where Pe is the Péclet number. This expression simplifies the convection-diffusion equation into:

$$S_0 y \frac{\partial c}{\partial x} = D \frac{\partial^2 c}{\partial y^2} \quad (2.13)$$

The resolution of the steady equation leads to the current density limit (I/A) at the electrode [121]:

$$\left(\frac{I}{A} \right) = 0.807 z_e F c_\infty \left(\frac{D^2 S_0}{l} \right)^{1/3} \quad (2.14)$$

The mass transfer coefficient is linked to the diffusional limit current by:

$$k_m = \frac{I}{z_e F A c_\infty} \quad (2.15)$$

For a rectangular electrode, it can be written as:

$$k_m = 0.807 \left(\frac{D^2 S_0}{l} \right)^{1/3} \quad (2.16)$$

A microelectrode of diameter d_s generates the same stationary current than a rectangular electrode with a length of $l = 0.82 d_s$. For a circular electrode with a surface A_s , the diffusion limiting current and the mass transfer coefficient are written as:

$$I = 0.862 z_e F c_\infty A_s \left(\frac{D^2 S_0}{d_s} \right)^{1/3} \quad (2.17)$$

$$k_m = 0.862 \left(\frac{D^2 S_0}{d_s} \right)^{1/3} \quad (2.18)$$

The diffusional limiting current can be deduced from the wall velocity gradient. It is proportional to the cube of the current. If the active surface of the electrode, the reactive concentration and the molecular diffusion coefficient are known, the wall velocity gradient can be calculated. For a Newtonian flow, the wall shear stress calculation is obtained from the velocity gradient with the next relationship:

$$\tau_0 = \mu_l S_0 \quad (2.19)$$

2.5.4 Frequency response of the microelectrodes

Application of the relationship $I \propto S^{1/3}$ exhibits to major problems from a dynamic point of view: the first is a linearity problem and the second a frequency response problem [122]. Therefore, it is not advisable to use directly this relationship. There is a capacitive effect inside the viscous sub-layer that creates a phase shift with an amplitude loss between the actual velocity gradient fluctuations and those obtained from the current measurements. The knowledge of the frequency response is an important experimental requisite, including the study of small and large amplitude fluctuations.

2.5.4.1 Small amplitude fluctuations

These types of fluctuations have been reviewed in numerous analytical and numerical studies [120,123,124,122]. They follow a linearity hypothesis. In accordance with the experimental conditions and the calculation hypothesis, most of these authors determine a transfer function $H(f)$, for a frequency domain.

They assume that the mass transfer inside the mass boundary layer occurs at a finite velocity. The boundary layer acts as a linear filter cutting the high frequencies. Its impulse response $h(t)$ is a convolution product linking the intensity response $i(t)$ to the sinusoidal perturbation $s(t)$, giving place to:

$$i(t) = h(t) \otimes s(t) \quad (2.20)$$

Inside the frequency domain, the power spectral density of the limit intensity W_{ii} can be linked to the wall velocity gradient one W_{ss} through the transfer function $H(f)$ represented by the Fourier transformation of the impulse response $h(t)$:

$$W_{ii} = |H(f)|^2 W_{ss} \quad (2.21)$$

In order to be able to use this relation, $H(f)$ should be accurately determined for the whole frequency domain and the homogeneity condition has to be verified.

Most authors have found an asymptotic behavior of $|H(f)|$ for high frequencies. The same frequency dependency can be obtained for the mass coefficient transfer [124]. When considering a

numerical application and a high frequency, $|H(f)|$ can be proportional to (f^{-1}) and with a phase shift of -90° [125].

The transfer equations are rarely presented as a function of f , but also as a function of a dimensionless frequency f^* . It depends of real pulsations ($\omega = 2\pi f$) and the time of diffusion. They are related to a mass boundary layer established over the electrodes, defined by:

$$f^* = \omega \left(\frac{d_s^2}{D S_0^2} \right)^{1/3} \quad (2.22)$$

The $H(\sigma)$ expression can be divided into three different domains:

- The quasi-stationary solution corresponding to the $\sigma < 1$ case:

$$\left| \frac{H(\sigma)}{H(0)} \right| = 1 \quad (2.23)$$

This case is obtained when $f \rightarrow 0$. The convection-diffusion equation result leads to the relationship:

$$\frac{W_{ss}(0)}{\bar{\tau}_0^2} = 9 \frac{W_{ii}(0)}{\bar{I}^2} \quad (2.24)$$

Where \bar{I} is the mean current and $\bar{\tau}_0$ is the mean wall velocity gradient. The value of the stationary transfer function can be also deduced:

$$H(0) = \left(\frac{W_{ii}(0)}{W_{ss}(0)} \right)^{1/2} = \frac{1}{3} \frac{\bar{I}}{\bar{\tau}_0} \quad (2.25)$$

- The solution for low frequency stationary transfer ($1 \leq \sigma \leq 6$) is:

$$\left| \frac{H(\sigma)}{H(0)} \right| = (1 + 0.049 \sigma^2 + 0.0006 \sigma^4)^{-1/2} \quad (2.26)$$

- The solution for high frequency stationary transfer ($\sigma > 6$) is:

$$\left| \frac{H(\sigma)}{H(0)} \right| = \frac{4.416}{\sigma} \left[1 - \frac{1.7}{\sqrt{\sigma}} + \frac{1.44}{\sigma} \right]^{1/2} \quad (2.27)$$

For any experimental approach, these solutions are only valid if $\sigma < 8$. These studies were based upon a transfer function, where they presented a linear behavior. Accordingly, they were only possible for the small amplitude fluctuation case.

2.5.4.2 Large amplitude fluctuations

A numerical solution was presented for the frequency response of a wall probe to the sinusoidal hydrodynamic oscillation [126]. It shows that increasing the oscillation frequency spreads away from the quasi-stationary L eveque response. Additionally, it reflects the change in the response signal form, a phase shift and an amplitude loss.

A mass transfer inverse method was later developed [127]. This allows evaluating the evolution of the wall velocity gradient from the measured current. It does not need linearization conditions. It uses a numerical approach from the mass balance equation in a transient non-linear regime. The instant velocity at the wall results from the mass transfer measurement varying in time.

A numerical and experimental study was presented for the case of small oscillations and strong amplitudes [128]. When assigned to the flow a parietal velocity gradient in a simple unsteady form, the following expression resulted:

$$S(t) = S_0 [1 + B \cos(\Omega t)] \quad (2.28)$$

where S_0 is the mean gradient, B is the oscillation amplitude and Ω the oscillation pulsation. The mass transfer equation becomes:

$$\frac{\partial c}{\partial t} + S_0[1 + B \cos(\Omega t)]y \frac{\partial c}{\partial x} = D \left(\frac{\partial^2 c}{\partial x^2} + \frac{\partial^2 c}{\partial y^2} \right) \quad (2.29)$$

Let us introduce the characteristics' scales for length and time, $x = x/l$; $Y = y/\delta_c$; $c^* = c/c_\infty$ and

$t^* = t(\Omega/2\pi)$, where Le is the electrode length and $\delta_c = Le \left(\frac{S_0 Le^2}{D} \right)^{-1/3}$ is the mass boundary layer.

The mass transfer equation takes a dimensionless form:

$$\left(\frac{\Omega Le^2}{2\pi D} \right) \frac{\partial c^*}{\partial t^*} + \left(\frac{S_0 Le^2}{D} \right)^{2/3} (1 + B \cos(2\pi t^*)) Y \frac{\partial c^*}{\partial X} = \left(\frac{S_0 Le^2}{D} \right)^{2/3} \frac{\partial^2 c^*}{\partial Y^2} + \frac{\partial^2 c^*}{\partial X^2} \quad (2.30)$$

or:

$$\frac{f^*}{Pe^{2/3}} \frac{\partial c^*}{\partial t^*} + (1 + B \cos(2\pi t^*)) Y \frac{\partial c^*}{\partial X} = \frac{\partial^2 c^*}{\partial Y^2} + \frac{1}{Pe^{2/3}} \frac{\partial^2 c^*}{\partial X^2} \quad (2.31)$$

where $Pe = S_0 Le^2 / D$ is the Péclet number and $f^* = \frac{\Omega Le^2}{2\pi D}$ is the dimensionless frequency. Inside this

equation, each term represents a particular physics phenomenon:

$$\begin{aligned} \frac{f^*}{Pe^{2/3}} \frac{\partial c^*}{\partial t^*} & : \text{Mass transfer inertia} \\ (1 + B \cos(2\pi t^*)) Y \frac{\partial c^*}{\partial X} & : \text{Forced convection} \\ \frac{\partial^2 c^*}{\partial Y^2} & : \text{Normal diffusion} \\ \frac{1}{Pe^{2/3}} \frac{\partial^2 c^*}{\partial X^2} & : \text{Tangential diffusion} \end{aligned}$$

The importance of each phenomenon is controlled by one of the following dimensionless mechanism:

$$\frac{f^*}{Pe^{2/3}}, B \text{ and } \frac{1}{Pe^{2/3}}$$

The instantaneous concentration c can be decomposed in mean \bar{c} , and fluctuating c' parts [128]. From this, the problem can be divided into two: the small amplitudes case (weak B) and the large amplitudes case (strong B).

In the case of week amplitudes, the mean value of the mass transfer is not affected by the probes frequency response. As for the fluctuant part of this transfer, it only depends of the parameter $\frac{f^*}{Pe^{2/3}}$. This one has to be corrected for each frequency. Therefore, it has used a transfer function between the excitation (wall gradient velocity) and the response (mass transfer), and it was expressed by a quasi-stationary frequency.

As for the case of strong amplitudes, the linear approach can no longer be used. The mass transfer is affected by frequency response problem. The mean mass transfer value is mannere by its fluctuating part. Therefore, the superposition principle cannot be used over the fluctuations. If it is applied, harmonic frequencies will appear over the mass transfer values, and the mean values will have to be corrected. The resolution of this problem is only possible for a sinusoidal velocity gradient.

Sobolik et al. [129] propose a model to calculate the wall velocity gradient based on the correction of the quasi-stationary response of the electrochemical probe. It is assumed that the concentration field near the exchange zone in a two-dimensional case can be defined as:

$$c(x, y, t) = c_0 \times \left[1 - F(t) \left(\frac{y}{\delta(t)} \times \left(\frac{Le}{x} \right)^{1/3} \right) \right] \quad (2.32)$$

where $\delta(t)$ is the thickness of the liquid layer and $F(t)$ is a reducing function normalized by the conditions: $F(0) = 1$, $F(\infty) = 0$ and $F'(0) = -1$. When including them in the convection-diffusion equation and integrating analytically over the whole space, the following relationship results:

$$S_c(t) = S_q(t) + \frac{2}{3} t_0 \left(\frac{\partial S_q}{\partial t} \right) \quad (2.33)$$

where $S_q(t)$ is the wall velocity gradient measured in quasi-stationary regime and $\left(\frac{\partial S_q}{\partial t} \right)$ is the variation of the time evolution of the wall velocity gradient. t_0 is the characteristic time of the electrochemical probe when passing from transitory regime to a quasi stationary one:

$$t_0 = \left(\frac{\alpha_{sp}}{I} \right)^2 \quad (2.34)$$

where α_{sp} corresponds to the asymptotic curve of Cottrel:

$$\alpha_{sp} = nF c_0 S \left(\frac{D}{\pi} \right)^{1/2} \quad (2.35)$$

When associating these two parameters together and the Levêque equation, it becomes:

$$t_0 = 0.428 \left(\frac{d_s^2}{DS_0^2} \right)^{1/3} \quad (2.36)$$

This way S_c gives the corrected value of the wall velocity gradient, considering the inertia of the electrochemical probes. S_c corresponds to the measurement of the velocity gradient in dynamic conditions. This relationship was experimentally verified [129,130] and it allows the calculation of the instantaneous wall velocity gradient, despite important fluctuations on the signals.

The probes frequency response has been object of numerous works and it is still a highly debated subject. For the small oscillations, the differences have already been solved. The mean value of the mass transfer is not affected by the fluctuation. As for the fluctuant part, this one needs to be corrected and for that a transfer function can be used. Each author has developed their own function and they all depend on the frequency range used. These ones can only be used in laminar regime. For the large amplitude fluctuations, the linear approach is no longer possible to use. Previous studies [122,128] shows that the mean value of the mass transfer is affected by the fluctuating part.

2.6 Conductimetry Method

In two-phase flows, there is option of methods to measure the wall-slip liquid layer close to the walls. They go from the micro-needles, capable of detecting the gas phase [131], to the x-ray absorption. As already noted, in previous cases, foam flow carries a liquid layer at the walls induced by the drainage and internal forces. To measure it, we used the conductimetry method. It registers the liquid film electric resistance -between the bubbles flowing over the walls- and the probes on them. This method can be applied to any electric conductive liquid flowing over a non-conductive surface or inert wall.

It is simple to use being a non-intrusive method; the probes don't influence the foam flow pattern. The probes form and choice are the most important factors to consider when applying this

method. They must consider the thickness of the liquid film being measured. The farther the probes are away from each other; more information will be obtained about the wall-slip layer. For rectangular probes, a conductimetry method calculation was developed [132].

The thickness of the wall-slip liquid layer is more relevant at the bottom of the channel than at the top and sides. At the top and sides, it can only measure around 10 micrometers, while at the bottom it can have a thickness of almost 2 millimeters [3]. The main reason for this difference is the drainage of the liquid inside the Plateau borders, due to gravitational force, the bubble-to-bubble interaction, and the wall shear stress.

3. Experimental arrangements

In this section, we'll cover different aspects that were taken into consideration concerning materials and conditions related to the experiments and measurements techniques.

3.1 Surfactant choice and quality

Many substances decrease a liquid surface tension allowing the generation of foam (surfactants, proteins, particles, lipids, etc.). Most of the foam studies selected appropriate surfactants concerning their particular objectives [56,2]. In our study the surfactant choice needed to satisfy the following characteristics:

- The foam should be “stable”, permitting it to flow through all the channels length without disappearing or breaking when crossing mechanisms presenting irregularities. But at the same time, a high stability diminishes the foam drainage. Meaning that the recuperation tank fills up quicker than the foam drains, and there is not enough time to obtain reliable information (1 hour for the most stable foam). A balance should then be attained, in regards to foam stability and its drainage time.
- Some measurement techniques use electrical currents and voltages to measure the foam flow, liquid film thickness and wall shear stress. Therefore, the surfactant should not affect the real interaction between the mechanical and physical aspects of the foam and the electrochemical responses, it should be recalled that previous works [51,113,32] showed how some surfactants are not suitable for the polarographic method.

After reviewing these requirements, we selected the SIMULSOL SL 826 surfactant distributed by the company SEPPIC. It is based on glucose, presents stable foaming properties and it is easy to handle down to 5°C. Being a non-ionic surfactant, facilitates the use of the electrical measurement techniques. For the stability requirements, a concentration of 0.15% (in volume) was used; it is approximately twice the Critical Miscellanea Concentration (CMC).

3.2 Foam flow characterization

A database that considers the foam velocity and quality is characterized by the flow of the liquid and gas phase inside the generators. The foam quality varies from 55% to 85%. As for the mean velocity, it was covered in the three cases shown in Table 2.1 [3]. These ones were choose due to the scientific background already done over these regimes and the limitations of the experimental facility. To be capable to increase the foam's velocity we will need to place more parallel foam generators, this way we won't alter the foam structure.

In all these cases the pressure losses, velocity fields and profiles, liquid film thickness, and the wall shear stress over the walls were studied, with and without flow disruption devices.

Case	Max Foam Velocity [cm/s]	Liquid Flow [L/h]	Gas Flow [L/h]	Foam Quality [%]	Pressure before generators [bar]
I	1.92	14.3	17.50	55	0.40
		12.7	19.05	60	0.40
		11.1	20.60	65	0.40
		9.5	22.23	70	0.42
		7.9	23.80	75	0.42
		6.4	25.40	80	0.44
		4.8	27.00	85	0.50
II	4.27	28.6	34.90	55	0.63
		25.4	38.10	60	0.64
		22.2	41.30	65	0.64
		19.1	44.45	70	0.64
		15.9	47.60	75	0.64
		12.7	50.80	80	0.64
		9.5	54.00	85	0.70
III	6.14	35.7	43.70	55	0.66
		31.8	47.63	60	0.66
		27.8	51.60	65	0.70
		23.8	55.57	70	0.70
		19.8	59.50	75	0.70
		15.9	63.50	80	0.71
		11.9	67.50	85	0.71

Table 2.1 Foam flow characterization cases

3.3 Foam generators calibration

It is important in any foam research project to verify the deviations that may exist concerning the foam generators specifications. As mentioned, the foam is produced by injecting gas, through a permeable media, into the liquid. The permeability of the three glass filtered medias goes from 10 to 15 μm . Therefore, it is impossible to generate the same bubble diameter inside each generator. To assure a correct experimental study, we need to quantify the difference and evaluate its possible final effect.

There are many factors related to the pressure losses inside a channel for a foam flow [3], the surfactant concentration, the bubbles diameter, the foam quality and the foam velocity. To quantify the error due to the permeable media (directly related to the bubble size created inside each generator) a study of the pressure losses was done under equal conditions, foam flow of 2 cm/s and foam quality of 70%, with the same disruption device (half sudden expansion) (Figure 2.15).

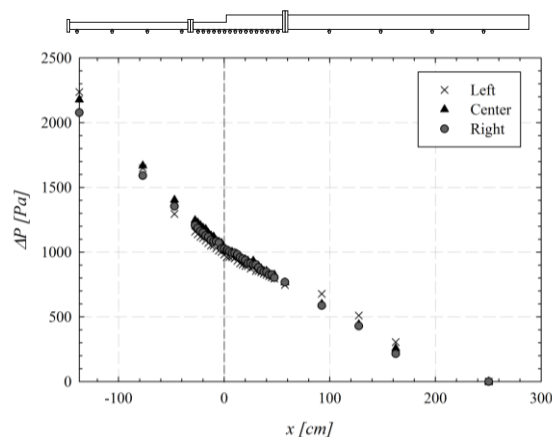


Figure 2.15 Pressure losses inside the test section with a half-sudden as flow disruption, a foam velocity of 2 cm/s and quality 70% for the three generators.

According to this figure, the foam generated inside each generator, under the same conditions, does not coincide. However the largest difference between the three pressure losses, due to the bubbles diameter, is of only 7%. It would mean that we could properly mix the three foam flows, for each generator, and not influence drastically the mean bubble size values.

3.4 Particle Imaging Velocimetry

The PIV method correlates a number of particles from an image to another with a known timestep and thereby obtains the velocity fields of the question area. In foam flow, the gas/liquid interphase is darker than the rest of the flow, and one the laser hits the bubbles contour, this one assigns the whole flow movement (not the movement of each bubble). Therefore, the use of particles is not necessary to track the flow. The close packing of the bubbles keeps them together along the channels length and through the FDD, avoiding the error that bubbles displacement might generate. Figure 2.16 shows an arrangement of ‘particles’ inside the question zone.

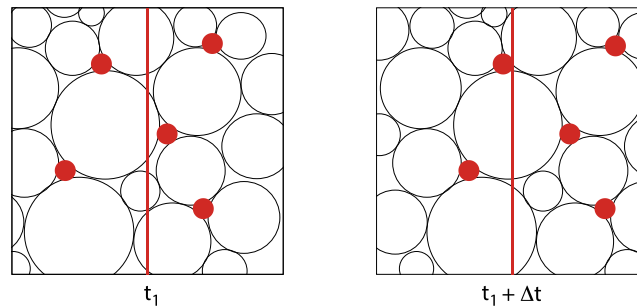


Figure 2.16 Schematic representation of the PIV behavior on the foam flow

The measurements were made over the channel lateral wall. Due to the opacity of the foam flow, and the reflections over the bubbles, it is impossible to see through it and obtain the internal velocity fields. Nevertheless, the main focus is the wall/foam interaction. The velocity fields at the wall allowed approximating a value of the wall velocity gradient.

The velocity measurements were done along the FDDs vicinity zone using a standard particle image velocimetry based on a TSI Powerview™ system, including a light sheets provided by a double-pulsed Nd-YAG laser operating at 532 nm (green), with a 7.25 Hz frequency, and high spatial resolution. It also used a Powerview™ 4MP camera, a synchronizer (TYPE) and Insight® software for the acquisition, processing and post processing. The maximum energy of each pulse was 200 mJ for 8 ns. The delay between the two pulses is fixed, so that particles move a fourth of the interrogation window during the delay. Table 2.2 shows the camera resolution, measured field size, interrogation window, and timestep used for each of the Flow Disruption Devices.

fdd	Resolution [$\mu\text{m}/\text{pixel}$]	Field Size [mm^2]	Interrogation Window [pixels^2]	Δt (I, II, III) [μs]
No-FDD	44	60 x 21	32 x 32	10000, 7000, 4000
Fence	43	60 x 21	32 x 32	8000, 5000, 3500
Cylinder	45	60 x 21	32 x 32	8000, 5000, 3500
Expansion	52	90 x 42	32 x 32	12000, 9000, 5000

Table 2.2 Spatial characteristics for each FDD

A 50% overlap rate has been applied to reduce the velocity grid spacing. The time-average fields are obtained from 500 instantaneous fields.

3.5 Polarographic method

3.5.1 Choice of an electrochemical reactive

Among the many redox couples available [118,123], we selected the ferri-ferrocyanide couple. It is suitable for this study, because of its power and its small sensitivity to the light [123]. The cathode reduction obeys to the chemical equation:



The couples exchange one electron. The chemical reaction is fast enough to not affect the electrodes surface. The active ions concentration is constant through the experiment. The support electrolyte used is potassium sulfate, K_2SO_4 [133]. Its ions have a weak influence in the redox reaction and don't create corrosion problems with the electrodes.

In order to restrain the amount of electrolysis reagent, the ferricyanide concentration was taken at $c = 10 \text{ mol/m}^3$. This amount allows measuring the intensity of the diffusion current (micro-amperes). The ferrocyanide concentration is $c = 15 \text{ mol/m}^3$, so the reaction in the anode is not a limitation for the current circulation. The concentration of potassium sulfate $c = 175 \text{ mol/m}^3$ reduces the solution resistivity, and neutralizes the ion migration due to the potential field created between the cathode and the anode.

3.5.2 Measurement Probes

The platinum electrodes in the polarographic measurements are located inside three exchangeable blocks at the bottom, lateral and top walls of the channel. They can be placed at the straight channel, with no FDD, and at the calibration duct. The platinum probes do not present the corrosion and electrolysis problems that the nickel ones do [51].

The anode should be located so that the diffusional limiting current is never reached, and the following relationship should be recalled:

$$A_{anode} \cdot C_{red} \gg A_{cathode} \cdot C_{ox} \quad (2.38)$$

The cathode has small dimensions, which allows the realization of local studies. The nickel anode is placed downstream from the probes. It is located inside the channel and its surface is more than 500 times larger than the electrodes one.

Three measurement blocks were used to determine the wall shear stress at the top, bottom and lateral walls of the channel (Figure 2.17). Each block contains 11 polarographic probes and can be moved from the test section to the auxiliary channel. They can be located at the middle of the channel test section (1.3 meters from the foam generators exit) at one of the lateral walls, at the bottom and at the top. To assure regular surfaces, and before actual operation, the probes were polished.

The probes diameter will affect the reading; the smaller the electrode, better will be the phenomenon acquisition and response. The relationship (2.22) confirms this point:

$$f^* = \omega \left(\frac{d_s^2}{D S_0^2} \right)^{1/3}$$

where f^* is the dimensionless frequency and d_s is the probe diameter.

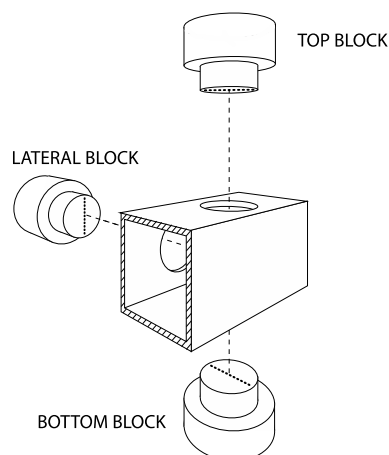


Figure 2.17 Setting arrangement of the three polarographic blocks

The probes in the experiment had a diameter around $d_s = 0.25 \text{ mm}$, equivalent to a theoretical rectangular probe with a length of $L_s = 0.82 d_s$ [134]. They were spaced 2mm from each other, and aligned perpendicularly to the flow (Figure 2.18).

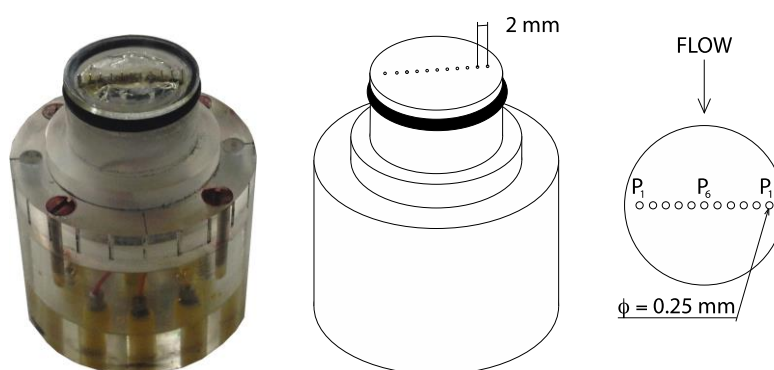


Figure 2.18 Polarographic Probes

3.5.3 Measurement system

The anode was linked to an electrical ground, and a negative potential ($-\Delta U$) was imposed to the measurement probes.

The main constraint of the polarography method is how to accurately measure the redox current (inside the microampere order) collected at the electrodes. Therefore, it is necessary to measure it with high impedance. With the use of an amplifier, the current was converted to voltage. The gain of the amplifier could be adjusted between three values ($K = 10^5, 5 \cdot 10^5$ and 10^6). This measurement system was made locally in the GEPEA Laboratory at Nantes (Figure 2.19). The polarographic experimental data was obtained over 5000 samples for a frequency of 125 Hz.

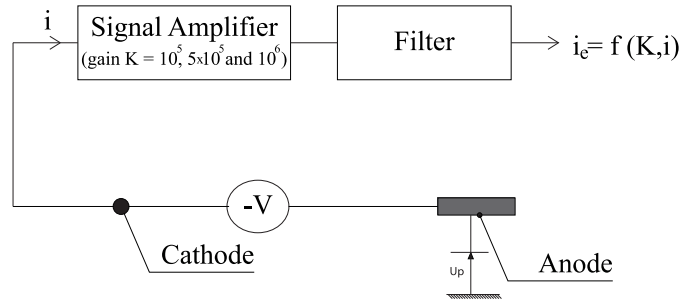


Figure 2.19 Simplified representation of the polarographic measurement system

3.5.4 Probes calibration

To accurately obtain the wall velocity gradient, related to the diffusional limit current, the real value of the probes active surface needs to be known. They were made of 0.25 mm diameter platinum wire but were polished, so the probes remain at the same height as the channel walls. This polishing changes drastically the probes shape. Therefore, a calibration of these ones was made and the real surface values were obtained. They were calibrated inside the calibration channel, where the pressure losses and velocity profile are known, and the active surface is deduced from these conditions.

Before calibrating the probes in the auxiliary channel, the horizontality of the diffusion plateau had to be verified for each used probe. Once this was done, a polarization tension was chosen, so there was no current saturation or concentration over the electrode ($c = 0$).

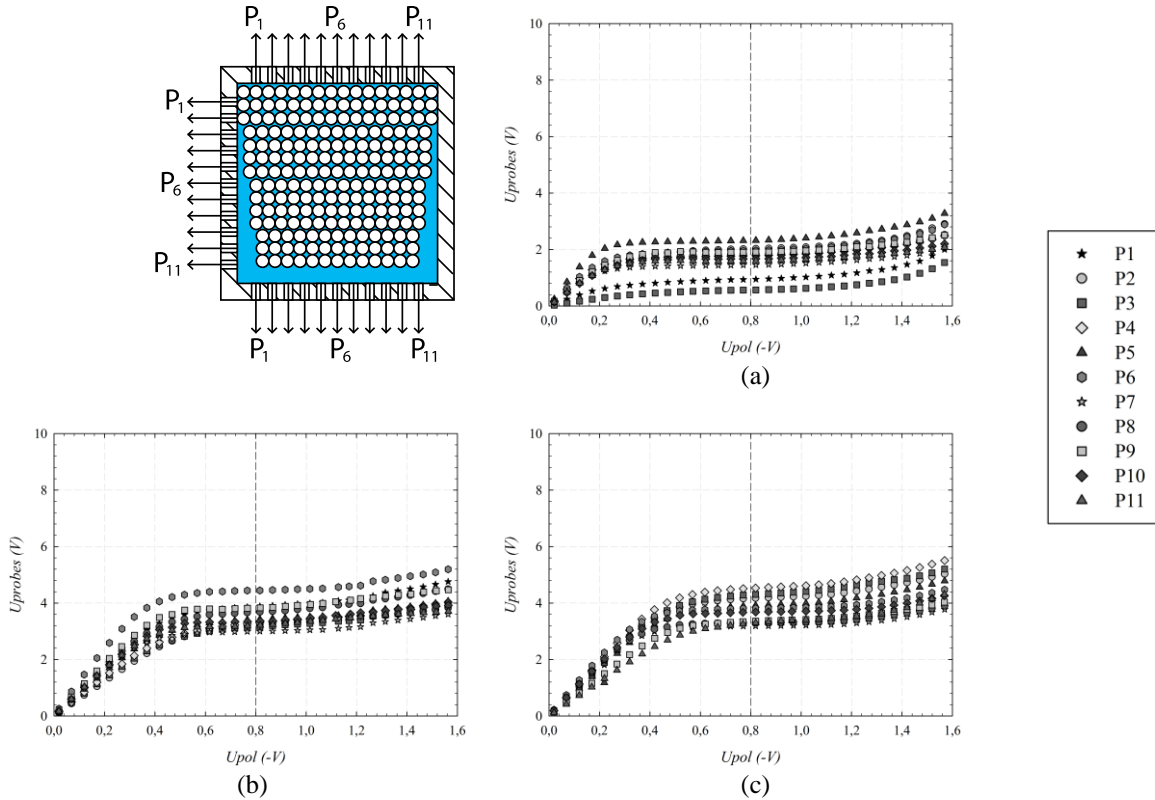


Figure 2.20 Polarograms of the three electrochemical blocks: (a) top, (b) lateral and (c) bottom

Figure 2.20 shows the polarograms (response of the probes against an imposed polarographic voltage) for the three blocks used, top lateral and bottom. They were studied independently. After reviewing these graphs, a -800V polarization voltage was selected for a controlled diffusion regime.

At this value, the measured current only depends of the flow hydrodynamics. The ferrocyanide concentration over the probes was supposed zero.

3.5.4.1 Flow inside the calibration channel

The calibration channel presents two pressure outlets located upstream and downstream of the emplacement of the polarographic blocks (Figure 1.8). They are 60 cm apart and allow measuring the pressure loss in the duct. The flow rate is verified at the first pressure outlet of the calibration channel. For a laminar regime, the establishment length, L_e , is a function of the hydraulic diameter, D_H , and the Reynolds number, Re :

$$\frac{L_e}{d_h} = 0.01 Re \quad (2.39)$$

where the hydraulic diameter is defined as $d_h = 4S/P_m$, with A as the surface, and P_m the wetted perimeter.

In our case, laminar regime calibration, the Reynolds number is under 2000. Accordingly, the maximal establishment length (for $Re = 2000$) is 3.8 cm, a value smaller than the distance to the first pressure outlet, 20 cm.

3.5.4.2 Velocity profile and pressure losses inside the calibration channel

For a streamline flow, the velocity field inside a rectangular duct of thickness $2B = 1\text{mm}$ and height $2A = 21\text{mm}$ can be presented as [135]:

$$u(y, z) = -\frac{1}{2\mu_L} \frac{dP}{dx} \left[b^2 - y^2 + \frac{4}{b} \sum_{i=0}^{\infty} (-1)^{i+1} \frac{\cos(N_i y) \cdot \cosh(N_i z)}{N_i^3 \cosh(N_i a)} \right] \quad (2.40)$$

Where $N_i = \frac{(2i+1)\pi}{2b}$

The dimensionless theoretical velocity profile inside the calibration channel is represented in Figure 2.21.

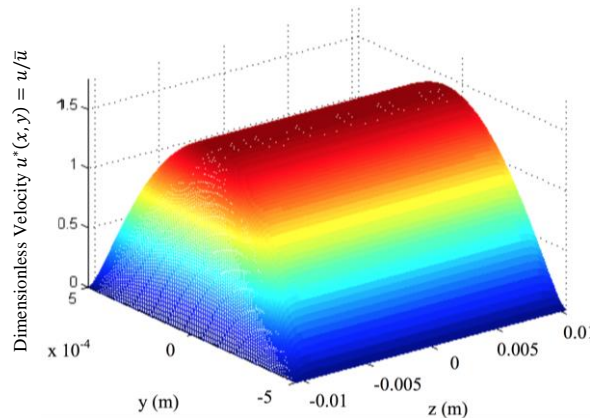


Figure 2.21 Theoretical dimensionless velocity profile inside the calibration channel

The Darcy-Weisbach equation relates the pressure losses, ΔP , inside a channel due to friction along a given length, L , and the average velocity of the fluid flow, \bar{u} [136]. It includes a dimensionless factor, $f_d = \lambda$, which depends on the characteristics of the pipe. For laminar flows, and accordance with the Poiseuille's law [137], the friction factor or flow coefficient becomes $\lambda = 64/Re$, where Re is the Reynolds number. The Darcy-Weisbach equation can be then stated as:

$$\Delta P = \frac{64 L \rho \bar{u}^2}{Re d_h 2g} \quad (2.41)$$

where, Re is the Reynolds number, L is the length of interest (in our case between the two pressure outlets), d_h is the hydraulic diameter, \bar{u} is the average velocity of the fluid flow, and g is the local acceleration due to gravity.

A comparison between the experimental pressure losses and the theoretical ones validated the use of the auxiliary duct to calibrate the electrochemical probes (Figure 2.22).

The curves fit, with a small deviation of 5% as we move closer to the laminar-turbulent transition; this is to be expected due to the assumption of laminar flow in the Darcy-Weisbach equation. Some of the deviations may be actual errors through the experimental measurement techniques.

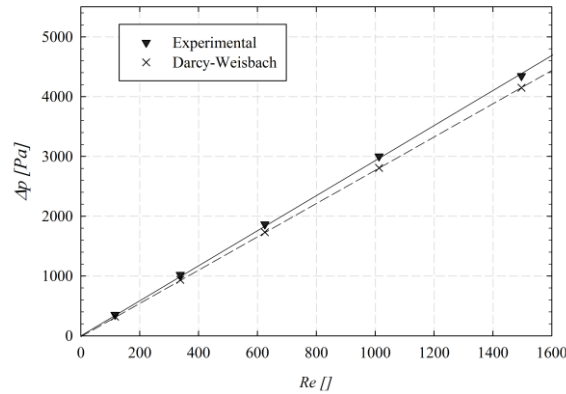


Figure 2.22 Experimental pressure losses vs. Darcy-Weisbach equation along the calibration duct

3.5.4.3 Probes active surface calculation

The calibration principle relies on the comparison of the current received by a probe in contact with a mono-phasic flow (liquid), and the velocity gradient acquired with the pressure difference between the two pressure outlets. Inside the calibration duct, the liquid flow is laminar. The pressure losses, Δp , and the diffusion limiting current, I , are measured; therefore the velocity gradient can be obtained from both techniques.

By keeping the polarization voltage constant, the diffusion limiting current response of the probes can be tracked against the variation of the liquid flow, while the velocity gradient can be deduced from the pressure losses:

$$S_0 = \frac{\tau_{loc}}{\mu_L} \quad (2.42)$$

Through the calculation of the friction factor:

$$CF = \frac{\Delta P}{2 \rho \bar{u}^2} \frac{d_h}{L} \quad (2.43)$$

The friction velocity:

$$u_\tau = \bar{u} \sqrt{\frac{CF}{2}} \quad (2.44)$$

and the local wall shear stress:

$$\tau_{loc} = u_\tau^2 \rho \quad (2.45)$$

where, ρ is the liquid's density, and μ_L is the liquid's dynamic viscosity.

Finally to calculate the active diameter of the probes, the theoretical relationship of the mean diffusional limiting current is used, $I = 0.807 z_e F c_\infty A_s \left(\frac{D^2 S_0}{d_s}\right)^{1/3}$. It can be written as a function of the probes diameter:

$$I = 0.633 z_e F c_\infty (D^2 S_0)^{1/3} d_s^{5/3} \quad (2.46)$$

The calibration of the electrochemical probes is carried out prior to each test. Table 2.3 shows the diameters of the probes in the exchangeable blocks.

The probes diameters values are close one to the other and they are also close to the size of the platinum wire used (0.25 mm). There are many aspects that could have altered the surface of the probes, like their polishing, the techniques used to install them and even previous experiments, these differences have been observed in other studies [138,139,140,51].

	Bottom Block	Lateral Block	Top Block
Probe 1	0.23	0.26	0.25
Probe 2	0.32	0.27	0.29
Probe 3	0.35	0.29	0.28
Probe 4	0.39	0.28	0.28
Probe 5	0.35	0.37	0.31
Probe 6	0.37	0.28	0.29
Probe 7	0.32	0.28	0.28
Probe 8	0.34	0.28	0.28
Probe 9	0.34	0.32	0.28
Probe 10	0.26	0.31	0.28
Probe 11	0.30	0.26	0.33

Table 2.3 Active probes diameters [mm]

3.6 Conductimetry method

To accurately measure different liquid thicknesses, two measurement blocks were set; each with a different probe size. The small one was used for the wall-slip layer at the top and lateral sides of the duct, and the large one for the thickest liquid film at the bottom.

The electrodes are powered in each block with an alternative tension of sinusoidal form (± 15 V). The frequency is high enough to neglect the polarization phenomena (between 50 and 100 KHz). Therefore, quantifying the micrometric liquid film can be considered. A simplified diagram of the conductimetric system is explained in Figure 2.23.

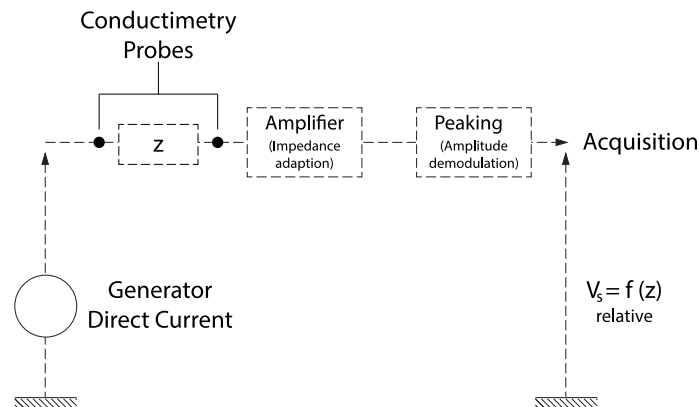


Figure 2.23 Simplified diagram of the conductimetry system

The two blocks used to measure the wall liquid thickness include the following elements:

- The first one (block A, the larger one) measures the thickness of the bottom liquid film. It is equipped with two electrodes. Each one has a 40 mm^2 surface, and they are 6 mm away from each other. They are made out of platinum.
- The second one (block B) is used to measure the smaller layers, at sides and top of the channel. It also carries two probes. Their diameter is 0.25 mm and they are spaced out 40 μm . They are made of platinum, and they were placed in a way that allows obtaining the thickness profile along the whole wall length. To achieve it, the block is graduated from 0 to 180° (Figure 2.24) and can turn around its center. The value $\alpha = 0^\circ$ corresponds to the highest position, 19.5 mm from the bottom of the channel, and $\alpha = 180^\circ$ is the lowest position, 1.5 mm from the bottom.

In both blocks, the probes were gently polished, so their surfaces won't disturb the flow and alter the measurements.

3.6.1 Calibration procedure

The conductimetry blocks are removable, allowing their placement in the test section or the auxiliary circuit. The calibrating unit is made of Plexiglas and is represented in Figure 2.25.

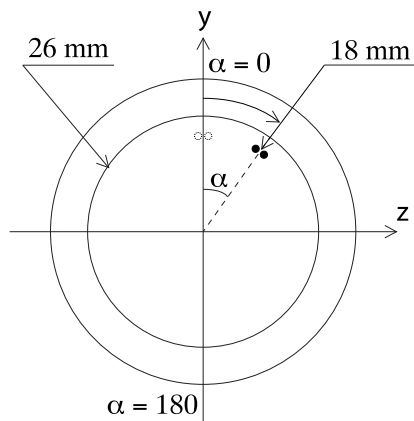


Figure 2.24 Positioning of the conductimetry probes over the exchangeable blocks

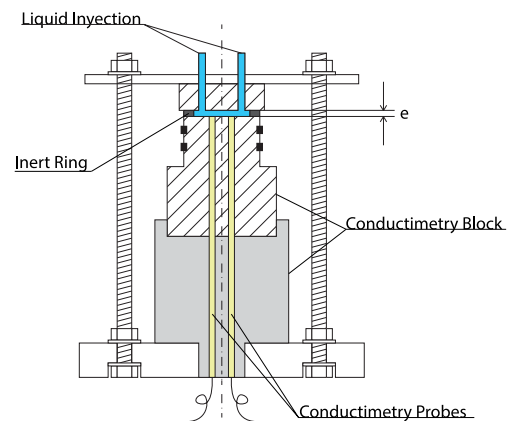


Figure 2.25 Calibration arrangement for the conductimetry blocks

Non-conductive stacking plastic sheets can control the thickness, h , between the conductimetry block and the injection holes. Once the liquid fills the empty space, the experimental relationship between the measured current and the thickness is obtained for each pair of probes.

Figure 2.26 shows the calibration curves for both blocks. Due to a limitation of the data acquisition system, the intensity maximum value was fixed to 10 V. At the block A, there is a significant deviation of the curve for small thickness ($<1,2 \text{ mm}$) tending to a plateau close to the limit intensity value, this block conceived for measuring the thicker underlying liquid film has a measurement precision of 0.1 mm. At the B one, used at the lateral and top walls, the response is similar, being more linear towards the smaller values. However, it allows measuring thickness 20 times smaller with a higher measurement precision of 2 micrometers.

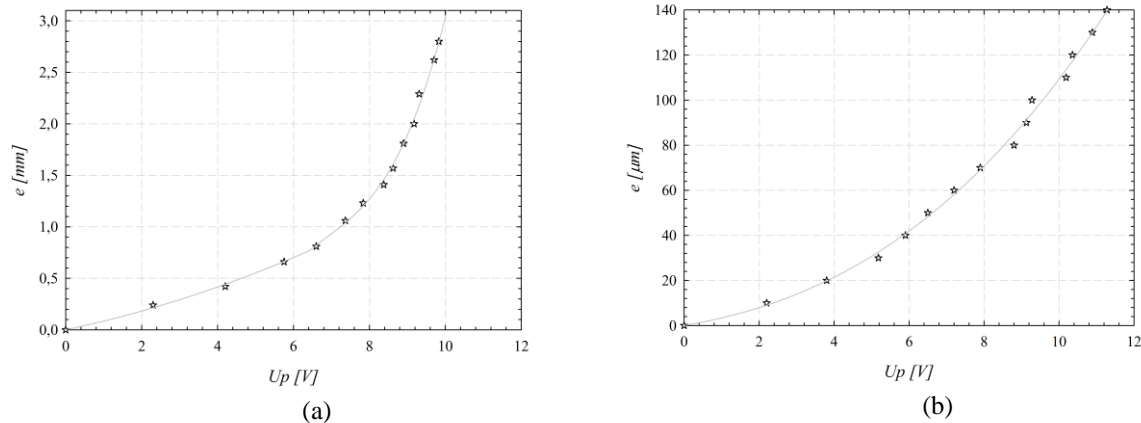


Figure 2.26 Calibration curves for the two conductimetry blocks (a) and (b).

3.7 Analog data acquisition system

The analog data acquisition system, used for the polarography and conductimetry method, comprehends a Keithley Das 1800 acquisition card. This component allows obtaining 16 different signals with a known sampling frequency, F_s , and total time, t_t . The measured analogic signal (bits) is converted into a digital one (at 12 bits) with the “TestPoint” software, which controls the card. The maximal acquisition frequency is 33 kHz. The resolution intensity is ± 2.5 mV over a range of -10 V / $+10$ V. It presents 4 different gains: ± 10 V, ± 5 V, ± 2.5 and ± 1.25 V. To cover values surpassing this threshold a tension divisor was implemented. The conductimetry data was obtained over 20000 sample points and a measurement time of 10 s.

4. Conclusions

In this chapter, we discussed characteristics of the experimental device, the measurement techniques and the settings arrangements. The device holds both a closed liquid circuit -and an open gas one- allowing the creation of an homogeneous foam, which will flow through a straight channel with three possible disruption devices: half sudden-expansion, fence, and circle. The results validated the choice of products, techniques, materials and probes, and why they are the best measurement arrangements alternatives. A non-ionic surfactant was selected, which stabilizes the foam and does not influence the electro-chemical acquisition. The three generators, made the same homogeneous foam structure. The conductimetry and polarographic probes were calibrated, so they provide reliable results in the most delicate tests (wall velocity gradient and liquid film thickness).

Altogether, the experimental arrangements proved to match our objectives in foam flow rheology studies. It may be noted that these experiments complement the ones by Blondin, Tisné and Madani [3,51,113] that covered single foam characteristic or aspects. In this work, seven void fractions were considered, in addition to three foam velocities and flow disruption devices. This experimental database could be a reliable support in future foam flow numerical studies simulations.

CHAPTER 3

EXPERIMENTAL AND CFD RESULTS AND DISCUSSIONS

This chapter presents the experimental results for the pressure losses, PIV measurements, conductimetry and polarographic method, next to their respective discussion. To have a control over the experimental measurements and properties of the foam, we separated the study in three parts. Firstly a study with no disruption devices was made to accurately measure the wall-shear stress and liquid film thicknesses over a horizontal square channel. Then, the FDD geometries were swapped to obtain the restructuration of foam flow when faced against a pattern change. Finally, numerical CFD simulations were done trying to represent the foam flow behavior around the three different disruption devices.

1. Foam flow along a straight channel with no FDD

As cited in previous studies, foam flowing inside ducts creates high wall shear stress, due to its particular properties (rheology, velocity fields, osmotic pressure, disjoining pressure, etc.). To better understand this phenomenon, the flow of foam through a straight channel with no devices (obstacles) was studied. This way the number of variables in the study (bubbles diameter, void fraction and foam velocity) were limited and controlled. The presence of FDD alters the foam's structure, generates bubbles reorganization and creates a forced drainage, difficult to measure. These parameters evidently complicate acquisition of accurate data by the polarographic and conductimetry methods.

1.1 Pressure losses and gradient

The pressure distribution generated by foam flowing along a horizontal channel is one of the most interesting characteristics of this complex fluid. The static pressure losses ($P - P_0$) inside the channel are presented in Figure 3.1. In all the cases, the static pressure varies linearly all through the channel. Regardless of the change in the foam quality, the deviation from one static pressure to the other is relatively small.

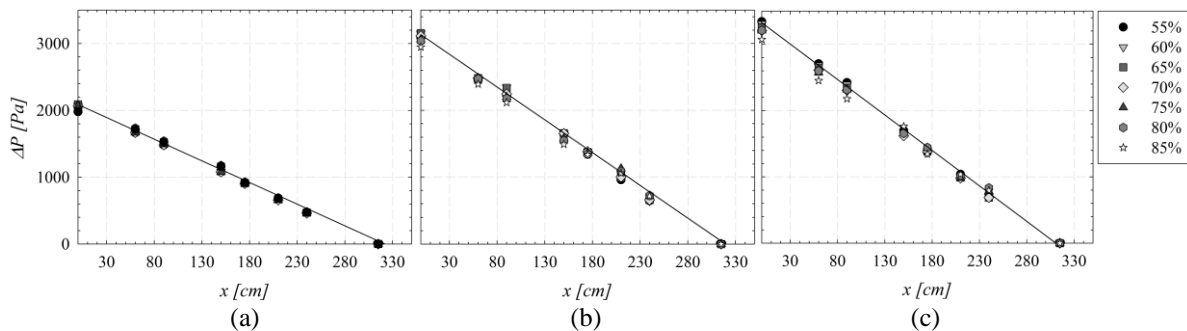


Figure 3.1 Static pressure losses along the square channel without flow restrictions: (a) case I; (b) case II and (c) case III.

The longitudinal pressure gradient was obtained from the static measurements for all foam cases and qualities. They are shown in Figure 3.2 as a function of the foam quality. Case III presents a linear pressure gradient. However, for cases II and III there is an influence of the foam quality over the value of the pressure gradients. They show that wetter foams generate higher pressure losses and that this change, in the linearity of the pressure gradients, can be a result of the change in the foam velocity profiles and the film liquid thickness at the walls. Therefore, a deeper study was carried to understand the real causes of this behavior, especially focused on the wall shear stress.

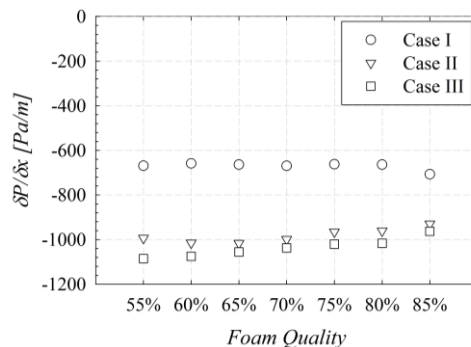


Figure 3.2 Pressure gradient for a foam flow inside a straight channel with no FDD for different foam qualities and velocities.

1.2 Velocity profiles

Indicated in previous works [3,51], the foam flowing through channels may be studied under three different regimes, as a function of axial velocity. This property may be measured by the PIV method (Particle Image Velocimetry). The experiments were carried over the foam flow close to the lateral wall, due to the opacity of the foam. The axial velocity profiles, for all cases and qualities, are presented as temporal average velocity values, taken over 500 images (Figure 3.3), the timesteps are showed in Table 2.2.

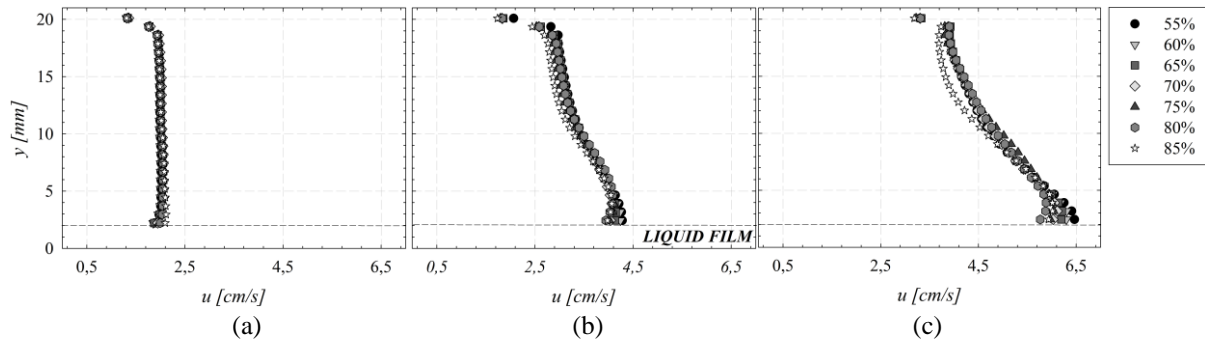


Figure 3.3 Averaged axial velocity profiles at the lateral wall of the foam flowing through a straight channel with different qualities for: case I (a), case II (b) and case III (c).

For the case I, where the foam flow behaves as a block (or piston), there is small influence of the void fraction, in comparison with the other cases. Due to thinner plateau borders, and weaker internal forces, dryer foams tend to shear easier than wet ones. However, as the liquid flow increases so do the thickness and velocity of the layer at the bottom of the channel. Therefore, for cases II and III, wetter foams have a higher velocity at the bottom of the duct. As the gas fraction increases, the liquid slip layer velocity decreases, arriving to a driest point ($\beta = 85\%$), where shear occurs and the foam at the bottom deforms easier. The higher the mean velocity is, the higher the influence of the liquid film.

Previous works [3,51] showed that for these velocity profiles, each case corresponds to a flow regime. Case I has a uniform axial velocity along the whole section (one-dimensional regime). The foam flow, for case II, is partially sheared at the bottom of the channel. Therefore, the axial velocity is not uniform and the flow becomes a two-dimensional regime. Finally, for the last case (III), the foam flow will be completely sheared and its axial velocity also is displaced on the z -coordinate. It can be called three-dimensional regime. The velocity profiles over the top of the channel are shown in Figure 3.4 below.

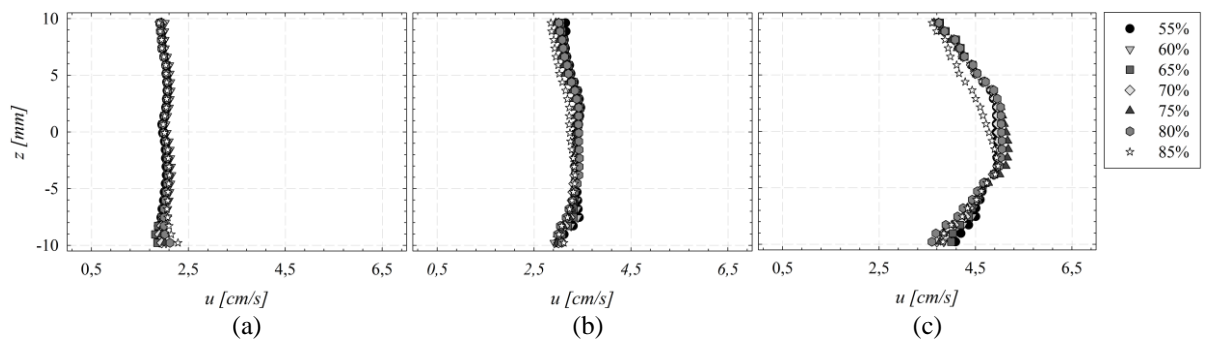


Figure 3.4 Axial velocity profiles at the top wall of the foam flowing through a straight channel with different qualities for: case I (a), case II (b) and case III (c).

They confirm the presence of three different foam flow regimes. The first two velocity profiles at the top of the channel behave as a piston. In the third case, the velocity profile is a function of the z -coordinate, presenting the three dimensional behavior. Finally, we present the evolution of the velocity profile of the bubbles flowing over the liquid/foam interface in Figure 3.5.

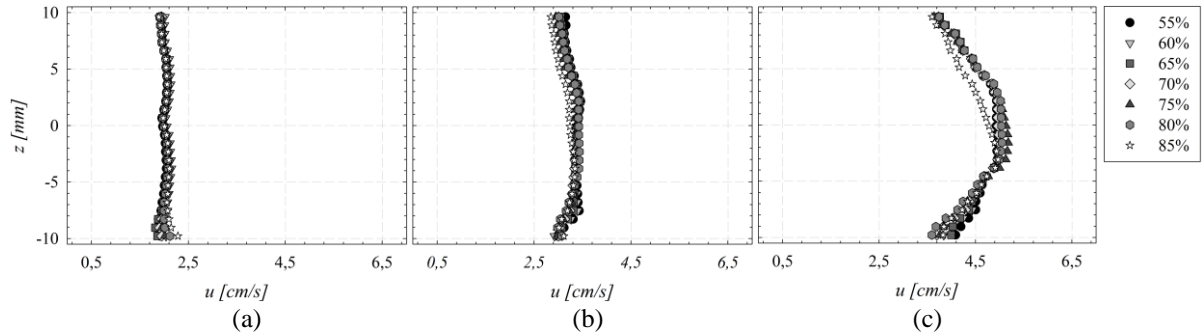


Figure 3.5 Axial velocity profiles at the liquid/foam interphase of the foam flowing through a straight channel with different qualities for: case I (a), case II (b) and case III (c).

1.3 Liquid film thickness

Aqueous foam flow consists of a mixture of water and air. Therefore, the gravitational force plays a major impact over its behavior, and more specifically its drainage. Drainage is the passage of liquid through foam, under the effects of gravity, the liquid inside the foam flows downward, and the gas bubbles are displaced upwards in the channel section. The conductimetry method allowed defining the liquid slip layer experimental thickness values over three of the four walls of the duct: bottom, lateral walls and top.

Because of the same evolution along the lateral walls, we decided to measure this liquid film only on one lateral wall. We will consider that the evolution on the other side will be the same.

1.3.1 Bottom wall

Figure 3.6 represents the thickness instantaneous evolution of the underlying liquid, over one second, for all three cases and foam qualities. They were obtained with the use of the conductimetry block A, located at the middle of the test section.

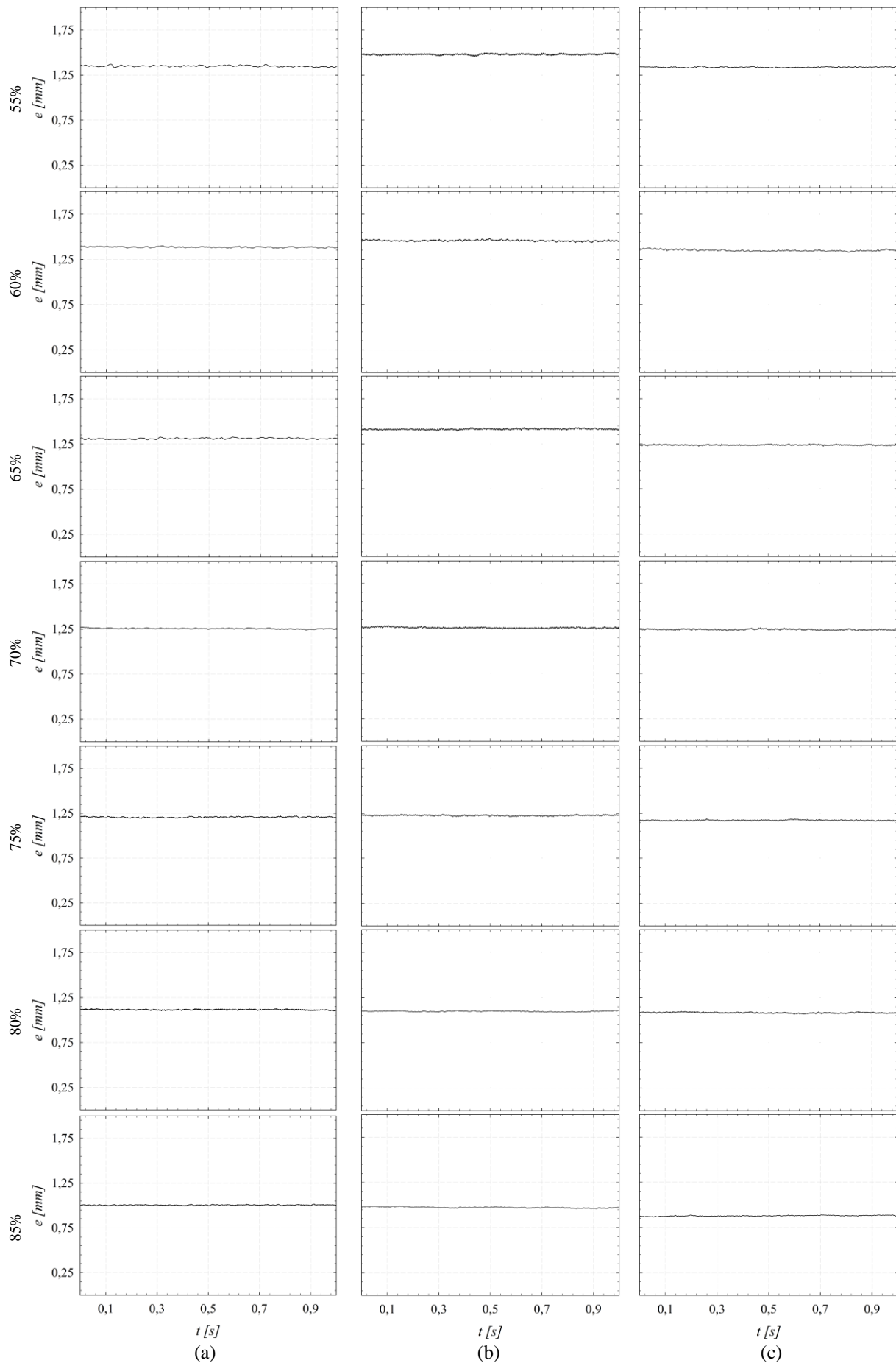


Figure 3.6 Conductimetry signal of the liquid film thickness over the bottom wall for all foam qualities (β) and cases: Case I; (b) Case II and (c) Case III.

These results show that the signal remains constant and has almost no fluctuations. The values of the liquid film thickness go from 1.5 to 0.9 millimeters and they are proportional to its void fraction. To better understand the differences and deviations, Figure 3.7 shows the mean values of the underlying liquid layer at the middle channel for the all cases and foam qualities.

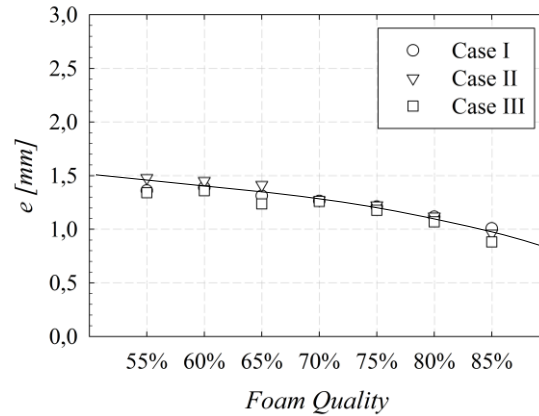


Figure 3.7 Mean liquid film thickness at the bottom of the channel for all cases studied and qualities.

It can be noted that the change of the foam velocity does not make an impact over the mean value of the liquid slip layer; there are no major deviations between the thicknesses of the three cases. However, as we alter the foam quality the value of liquid film changes importantly. Therefore, for wetter foams, the underlying slip layer is thicker than for dryer ones. Previous works also have shown that there is no major thickness evolution along the channel's length, meaning that the liquid quantity lost, due to the gravitational drainage over horizontal flowing foam inside a square channel, is small [51].

1.3.2 Lateral wall

The lateral wall measurements were made with the conductimetry block B. By turning it around its center, it allows the data acquisition of the liquid film thickness over the lateral wall (from $y=1.5$ mm to 19.5 mm), remembering that the square duct cross-section is 21×21 mm². Figures 3.8 to 3.10 represent the instantaneous conductimetry signals evolution over one of the two lateral walls, for all cases and qualities. For each condition, we represent four of the thirteen instantaneous signals available. The rest of them were used to obtain the mean value evolution. Over the lateral wall, the conductimetric probe was located near the top ($y = 19.5$ mm), the middle ($y = 16.9$ mm and 4.1 mm) and the bottom ($y=1.5$ mm) of the channel. These four ones, allow to visualize partially the fluctuating evolution over the lateral wall.

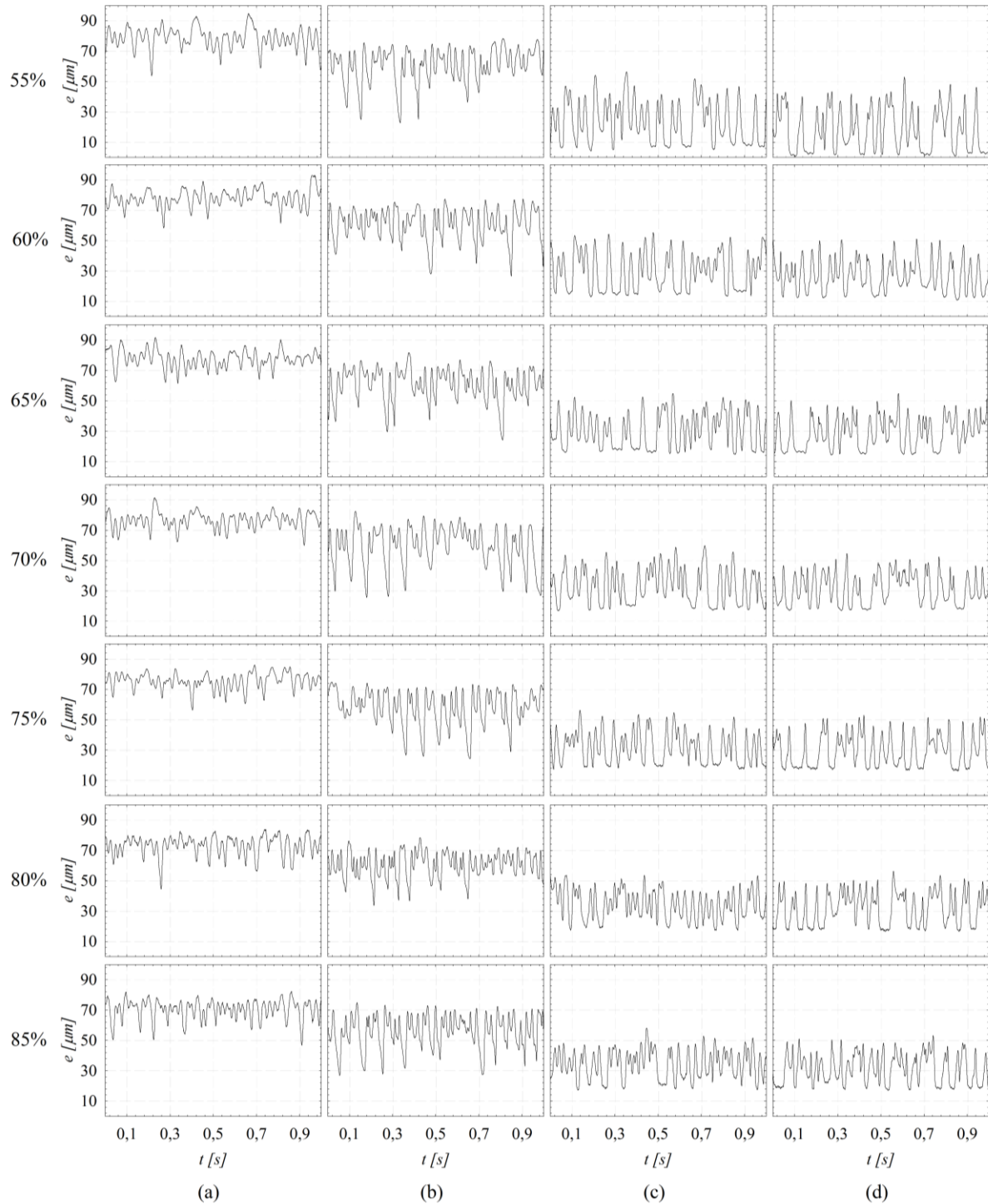


Figure 3.8 Conductimetry signal over the lateral wall for a foam velocity of 2 cm/s at:
 (a) $y = 1.5$ mm; (b) $y = 4.1$ mm; (c) $y = 16.9$ mm and (d) $y = 19.5$ mm for all foam qualities (β).

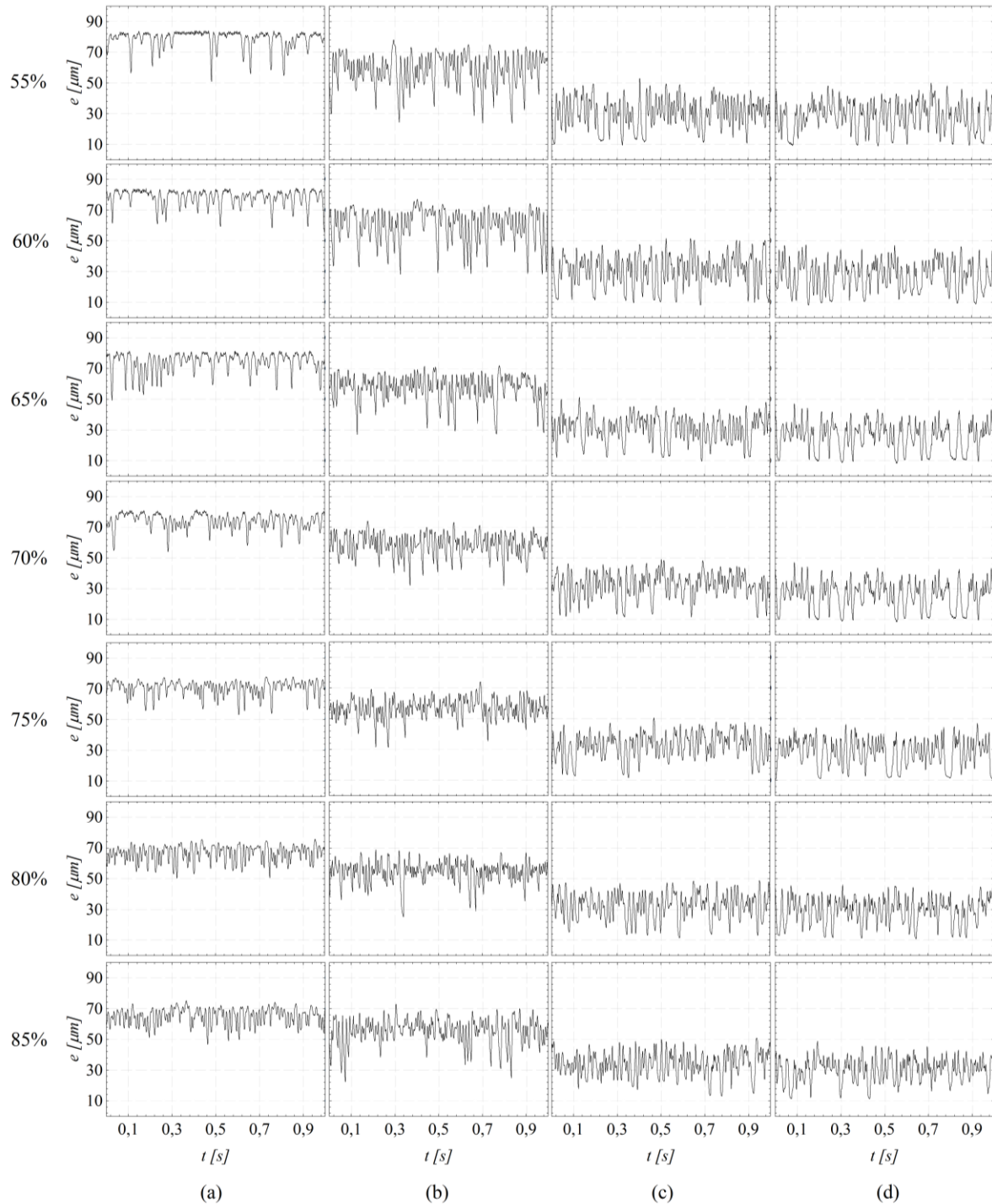


Figure 3.9 Conductimetry signal over the lateral wall for a foam velocity of 4 cm/s at: (a) $y = 1.5$ mm; (b) $y = 4.1$ mm; (c) $y = 16.9$ mm and (d) $y = 19.5$ mm for all foam qualities (β).

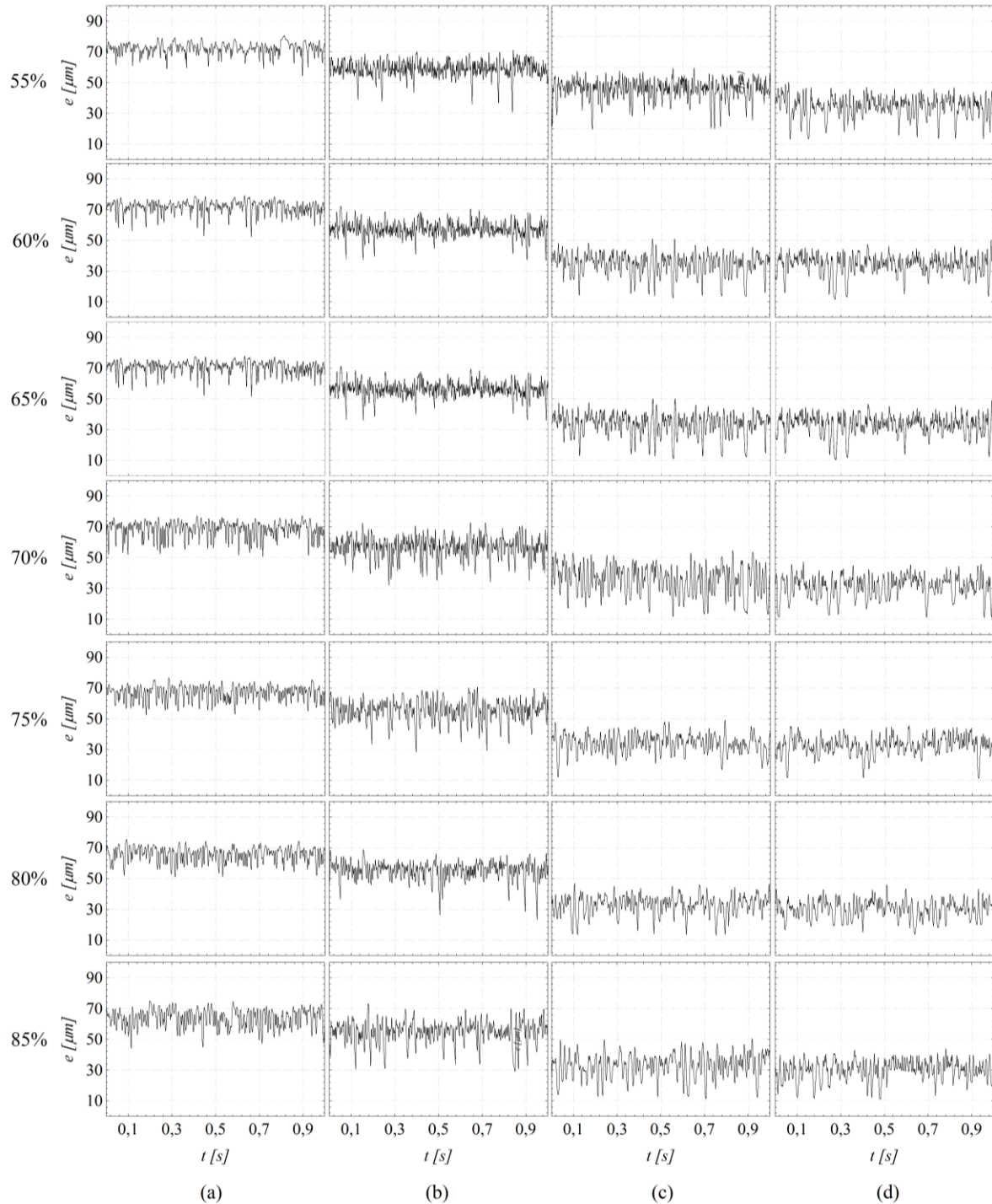


Figure 3.10 Conductimetry signal over the lateral wall for a foam velocity of 6 cm/s at: (a) $y = 1.5$ mm; (b) $y = 4.1$ mm; (c) $y = 16.9$ mm and (d) $y = 19.5$ mm for all foam qualities (β).

For all conditions, the instantaneous signal obtained at the conductivity probe shows important fluctuations all over the lateral wall. Previous works have made an emphasis over this phenomenon and its causes [51,32]. Figure 3.11 shows a schematic representation of their conclusions. They synchronized the bubbles passage over the conductivity probe. They verified, in effect, that the fluctuations are due to the bubbles passage as they make vary the thickness of the film. When the bubble A passes through the probe, it generates a signal A' that is smaller than the mean value. The liquid film decreases as the bubble flows over the wall. This remark can be extrapolated to our case and measurements.

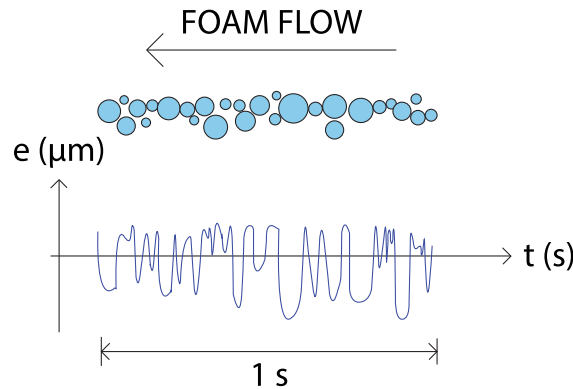


Figure 3.11 Schematic representation of the fluctuations of the conductivity signal [51].

An increase in the number of fluctuations per second can be noted as the foam velocity increases. Therefore, for the case I, the slowest foam, we see lesser fluctuations than for the case II; and so the case III, with a foam velocity of 6 cm/s, presents the highest number of fluctuations. Also, as the probe moves closer to the interphase liquid/foam, the amplitude of the fluctuations diminishes; tending to a constant value as observed over the bottom of the channel. This means that the thicker the underlying slip layer, the smaller the amplitude fluctuations. All of these phenomena will be analyze, thoroughly, further ahead when we compare the standard deviation, the skewness and the flatness factors for all the conditions.

The mean values, of the conductivity signal over the lateral wall, are represented in Figure 3.12 for all cases and qualities (β). They allow seeing the evolution of the thickness and the influence of the drainage over this one. The liquid inside the foam, due to the gravity force, tends to the bottom of the channel. Therefore, at this region the film is thicker.

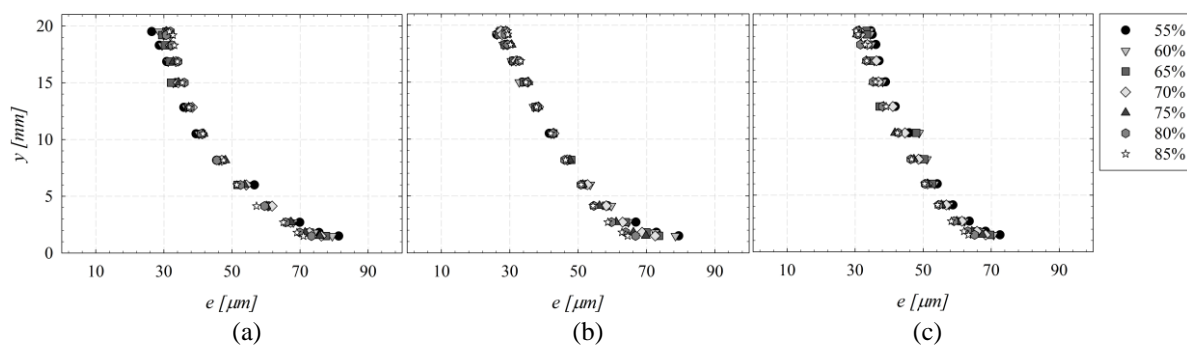


Figure 3.12 Evolution of the mean liquid film thickness value over the lateral wall for all foam qualities and the three cases: (a) Case I; (b) Case II and (c) Case III.

Over the lateral wall, for all our cases and qualities, we see more important mean thickness value near the liquid/foam interphase than at the top of the channel. This thickness difference over the

lateral wall is a cause of the gravitational drainage, which can be put into evidence. The slip-layer thickness diminishes almost 40 μm along the whole wall. For all three cases, the minimum value is of 30 μm at the top of the duct and 70 μm near the bottom. There is no big differences between foam velocities or qualities. They stay constant one another. This shows the equal distribution of the dispersed bubbles inside the liquid and the good performance of the foam generators.

1.3.3 Top wall

Finally, Figures 3.14 to 3.16 present the instantaneous evolution of the slip layer thickness over the top wall for all foam qualities and velocities. These values were also obtained with the conductivity block B, which has smaller probes and precision. It was turned around its center and allowed the measure over the whole wall. We present three instantaneous signals near the lateral walls ($z = -9$ mm and 9 mm) and at the center of the channel ($z = 0$ mm). These ones are more than enough to obtain a partial view of the evolution along the wall.

They show that regardless the velocity, the quality and the position of the probes the amplitude of the signals remains the same. The slip layer thickness goes from 2 μm to 40 μm . The smallest values, as showed for the lateral results, correspond to the lower part of a bubble as it passes through the probes. As for the number of fluctuations per second, it can be seen an increase in its number as the foam moves faster. Some statistical values can be and will be obtained from these phenomena. There are no differences as the foam quality is changed.

The mean liquid film thicknesses may be obtained from the instantaneous values of the conductivity signal over the top wall. These ones are shown in Figure 3.13 for all foam qualities and the three cases.

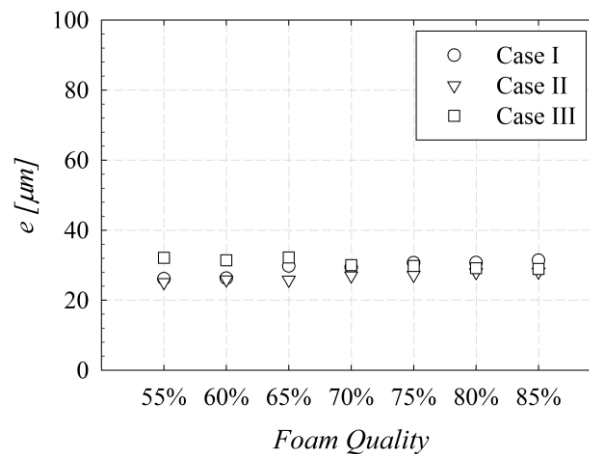


Figure 3.13 Mean liquid film thickness at the bottom of the channel for all cases and qualities.

As expected from the instantaneous fluctuations, on the three cases, the mean liquid film thickness over the top wall presents similar values for all qualities and velocities. They tend to 30 μm .

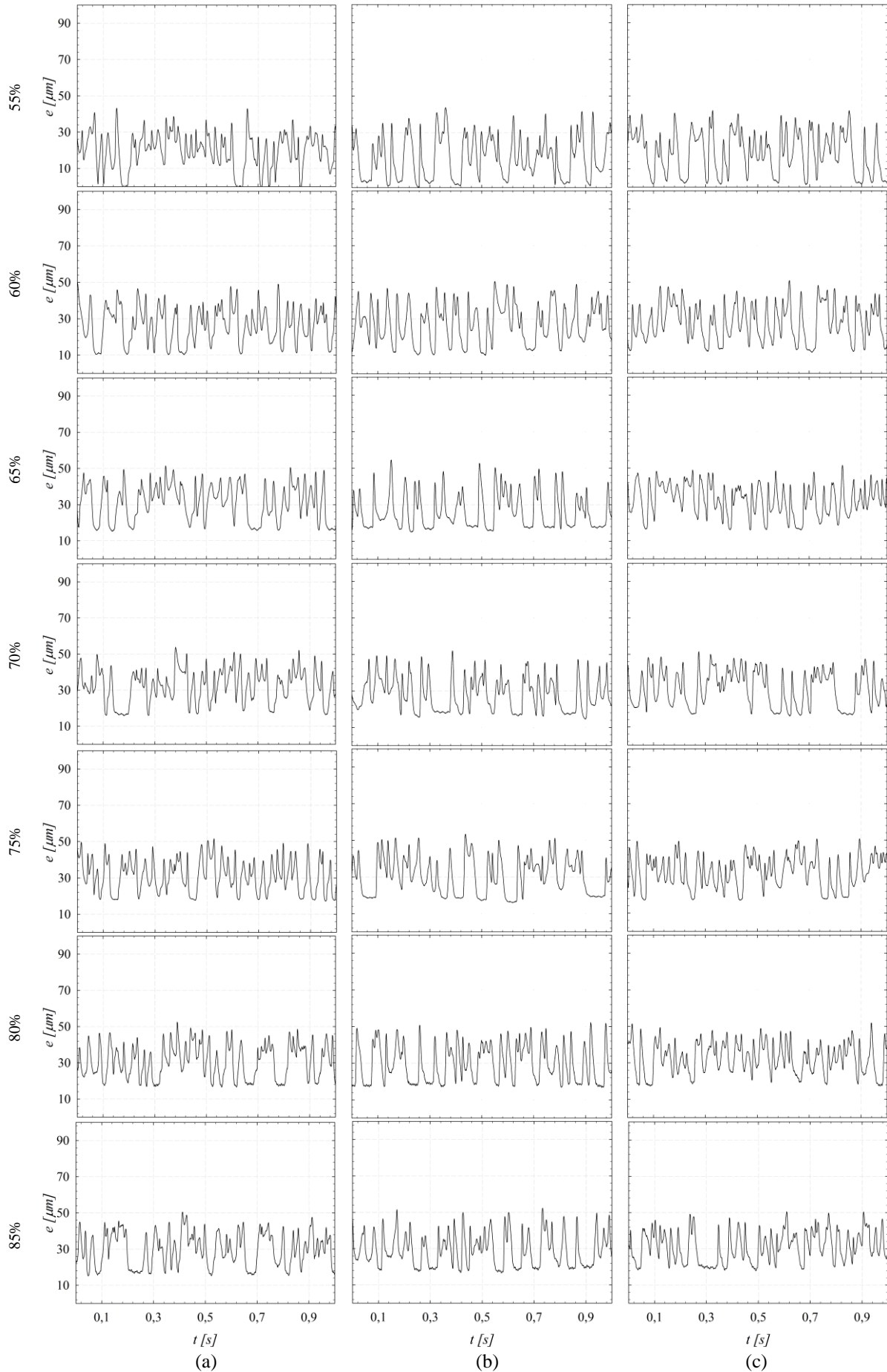


Figure 3.14 Conductimetry signal over the top wall for the Case I at: (a) $z = -9$ mm; (b) $z = 0$ mm and $z = 9$ mm for all foam qualities (β).

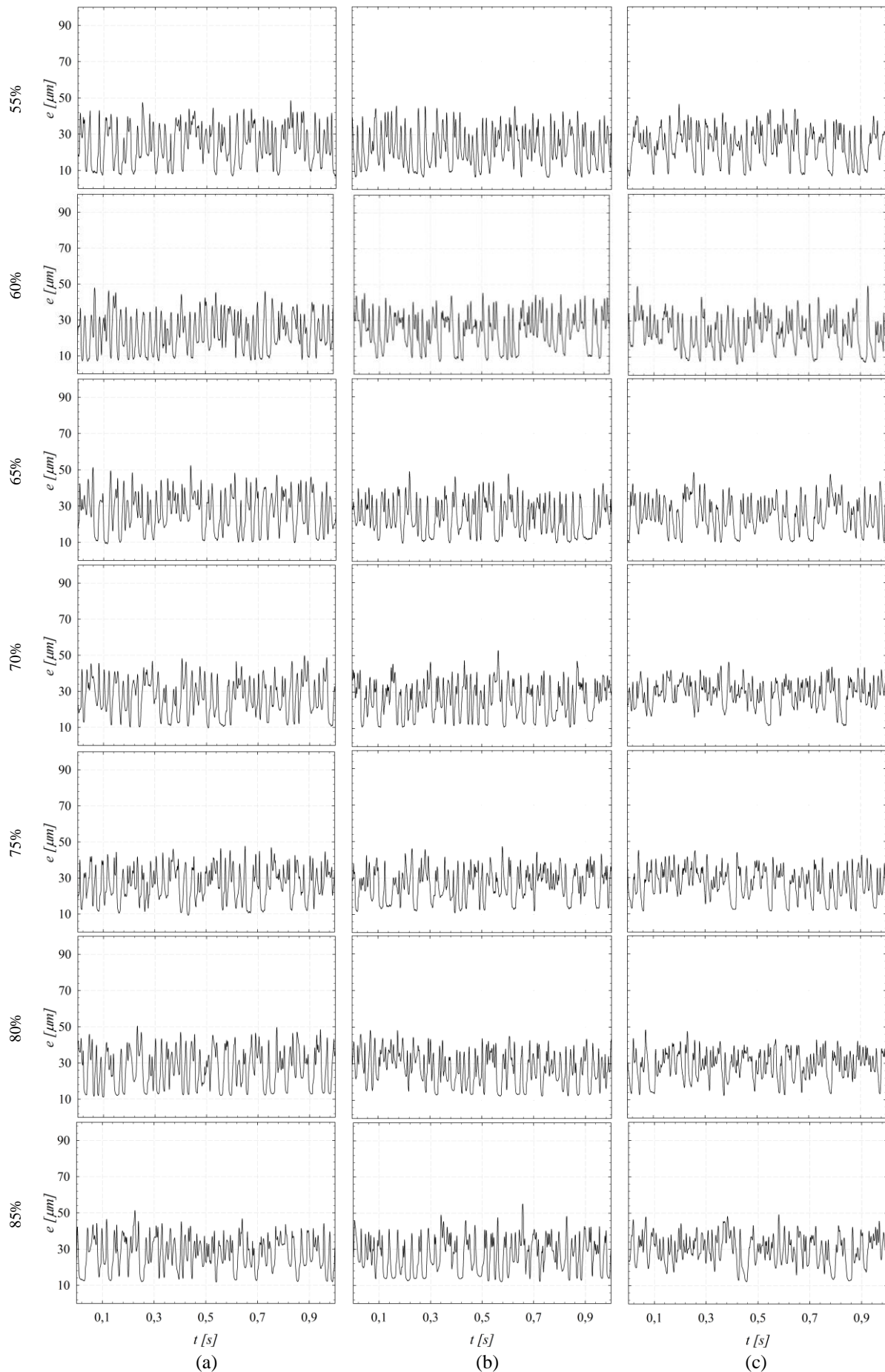


Figure 3.15 Conductimetry signal over the top wall for the Case II at: (a) $z = -9$ mm; (b) $z = 0$ mm and $z = 9$ mm for all foam qualities (β).

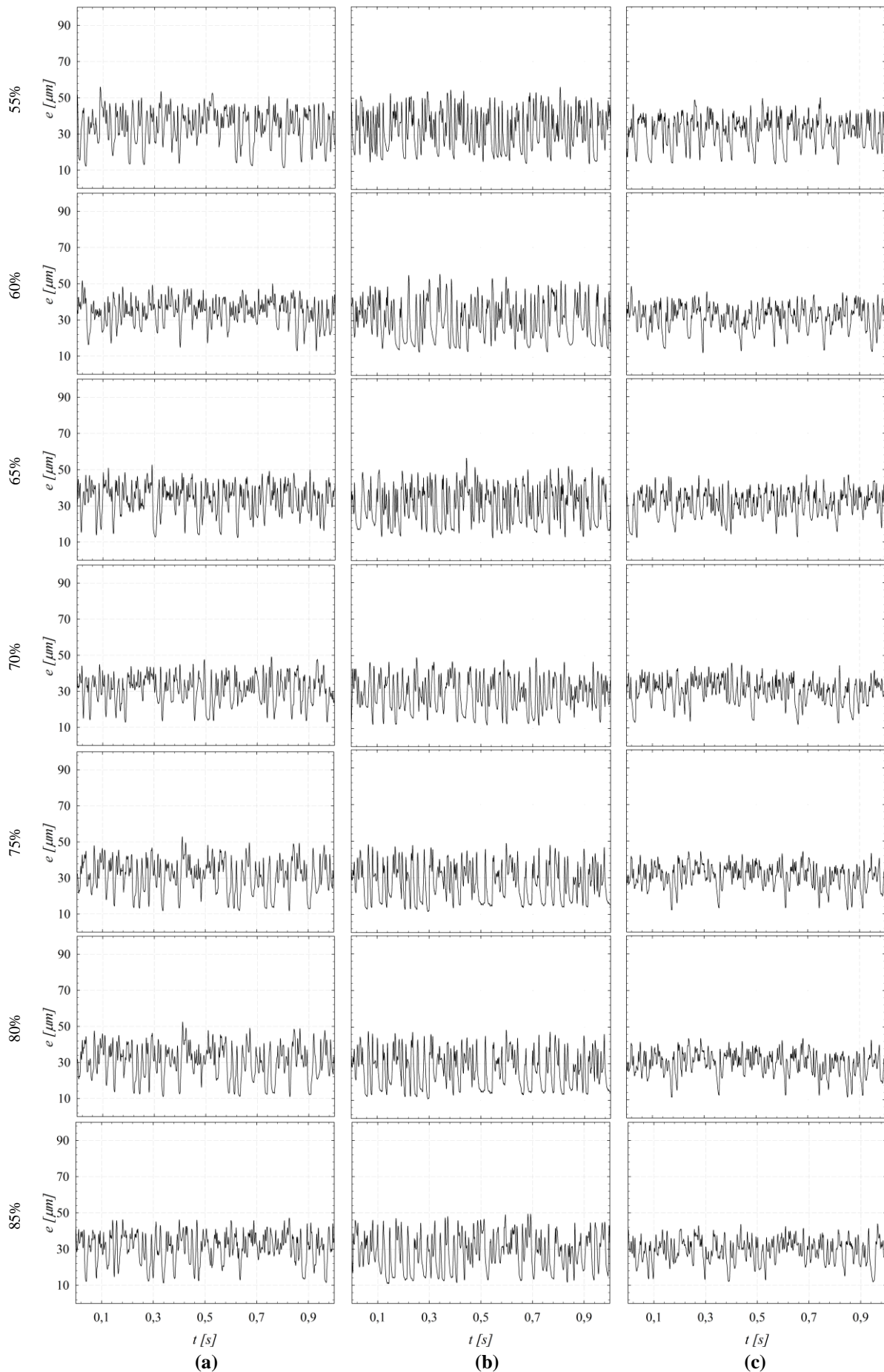


Figure 3.16 Conductimetry signal over the top wall for the Case III at: (a) $z = -9$ mm; (b) $z = 0$ mm and $z = 9$ mm for all foam qualities (β).

1.3.4 Statistical description of the conductimetry signal

The evolution of the signals shows to be complex. It might appear highly disorganized and unpredictable in their behavior. However, some statistical properties of the flow can be interpreted. It should be useful for a better understanding of the liquid slip layer to seek a statistical description at the wall.

$$\int_{-\infty}^{+\infty} P(v)dv \quad (3.1)$$

The PDF can be estimated by constructing a histogram of an ensemble of measurements of v at the specific location. The larger the ensemble, the more closely the histogram will approximate the PDF. The *moments* of the variable v are derived from the PDF. The n^{th} moment $\langle v^n \rangle$ is defined as:

$$\langle v^n \rangle = \int_{-\infty}^{+\infty} v^n P(v)dv \quad (3.2)$$

The first moment $\langle v \rangle$ is the *mean*:

$$\langle v \rangle = \int_{-\infty}^{+\infty} v P(v)dv \quad (3.3)$$

The *variance* is the second moment of the perturbation quantity $v' = v - \langle v \rangle$, and describes the level of variability about this mean:

$$\langle v'^2 \rangle = \int_{-\infty}^{+\infty} (v - \langle v \rangle)^2 P(v)dv \quad (3.4)$$

The *skewness* factor is the third moment of v' , normalized by the variance:

$$\mathfrak{S} = \text{skewness} = \frac{\langle v'^3 \rangle}{\langle v'^2 \rangle^{3/2}} \quad (3.5)$$

A PDF that is symmetric about the mean $\langle v \rangle$ will have zero skewness. All higher order moments of such PDF will also be identically zero. The skewness reveals information about the asymmetry of the PDF. Positive skewness factor indicates that the PDF has a longer tail for $v - \langle v \rangle > 0$ than for $v - \langle v \rangle < 0$. Hence a positive skewness means that the variable v' is more likely to take on large positive values than large negative values. A time series with long stretches of small negative values and a few instances of large positive values, with zero time mean, has positive skewness factor (Figure 3.17).

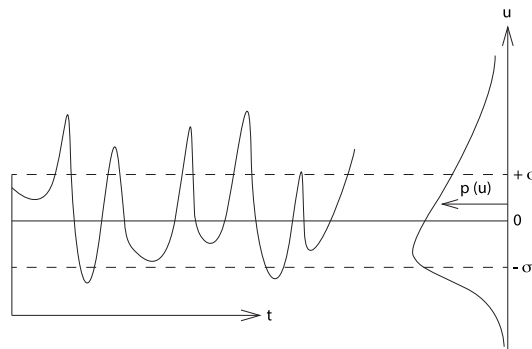


Figure 3.17 Signal with a positive Skewness factor \mathfrak{S} .

The *kurtosis* (or flatness) factor is the fourth moment of the v' , normalized by the variance.

$$\mathcal{F} = \text{kurtosis} = \frac{\langle v'^4 \rangle}{\langle v'^2 \rangle^2} \quad (3.5)$$

A PDF with longer tails have a larger kurtosis factor than a PDF with narrower tails. A time series with most measurements clustered around the mean has low kurtosis factor; a time series dominated by intermittent extreme events has high kurtosis factor (Figure 3.18).

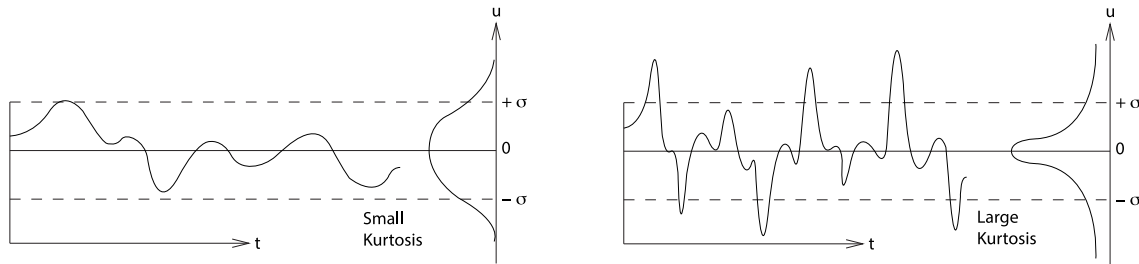


Figure 3.18 Signals with small and large Kurtosis factor (\mathcal{F})

Figures 3.19 to 3.24 show the standard deviation, the skewness and the kurtosis of the oscillatory thickness for different foam qualities and cases over the lateral and the top wall.

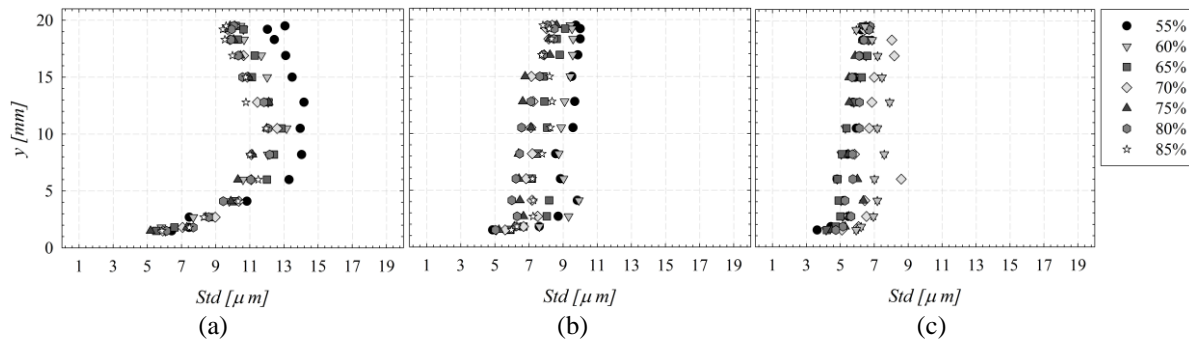


Figure 3.19 Standard deviations of the conductivity thicknesses over the lateral wall for all foam qualities and velocities: (a) Case I; (b) Case II and (c) Case III.

The standard deviation (SI) measures the amount of dispersion from the average. A low value indicates that the data points to be close to the mean; a high value indicates that the points are spread out over a large range value. The lateral wall results show that for small foam velocities, the SI is higher near the liquid/foam interphase. As the foam flow velocity increases the SI values group together and diminish along the mean thickness values. There is also a difference in the foam quality; wetter foams show higher standard deviation than the dryer ones. This agrees with the conductivity probe response, when the bubbles are close to the probe (small thicknesses), the standard deviation value increases. The bubbles movement as could be expected creates important fluctuations of the SI.

The SI values over the topside of the channel are similar one another, despite the foam velocity. The main differences occur between foam qualities, where the standard deviation value is inversely proportional to the void fraction. As seen in the lateral results, dryer foams present smaller standard deviation than wetter ones. Smaller values also occur near the lateral walls, because bigger bubbles tend to flow closer to the middle of the channel, repelling the smaller ones to the sides.

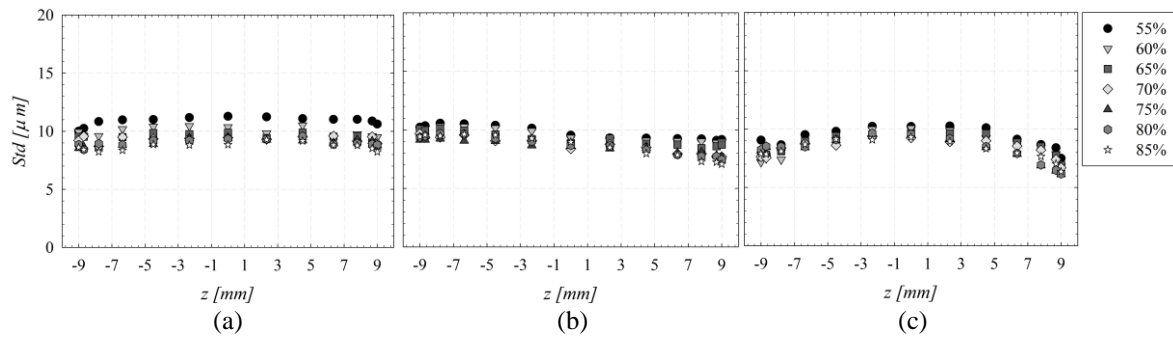


Figure 3.20 Standard deviations of the conductivity thicknesses over the top wall for all foam qualities (β) and velocities: (a) Case I; (b) Case II and (c) Case III.

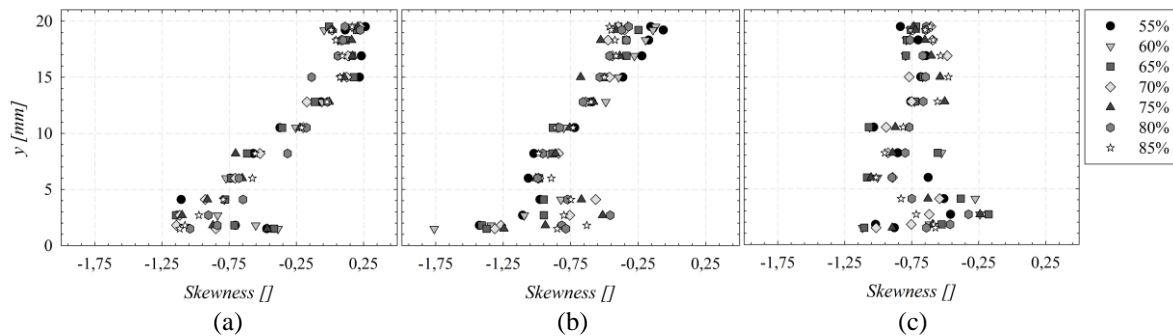


Figure 3.21 Skewness factors of the conductivity thicknesses over the top wall for all foam qualities (β) and velocities: (a) Case I; (b) Case II and (c) Case III.

Skewness factor is a measure of asymmetry; a negative Skewness describes a time series with long stretches of small positive values and few instances of large negative values, over the mean line. For the slower foam flows (Case I and Case II) a higher measure of Skewness occurs near the top of the channel where the liquid film is thinner. As the velocity increases, Skewness factor tends to a constant value near -0.75. There is no notable difference between foam qualities. As seen for the standard deviation, the fluctuations are due to the bubbles passage over the probe. Most of the values are small positive values because the mean diameter of the bubbles remains similar; there are small amounts of big bubbles, which generate the few instances of large negative Skewness.

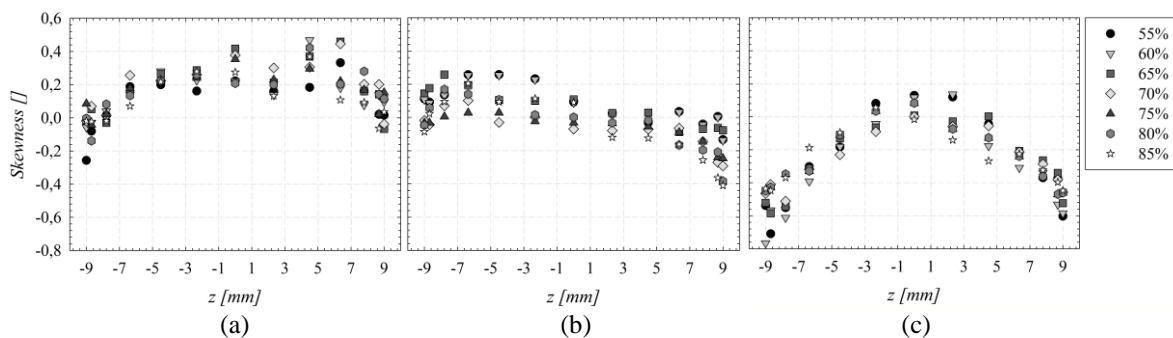


Figure 3.22 Skewness factor of the conductivity thicknesses over the top wall for all foam qualities (β) and velocities: (a) Case I; (b) Case II and (c) Case III.

At the top of the channel, an evolution of the Skewness can be observed. As the velocity of the foam increases, so does the mean thickness, and the Skewness value decreases, similar to the behavior seen over the lateral wall. Bigger bubbles concentrate at the top center of the channel, repelling the smaller ones to the sides; this increases the number of large negative perturbation values and the Skewness factor.

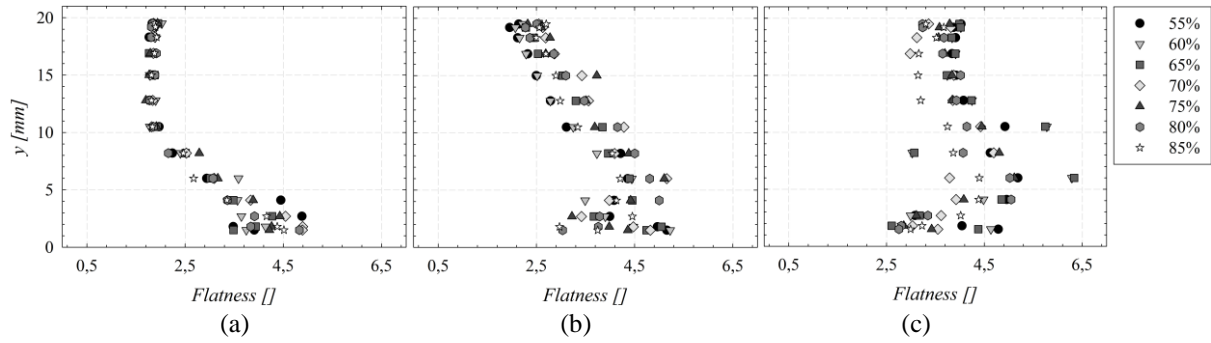


Figure 3.23 Flatness factor of the conductivity thicknesses over the lateral wall for all foam qualities (β) and velocities: (a) Case I; (b) Case II and (c) Case III.

The flatness, or kurtosis factor represents the probability to obtain values close to the mean. In the lateral measurements, the flatness behavior coincides with the mean thickness one. Thereby, for smaller slip-layer thicknesses, there are bigger fluctuations with values farther away from the mean, which distributes more equally the values along the Gaussian histogram. As the foam velocity increases, so does the thickness of the liquid film and the Flatness values. Major foam quality differences occur near the bottom of the channel and, for higher velocities. The wetter foams present higher kurtosis values than the dryer ones. This behavior is also a consequence of the liquid film thickness.

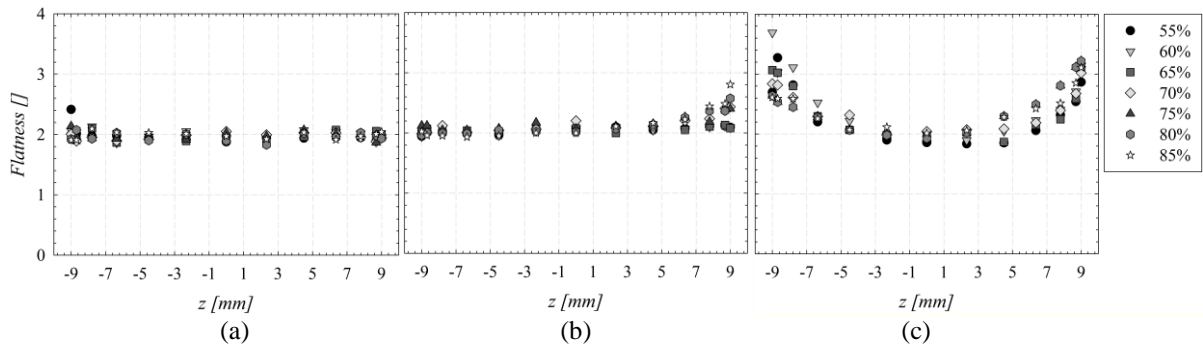


Figure 3.24 Flatness factors of the conductivity thicknesses over the lateral wall for all foam qualities (β) and velocities: (a) Case I; (b) Case II and (c) Case III.

The Kurtosis factor measurements over the top wall of the channel show similarities with the ones at slower velocities. It is constant all over the lateral wall with a small deviation near the lateral walls. The fastest velocity, case III, has different Kurtosis values along the channel length. The higher Flatness values diminish towards the center of the channel. This is related to the presence of bigger bubbles near the center of the channel, generating smaller amplitude fluctuations and thicknesses.

1.4 Polarographic signals

The instantaneous polarographic signals are shown in Figures 3.25 to 3.31. They were obtained at the middle of the test section; over three of the four walls: bottom, one lateral and top; for the case I, and all the foam qualities: 55%, 60%, 65%, 70%, 75%, 80% and 85%. These results represent the evolution of the Sherwood number “ Sh ” over one second. This dimensionless number is linked to the probes’ diameter “ d_s ” and the measured current “ I ”, through the following relationship:

$$Sh = \frac{I}{z_e F A_s c_\infty D} d_s = \frac{4}{\pi F c_\infty D d_s z_e} I \quad (3.6)$$

where z_e is the electrons number involved, F is the Faraday number, c_∞ is the concentration at the flow core, D is the diffusion coefficient and $A_s = \frac{\pi d_s^2}{4}$ is the probe’s surface.

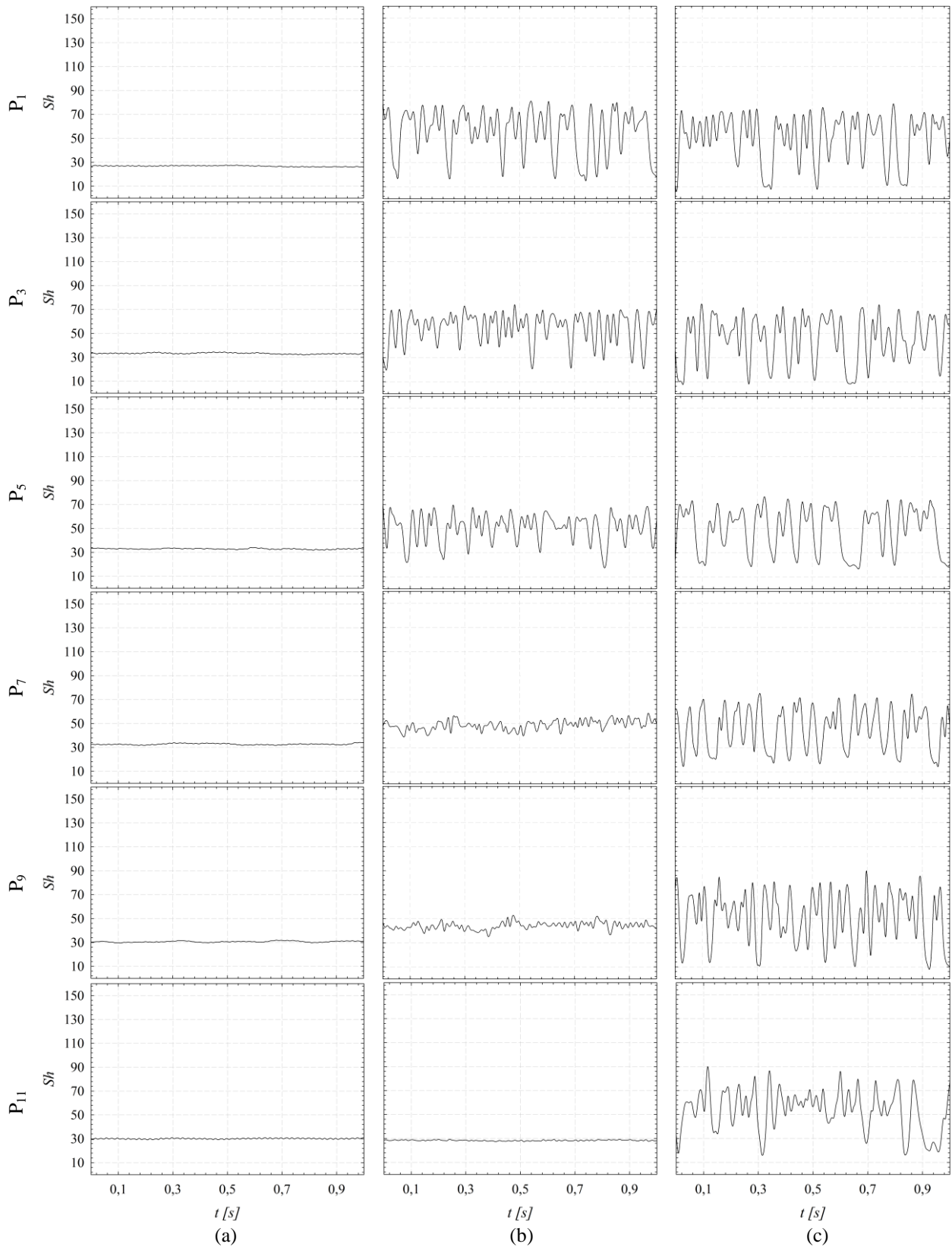


Figure 3.25 Polarographic signals over three walls: (a) bottom; (b) lateral and (c) top; for a foam quality of 55% at a foam velocity of 2 cm/s.

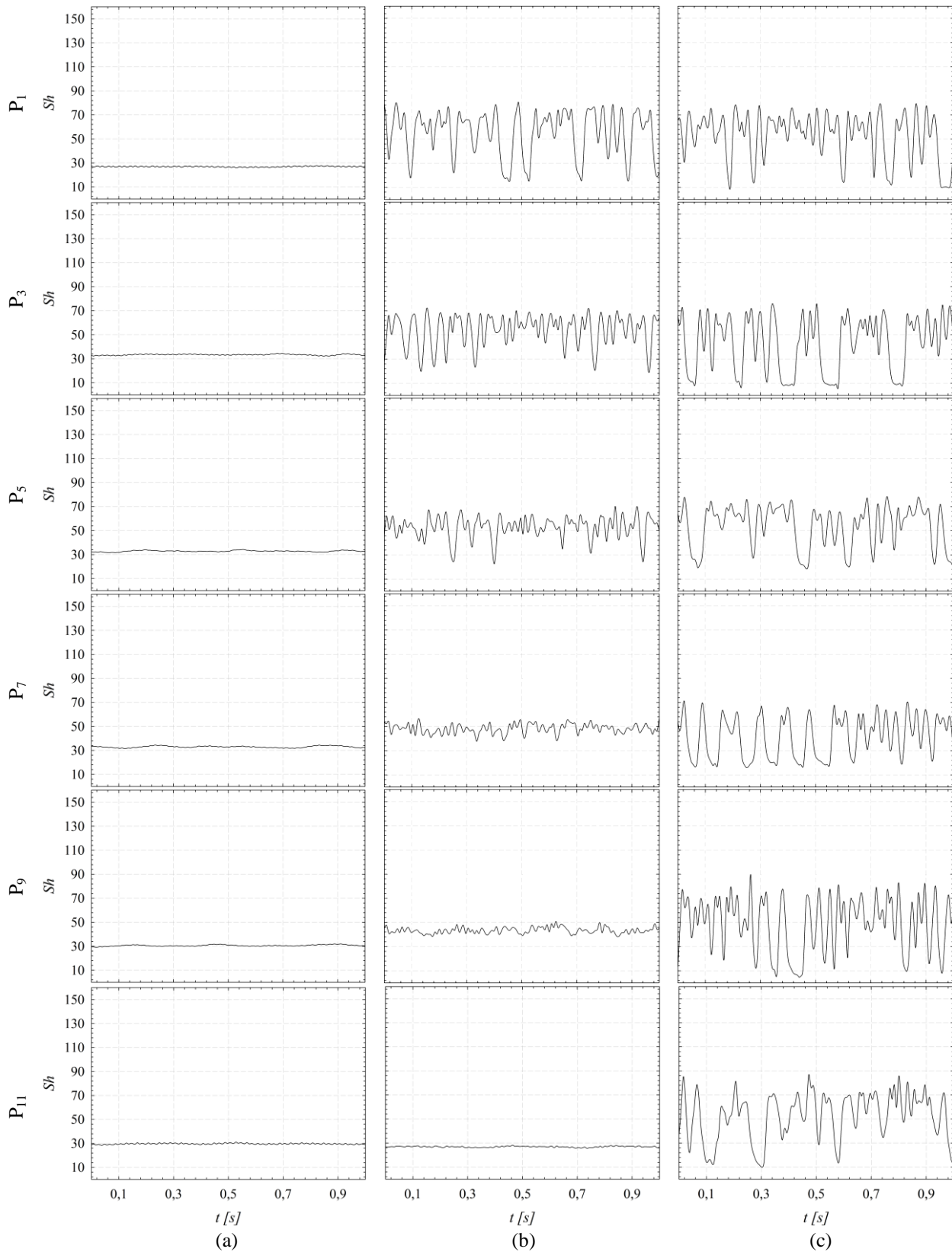


Figure 3.26 Polarographic signals over three walls: (a) bottom; (b) lateral and (c) top; for a foam quality of 60% at a foam velocity of 2 cm/s.

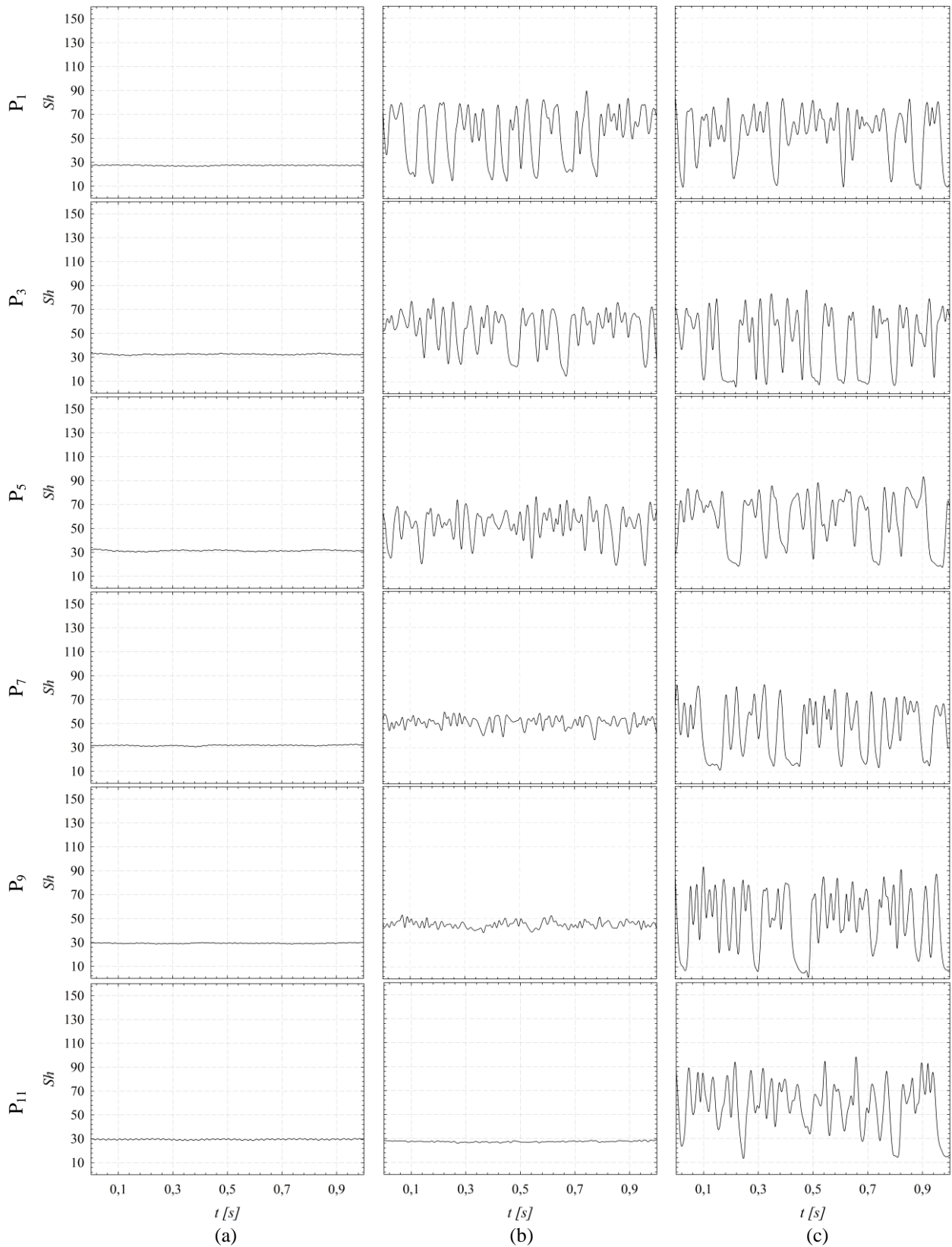


Figure 3.27 Polarographic signals over three walls: (a) bottom; (b) lateral and (c) top; for a foam quality of 65% at a foam velocity of 2 cm/s.

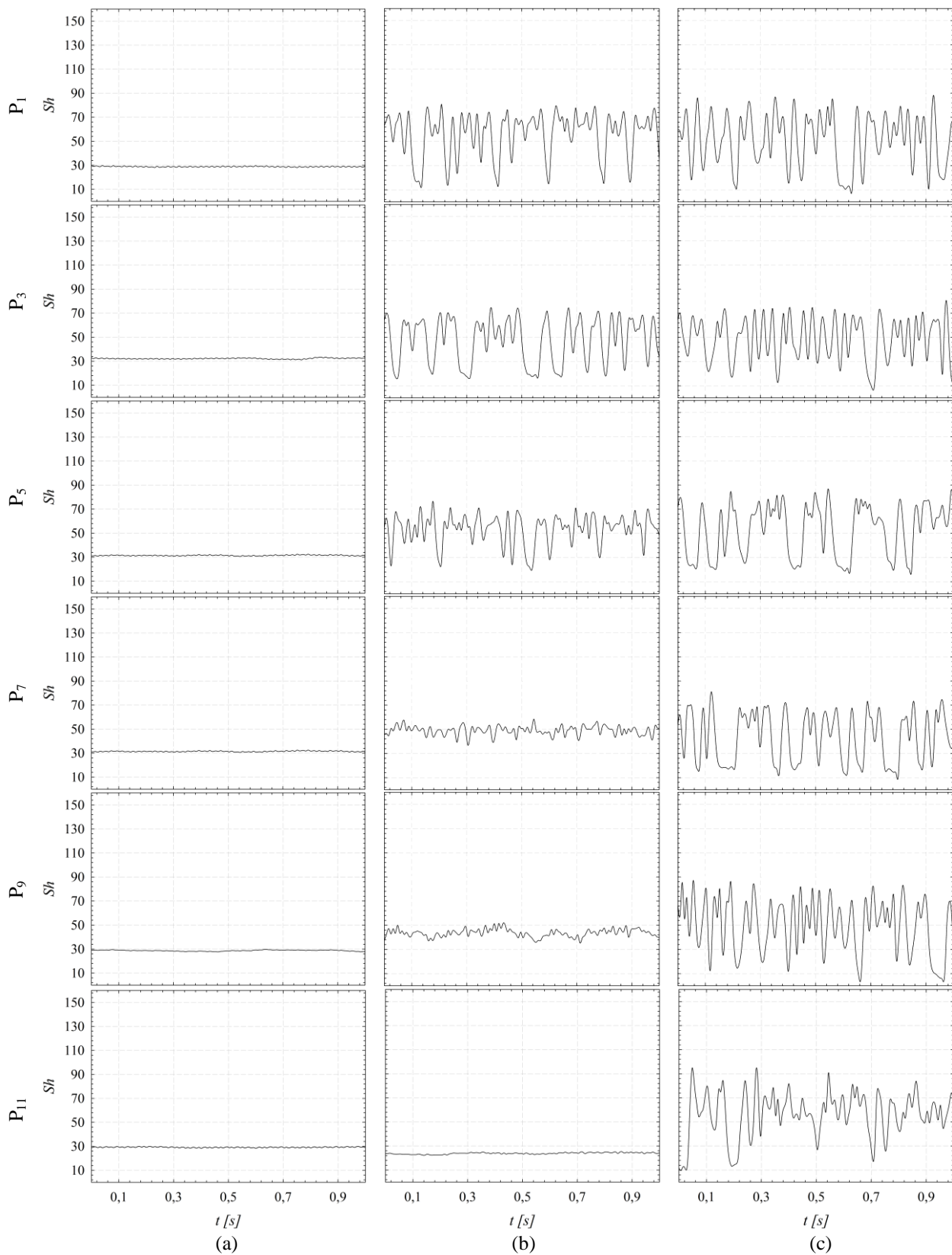


Figure 3.28 Polarographic signals over three walls: (a) bottom; (b) lateral and (c) top; for a foam quality of 70% at a foam velocity of 2 cm/s.

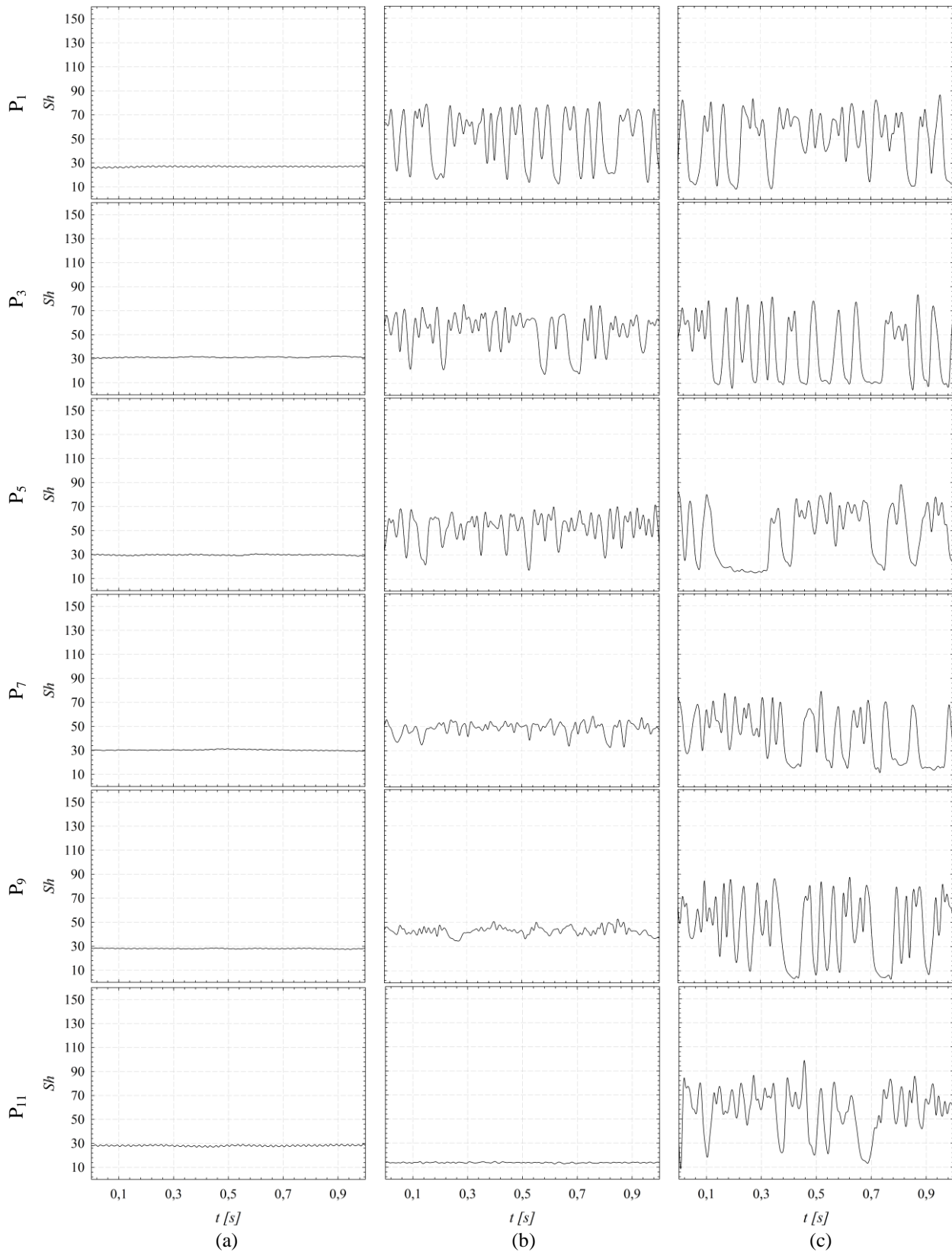


Figure 3.29 Polarographic signals over three walls: (a) bottom; (b) lateral and (c) top; for a foam quality of 75% at a foam velocity of 2 cm/s.

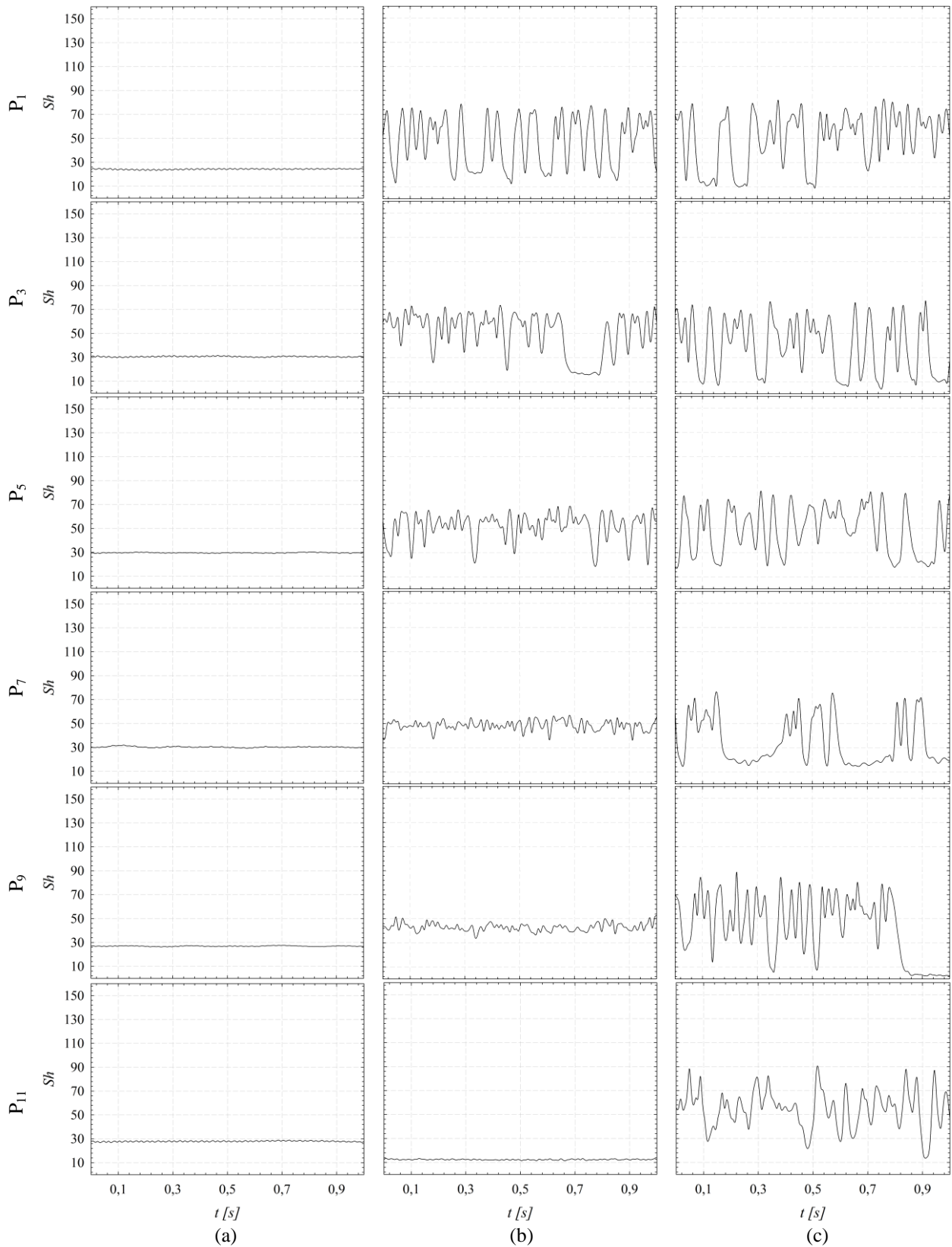


Figure 3.30 Polarographic signals over three walls: (a) bottom; (b) lateral and (c) top; for a foam quality of 80% at a foam velocity of 2 cm/s.

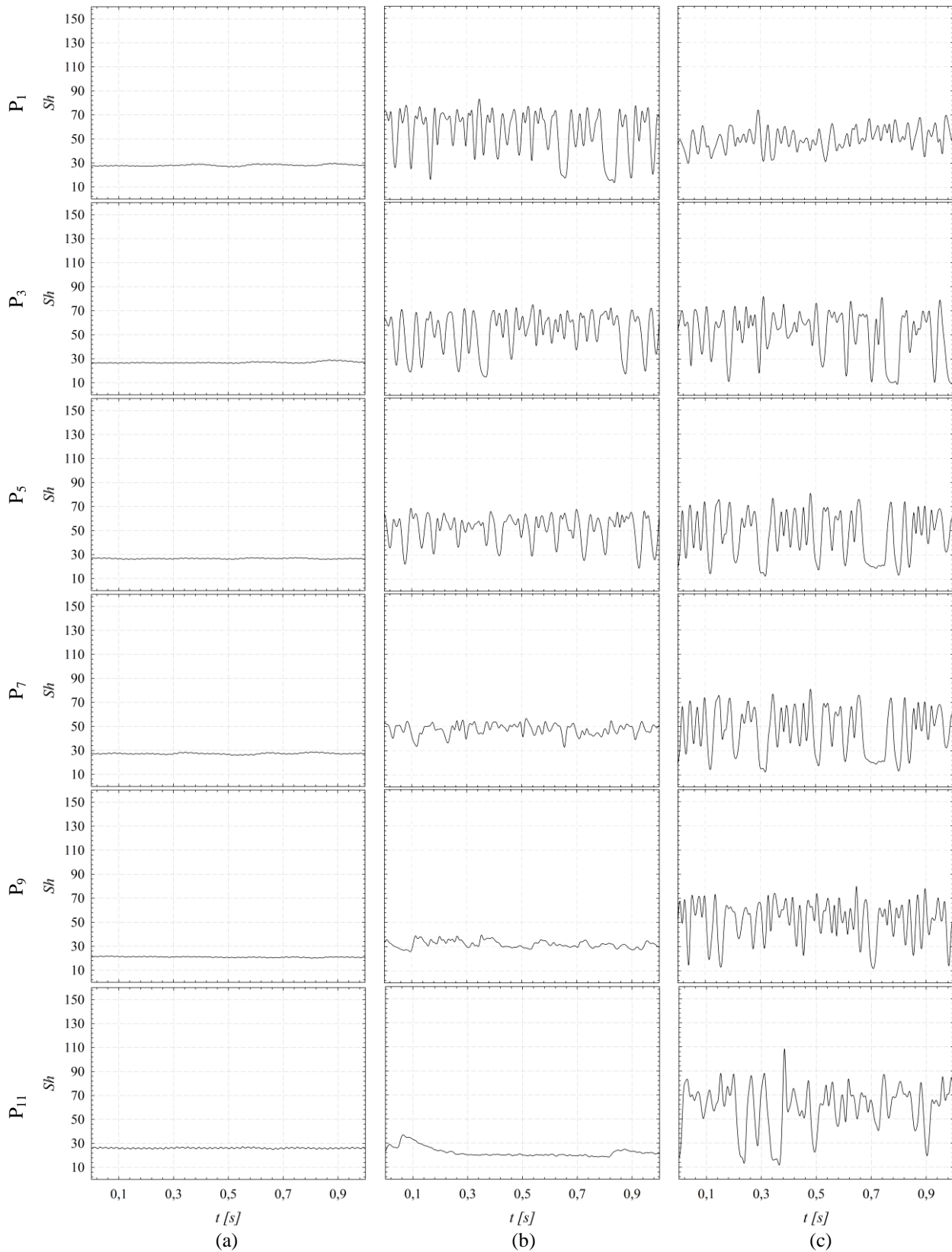


Figure 3.31 Polarographic signals over three walls: (a) bottom; (b) lateral and (c) top; for a foam quality of 85% at a foam velocity of 2 cm/s.

We can see that the fluctuations are a result of the bubbles' passage over the probe. Due to the gravitational drainage, water tends to go to the bottom of the channel, as showed in the conductimetry results. Therefore, the probes closer to this part of the channel present less Sherwood fluctuations than the ones at the top. Here, the liquid film thickness is smaller and the bubbles influence is important. A clear example is noted for the probe 1 near the bottom of the channel for a foam quality of 85%. As the foam becomes dryer, the liquid films at the walls diminish and, consequently, the polarographic probes do a better register of the bubbles passage.

Despite this observation, there is no great difference due to foam qualities. Sherwood number fluctuations have shown the same size and number at the top of the channel and they present the same fluctuation evolution along the lateral probe, with big fluctuations near the highest point and a constant value at the bottom.

These oscillations were described in previous works [51,113]. They made a simultaneous acquisition of the polarographic current and a video of the bubbles flowing through the probe. This process is called signal synchronization. Figure 3.32 shows a schematic representation of the process.

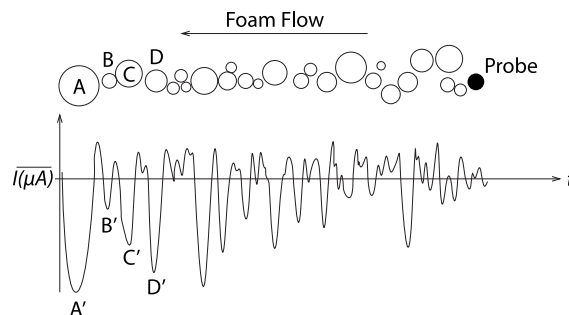


Figure 3.32 Synchronization between the bubbles passage over the polarographic probe and the measured current.

As the first bubble A passes through the probe, it generates a measured current A'. Its value is weaker than the ones obtained before and after its passage. This same response is obtained for all the bubbles that go through the probe. The lowest values are related to the bubbles deformed at the wall. The number of fluctuations per second obtained, for all quantities, is near the same value. A statistical analysis is explained further ahead to better understand the fluctuations behavior, amplitude and characteristics. The Sherwood fluctuations, for the two remaining cases (4 cm/s and 6 cm/s) are shown in Figures 3.33 to 3.53.

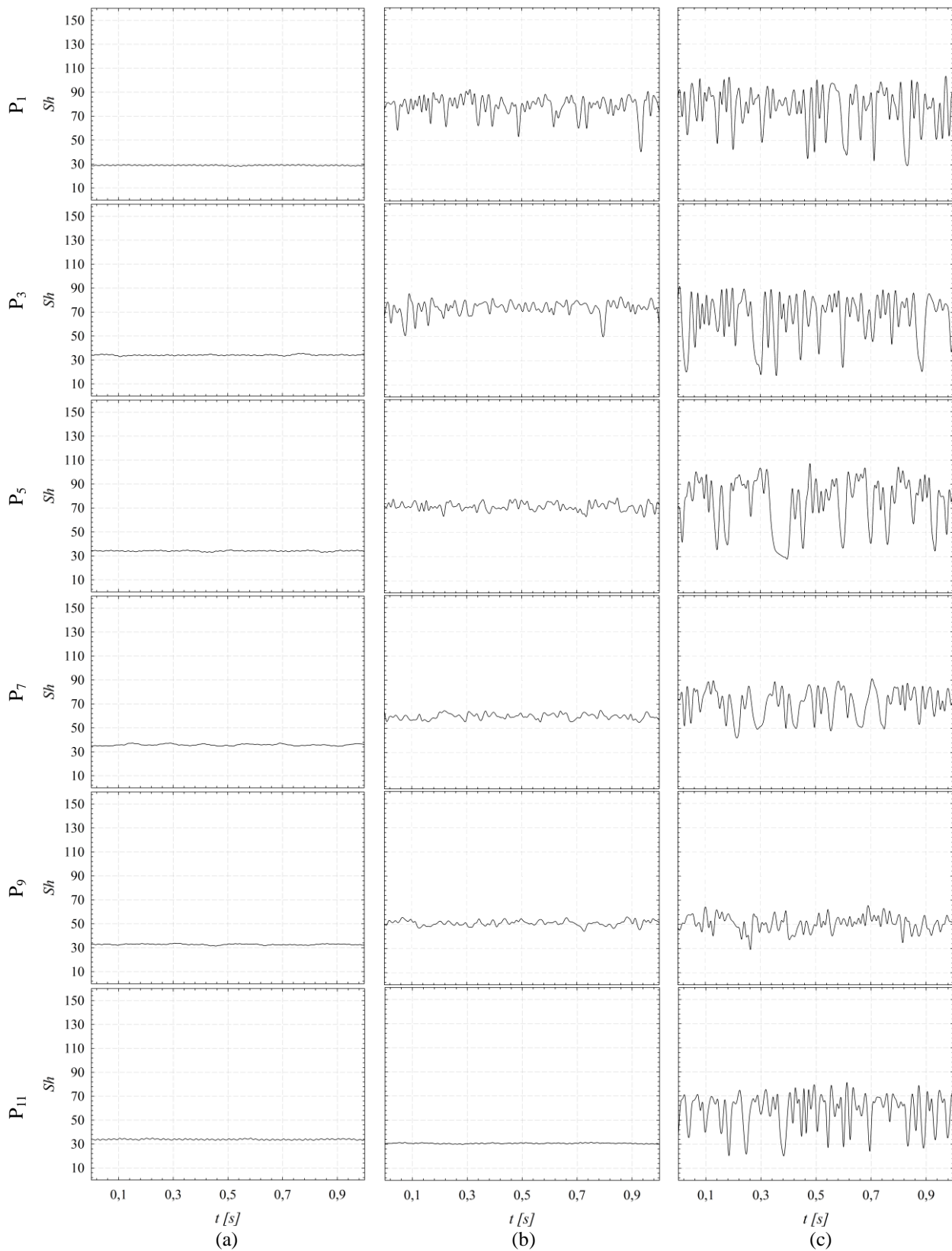


Figure 3.33 Polarographic signals over three walls: (a) bottom; (b) lateral and (c) top; for a foam quality of 55% at a foam velocity of 4 cm/s.

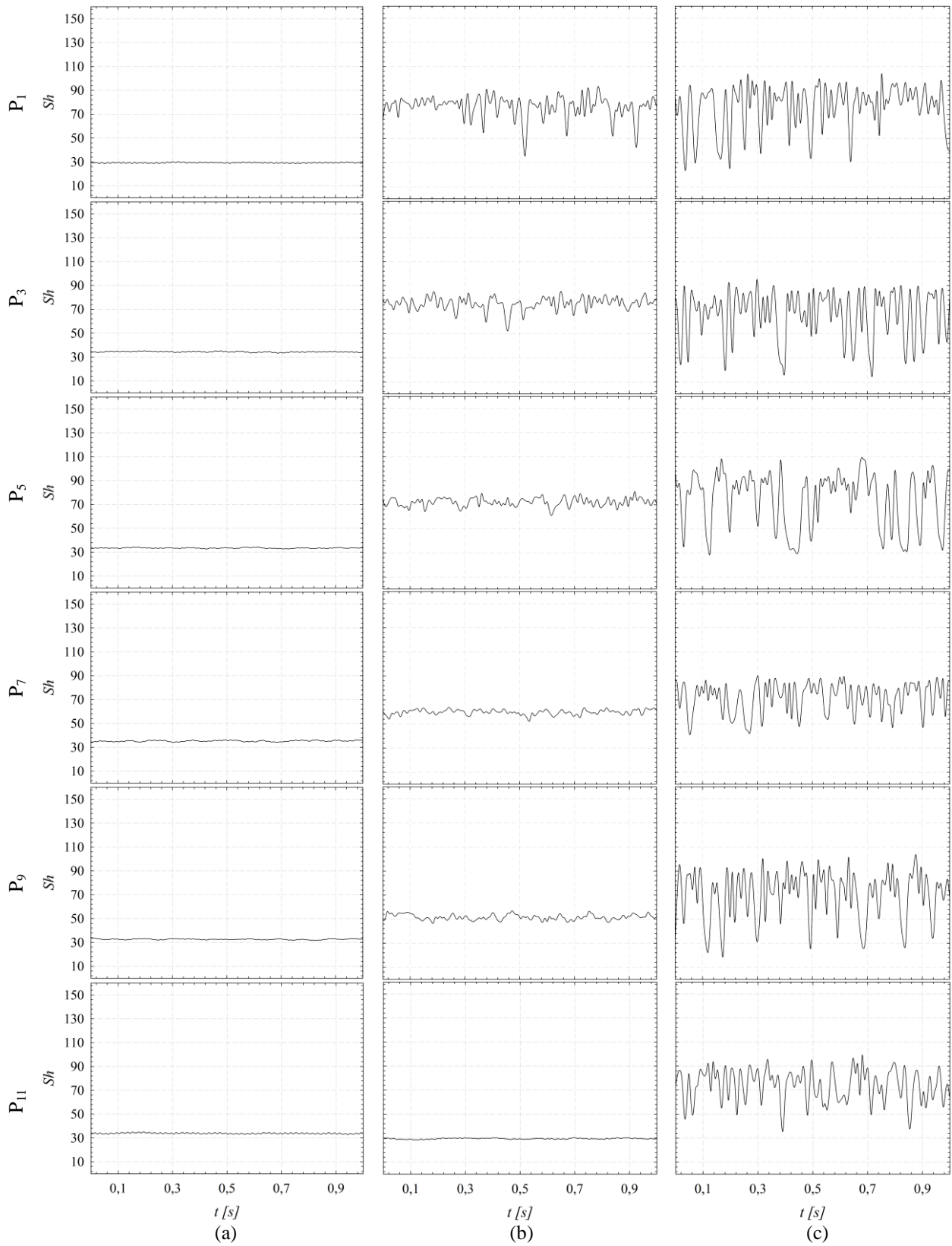


Figure 3.34 Polarographic signals over three walls: (a) bottom; (b) lateral and (c) top; for a foam quality of 60% at a foam velocity of 4 cm/s.

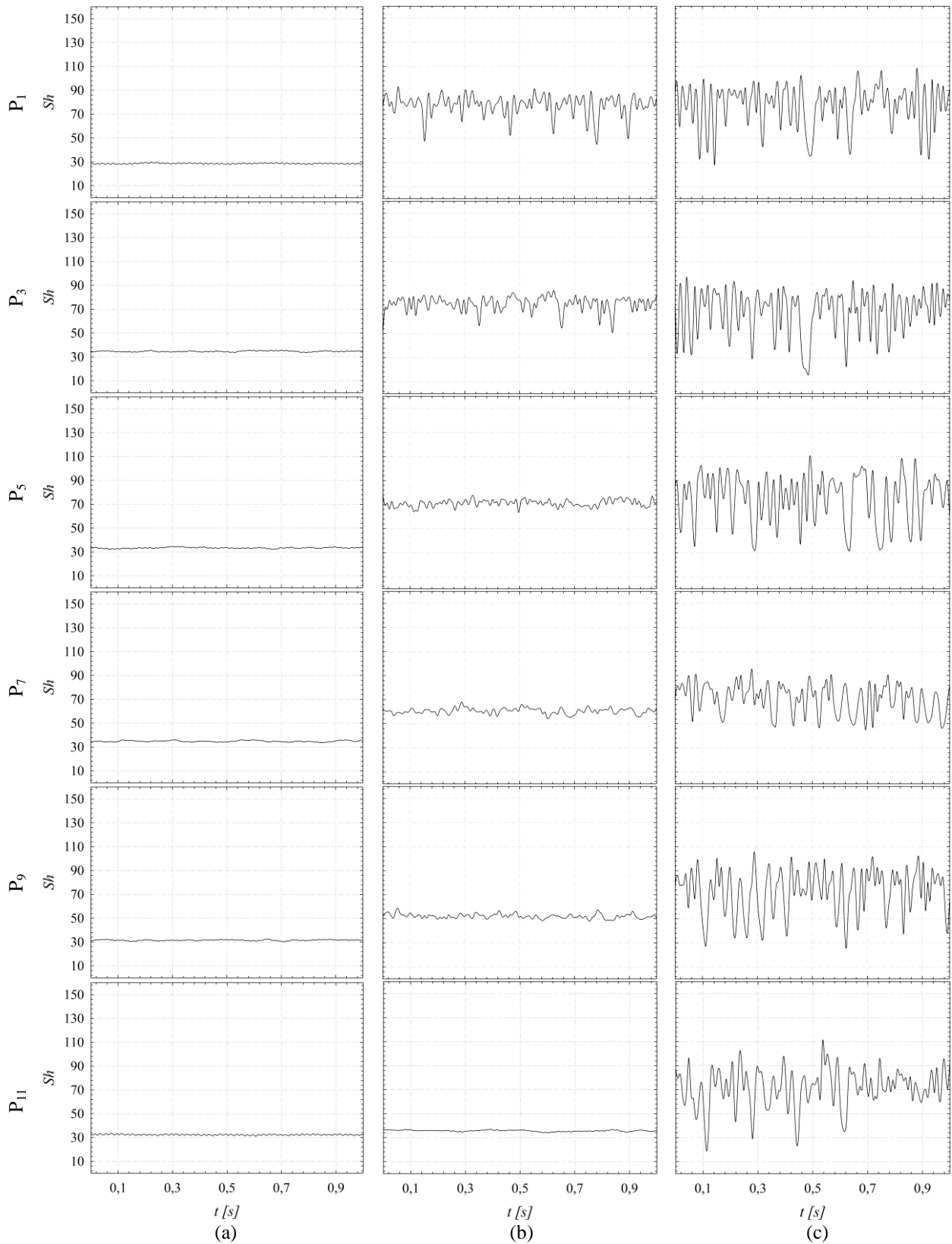


Figure 3.35 Polarographic signals over three walls: (a) bottom; (b) lateral and (c) top; for a foam quality of 65% at a foam velocity of 4 cm/s.

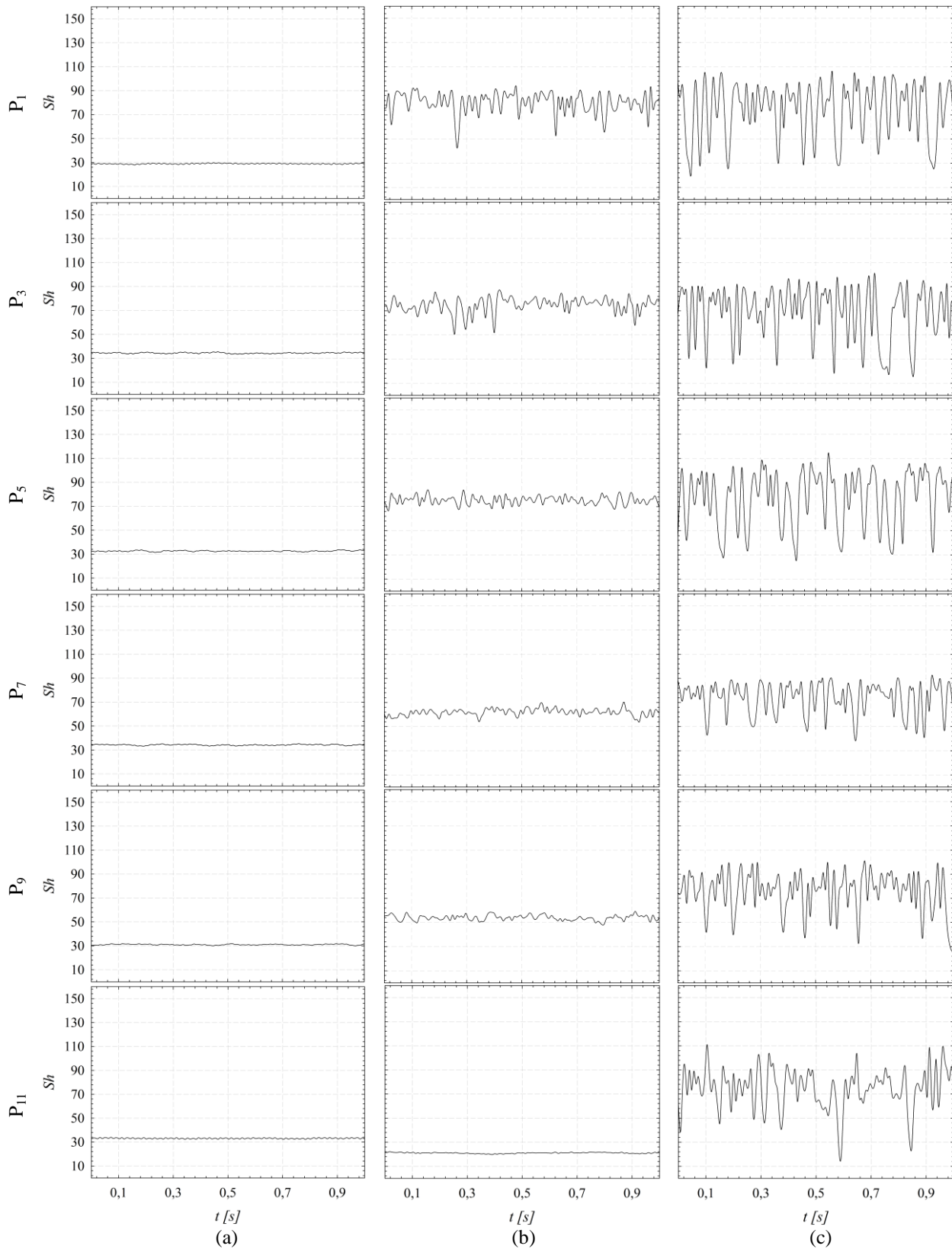


Figure 3.36 Polarographic signals over three walls: (a) bottom; (b) lateral and (c) top; for a foam quality of 70% at a foam velocity of 4 cm/s.

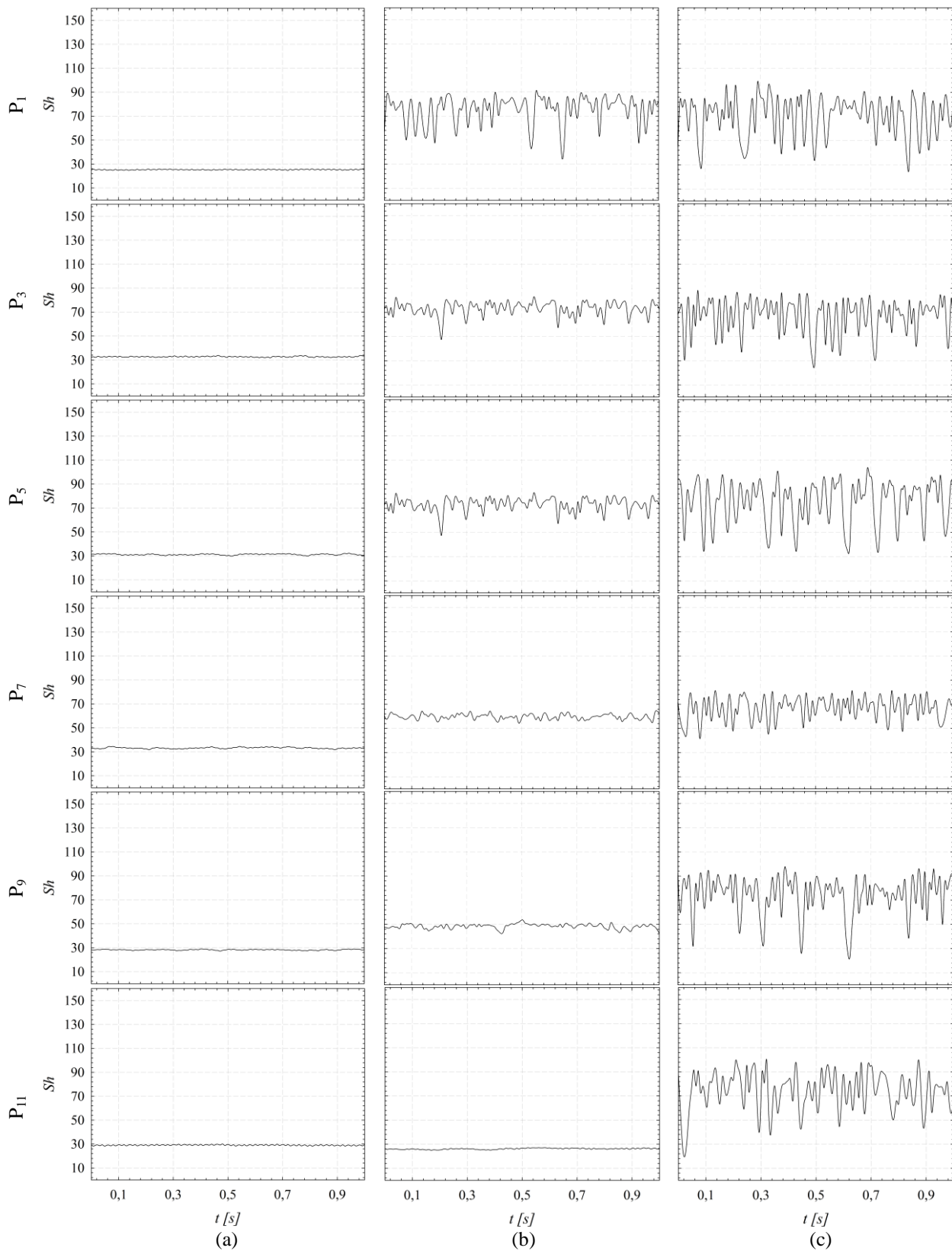


Figure 3.37 Polarographic signals over three walls: (a) bottom; (b) lateral and (c) top; for a foam quality of 75% at a foam velocity of 4 cm/s.

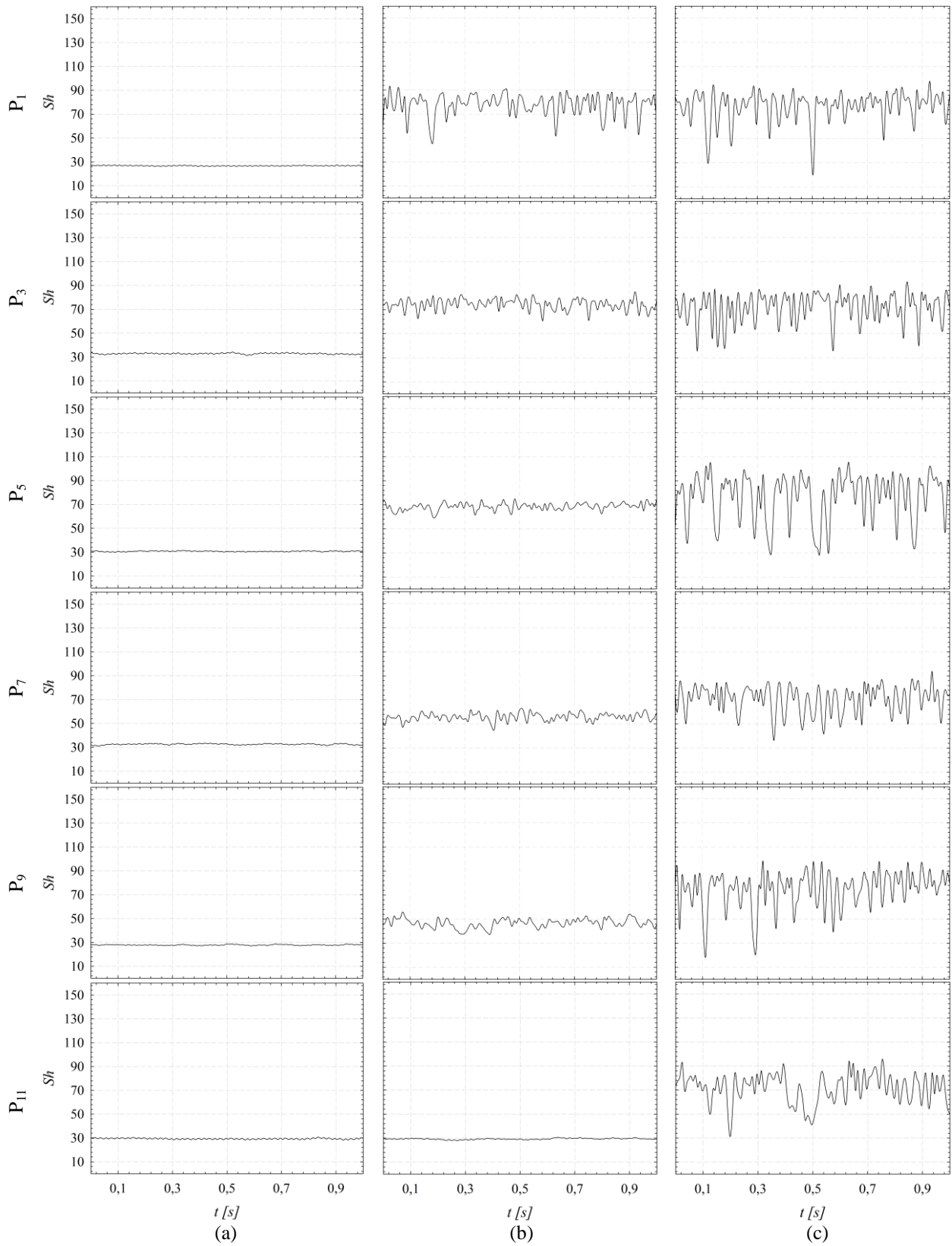


Figure 3.38 Polarographic signals over three walls: (a) bottom; (b) lateral and (c) top; for a foam quality of 80% at a foam velocity of 4 cm/s.

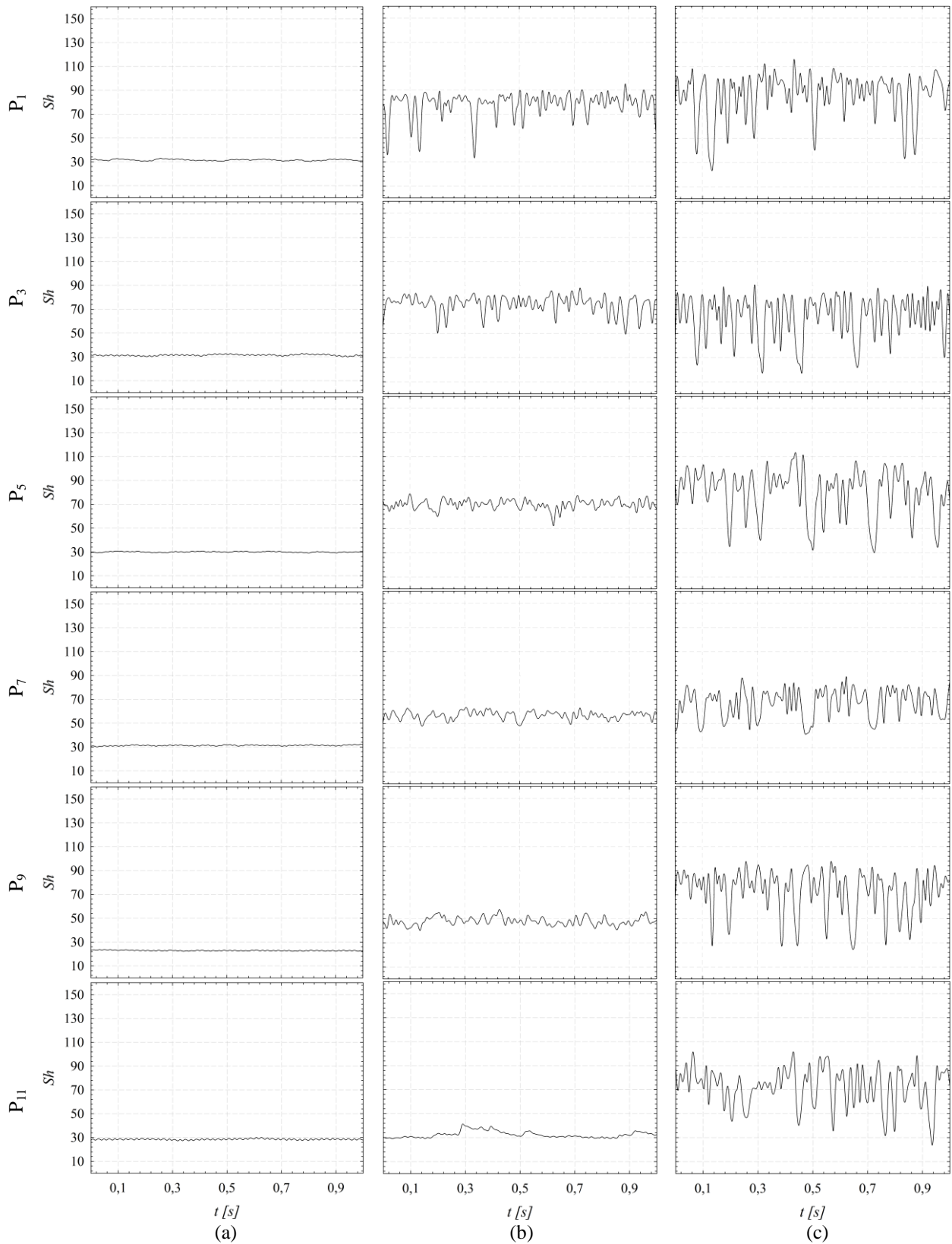


Figure 3.39 Polarographic signals over three walls: (a) bottom; (b) lateral and (c) top; for a foam quality of 85% at a foam velocity of 4 cm/s.

When comparing the case I to the II, it should be noted how the mean value of the Sherwood number increases with the velocity. The Sherwood number's fluctuations amplitudes seem to be somewhat related to the liquid film thickness value, the foam velocity and the foam quality. The number of fluctuations per second is directly linked to the number of bubbles passing by the probe.

From a theoretical point of view, the polarographic signal is related to the fluid velocity and the thickness of the film. To measure the wall shear stress with this method, the thickness of the liquid film should be defined. It may have special interest when it is smaller to a critical value numerically obtained. By analyzing the influence of the slip layer thickness over the mass transfer, it can be verified if the film is thick enough to use this measurement technique [4].

For a two-dimension flow over a horizontal plate, the general mass transfer equation can be written:

$$\frac{\partial c}{\partial t} + u \frac{\partial c}{\partial x} + v \frac{\partial c}{\partial y} = D \left(\frac{\partial^2 c}{\partial x^2} + \frac{\partial^2 c}{\partial y^2} \right) \quad (3.7)$$

where x is the axial flow direction, y is the vertical direction, u is the axial velocity component of the flow, v is the vertical velocity component of the flow, c is the ferricyanide concentration and D is the molecular diffusion coefficient.

By using the hypothesis of a permanent flow, a linear and unidirectional velocity profile ($u = S_0 y$) at the viscous sublayer, as seen before, the mass transfer equation becomes:

$$S_0 y \frac{\partial c}{\partial x} = D \left(\frac{\partial^2 c}{\partial x^2} + \frac{\partial^2 c}{\partial y^2} \right) \quad (3.8)$$

The magnitude of the diffusion layer, for an electrode of length L_s , is [123,139]:

$$\delta_c = \left(\frac{D L_s}{S_0} \right)^{1/3} \quad (3.9)$$

For this, dimensionless quantities can be introduced: $C = c/c_\infty$; $X = x/L_s$ and $Y = y/\delta_c$. These elements may be included in the mass transfer equation, which becomes:

$$Y \frac{\partial C}{\partial X} = \left(\frac{\delta_c}{L_s} \right)^2 \frac{\partial^2 C}{\partial X^2} + \frac{\partial^2 C}{\partial Y^2} \quad (3.10)$$

The Péclet number, Pe , is a dimensionless number defined as the ratio of the rate of advection of a physical quantity by the flow to the rate of diffusion of the same quantity driven by an appropriate gradient. It can represent the dimensionless wall velocity gradient (shear rate) by:

$$Pe = \left(\frac{S_0 L_s^2}{D} \right) \quad (3.11)$$

The equation of the mass transfer is then reduced to:

$$Y \frac{\partial C}{\partial X} = Pe^{-2/3} \frac{\partial^2 C}{\partial X^2} + \frac{\partial^2 C}{\partial Y^2} \quad (3.12)$$

The liquid slip layer has a finite thickness. The boundary conditions are represented in Figure 3.40 and they can be defined as:

- $C = 0$ for [B, C]
- $C = 1$ for [A, F]
- $\frac{\partial C}{\partial Y} = 0$ for [A, B] \cup [C, D] \cup [E, F]
- $\frac{\partial C}{\partial X} = 0$ for [A, B] \cup [C, D] \cup [E, F]

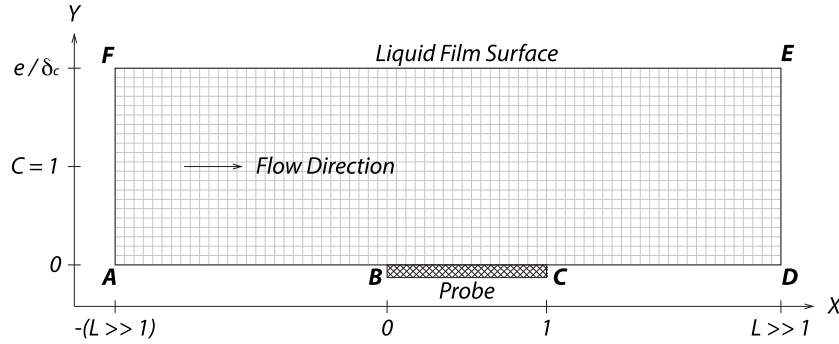


Figure 3.40 Boundaries of the numerical solution.

The convection-diffusion equation can be numerically solved using the finite volume method for $10^{-4} \leq Pe \leq 10^8$. For these parameters, the relationship (e/δ_c) is varied between 1 and 15 to determine the critical value when $C \approx 1$ at the liquid film's surface. This way, the layer can be considered a semi-infinite.

The numerical solution of the dimensionless concentration over the (x, y) plane can show an example of the concentration for a wall shear stress of 2 Pa (or a Peclet number $Pe = 115771$), which corresponds to an approximate shear stress value exerted by the foam flow over the wall.

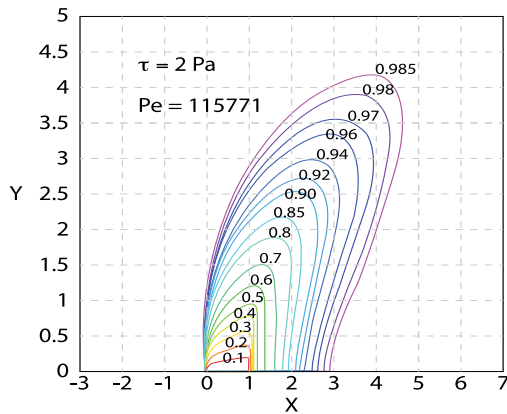


Figure 3.41 Isoconcentration lines

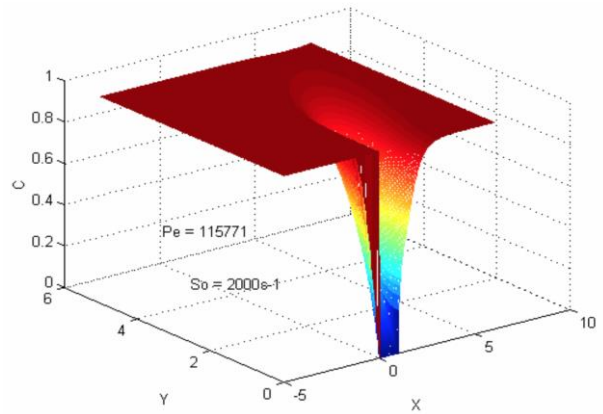


Figure 3.42 Evolution of the Concentration “C” in a three-dimensional domain

The concentration's numerical solution leads to the determination of the diffusion limit current, defined as:

$$I = z_e F \iint_A D \left(\frac{\partial c}{\partial y} \right)_{y=0} dA_s \tag{3.13}$$

This current can be characterized by the Sherwood number \overline{Sh} over the probe's surface. This number is defined as:

$$\overline{Sh} = \frac{I}{z_e F A_s c_\infty D} l \tag{3.14}$$

For a two-dimensional flow:

$$\overline{Sh} = \frac{l}{\delta_c} \int_0^1 \left. \frac{\partial C}{\partial Y} \right]_{y=0} dx = Pe^{1/3} \int_0^1 \left. \frac{\partial C}{\partial Y} \right]_{y=0} dx \tag{3.15}$$

The integration of the dimensionless concentration gradient using the Simpson method over the dimensionless length of the probe $\left(\int_0^1 \frac{\partial C}{\partial Y}\bigg|_{Y=0} dX\right)$ can be represented (Figure 3.43) for the neighbor conditions of our experimental ones ($\tau \approx 2 Pa$).

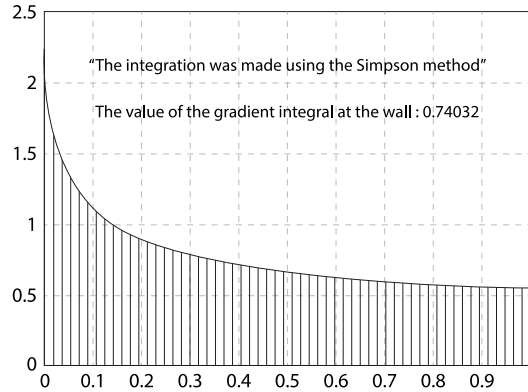


Figure 3.43 $\int_0^1 \frac{\partial C}{\partial Y}\bigg|_{Y=0} dX$ evolution for $Pe = 115771$

For high Péclet numbers, the diffusion can be neglected. Therefore, for a semi-infinite medium and a rectangular probe, the convection-diffusion equation solution can be reduced to the Levêque equation [121].

$$\bar{Sh} = 0.807 Pe^{1/3} \quad (3.16)$$

This solution is commonly called “the one-third power law”. A comparison against the determined numerical solution for $Pe \geq 0.01$ was made in Figure 3.44.

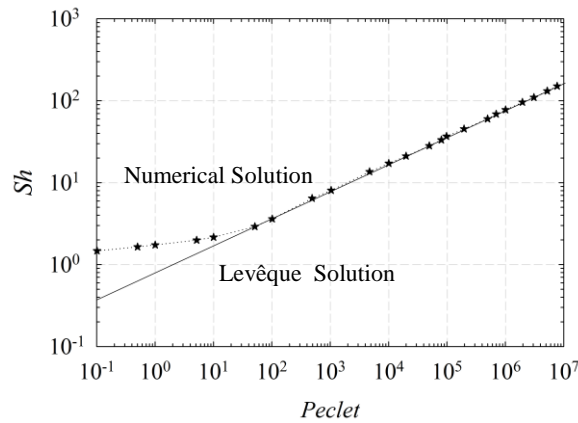


Figure 3.44 Mean Sherwood number evolution versus the Peclet number according to the numerical solution and the Levêque equation.

Regarding this figure, we may note that the numerical solution and the Levêque one merge together from $Pe \approx 100$.

For a circular probe of diameter d_s with a surface A , it has been shown that the Sherwood relationship can be written as [134]:

$$\bar{Sh}_{circ} = \frac{I}{z_e F A_s c_\infty D} ds = 0.862 \left(\frac{d_s^2 S_0}{D} \right)^{1/3} \quad (3.17)$$

The \overline{Sh}_{circ} curves as a function of the thickness, “ e ”, for different values of wall shear stress ($\tau_0 = \mu_l S_0$) and at our experimental conditions ($\mu_l = 1.1 \cdot 10^{-3}$; $d_s = 0.3mm$; $l = 0.82 d_s$ and $D = 7.26 \cdot 10^{-10} m^2 s^{-1}$) are represented in Figure 3.45.

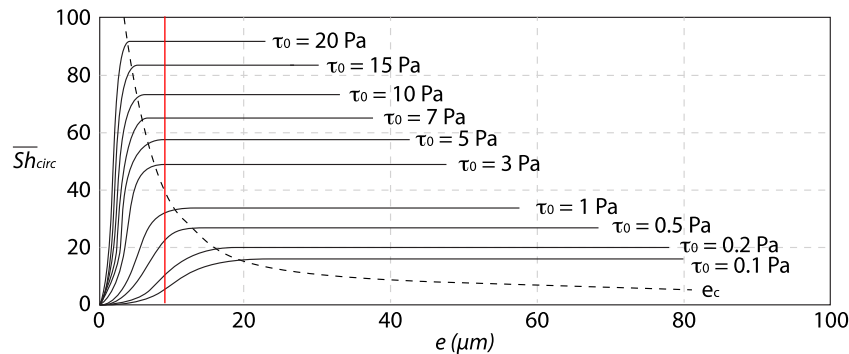


Figure 3.45 Mean Sherwood number evolution as a function of the liquid film thickness for different values of the wall shear stress τ_0 .

Simultaneously, for a given liquid film thickness, between the wall and the foam, Figure 3.46 shows the threshold that the wall shear stress must exceed. For our case, the Sherwood numbers are not affected by the slip-layer thickness.

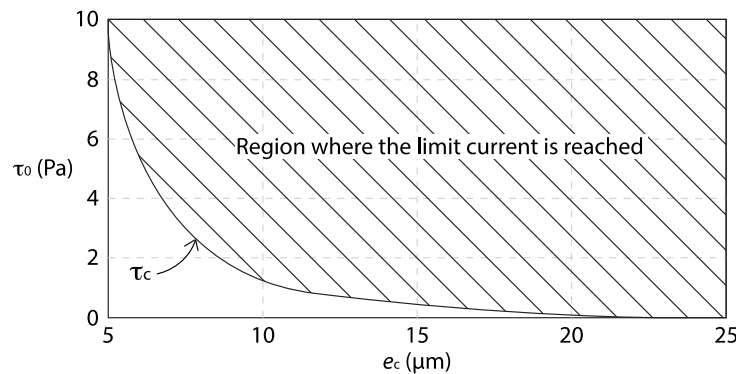


Figure 3.46 Curve limiting the region where the polarographic signal does not depend on the liquid film thickness obtained numerically

These two curves allow the numerical estimation of the liquid film critical thickness for different wall shear stresses. The instantaneous measurement of the slip layer over the later and top wall allowed verifying any critical point. Being under the region where the limit current is reached, the shear stress should be corrected using either the Sobolik or the inverse method. From the conductimetry values, our values were between these two regions, due to the fluctuations they present. The conductimetry results showed that the thickness is not constant and the bubbles sliding over the liquid film varies. The numerical results allow estimating the thickness limits of the minimal liquid slip layer in which the polarographic method can be applied.

Once the theoretical framework concerning the influence of the liquid thickness and the wall shear stress over the polarographic results has been drawn out, we present the Sherwood fluctuation for the final case ($u = 6 cm/s$), where the liquid content of the slip-layer and the wall shear stress generated, over the lateral wall, are slightly higher than for the other two ones (Figures 3.47 to 3.53).

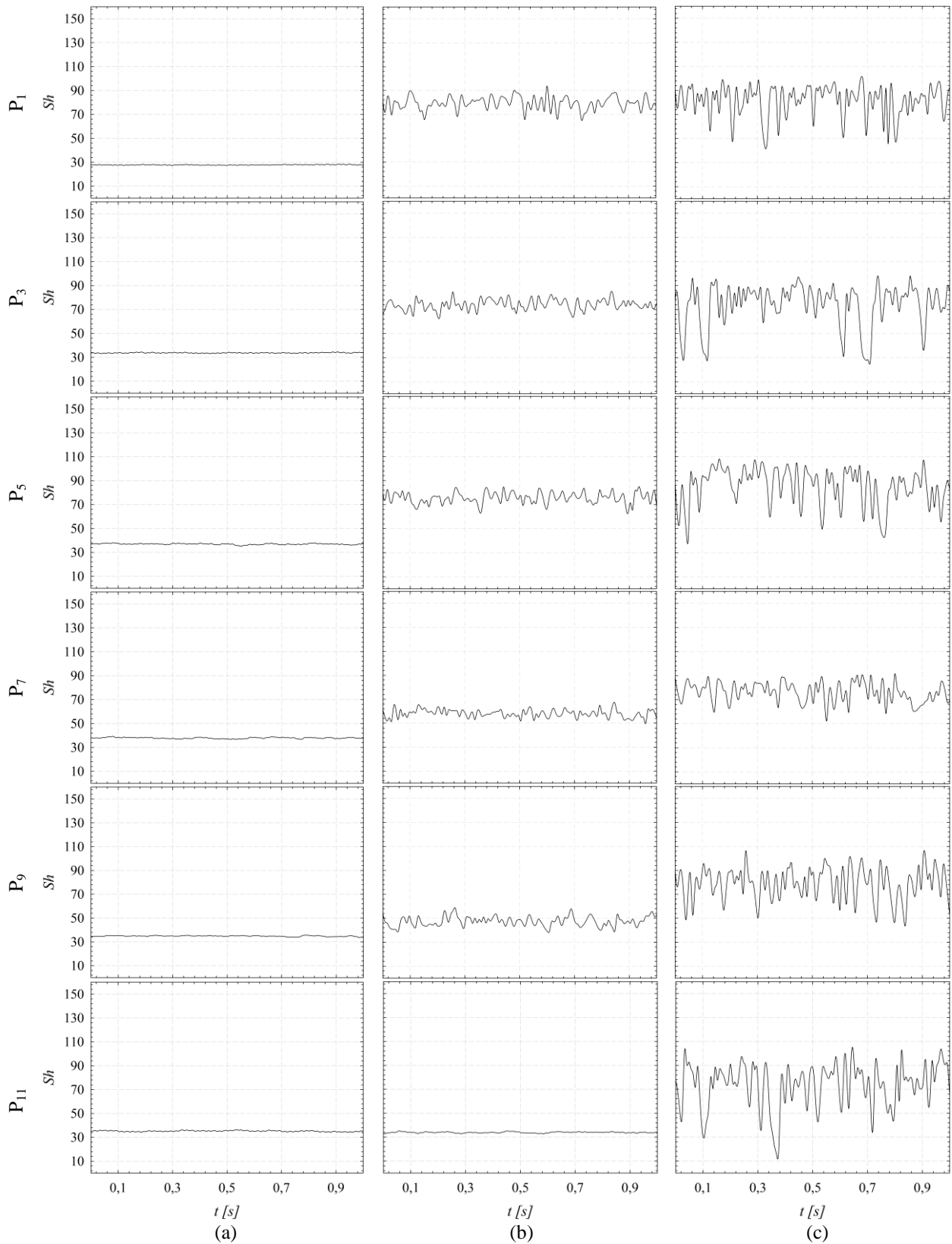


Figure 3.47 Polarographic signals over three walls: (a) bottom; (b) lateral and (c) top; for a foam quality of 55% at a foam velocity of 6 cm/s.

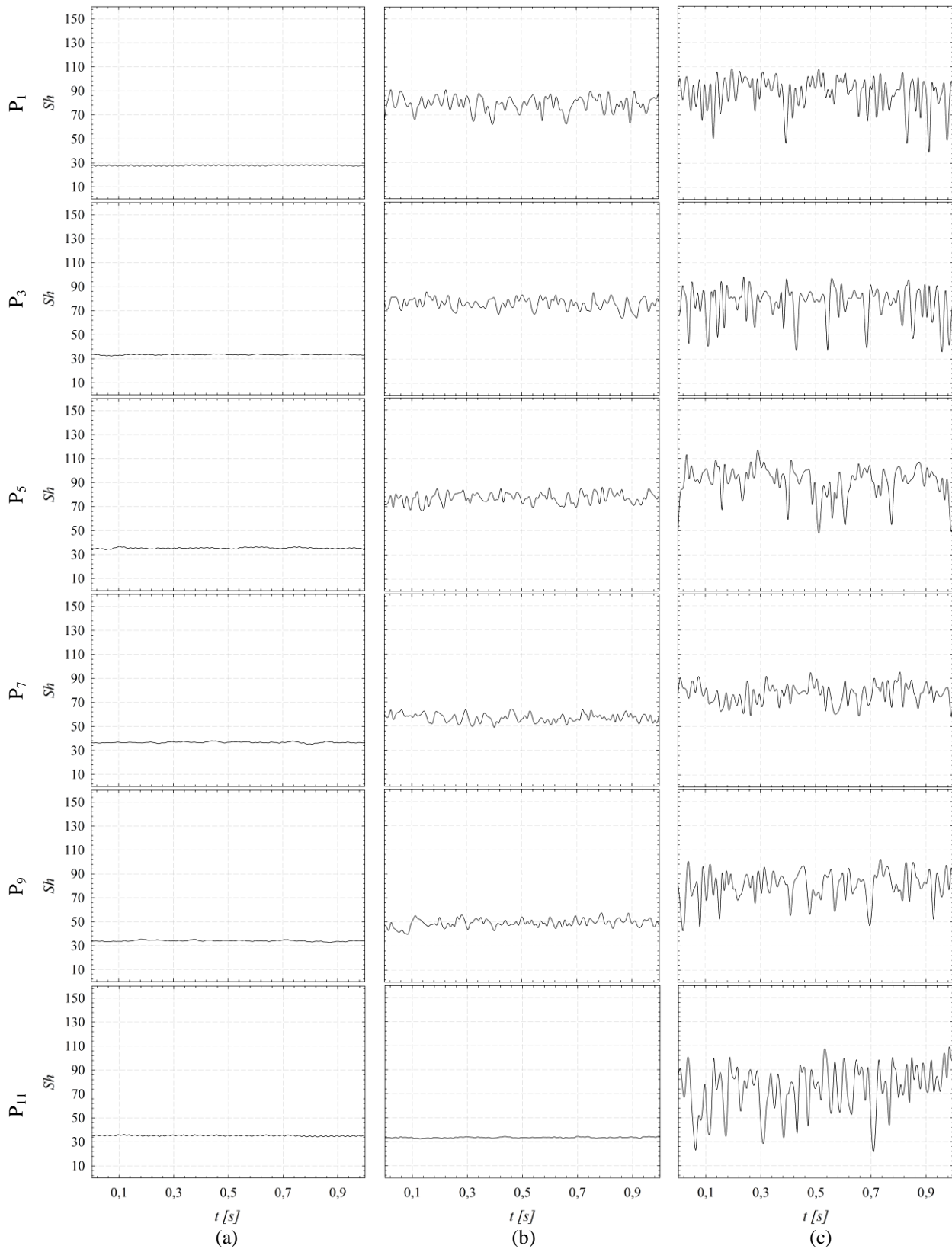


Figure 3.48 Polarographic signals over three walls: (a) bottom; (b) lateral and (c) top; for a foam quality of 60% at a foam velocity of 6 cm/s.

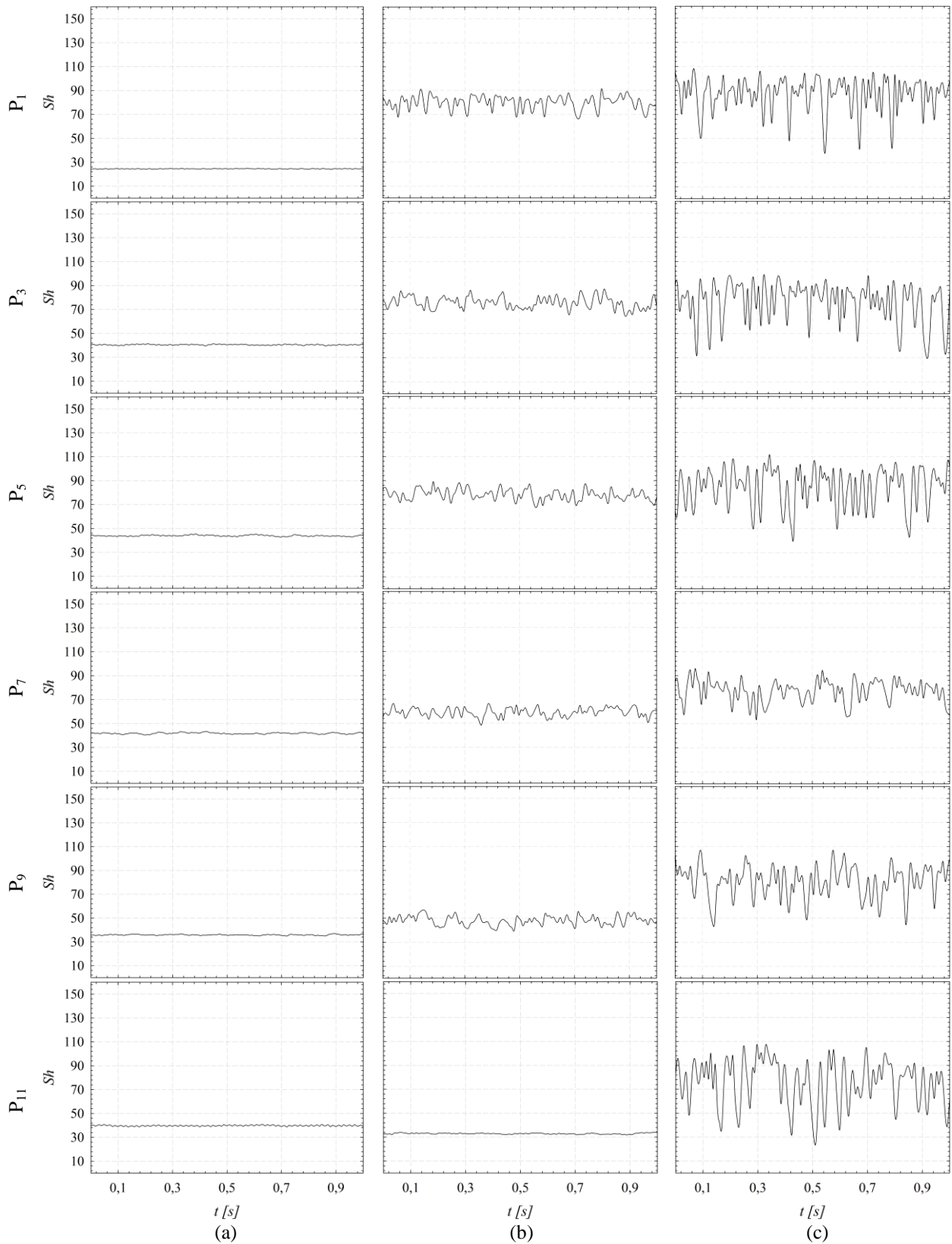


Figure 3.49 Polarographic signals over three walls: (a) bottom; (b) lateral and (c) top; for a foam quality of 65% at a foam velocity of 6 cm/s.

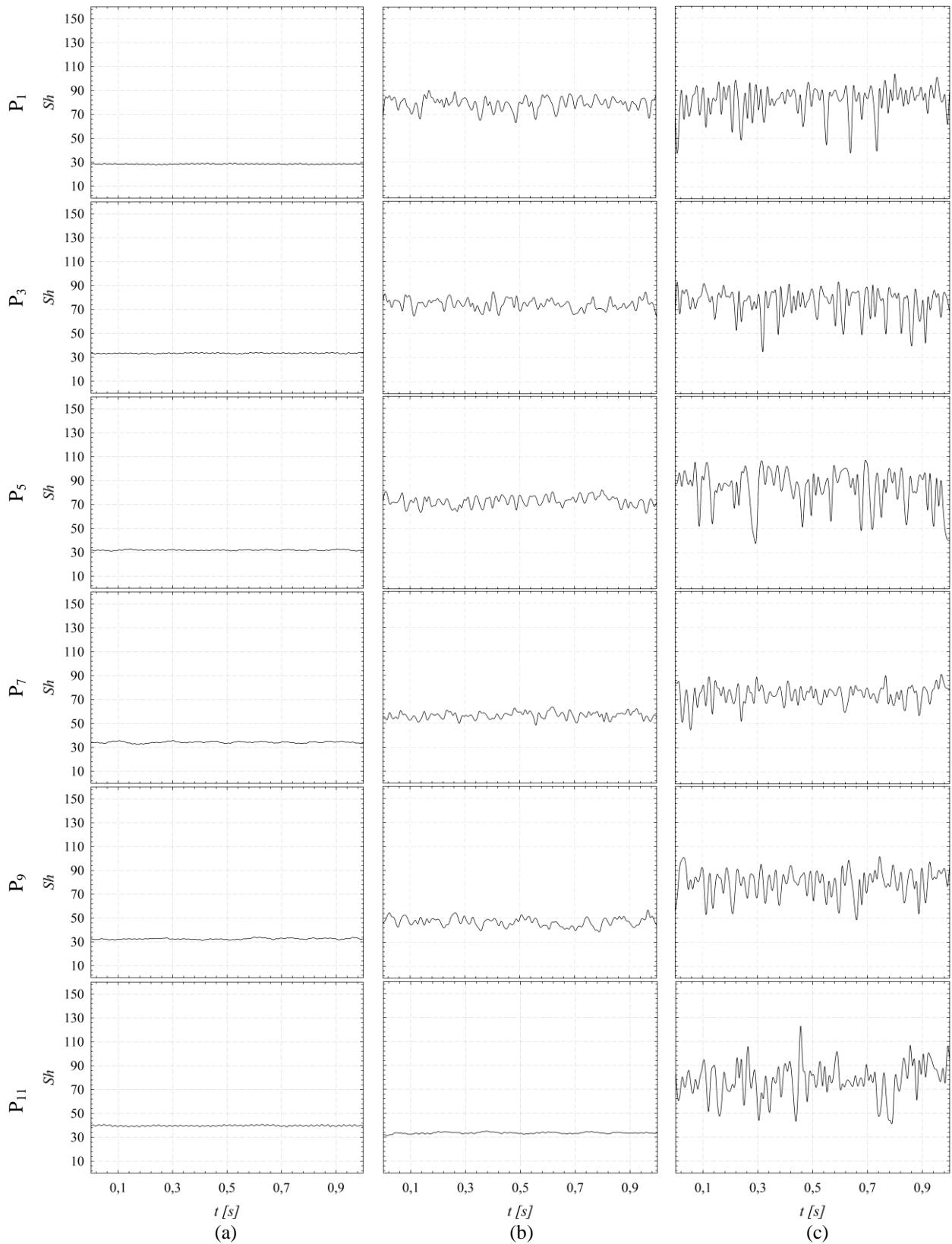


Figure 3.50 Polarographic signals over three walls: (a) bottom; (b) lateral and (c) top; for a foam quality of 70% at a foam velocity of 6 cm/s.

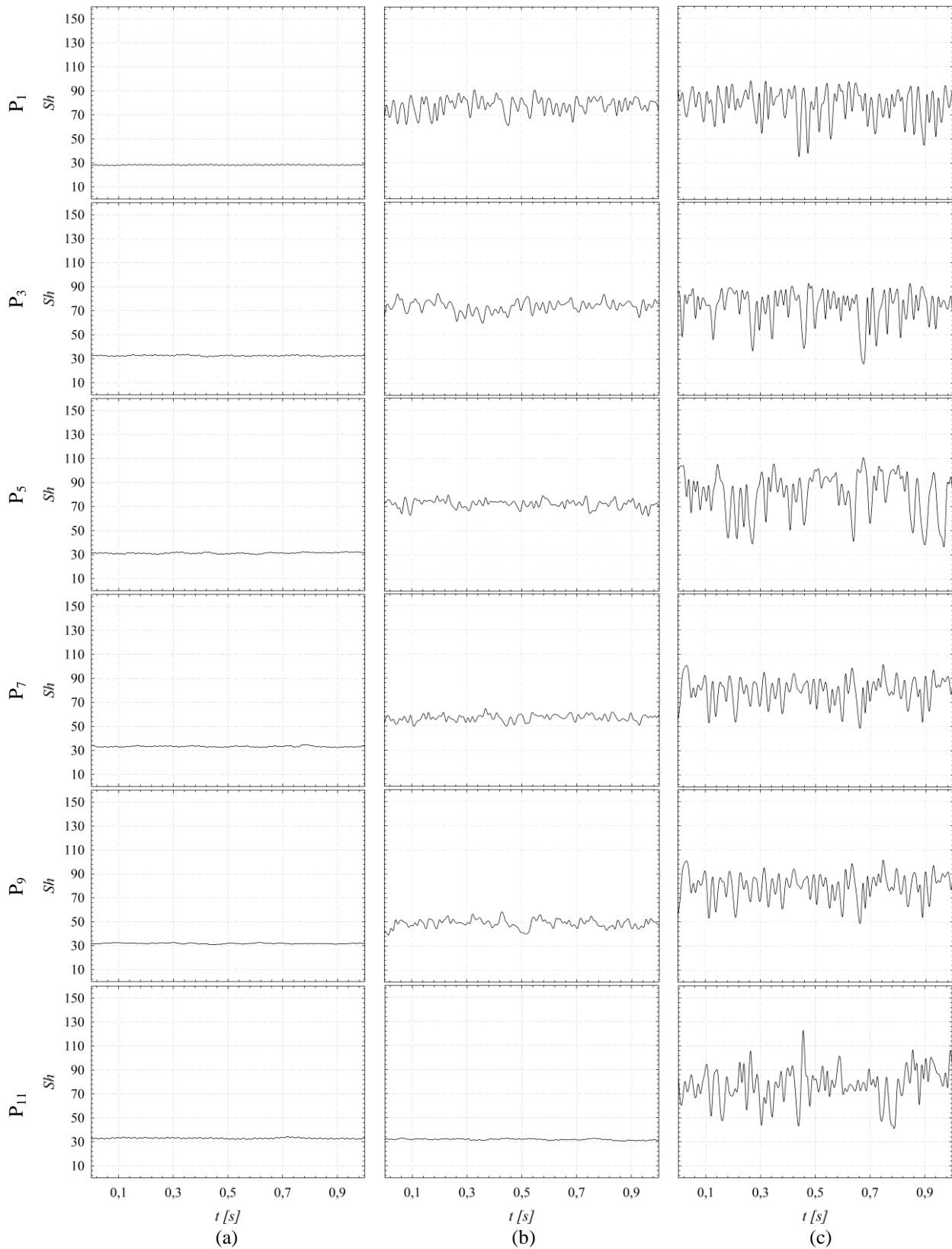


Figure 3.51 Polarographic signals over three walls: (a) bottom; (b) lateral and (c) top; for a foam quality of 75% at a foam velocity of 6 cm/s.

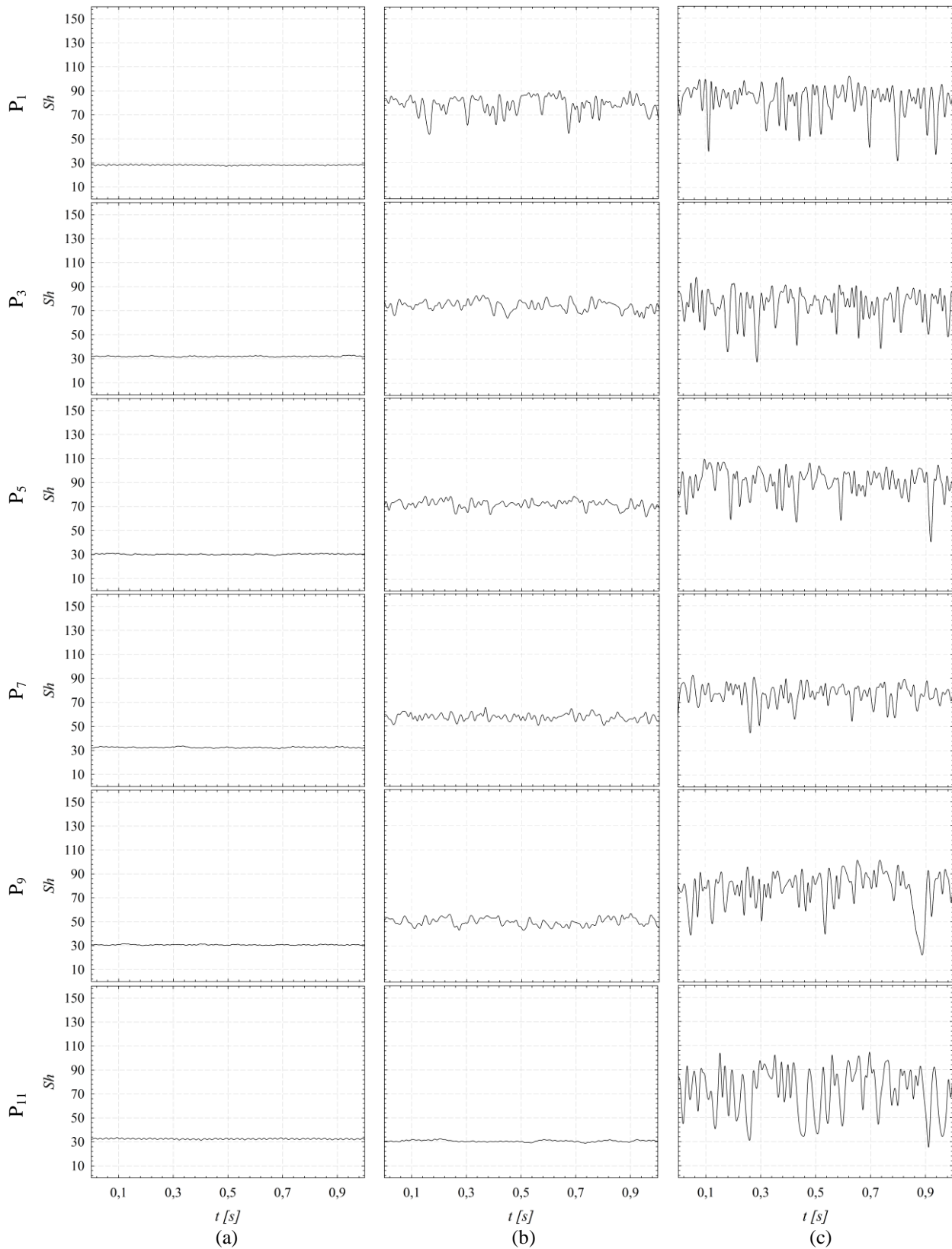


Figure 3.52 Polarographic signals over three walls: (a) bottom; (b) lateral and (c) top; for a foam quality of 80% at a foam velocity of 6 cm/s.

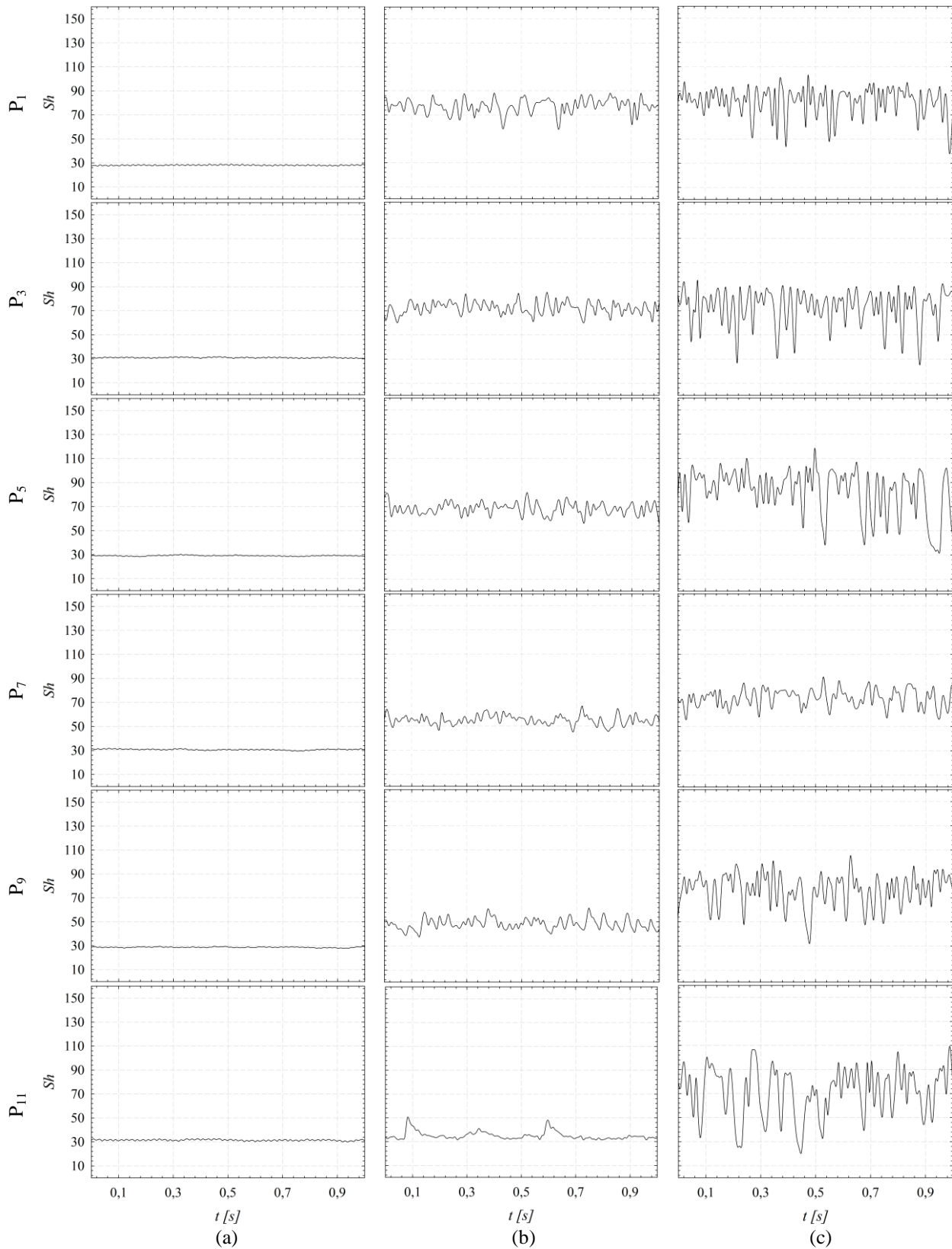


Figure 3.53 Polarographic signals over three walls: (a) bottom; (b) lateral and (c) top; for a foam quality of 85% at a foam velocity of 6 cm/s.

When comparing the Sherwood fluctuations for the three foam velocities several similarities may be noted. First, the resemblance for all bottom and top fluctuations. As seen in the conductimetry fluctuating results, the thickness values are similar for all cases and qualities in these regions of the channel, and this is confirmed by the polarographic results. As for the lateral wall results, an influence of the mean thickness value can be noted. They showed a small increase proportional to the foam velocities, which seems to affect our polarographic results. The amplitude of the Sherwood fluctuations decreases in the case of faster foams.

1.5 Statistical description of the micro-turbulence

As seen in Figure 3.45, the Sherwood values are between the regions where the diffusion limiting current may or not be reached. Therefore, the wall velocity gradient obtained from the instantaneous Sherwood measurements had to be corrected through the Sobolik method [51]. The statistical description of the velocity gradient results at the wall can be linked to the micro-turbulence inside the liquid slip-layer.

As said for the statistical description of the conductimetry results, the skewness and kurtosis factors of a f quantity, which can represent a velocity, pressure or temperature components, can be written as:

$$\mathfrak{S}_f = \frac{\langle f^3 \rangle}{\sigma_f^3} \quad (3.18)$$

$$\mathcal{F}_f = \frac{\langle f^4 \rangle}{\sigma_f^4} \quad (3.19)$$

where σ_f is the dispersion factor of f . When the PDF of the f quantity follows a Gaussian distribution, which is normally the case for substantially homogeneous turbulent flows, these two coefficients take the values of 0 and 3, respectively. However, a homogeneous isotropic turbulence (HIT) is characterized by a negative skewness of the velocity derivative ($\partial u_i / \partial x_i$), where u_i is the velocity component along x_i . In HIT, the skewness represents the rate of production of vorticity through vortex stretching [141].

From the relationship (3.6) between the Sherwood number, Sh , and the diffusion limiting current, I , we have:

$$Sh = \frac{I}{z_e F A c_\infty D} l$$

and the relationship (2.17):

$$I = 0.633 z_e F c_\infty (D^2 S_0)^{1/3} d_s^{5/3}$$

The velocity gradient can be obtained. In this case, it was corrected through the Sobolik method. As an example to understand the influence of skewness and flatness factors, Figure 3.54 and Figure 3.55 show the Probability Density Function (PDF) of the velocity gradient signals over the lateral and the top wall, for three foam velocities and 70% quality.

These figures allow describing the relative likelihood that the velocity gradient may take a given value on the x-axis, closer to the root mean square. For each case, the Gaussian curves remain close, one to another; which was expected, due to the similarity of the polarographic signals over the whole topside of the channel. When comparing them against the normal distribution of the Gaussian function, in blue, we see no big difference between the velocities gradient PDFs and this one. This shows that the probability to arrive to values close to the RMS ones, along all the instantaneous measurements, is greater than in the other ones.

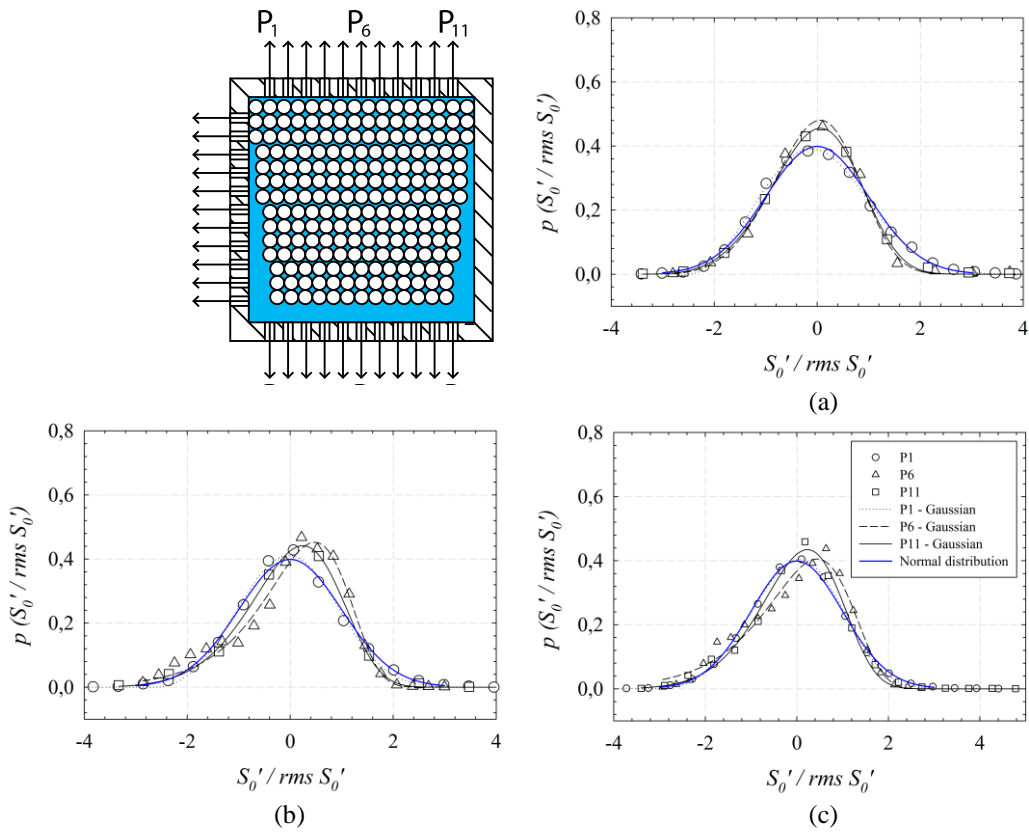


Figure 3.54 Probability Density Function of the velocity gradient obtained with three polarographic probes over the top wall for: (a) Case I; (b) Case II and (c) Case III.

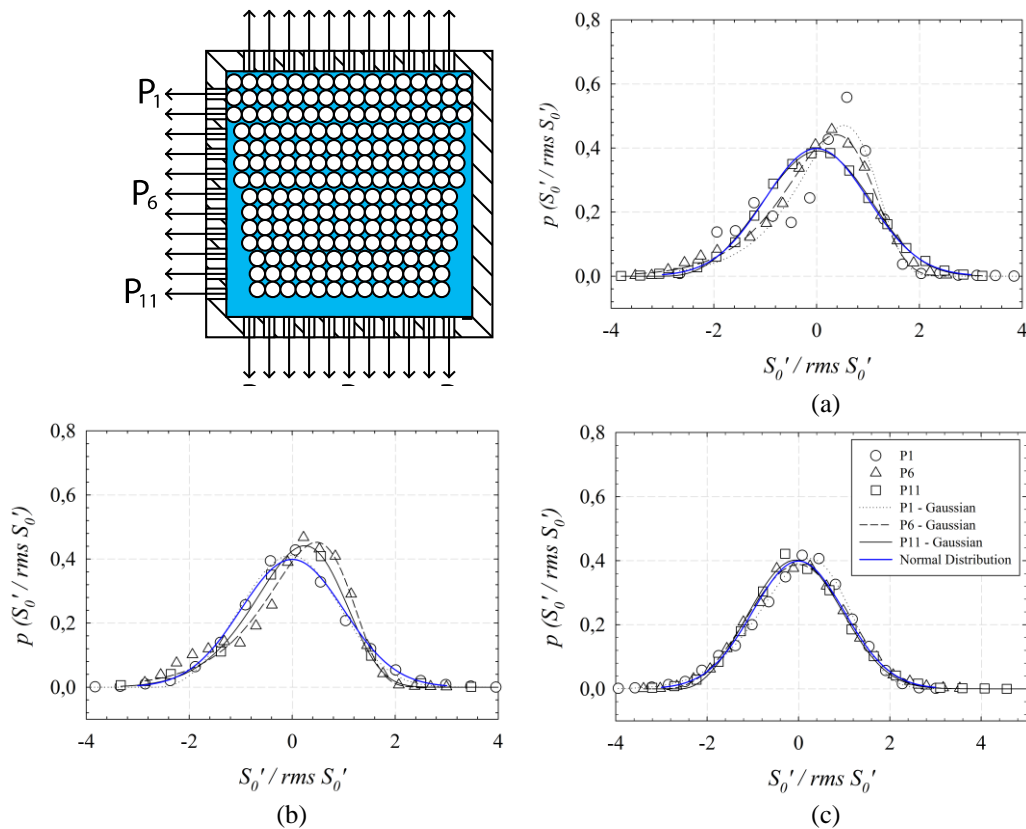


Figure 3.55 Probability Density Function of the velocity gradient obtained with three polarographic probes over the lateral wall for: (a) Case I; (b) Case II and (c) Case III.

For the PDF obtained over the lateral wall, we see a similar behavior. Despite the difference in the instantaneous Sherwood fluctuations, when compared to its own RMS values, the probability density function remains close to one another. These are also close to the normal distribution behavior. It merits noticing that the bigger the velocity of the foam flow, the closer the behavior to the normal distribution function. This is also due to the increase in the wall shear stress and the non-influence of the liquid film thickness over this the diffusion limiting current.

Once the behavior of the PDF for a given case is recognized, the Standard Deviation, the Skewness and the Flatness factors must be determined for the polarographic wall velocity gradient, and relate them to the behavior of this previous curves and the Sherwood fluctuating signals, directly related to the velocity gradient. Figures 3.56 to 3.61 show the Standard Deviation, Skewness and Flatness factors of the polarographic instantaneous wall velocity gradients corrected using the Sobolik method, for all foam velocities and qualities.

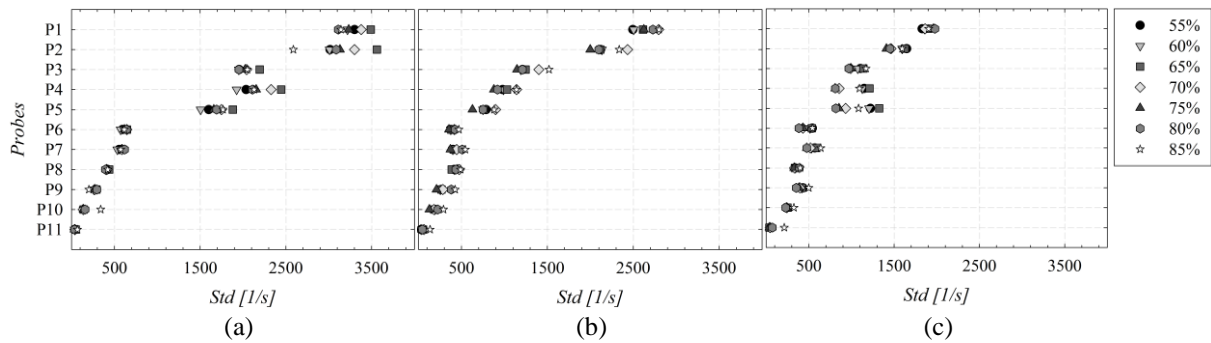


Figure 3.56 Standard deviations of the velocity gradients obtained with the polarographic probes over the lateral wall for all foam qualities and velocities: (a) Case I; (b) Case II and (c) Case III.

The Standard deviation values act as a mean representation of the amplitude of the fluctuations. From this point of view, larger fluctuations occur at the top of the channel, where the liquid film is thinner and the influence of the bubbles passage higher. At the bottom of the channel, there are no fluctuations for the polarographic velocity gradients and the value of the standard deviation tends to 0. As the velocity increases, so does –slightly- the value of the thickness of the slip layer, this lowers the amplitude of the fluctuations and the standard deviation.

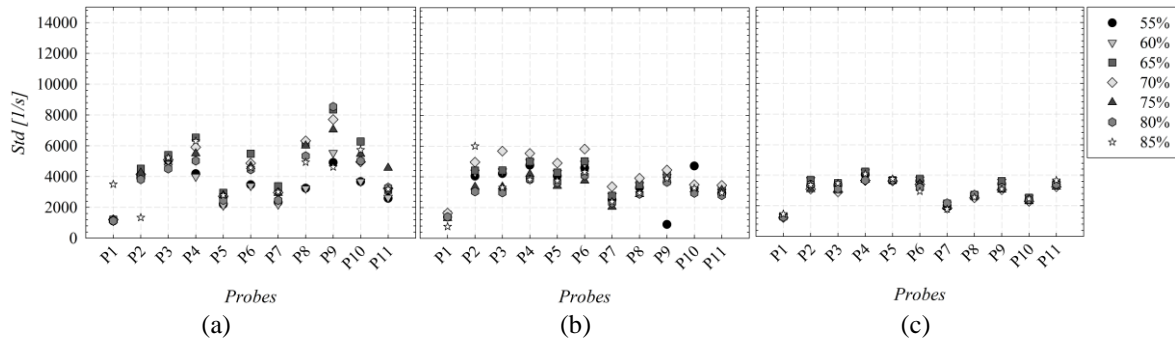


Figure 3.57 Standard deviations of the velocity gradients obtained with the polarographic probes over the top wall for all foam qualities and velocities: (a) Case I; (b) Case II and (c) Case III.

The Standard Deviation values, at the top of the channel, presented similar values, all along its length for the three cases. However, larger deviations occurred between the signals acquired at different probes for slower foam flows. As the foam velocity increases, so does the wall shear stress. From the theoretical study of the critical film thickness as a function of the wall shear stress, it can be seen that for bigger stresses the thickness of the slip-layer, where the diffusion limiting current is

achieved, is smaller. This explains the behavior of the standard deviation over the top wall, when the foam velocity increases the liquid film thickness and it no longer plays an important factor over the diffusion limiting current.

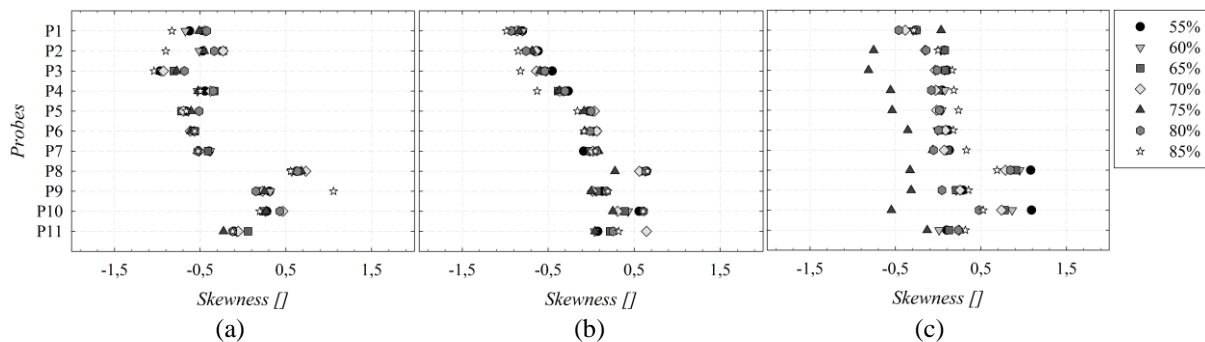


Figure 3.58 Skewness coefficients of the velocity gradients obtained with the polarographic probes over the lateral wall for all foam qualities and velocities: (a) Case I; (b) Case II and (c) Case III.

From the PDF point of view, the Skewness coefficient represents the asymmetry of the Gaussian curve. Negative skewness numbers for the turbulence inside the liquid slip-layer represent a homogeneous isotropic turbulence. Along the lateral wall, the Skewness tends to 0; fluctuating between the positive and negative values. At the top of the channel, it leans towards negative values, and the opposite near the bottom. This behavior was also seen at the PDF curves, where the Probe 1 (top side of the channel) presented a slightly longer tail at the left of the top of the Gaussian bell, while at the Probe 11 (bottom of the channel) both side of the curve present similar length.

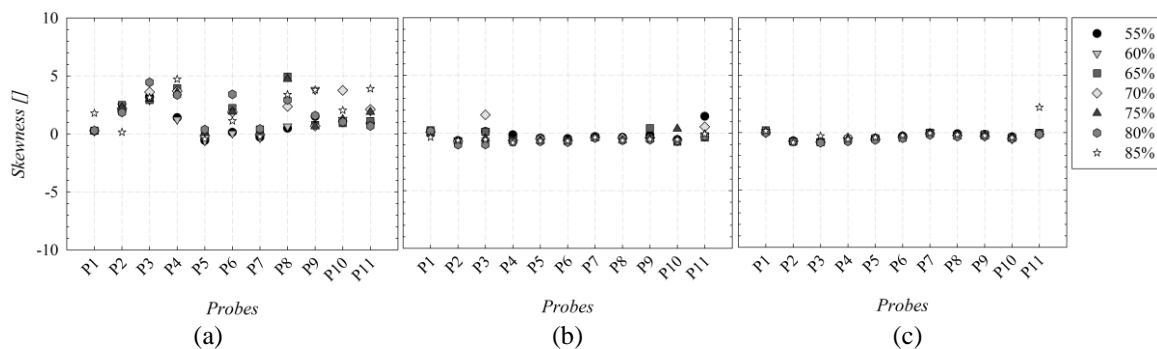


Figure 3.59 Skewness coefficients of the velocity gradients obtained with the polarographic probes over the top wall for all foam qualities and velocities: (a) Case I; (b) Case II and (c) Case III.

At the top of the channel, the liquid film mean thickness value is constant for all cases and qualities. However, the wall shear stress increases with the foam velocity. As seen with the standard deviation results, the Skewness along the top of the channel presents constant values for all cases, positions and qualities. Nevertheless, larger deviations between qualities are seen for slower foam. In these cases, the diffusion limiting current is more sensitive to smaller shear than to higher ones. The PDF curves showed the same behavior of small deviation between the length of the tails.

When analyzing the Sherwood fluctuations, a difference between the top and the bottom of the channel could be appreciated. The fluctuations at the top of the channel, where the liquid film is thinner, showed greater amplitude values than the ones near the bottom. In spite of this behavior, the flatness values remain the same; the PDF curves along the whole length of the lateral wall present the same height. For a unimodal distribution (those whose skewness is 0), which is close to our case, the kurtosis factor represents both the *peakness* of the distribution and the heaviness of its tail. However, it does not express how high the peaks are. It is a relationship between its fluctuation and RMS values,

making it dimensionless. Despite the difference seen in the Sherwood fluctuations and the liquid film thickness, the flatness for our three cases and qualities remain close to the same value 3, the flatness value for a normal distribution Gaussian function.

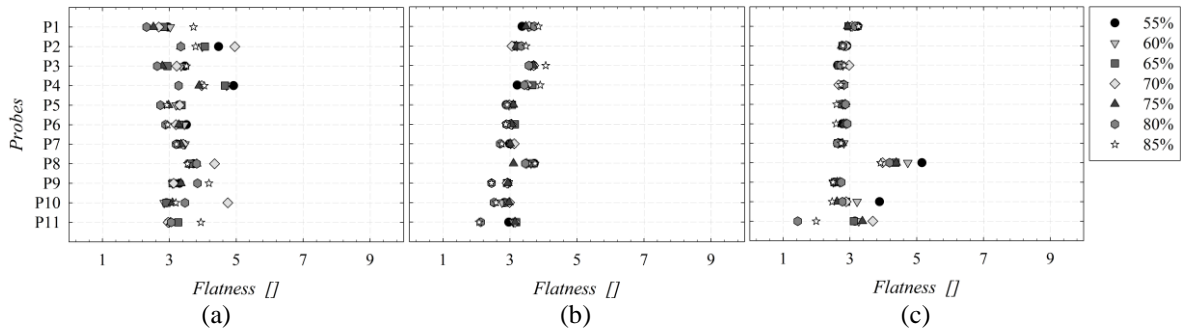


Figure 3.60 Flatness factors of the wall velocity gradients obtained with the polarographic probes over the lateral wall for all foam qualities and velocities: (a) Case I; (b) Case II and (c) Case III.

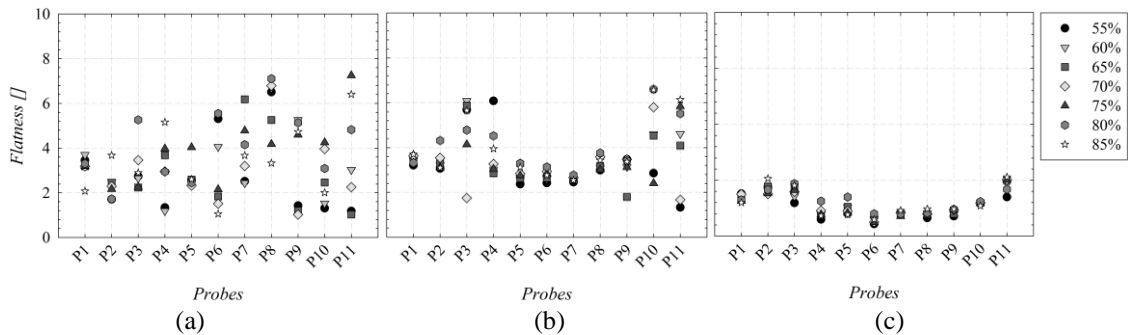


Figure 3.61 Flatness factors of the velocity gradients obtained with the polarographic probes over the lateral wall for all foam qualities and velocities: (a) Case I; (b) Case II and (c) Case III.

Finally, the values of the Flatness over the top wall of the channel present the same behavior as seen for the Skewness and the standard deviation. It can be said that they present similar values. However, bigger deviations are seen for the slower foam flows, due to the relationship between the wall shear stress and the diffusion limit current. Once the behavior of the polarographic signals and what they represent are analyzed, this method should be validated over aqueous foam flowing along a horizontal channel, and the comparison of the mean wall shear stress along the channel’s section.

1.6 Wall shear stress

A notable aspect of the foam flow is its capacity to generate wall shear stress values 2000 times bigger than the water under the same flow regime. There are many ways to measure the wall shear stress of a fluid inside a channel. It depends of the velocity gradient inside the viscous boundary layer and the pressure losses along a characteristic length. The pressure outlets located along the channel allow obtaining an accurate value of the pressure losses generated by the wall shear stress, and validating our other results and assumptions.

The wall shear stress can be obtained through the expression (Newtonian fluid inside the liquid film):

$$\tau(y) = \mu_l \frac{\partial u}{\partial y} \tag{3.20}$$

where μ_l is the liquid’s dynamic viscosity and $\frac{\partial u}{\partial y}$ is the wall velocity gradient.

Foam flow presents complex properties that makes it difficult to define the wall shear stress and the velocity gradient (opacity, reflections, small scales, etc.). We have followed three ways to obtain the mean wall shear stress over the channel's square section.

One way to obtain the wall shear stress of a horizontal foam flow is to assume that the velocity gradient is equal to the bubbles velocity over the channels wall, related to the thickness of the liquid slip layer ($\frac{u}{e} = \frac{\delta u}{\delta y}$). From this, equation 3.20 becomes:

$$\tau_{velocity} = \mu_l \frac{u}{e} \quad (3.21)$$

Figures 3.62 to 3.64 show the evolution of the wall shear stress, as a function of the bubbles velocities profiles (Figures 3.3, 3.4 and 3.5) and liquid film thicknesses (Figures 3.7, 3.12 and 3.13), over the lateral, the top walls of the channel, and the liquid/foam interphase.

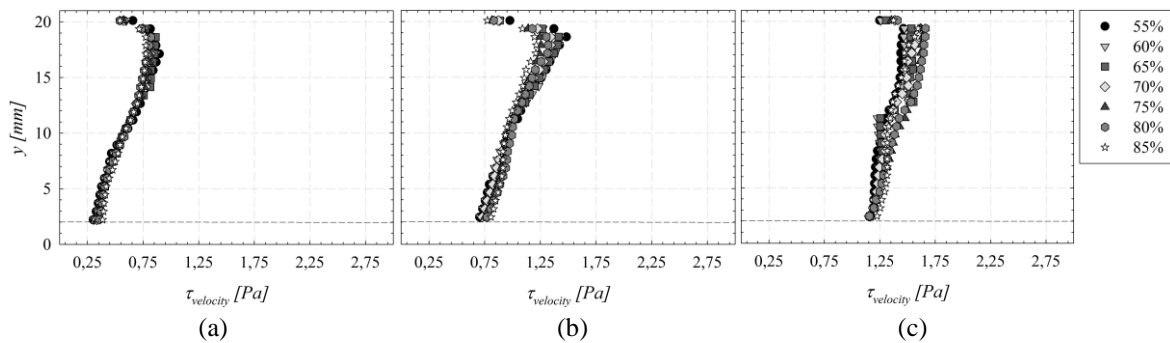


Figure 3.62 Wall shear stress obtained over the lateral wall with the velocity profiles and the liquid film thicknesses for all foam qualities and velocities: (a) Case I; (b) Case II and (c) Case III.

Reviewing the wall shear stress profiles at the lateral wall, it is concluded that the liquid film thickness exerts an important influence over the wall shear stress. Despite finding higher velocities values near the bottom of the channel, the largest wall shear stresses are located at the top. It is in this place where the mean liquid film thickness is thinner; this increases the overall wall shear stress value. However, despite the important influence of the slip-layer, the velocity does play a role in the wall shear stress value, as can be appreciated in faster foams. When the velocity increased the liquid film thicknesses does not vary much. However, higher wall shear stresses values occur in faster foam flows. These can reach the 1.75 Pa for the Case III, 1.5 Pa for the case II and 1 Pa for the Case I.

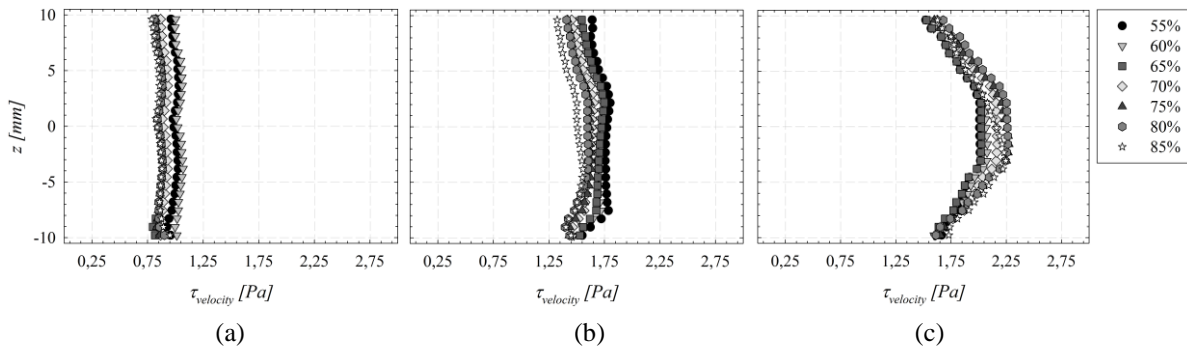


Figure 3.63 Wall shear stress obtained over the top wall with the velocity profiles and the liquid film thicknesses for all foam qualities and velocities: (a) Case I; (b) Case II and (c) Case III.

As for the top and bottom of the channel, the liquid film thickness doesn't influence the behavior of the wall shear stress that remains constant all along the length of the walls. In these sections of the duct, the velocity profiles must be reviewed. In both walls a constant wall shear stress

value occurs in cases I and II, following the behavior of the velocity profiles. However, when the foam flow reaches a three-dimensional state, Case III, the wall shear stress is also dependent of the z -coordinate and presents larger values near the center of the top channel.

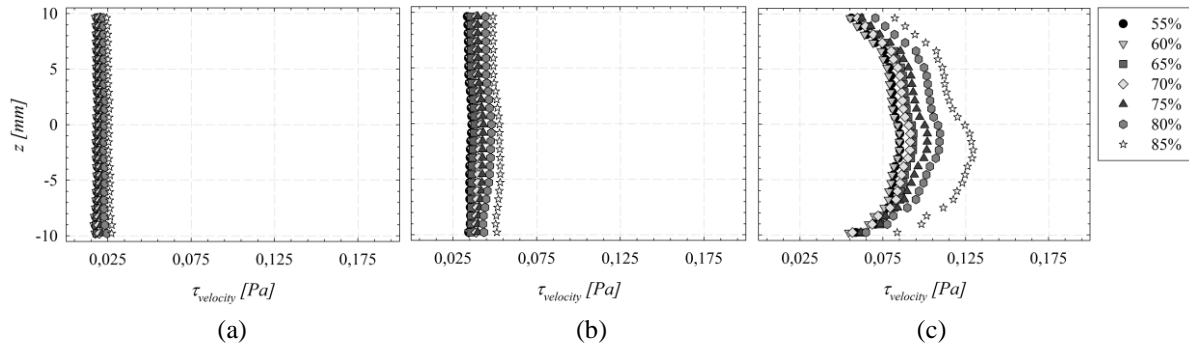


Figure 3.64 Wall shear stress obtained over the bottom wall with the velocity profiles and the liquid film thicknesses for all foam qualities and velocities: (a) Case I; (b) Case II and (c) Case III.

From the polarographic signals, we can deduct the mean wall shear stress values along the length of the channel's walls, through the diffusion limiting current:

$$\tau_p = \frac{\mu_l}{(0.633 z_e F c_\infty)^3 D^2 d_s^5} I^3 \quad (3.22)$$

It has been shown for a polarographic probe of diameter d_s , the mean values of the Sherwood number \overline{Sh} , the characteristics of the liquid, which are the dynamic viscosity μ_l and the diffusion coefficient D , the mean wall shear stress value, τ_p , can be obtained through.

$$\tau_p = \frac{\mu_l}{(0.633 z_e F c_\infty)^3 D^2 d_s^5} \frac{(z_e F c_\infty A D)^3}{l^3} Sh^3 \quad (3.23)$$

or:

$$\tau_p = \frac{\pi^3 \mu_l D}{8.95 d_s^2} Sh^3 \quad (3.24)$$

Figures 3.65 to 3.67 show the evolution of the wall shear stress along the lateral, top and bottom walls of the square channel cross-section for all cases and qualities.

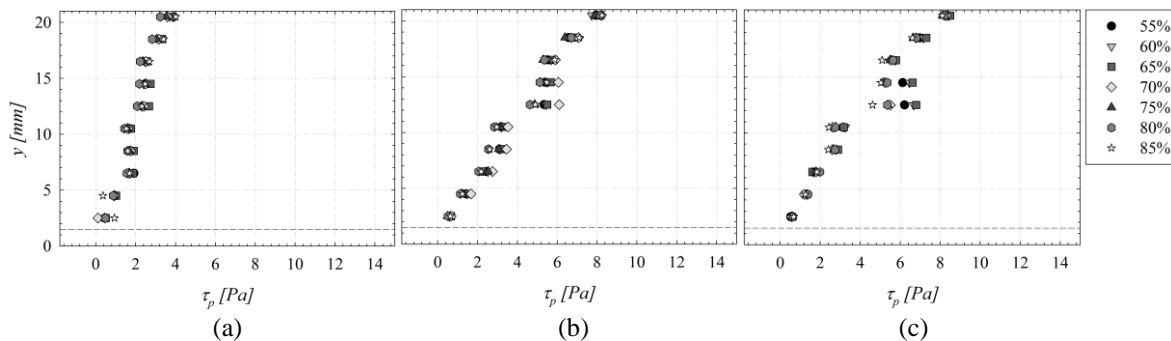


Figure 3.65 Wall shear stress obtained over the lateral wall with the polarographic probes for all foam qualities and velocities: (a) Case I; (b) Case II and (c) Case III.

These figures confirm the influence, of the liquid film over the wall shear stress. Higher shear stresses are obtained close to the top of the channel, where the liquid slip-layer is thinner. As for the velocity influence, faster foams present bigger wall shear stresses. However, at the bottom of the channel all of them tend to the zero value. Despite the similarities in the nature of the wall shear

stresses obtained with two different techniques (velocity profiles and polarographic method), the magnitude of the values is different. The polarographic results present a larger wall shear stress than the velocity profile ones.

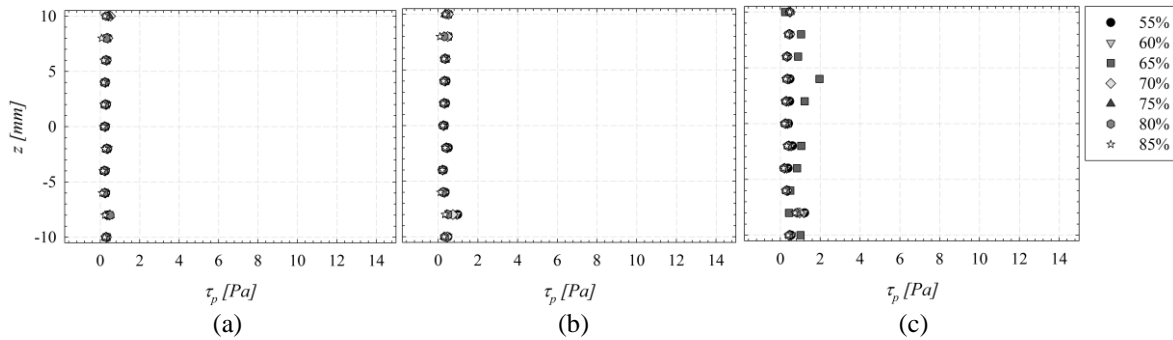


Figure 3.66 Wall shear stress obtained over the bottom wall with the polarographic probes for all foam qualities and velocities: (a) Case I; (b) Case II and (c) Case III.

The wall shear stress obtained from the polarography technique at the bottom of the channel present the similar constant values in all three cases and qualities, close to 0.5 Pa. In difference to the velocity profiles, they present a block profile, meaning that they are not influenced by the velocity profile at the wall. However, at the top of the channel there is a difference between wall shear stresses, despite the similarity of the liquid film thickness.

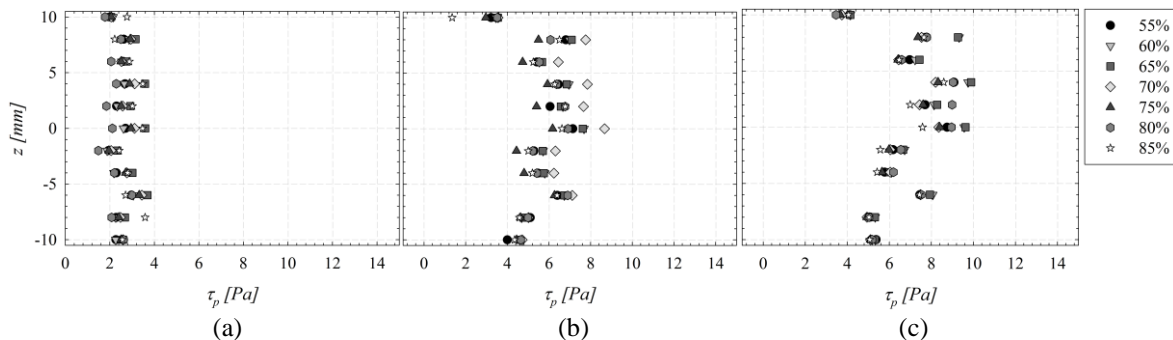


Figure 3.67 Wall shear stress obtained over the top wall with the polarographic probes for all foam qualities and velocities: (a) Case I; (b) Case II and (c) Case III.

At the top of the channel, the velocity profiles and the foam flow regime have significant implications for the foam flow. Slower foams, Cases I and II, present a constant wall shear stress profile (one and two dimensional regimes). An increase in the value of the wall shear stress can be seen for bigger velocities. As for the last case where the foam flow can be considered three-dimensional, and its profile depends on all three coordinates, we see higher stresses near the center of the channel, than at the sides.

The most reliable way to define the mean wall shear stress, along the channels surface, is through the pressure losses. They allowed obtaining the pressure gradient along the length of the channel. The pressure gradient for our different cases and qualities allow deducting the mean wall shear stress through the following relationship:

$$\bar{\tau} = \frac{\Delta P d_h}{L 4} \tag{3.25}$$

where $\frac{\Delta P}{L}$ is the pressure gradient and $d_h (= 21mm)$ is the hydraulic diameter.

These values were compared to the wall shear stresses obtained through the polarographic method and the velocity profiles, to validate these measurement techniques and assumptions. For the two cases the mean wall shear stress along the channel's surface was calculated through the following equation (here $\Delta y = \Delta z = 2 \text{ mm}$):

$$\bar{\tau} = \frac{1}{4n} \left[\sum_i^n \tau_{bottom_i} + 2 \sum_i^n \tau_{lateral_i} + \sum_i^n \tau_{top_i} \right] \quad (3.26)$$

The mean wall shear stress values obtained with the pressure losses, the velocity profiles, and the polarographic signals are shown in Figure 3.68 for all foam qualities and velocities.

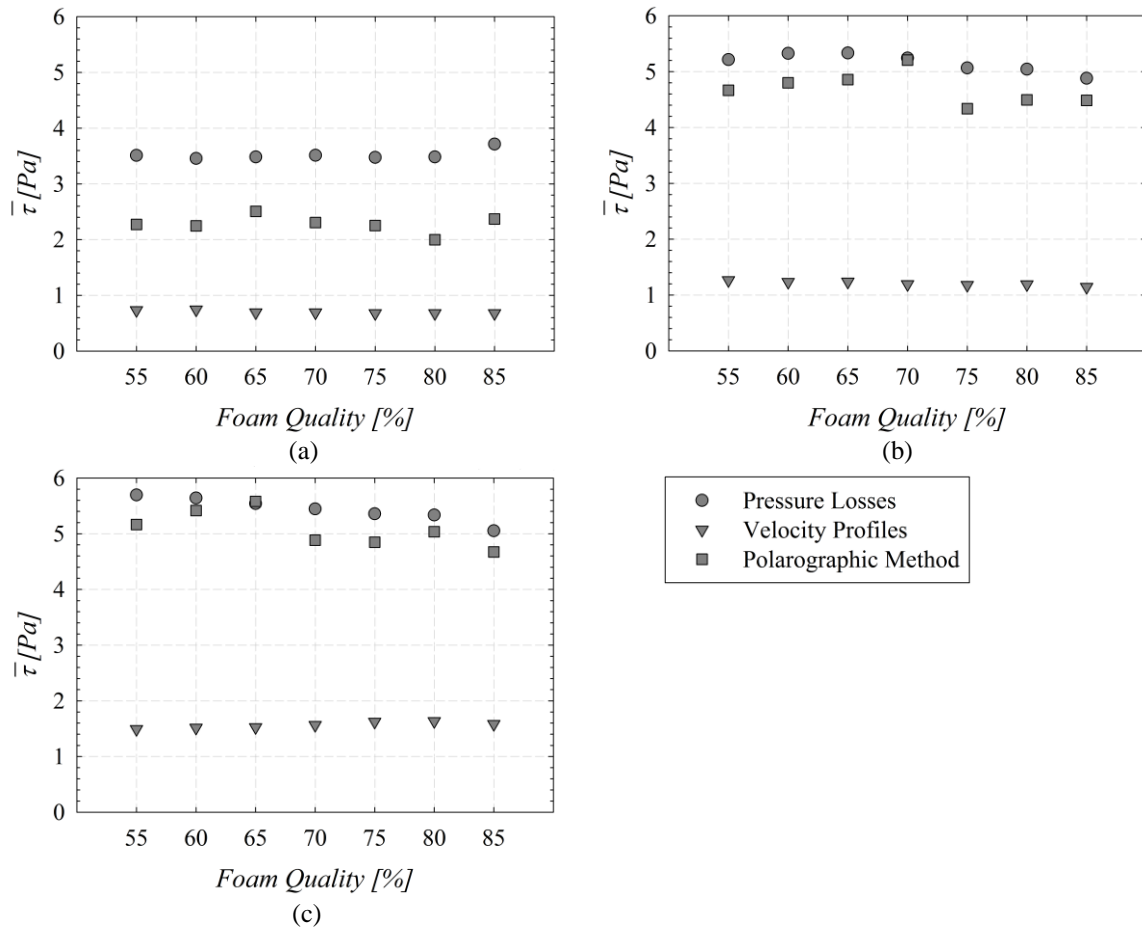


Figure 3.68 Mean wall shear stress along the square channel's surface for all foam qualities and velocities: (a) Case I; (b) Case II and (c) Case III.

The representation of the mean wall shear stress along the channel's surface, obtained with three different approaches (pressure losses, velocity profiles and Sherwood number signals), allows us to validate the polarographic method, for certain shears, and to discard the hypothesis of a velocity gradient related to the bubbles velocity over the slip-layer. To better understand the behavior of our mean shear stress value we refer to Figure 3.46, which relates numerically the wall shear stress, the diffusion limiting current and the liquid film thickness.

It can be noticed that the wall shear stress calculated using the velocity profiles near the wall is not accurate. This is because we assumed that the velocity profile inside the slip-liquid films presents a linear behavior for the bubbles velocity. In fact, the high turbulence seen from the polarographic results show that this velocity profile (inside the liquid layers) is higher than the assumed value. That is why a deviation is seen when compared this wall shear stress assumption to the other ones.

The influence of the wall shear stress over the diffusion limiting current is clearly defined. The area in which this one is reached is a function of the wall shear stress and the liquid film thickness (see figure 3.46). The conductimetry results showed that, despite the increase in the liquid quantities, the mean liquid film thickness evolution along the channels walls remains constant in all cases and qualities. However, from the pressure losses, it is denoted that the wall shear stress increases with the foam flow velocity.

All the cases present similar liquid film thickness evolution but different wall shear stresses. Slower foams are more susceptible to fall inside the region where the diffusion limiting current is not reached, and therefore not be able to measure the velocity gradient through the polarographic method. As the foam moves faster, the threshold between the two regions diminishes and the limit diffusion current will be reached most of the times. This phenomenon can be seen over the mean shear stress comparison; as the foam velocity increases, the polarographic values resemble more to the pressure losses ones; which are the most credible.

The largest gap between the polarographic method and the pressure losses is of 43% for the Case I, and wall shear stress values around 2 and 4 Pa fluctuating between the two regions, making less accurate the velocity gradient calculation. For the Case III the deviation is reduced to 10%, the wall shear stress tends to 5.5 Pa; and the diffusion limiting current is reached most of the time.

Also, as seen before, bubbles' passage directly influences the liquid film thickness, which will alter the concentration evolution near the electrodes (Figure 3.69).

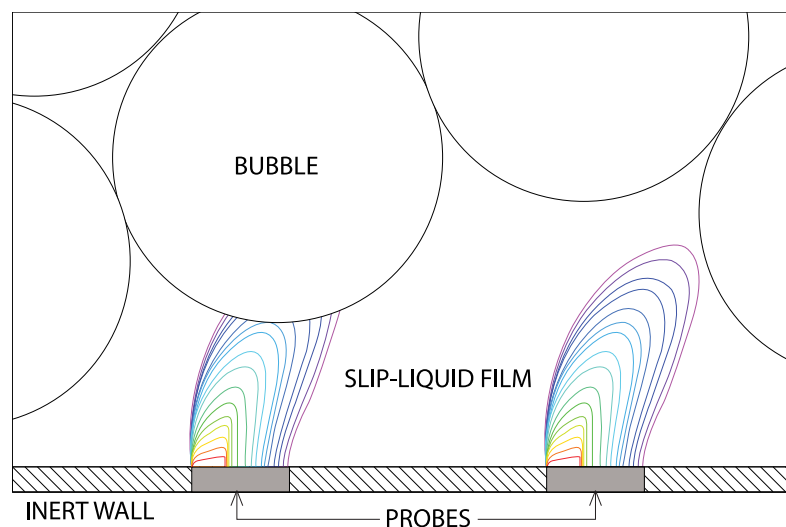


Figure 3.69 Influence of the bubbles passage over the isoconcentration lines on the electrochemical electrodes

Taking this into consideration, a numerical solution of the dimensionless concentration over the (x, y) plane, and its 3D representation, is shown for a wall shear stress of 2 Pa and influenced by the passage of a bubble over the electrochemical electrode, diminishing the characteristic length ($Y = 2.5$) (Figure 3.70 and Figure 3.71). It shows that the concentration evolution is not fully developed when a given bubbles passes and diminishes the liquid film thickness under a critical value.

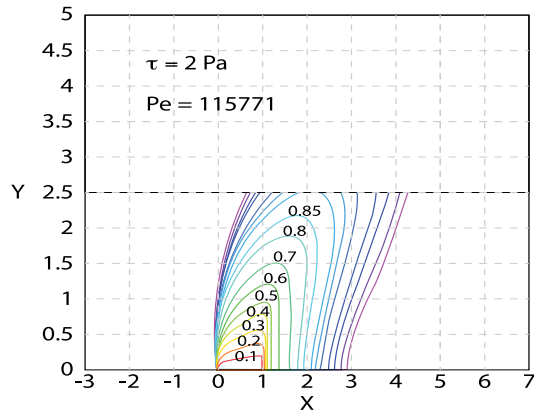


Figure 3.70 Iso-concentration lines for $Y=2.5$ (obtained numerically)

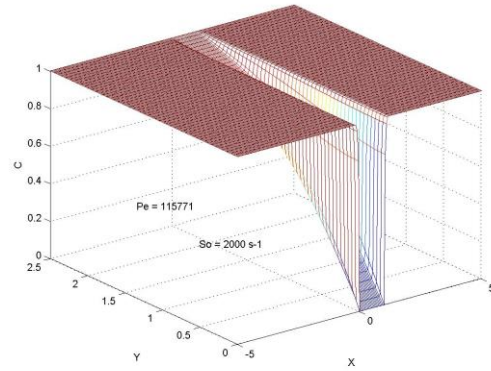


Figure 3.71 Evolution of the Concentration “C” in three-dimensions for $Y=2.5$ (obtained numerically)

The sensitive study done for the critical characteristic length is represented in Table 3.1. This one alters the concentration evolution over the electrochemical probes, when influenced by the liquid film fluctuations and the wall shear stress generated by our three foam regimes. Analyzing them, we realize that slower foams are more sensitive to the thickness fluctuations, because they present bigger critical characteristic length.

$\bar{\tau}_p$ [Pa]	S [1/s]	Pe []	$Y = e/\delta_c$ []	e_{crit} [μm]	e_{min} obtained [μm]
3.5	3512	205613	4.35	15.1	15.14
5.2	5148	301341	3.86	11.8	10.86
5.4	5427	317699	3.73	11.2	10.12

Table 3.1 Sensitive study of the Peclet number and critical thickness of the mass boundary layer in order to attain a diffusion limiting current.

As for the assumption that the bubbles velocity over the slip-layer is equal to the velocity gradient at the wall, it has been shown not to be correct, despite the precision of the measurements. The wall shear stresses are far away from the ones calculated through the pressure losses and the polarographic results. The values do increase with the foam velocity, but they are 5 times smaller than the real ones, at the worst case. It means that the wall velocity gradient is steeper than the velocity profiles obtained through the PIV method.

1.7 Conclusions

The measurement of the static pressure, the velocity profiles, the liquid film thickness and the wall shear stress allowed us to understand the hydrodynamic behavior of the foam flow through a straight channel for three different velocities and seven foam qualities. From pressure outlets located all along the channel’s length, we defined the pressure losses. They are directly related to the foam velocity and are not influenced by the foam quality. Higher velocity generates higher pressure gradient.

Using the Particle Imaging Velocimetry (PIV), we were able to determine the local axial velocity of the foam over the periphery of the flow at the top wall, lateral wall and liquid/foam interphase. However, the velocity fields inside the liquid film, located between the bubbles and the walls, could not be properly defined. The slip-layer presents micro-thicknesses, which are hard to analyze by the PIV. To examine the flow at the bottom of the channel, with the biggest thickness, it would have been necessary to add Polyamide seeding particles to track the liquid flow. However,

adding these particles alter the properties of the foam and its rheological properties. The axial velocity profiles allowed us to verify the three foam regimes described by previous works.

The liquid film thickness along the lateral wall, obtained with conductimetry probes, evidences the gravitational drainage of the foam. The top liquid slip-layer thickness remains uniform along the wall. Despite the difference in liquid quantity for the different cases and qualities, thickness remains constant through all fabrication foam conditions. The Standard Deviation, the Skewness and Flatness factors confirm the difference between these fluctuating signals that look similar, especially along the lateral wall, when the probe is closer to the liquid/foam interphase, the amplitude fluctuations diminishes. At the top of the channel, this statistical study shows the presence of larger bubbles near the center of the channel and smaller at the sides. The only important influence of the foam quality over the slip-layer is at the bottom of the channel, where wetter foams present thicker liquid films.

Finally, the polarographic method was verified. Polarographic currents were acquired for all cases and qualities. From these currents, we were able to calculate the velocity gradient and do a statistical analysis that allowed a better understanding of the micro-turbulences inside the liquid film thickness. At the bottom of the channel, the signals are uniform all over the probes. But, when in contact with the foam (lateral and top wall) the signals fluctuate in the same way as the conductimetry ones, which are a function of the positioning of the probe. Along the lateral wall, the probes closer to the top present signals with bigger fluctuation than the ones at the bottom.

To evaluate the use of the polarographic method, the wall shear stress obtained was compared to that one calculated through the pressure losses and the velocity profiles, assuming that the velocity of the bubbles passage over the liquid slip-layer (obtained with the PIV method) is proportional to the velocity gradient. These results, validated the use of the polarographic method in the case of foams that present velocities over 6 cm/s, they generate higher wall shear stresses and are not dependent on the thickness of the liquid film to reach a limit diffusion current. As regards to the wall shear stress obtained through the velocity profiles and film thicknesses, their values were far away from the most reliable ones obtained through the pressure losses measurement; due to the non-linearity between the velocity and the wall shear stress via the liquid film thickness.

2. Foam flow along a horizontal straight channel with FDD

Our characterization of foam flow along a horizontal straight channel with no FDD (obstacles) allowed us to better understand certain aspects of the phenomenon. Factor that showed interest were the slip-layer thickness, the different foam regimes, and the high wall shear stress that it can create. We were also able to review the rheological properties and visco-elasto-plastic behavior that foams present. For all our cases and qualities, we made our aqueous foam flow through three different FDD (half-sudden expansion, fence and cylinder) that allowed a better appreciation of this intricate fluid (Figure 3.72).

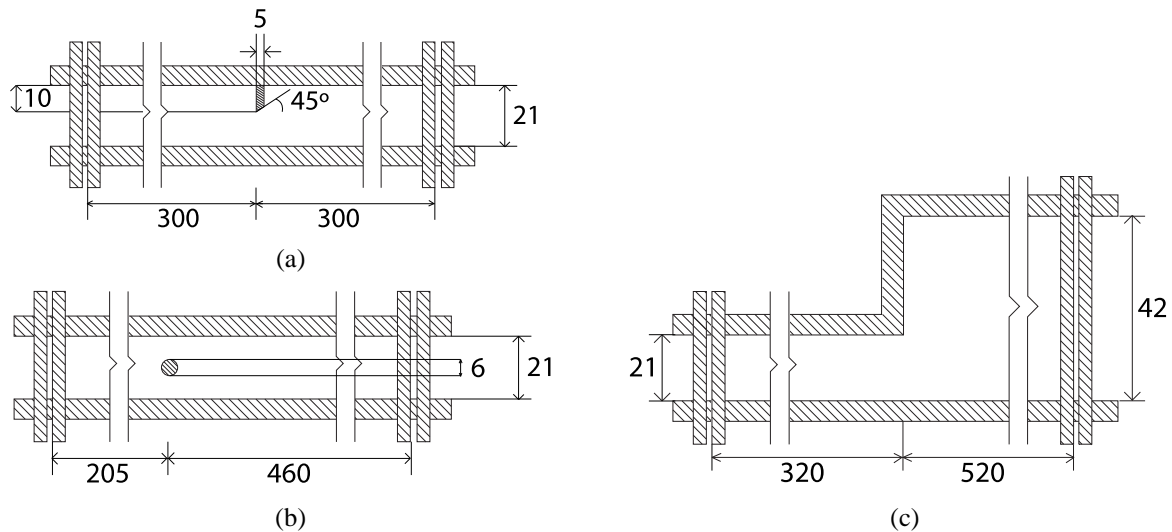


Figure 3.72 Lateral schematic representations of the three fdd: (a) fence; (b) cylinder and (c) half-sudden expansion (dimensions in mm)

2.1 Validation of the velocity profile upstream the disruption devices

To evaluate the rheological behavior of the foam flowing through the three FDD, we had to verify the similarity of the velocity profiles, for all our foam qualities, before passing across the half-sudden expansion, the fence and the cylinder, for each case. Figure 3.73 represents the velocity profiles upstream ($x = -35 \text{ mm}$) of the three FDD configurations for all cases and qualities.

The similarities for the three cases of FDD are shown in Figure 3.73. The behaviors of the velocity profiles remain analogous for qualities in each case. They exhibit a block piston effect for foam flows of 2 cm/s , with an increase in the bubbles velocities close to the bottom slip-layer for cases II and III. There are some differences between the three FDD, especially at higher velocities. Together with the visco-elasto-plastic properties of the foam: the half-sudden expansion, the fence and the cylinder affect the upstream velocity profiles. The FDD create a first barrier for bubbles that make a “stagnant” cover, altering the velocity of other bubbles passing through and connected to them. This creates a domino effect that will influence the characteristics along the whole channel’s length. Henceforth, in the case of the fence, the velocity near the top of the channel is smaller than the one for the cylinder and the half-sudden expansion. We can conclude that the foams properties are similar for all cases and qualities, before going through the half-sudden expansion, the fence and the cylinder obstacles.

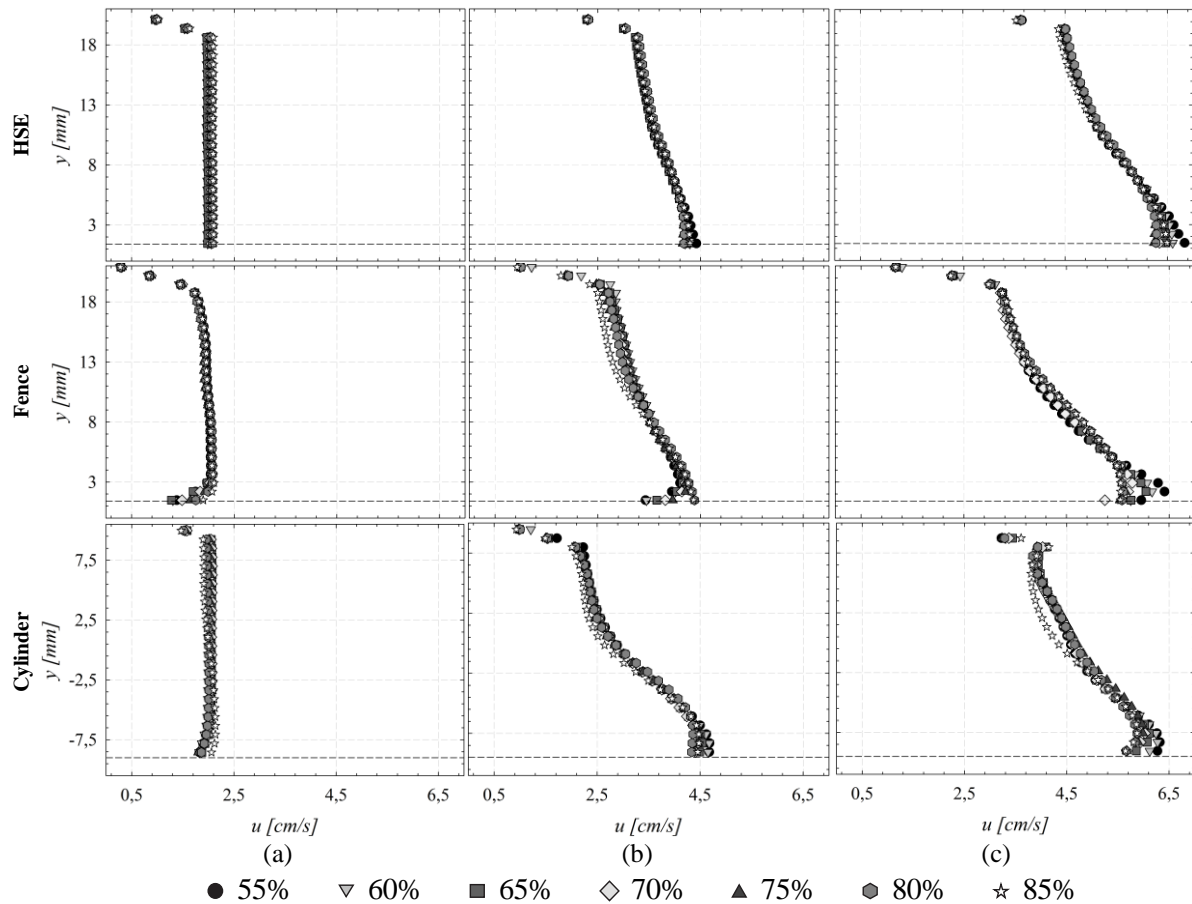


Figure 3.73 Axial velocity profiles upstream of the three FDD at $x = -35\text{mm}$ for all qualities and cases: (a) case I; (b) case II and (c) case III

2.2 Pressure losses and pressure gradient

As seen for the case with no FDD present, the wall shear stress generated by foam flow is one of the most important concepts reviewed by this study. It can be directly related to the longitudinal pressure gradient obtained through a series of pressure outlets all along the channel's length. Figures 3.74 to 3.76 present the pressure losses along the channels' length for the three FDD, all studied cases and foam qualities.

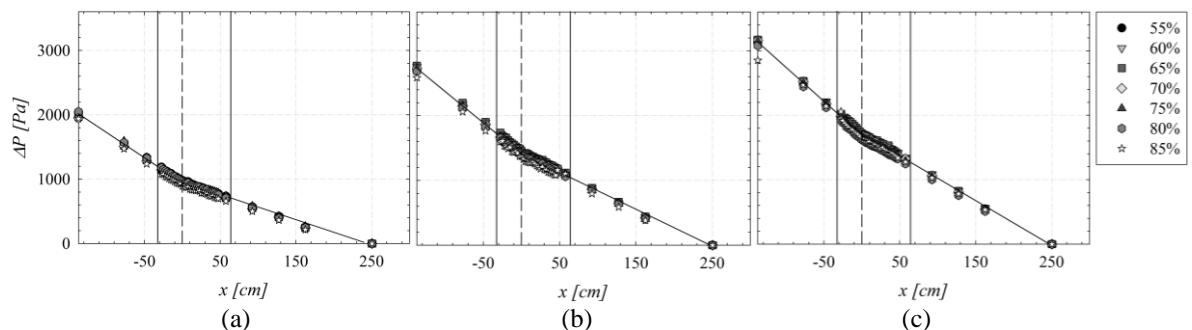


Figure 3.74 Evolution of the static pressure along the test channel with a Half-Sudden Expansion for all foam qualities and cases: (a) case I; (b) case II and (c) case III.

The half-sudden expansion results would show that there is no difference between foam qualities, as they all resemble one and other for each case. However, as the velocity of the foam increases, there is a noteworthy change in the pressure values. Faster foam flows are associated to larger pressure losses and gradients. An interesting aspect that can be appreciated is that the static

pressure varies linearly upstream and downstream of the FDD located at 0 (x coordinate). In the vicinity of the FDD, we see a transition from one state to another that affects the pressure gradient.

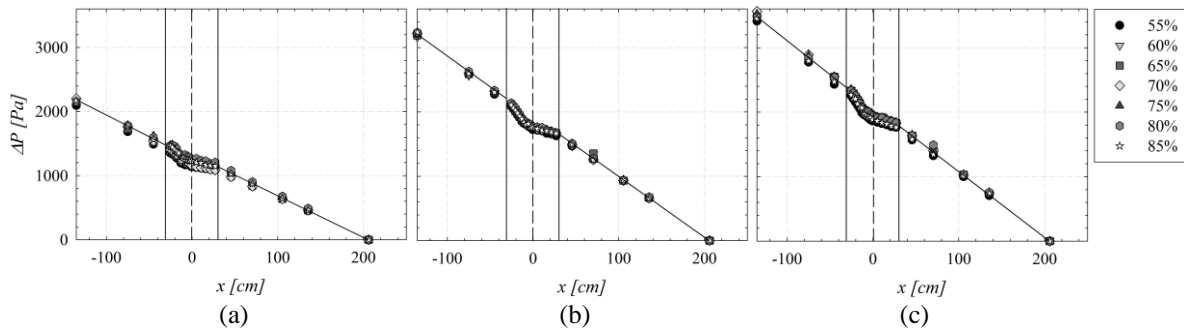


Figure 3.75 Evolution of the static pressure along the test channel with a Fence for all foam qualities and cases: (a) case I; (b) case II and (c) case III.

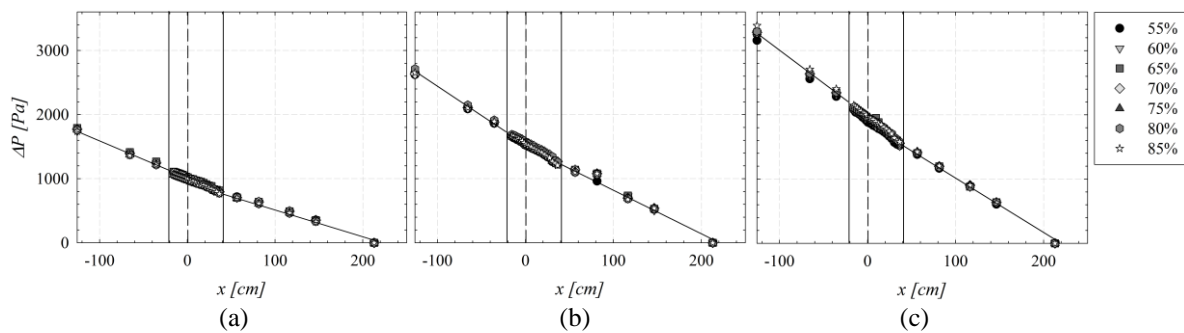


Figure 3.76 Evolution of the static pressure along the test channel with a Cylinder for all foam qualities and cases: (a) case I; (b) case II and (c) case III.

For the fence and the cylinder, the static pressure losses have a similar behavior than those at the half sudden-expansion fdd. There is no difference once the foam quality changes. When the velocity of the foam increases so do the pressure losses and pressure gradients. Also, there is a linear pressure loss upstream and downstream of the fdd, and a transition from one state to another near its vicinity, especially at the fence. However, the change in pressure seems to depend on the fdd and the channel's surface. In the case of the fence and the cylinder, the pressure gradients at both side of the obstacle are near the same value. To better understand the consequences and behavior of this phenomenon, we represent in Figures 3.77 to 3.79 the pressure gradients upstream and downstream of our three FDD for the different cases and foam qualities.

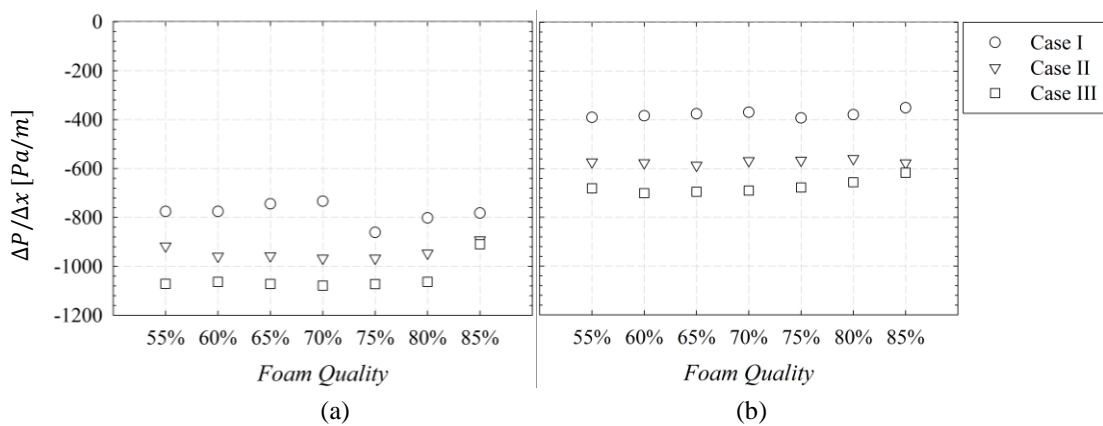


Figure 3.77 Pressure gradient for all foam qualities and cases: (a) upstream and (b) downstream of the half-sudden expansion

The pressure gradient shows to be more significant upstream of the half sudden expansion, than of its downstream, in all cases and qualities. This difference is essentially caused by the variation of the channel's section. As the flow goes through the fdd, there is a change in the foam's texture and structure, as a product of the bubbles reorganization and phase separation (forced gravitational drainage and coalescence). The same behavior can be seen in the other cases (4 cm/s and 6 cm/s), and upstream of the half-sudden expansion the pressure gradients are more significant than downstream. Regardless of the foam quality, this energy degradation stays constant for a given foam flow case, at both sides of the fdd.

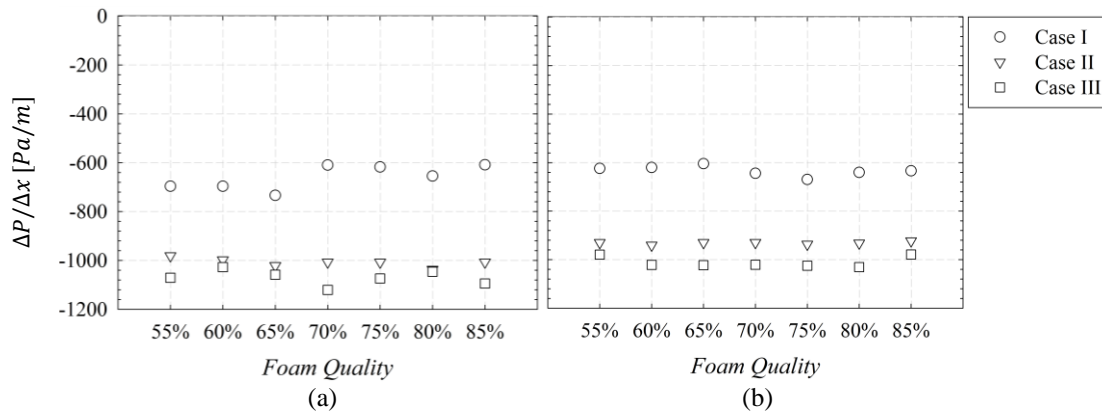


Figure 3.78 Pressure gradient for all foam qualities and cases: (a) upstream and (b) downstream of the fence

Despite the important influence that the fence had over the static pressure losses, these results show the similarity of the pressure gradient at both side of the fdd. In all the cases, the foam qualities present similar values upstream and downstream of the fdd. The difference between them is not as large as the one seen on the half-sudden expansion. Yet, there is a difference in the three cases: faster foams generate higher pressure losses and gradient.

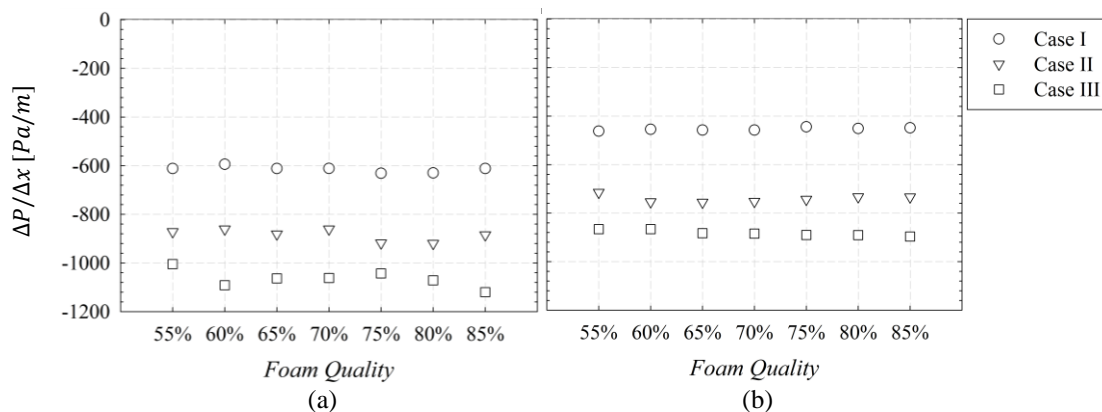


Figure 3.79 Pressure gradient for all foam qualities and cases: (a) upstream and (b) downstream of the cylinder

In the case of the cylinder, it may be considered as an in-between case. Having the same constant value for all foam qualities, there is an effect of the flow restriction over the difference of pressure gradients of its upstream and downstream. This influence is not important as that created by the half sudden expansion, and more than the one by the fence. A constant characteristic of all our pressure gradients, with and without fdd, is their increase in value as the foam moves faster.

The significant pressure gradient evolution induced by the half-sudden expansion is mostly related to change of the channel's section (two-times larger). Nevertheless, both the fence and the cylinder present the same dimensions along the whole length of the ducts. Despite of that, they do present a difference in the behavior of the pressure losses upstream and downstream of the fdd. This led us to consider the direct influence of the fdd over the foam flow. To better understand these observations, a study was carried on the velocity of field -for all our cases and qualities- with the help of the Particle Imaging Velocimetry system (PIV), over the lateral wall of the three fdd.

2.3 Local averaged velocity fields

The local average axial and vertical velocity fields and profiles were defined for all cases and qualities. They are obtained over the lateral wall of the three fdd. Analyzing the half-sudden expansion, the fence and the cylinder separately allow isolating the rheological changes that the foam may present when alternating its laminar flow with geometrical variations.

2.3.1 Half sudden expansion

The half-sudden expansion fdd is located at 1.35 m from the foam generators exit. It presents a expansion of its cross-section surface, from $21 \times 21 \text{ mm}^2$ to $21 \times 42 \text{ mm}^2$. This duct expansion generates a mechanical energy loss over the fluid that passes through it. This was seen for the pressure gradient evolution. Figures 3.80 to 3.82 represent the average axial and vertical velocity fields of the foam flow for all cases and qualities going across the half-sudden expansion for 500 PIV images.

The mechanical and rheological properties of the foam make it expand and fill the whole channel's height. In the immediate upper vicinity of the channel's expansion, the foam moves slower and can even stagnate creating a stagnation region, with a mean axial and vertical velocity of zero. Upstream of this fdd, the average axial velocity becomes lower.

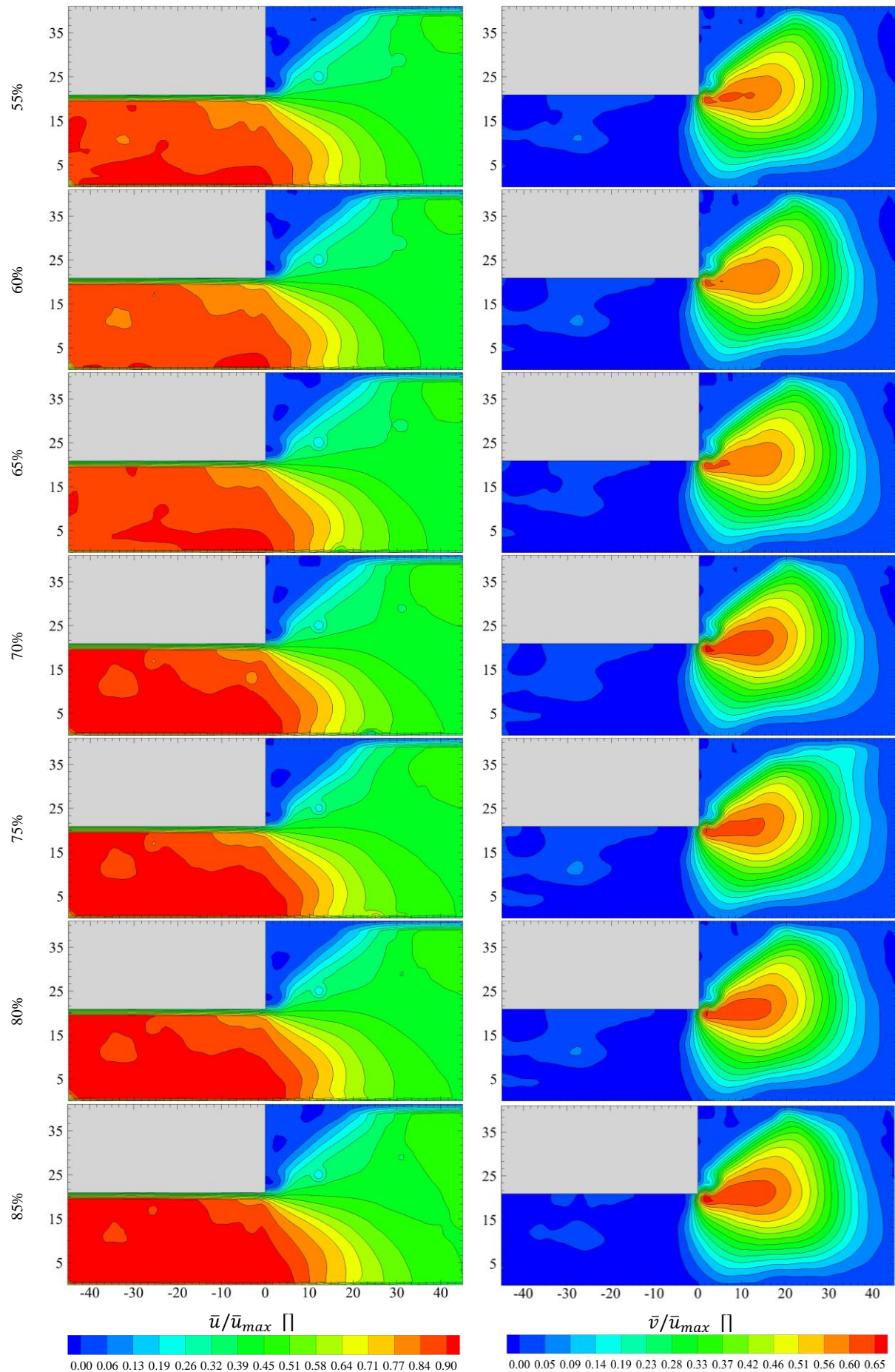


Figure 3.80 Averaged axial and vertical mean velocity fields for all qualities and the case I over the half-sudden expansion.

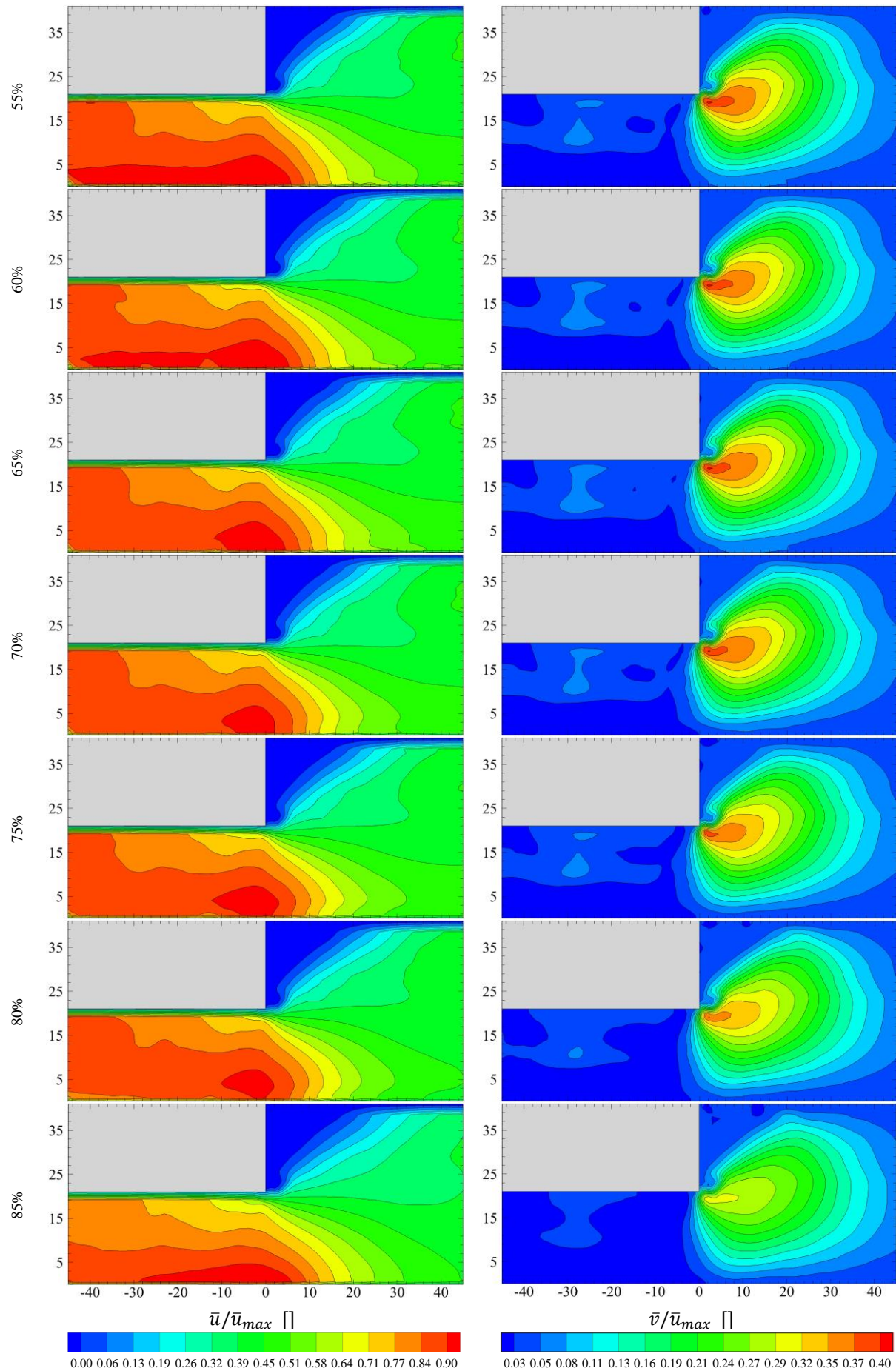


Figure 3.81 Averaged axial and vertical mean velocity fields for all qualities and the case II over the half-sudden expansion.

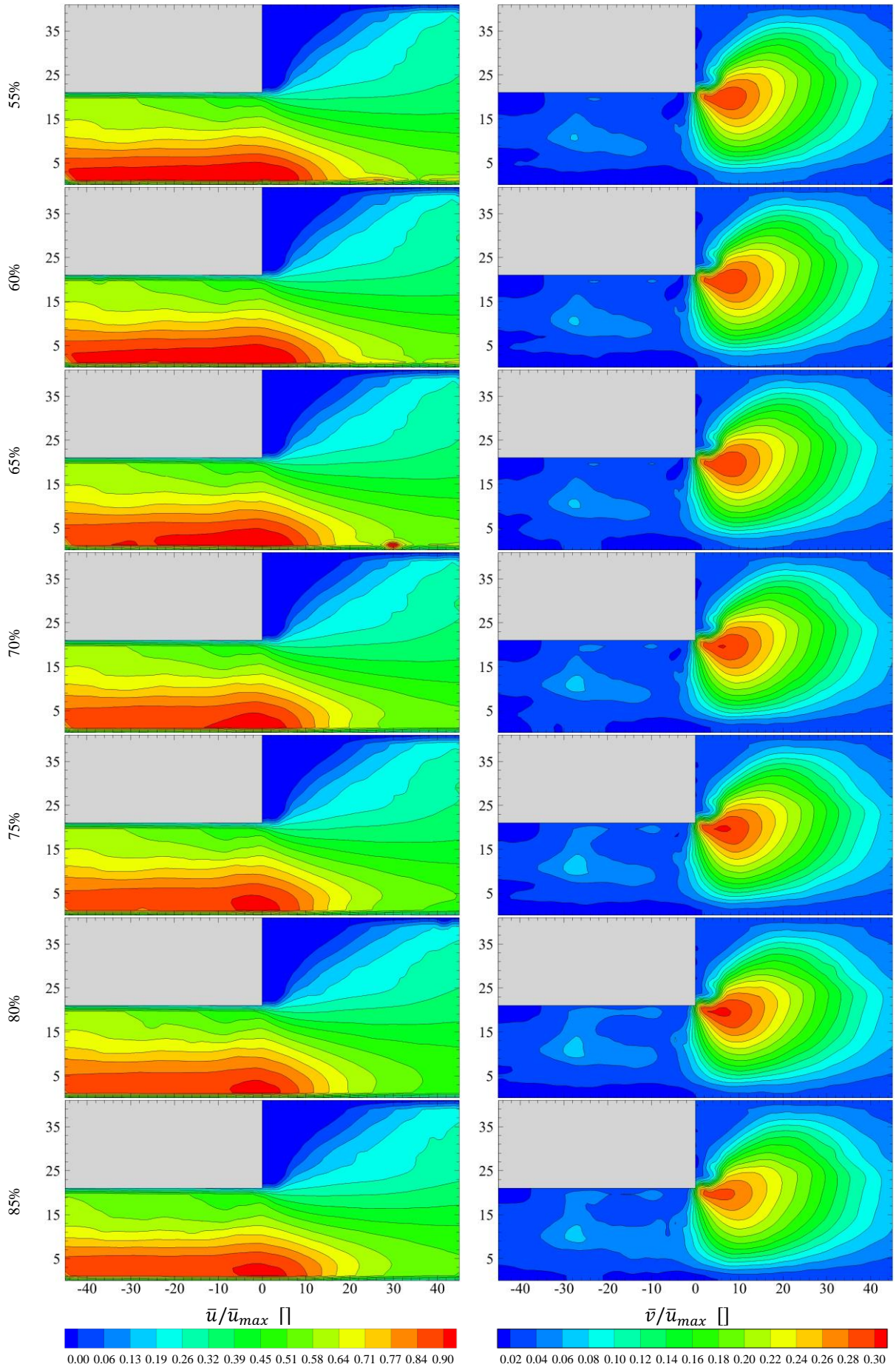


Figure 3.82 Averaged axial and vertical mean velocity fields for all qualities and the case III over the half-sudden expansion.

The flow can be evaluated in three zones: upstream of the fdd, where the foam maintains the same velocity profile until reaching the expansion, a transition zone, where there is an evolution of the foam properties and it goes from one state to the other after the fdd, and downstream of the fdd, where the foam recovers a constant velocity profile until the end of the channel.

The average axial velocity fields validate at the fdd the presence of the three flowing foam regimes over horizontal straight ducts. Case I presents a piston flow before entering the fdd, with a uniform axial component in the flow direction. As the velocities increases, the axial velocity component of cases II and III, upstream of the fdd, depend on the y coordinate. For these two cases, the maximum velocity is achieved near the bottom of the channel where the liquid slip layer presents a higher velocity and drags the bottom bubbles with it. There is no significant difference between foam qualities; they all behave the same when faced against the half-sudden expansion.

The average vertical velocity fields show the gravity influence over the foam and the path it takes to fill the whole channel's height. All cases and qualities present a similar behavior. As soon as the flow enters into the restriction, its low density is influenced by the expansion, which makes it raise to the top of the channel; accelerating its vertical displacement and increasing its velocity. Therefore, the maximum average vertical velocity is obtained in the immediate vicinity of the half-sudden expansion where the bubbles raise faster. Once through the fdd, the foam is no longer influenced by the expansion and it returns to the first flow regime, where its velocity only depends on the axial component and the vertical one is zero.

The velocity fields allowed us to evaluate the influence of the half-sudden expansion over the foam flow, for all our cases and qualities. We carried out a more detailed study of the behavior of the foam flow when going through the fdd. This will be done with the evolution of the axial and vertical velocity profiles along the x -coordinate in the vicinity of the half-sudden expansion for different positions (Figures 3.83 to 3.85). As for the velocity fields, these profiles were obtained only over the lateral wall of the channel due to the opacity of the foam.

From the mean axial velocity profiles for all cases and qualities, we considered a foam flow that maintains its axial component upstream of the fdd until reaching the half-sudden expansion. Once it reaches the expansion, the foam starts to fill the whole height of the channel diminishing its velocity until reaching a balanced state, and keeping it, until the outlet of the channel, and into the recovery tank. The maximum value (\bar{u}_{max}) of the foam is obtained upstream of the fdd with a value of 2 cm/s, for the case I with a piston flow, 4 cm/s, for the case II, and 6.5 cm/s, for the case III. For these last two cases, the fastest velocity occurs near the bottom of the channel, where the influence of the liquid slip-layer is more important. The inexistence of negative axial velocity components over the stagnation zone, in the vicinity downstream of the fdd, indicates that there is no back flow, or vortices in the opposite direction to the main stream. This is mainly due to the yield stress, at this point the velocity of the foam reaches a value close to zero, therefore the yield stress is not reached and the foam remains stagnated inside this region. A similar behavior is seen for the other obstacles.

For the vertical velocities, the mean values are important near the downstream vicinity of the half-sudden expansion. The expansion accelerates the flow in the vertical coordinate once it reaches it. Due to the density of the foam, it raises with a positive vertical velocity. The maximum values are 0.6, 1.4 and 1.7 cm/s for cases I, II and III respectively. The important vertical velocities in the immediate vicinity of the fdd are related to the upward movement of the flow trying to occupy the rest of the duct. Zero values are obtained upstream of the fdd where the foam flow is only influenced by its axial movement. After a certain distance, downstream of the fdd, the vertical component returns to a null value when a fully developed flow is reached. This flow does not present vertical component.

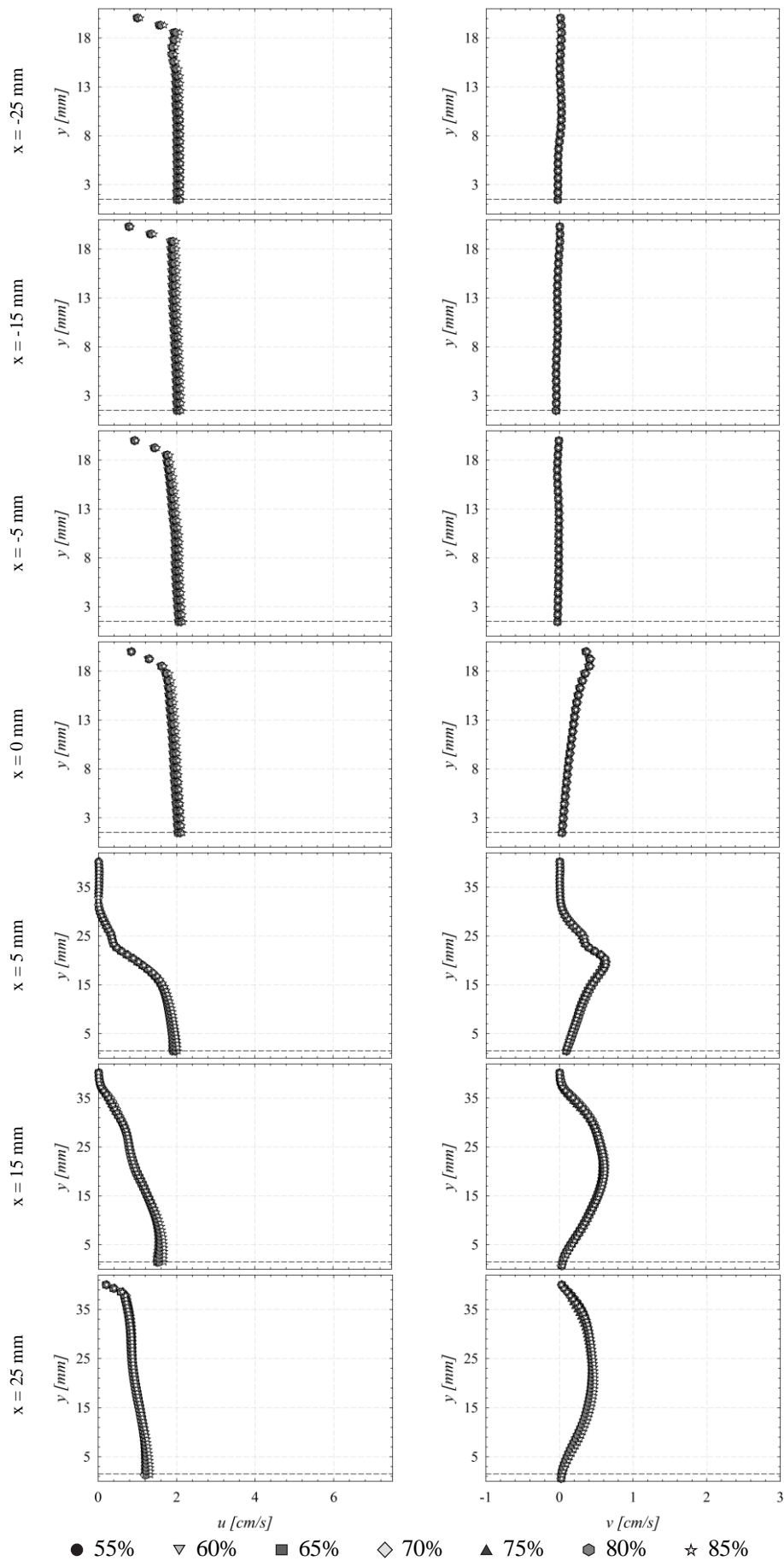


Figure 3.83 Averaged axial and vertical mean velocity profiles for all qualities, the case I and different distances over the half-sudden expansion.

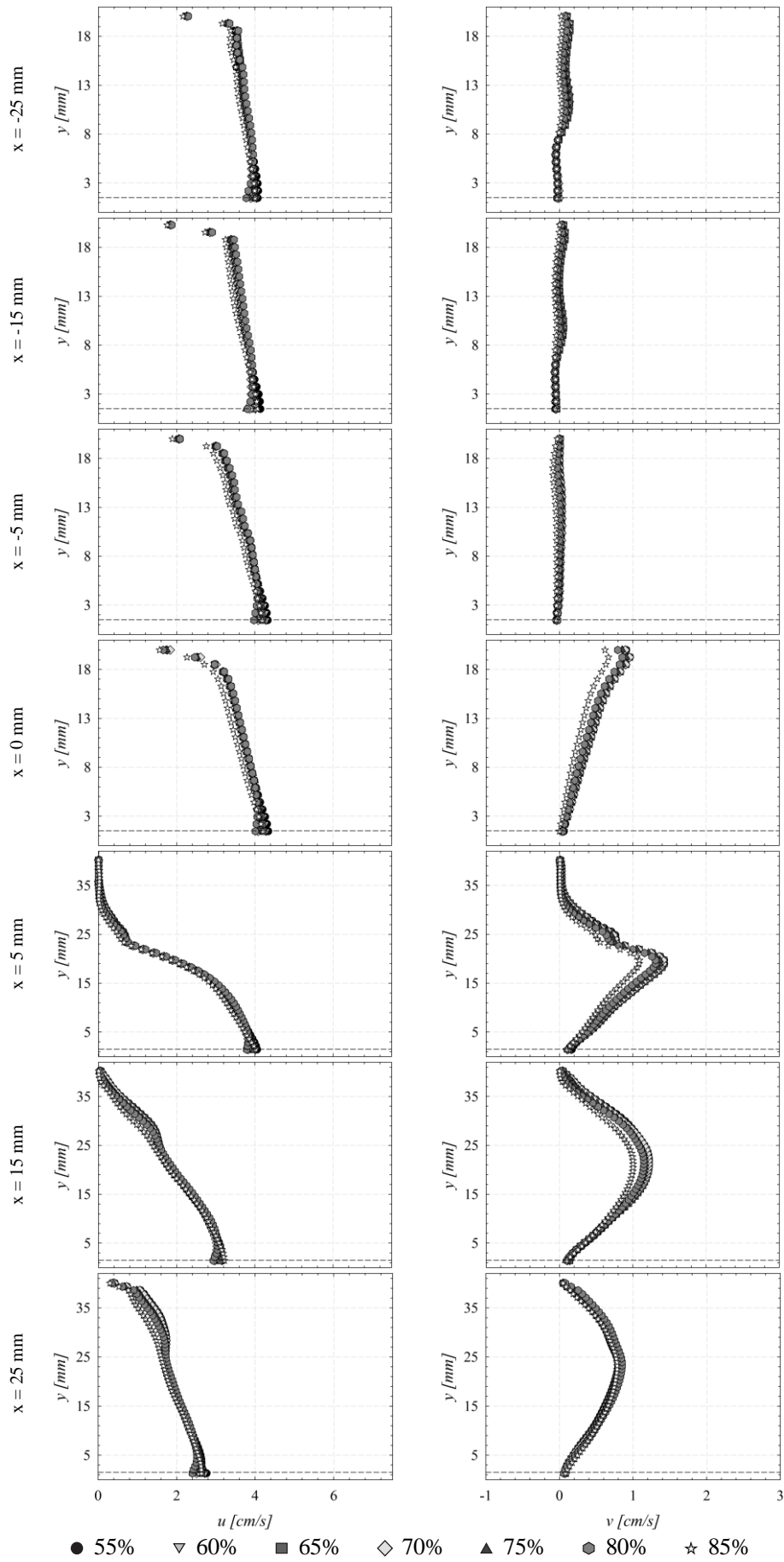


Figure 3.84 Averaged axial and vertical mean velocity profiles for all qualities, the case II and different distances over the half-sudden expansion.

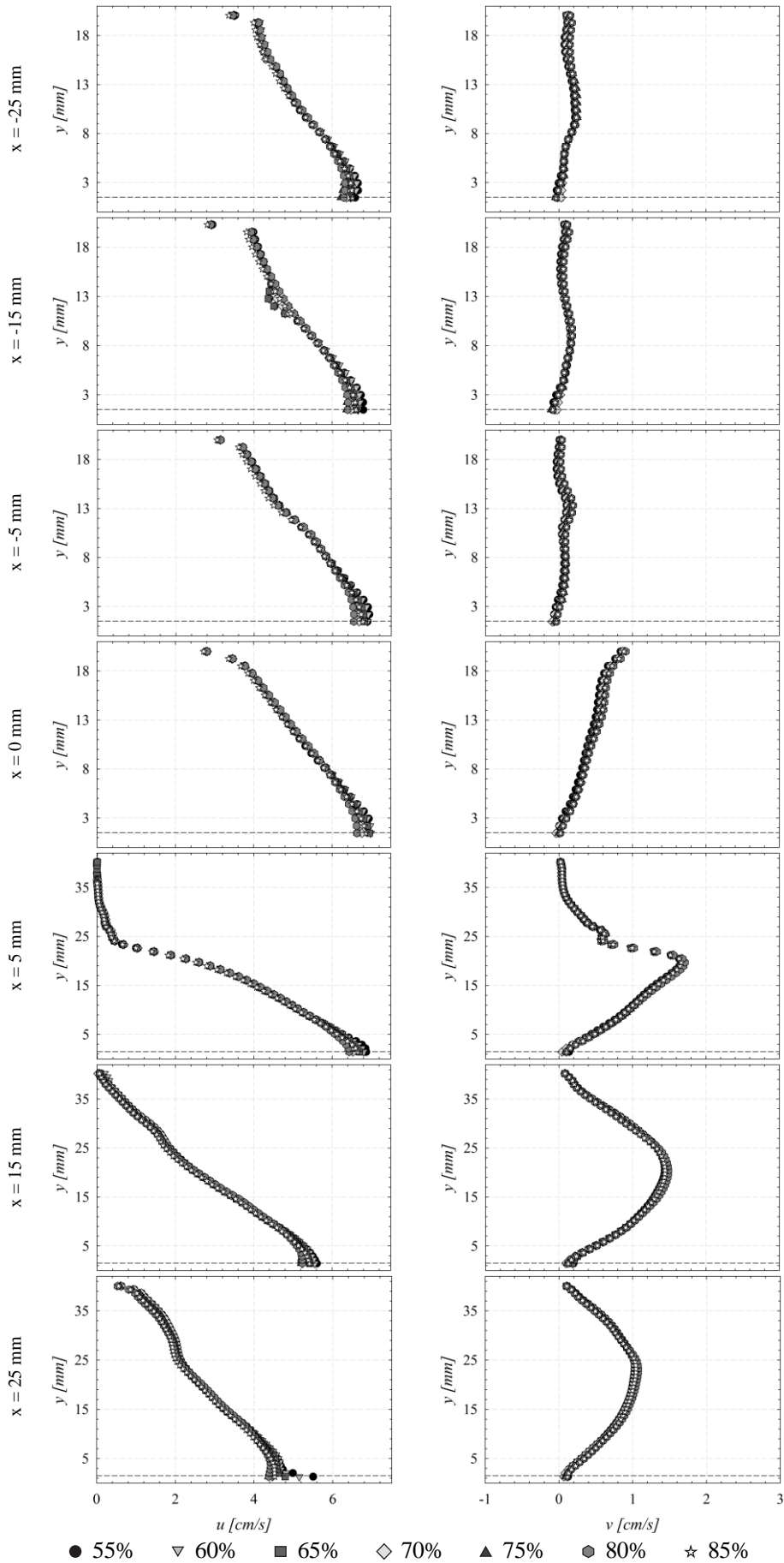


Figure 3.85 Averaged axial and vertical mean velocity profiles for all qualities, the case III and different distances over the half-sudden expansion.

2.3.2 Fence

The fence presents a height of 10 mm, a width of 5 mm and an escape angle of 45°. Both sides of the fence, upstream and downstream, present the same cross section, 21 x 21 mm². The similarity in the cross section at both sides of the channel affects the behavior of the foam flow through it. The pressure losses showed a similarity in the pressure gradient, upstream and downstream of the fence, and a transition behavior, between one and the other side of the fdd. To properly analyze the causes of this transition a PIV study was made over the lateral wall of the channel at the vicinity of the fence over 500 PIV images, they were made at 1.3 m from the foam generators outlet. Figures 3.86 to 3.88 show the averaged axial and vertical velocity fields for all the studied cases and qualities.

The presence of the fence induces the development of stagnation zones in the fdd surrounding area. In its upstream the foam slows down, due to the presence of the obstacle, and it stagnates. Downstream, a similar behavior occurs like the case of the half sudden expansion. Once the foam flow goes through the section reduction, created by the fence, the foam occupies once again, the whole length of the channel's height. This behavior will form the second stagnation region in the upper side of the duct, close to the fence. The foam can then be divided into two regions: the main flow and the dead zones, where the bubbles can be completely motionless.

The average axial velocity fields show how the foam flow accelerates under the fence. Upstream of the obstacle, the three foam flow qualification regimes are validated in the three cases. Case I presents a piston flow with a mean velocity of 2 cm/s. As the velocity increases, Cases II and III axial velocities component depend on the *y coordinate*. For all cases and qualities, the maximum axial velocities (\bar{u}_{max}) occur under the fence: 4, 9 and 12 cm/s for cases I, II and III respectively. Due to the elastic properties presented by this fluid, the foam flow coming out of the obstacle tends to return to its initial state, meaning that the upstream velocity profiles should be similar to the downstream ones. An influence of the liquid slip-layer is seen for higher velocities. The axial velocity fields under the fence for case I, show no difference for foam qualities. However, in cases II and III the important influence of the liquid film, flowing at the bottom of the channel, can be observed. From the liquid film thickness results, it was concluded that the bottom slip layers depend on the foam qualities. Wetter foams possess thicker liquid slip layers and accelerate the bottom bubbles of the foam, due to a higher liquid slip-layer influence.

The vertical velocity fields clearly show the movement of the foam when going through the fdd. Upstream of the fence, the flow presents a downward acceleration, to pass under the obstacle. Once through the fdd, the foam starts an upward displacement, filling the channel's height. The stagnation zones in the vicinity of the fence are also observed in these phenomena. An interesting characteristic observed is the asymmetry in the results. The negative velocities, before the fdd, present smaller values than the positive ones. This phenomenon is a consequence of the foam's properties. Foam will try to resist to any compression due to the air inside the bubbles exerting an opposite pressure and the high surface tension resisting to the coalescence of the bubbles. Once the fluid has gone through this change, the air inside the bubbles will expand and fill as fast as possible the whole channel. For high velocities, especially case III, the density of the foam and its quality show their importance in the process. Wetter foams present higher densities, therefore they will move faster towards the bottom of the channel, in the direction of the gravity, and slower when coming out of the fence with a positive velocity. The opposite can be appreciated with dryer foams with lower density.

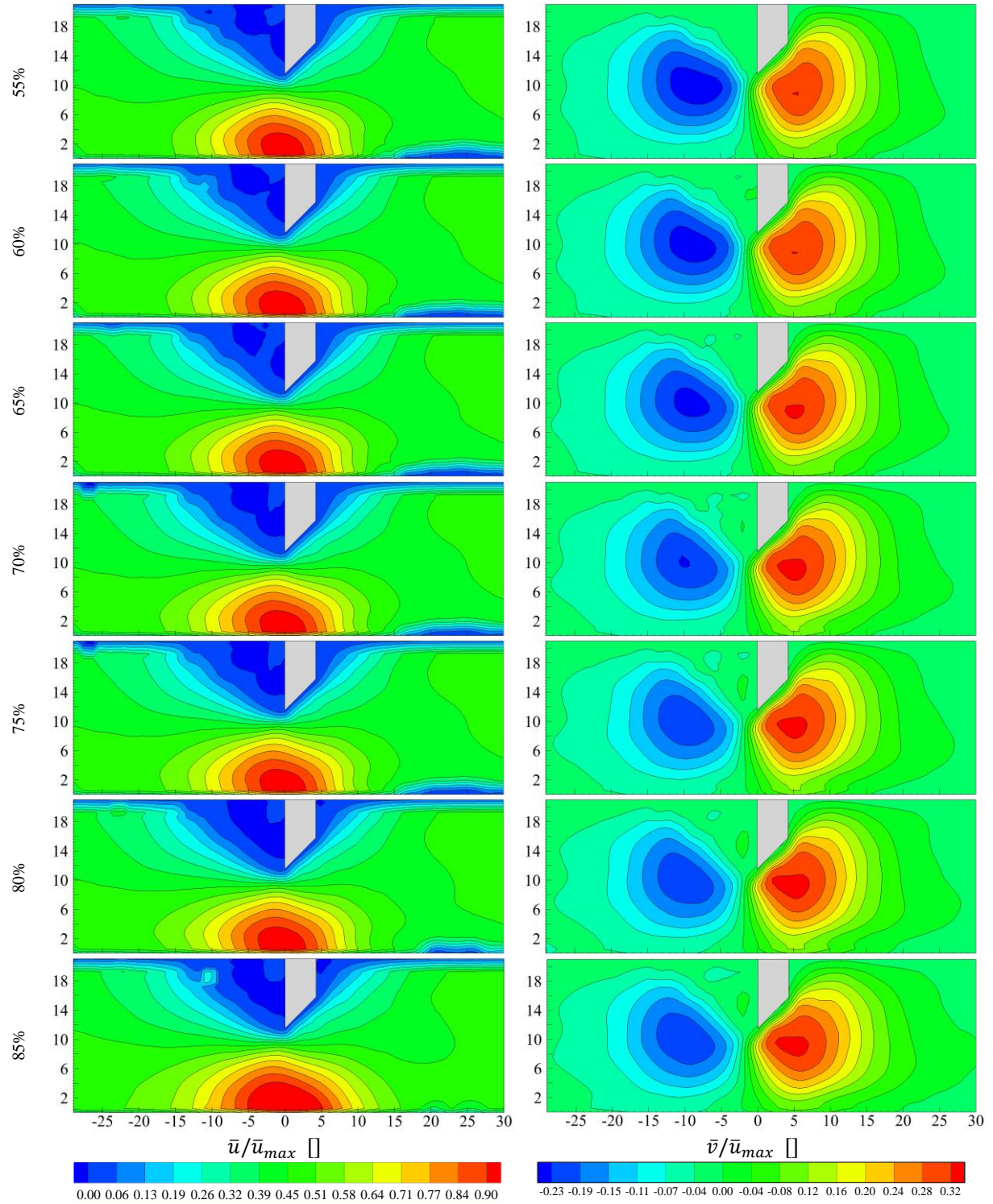


Figure 3.86 Averaged axial and vertical mean velocity fields for all qualities and the case I over the fence.

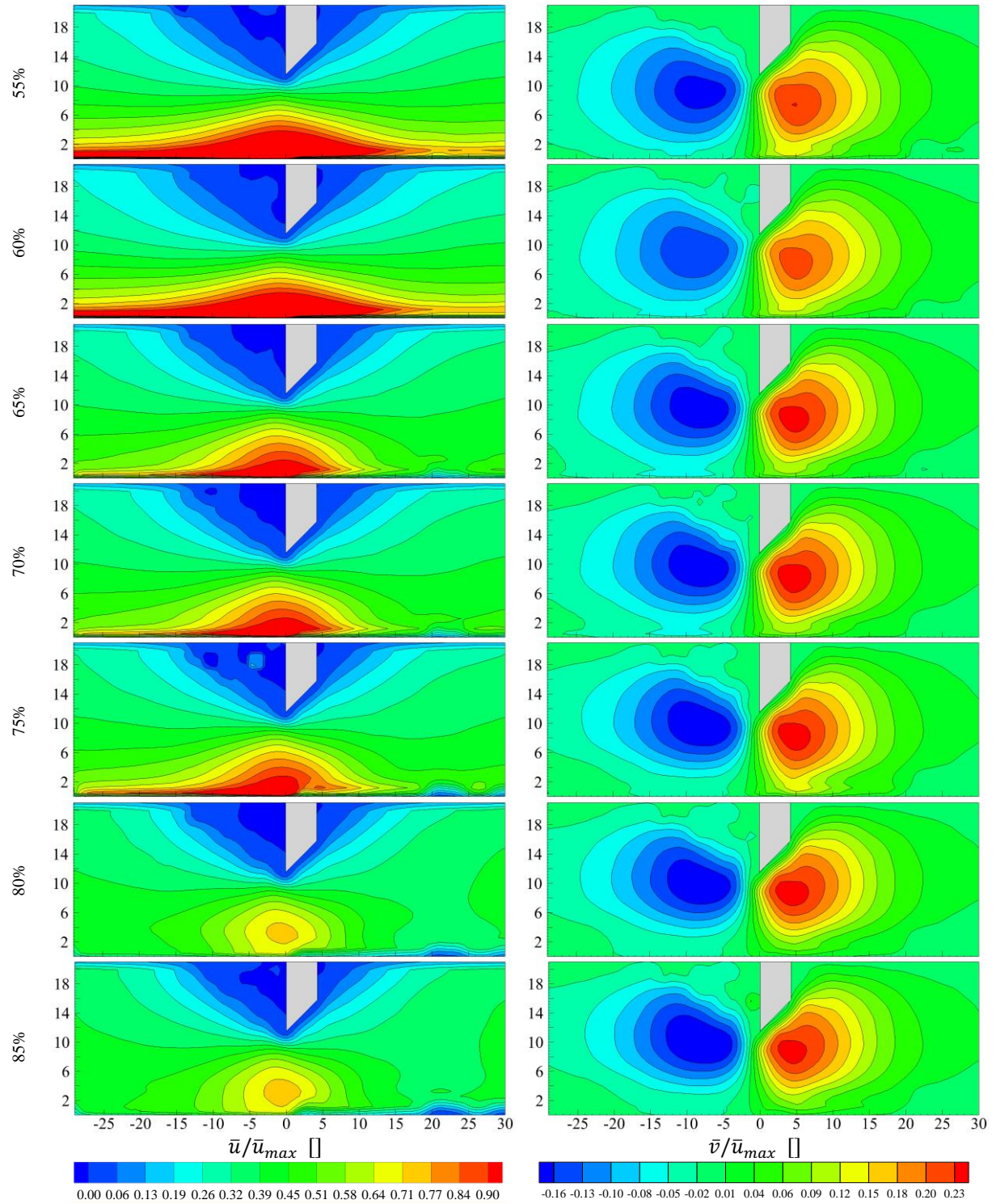


Figure 3.87 Averaged axial and vertical mean velocity fields for all qualities and the case II over the fence.

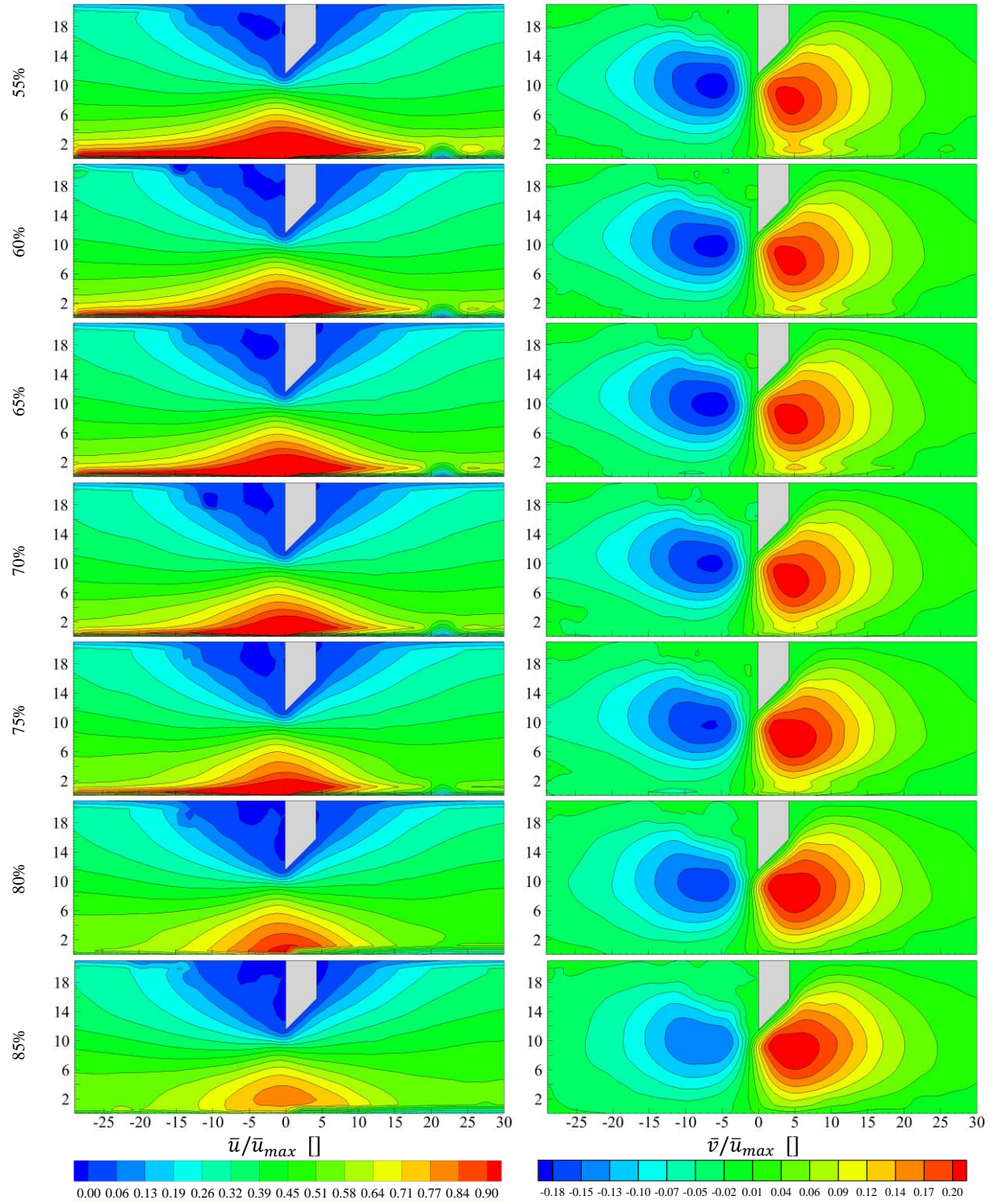


Figure 3.88 Averaged axial and vertical mean velocity fields for all qualities and the case III over the fence.

Figures 3.89 to 3.91 provide a comparison of the average axial and velocity profiles for all the cases and qualities, as the foam passes through the fdd starting at $x = -25 \text{ mm}$ and finishing at $x = 25 \text{ mm}$. The rheological properties of the foam can be seen in these results. The fluid movement is a function of a yield stress; once it passes under the fdd, which inflict a change in its behavior and increase in stress, the foam yield passes a certain threshold and flows like a viscous liquid. As for the elastic properties, the velocity profiles show the influence of the obstacle far away from the immediate vicinity.

The axial velocity profiles show a sudden acceleration as the fluids moves closer to the obstacle ($x = 0 \text{ mm}$). It reaches a maximum value at a point located exactly underneath the fence. Velocities of 4, 9 and 12 cm/s are note near the bottom of the channel under the disruption device, at this point the influence of the underlying liquid film is clearly noted. After this acceleration forced by the fdd, the flow achieves an equilibrium state with a velocity profile and regime similar to the one seen upstream of the channel before the obstacle, confirming once more the elastic properties. The presence of stagnation zones are clearly noticeable in the vicinities of the fence for $x = -5 \text{ mm}, 0 \text{ mm}$ and 5 mm , the top of the channel presents velocities values of zero or close to this one. The absence of negative values indicates that there are no recirculation zones, or vortices, and the foam stagnates at the upper part of the duct, close to the fence. For the higher velocities (cases II and III), the influence of the bottom liquid slip-layer is confirmed. Wetter foams present a thicker liquid film; at the bottom of the channel, and their velocities influence the displacement of the attached bubbles. The slower foam, case I, also presents a difference in slip-layers thicknesses, but their velocity does not have as high impact as in the two obstacles. The difference between the maximum velocity values can be as high as 30%, under the fence in case III.

The average vertical velocity profiles were obtained over the same plane. Upstream and downstream of the fence, there is no vertical acceleration, and the foam flow mainly responds to axial movement. The reduction of the square section's surface, induced by the fence, creates a downward acceleration, so the fluid can pass below the fdd. Once through the obstacle, exactly at $x = 0 \text{ mm}$, the low density and the high active surface push the bubbles up in the channel, and start to occupy its rest, while decelerating, both velocity component, and later reaching a zero value in the vertical direction. The density difference between foam qualities is seen at $x = 0 \text{ mm}$ for high velocities. Dryer, less dense, foam tends to fight against the negative movement and the bubbles compression, and accelerates faster once pass across the fdd. The contrary behavior can be seen for wetter and denser foams. The opposition of foam to compression is so important that at $x = 0 \text{ mm}$ a high positive value occurs near the escape point of the fence and a higher acceleration. The biggest asymmetry at both sides of the fence can be accurately quantified, it is of 47%, 38% and 29% for cases I, II and III respectively. This means that the velocity of the bottom bubbles influences the vertical velocity and reduces the asymmetry that both sides of the fence have.

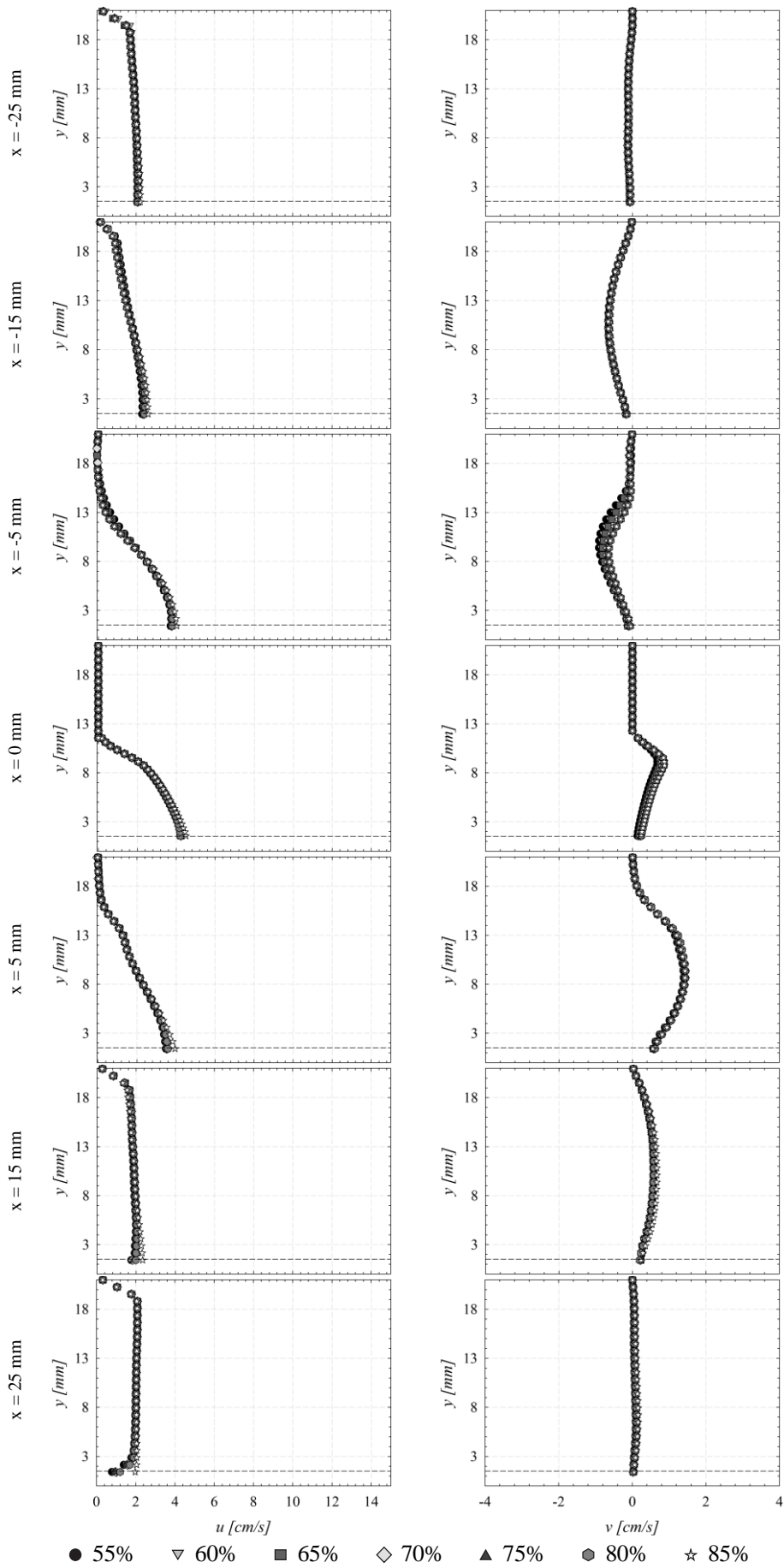


Figure 3.89 Averaged axial and vertical mean velocity profiles for all qualities, the case I and different distances over the fence.

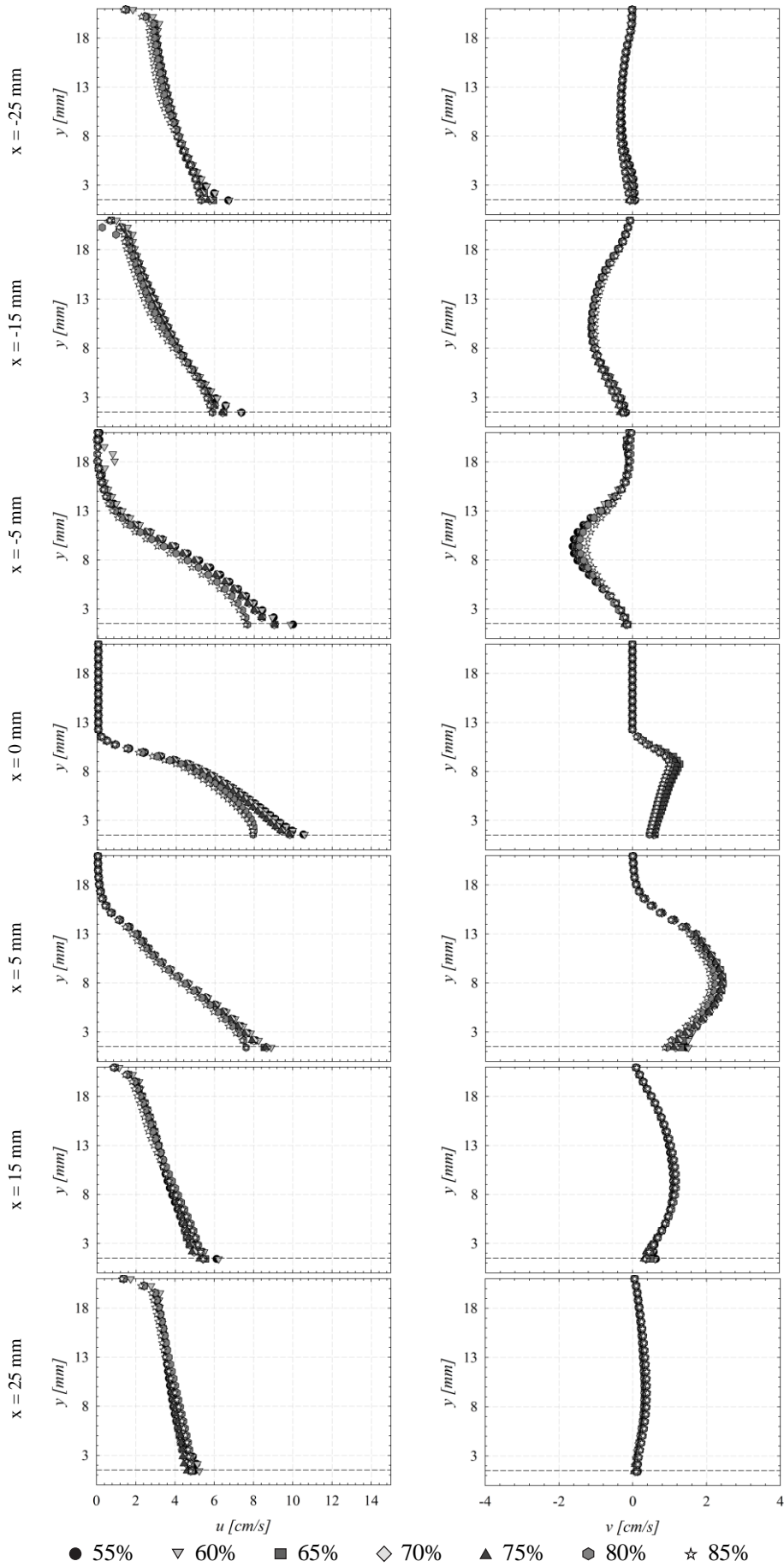


Figure 3.90 Averaged axial and vertical mean velocity profiles for all qualities, the case II and different distances over the fence.

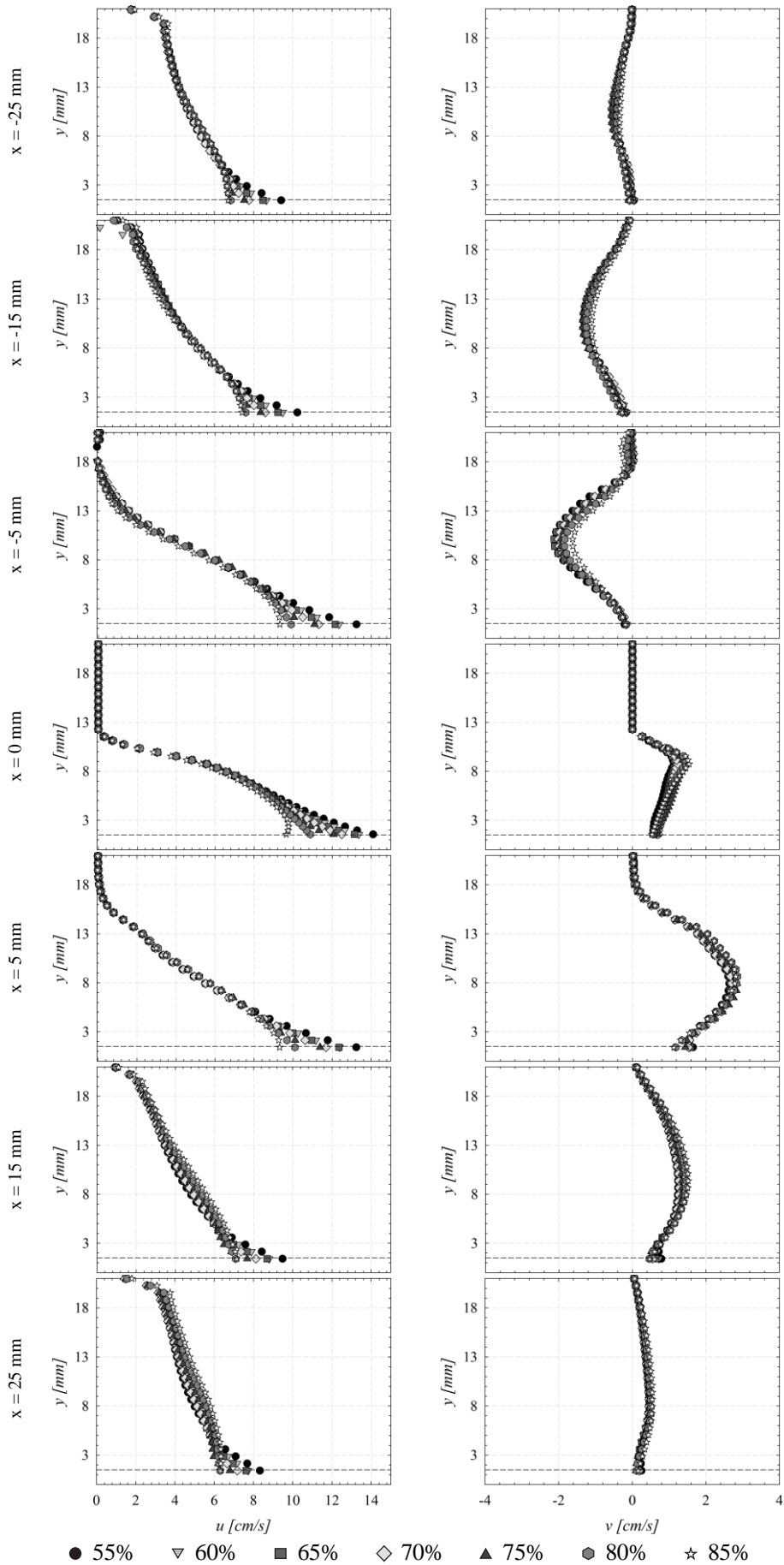


Figure 3.91 Averaged axial and vertical mean velocity profiles for all qualities, the case III and different distances over the fence.

2.3.3 Cylinder

The cylinder fdd located along a Plexiglas channel 3.4 m long, with a square section of 21 x 21 mm² at both sides of the cylinder. The measurement section is located 1.25 m from the duct's entry. This configuration allows the PIV to study the foam flow when it faces a disrupting pattern change, and its reorganization once passes the fdd. In our previous case, the foam flow had only one way to go, upward for the half-sudden expansion and downwards for the fence. In this case, the fluid is obliged to travel across both, the upper and lower parts of the channel at the same time. The coordinate system is located at the middle of the test section over the fdd.

Figures 3.92 to 3.94 show the average axial and vertical velocity fields of foam flowing through a cylinder for all cases and qualities. A stagnation zone can be identified, for all cases, near the obstacle. As the foam approaches the disruption, its behavior and direction changes, and the bubbles in contact with the cylinder stagnate against its surface. These results validate the three foam flow regimes presented by Blondin [3]. It is known that horizontal flowing foam has one uniform axial component, in the axial flow direction, until surpassing a certain yield stress, as seen in case I. As the liquid slip-layer drags the bottom, bubbles velocity increases, with a profile that only depends on the *y coordinate*, cases II and III. This behavior was also seen on the other disruptions. Another similarity is the capacity of the foam flow of returning to its initial state, once the obstacle has altered it. Meaning that the velocities profiles, upstream and downstream of the cylinder, are similar. Despite the low density presented by this kind of fluid, it still depend on the gravity forces, which will accelerate the foam that passes under the obstacle and slow down the one that goes over it. This velocity difference is of 21%, 60% and 57% for cases I, II and III. As the velocity increases the bottom liquid film has a greater effect over the foam flowing under the obstacle, which accelerates the foam, increasing therefore its velocity difference with the upper part of the obstacle. Even though there is a velocity difference at both parts of the cylinder, up and down, they tend to an equilibrium state after going across it. For higher velocities, cases II and III, there are also differences related to the foam quality, and the influence of the liquid slip-layer over the bubbles movement near the bottom of the channel.

The gravitational forces also influence the average vertical velocity fields. Therefore, a higher acceleration occurs on the lower part of the channel. There is no vertical movement upstream and downstream of the cylinder, proving the predominance of the one-dimensional axial displacement. When approaching the cylinder, two acceleration process initiate: one over, and the other under the fdd. Once across the cylinder, the foam flow tends to its initial, balanced, state with an opposite behavior as the one seen upstream, positive velocity at the bottom of the channel and negative one near the top. This indicates again, the mechanical properties of this complex fluid. The downward acceleration, previous to the obstacle, presents a lower velocity that the upward one. This is due to the resistance exerted by the air inside the bubbles, and by the surface tension, to any kind of outside compression.

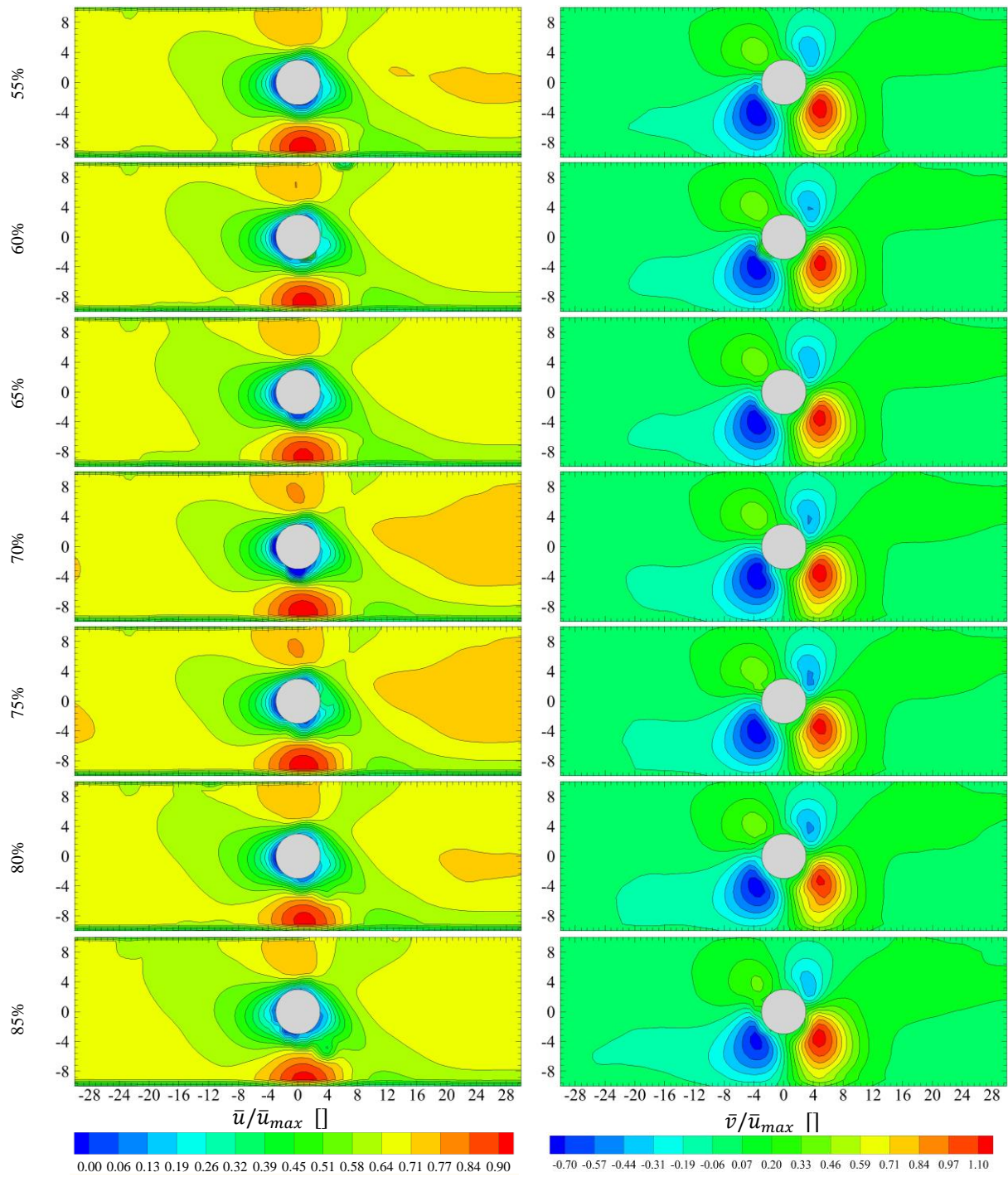


Figure 3.92 Averaged axial and vertical mean velocity fields for all qualities and the case I over the circle

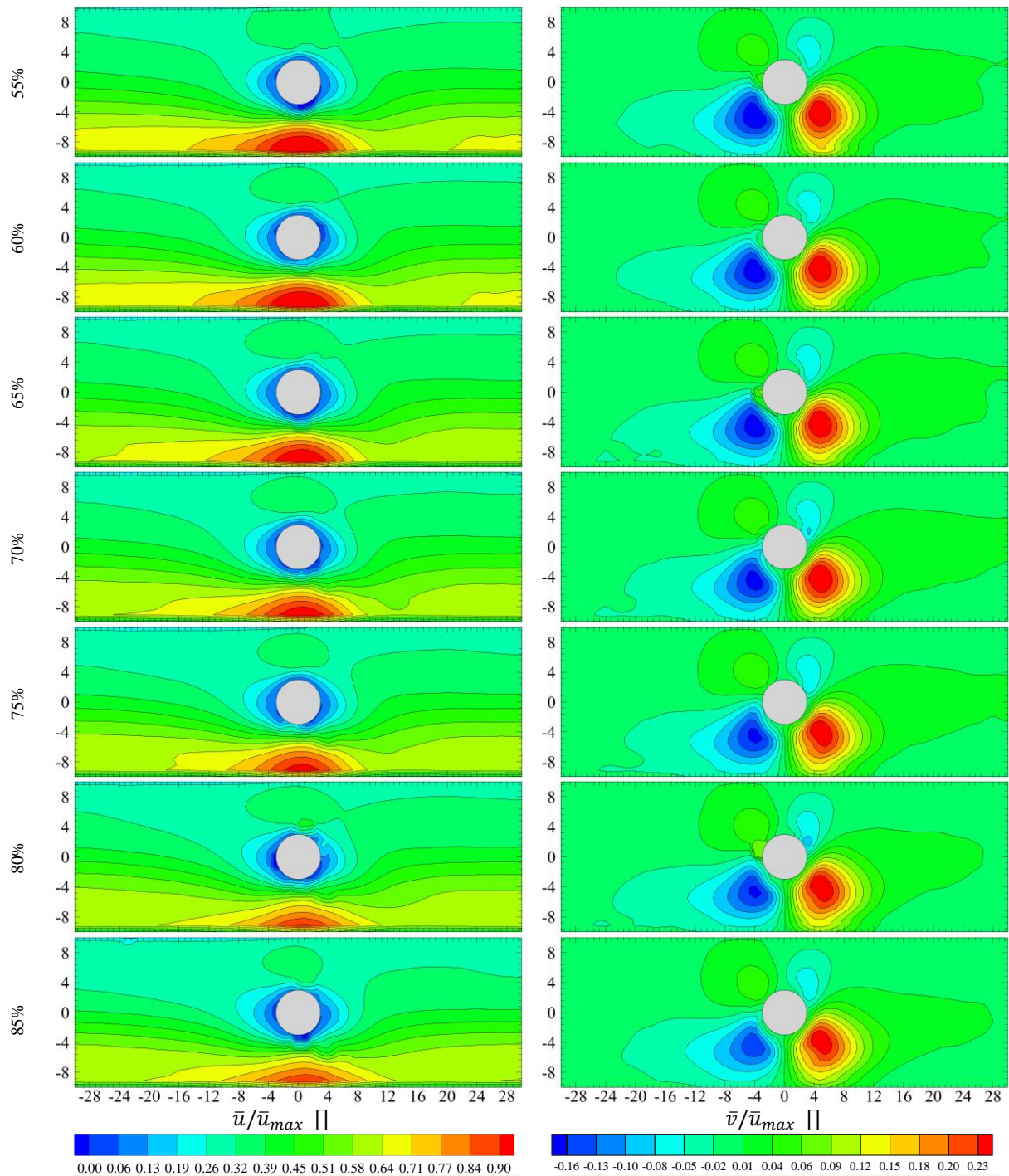


Figure 3.93 Averaged axial and vertical mean velocity fields for all qualities and the case II over the circle.

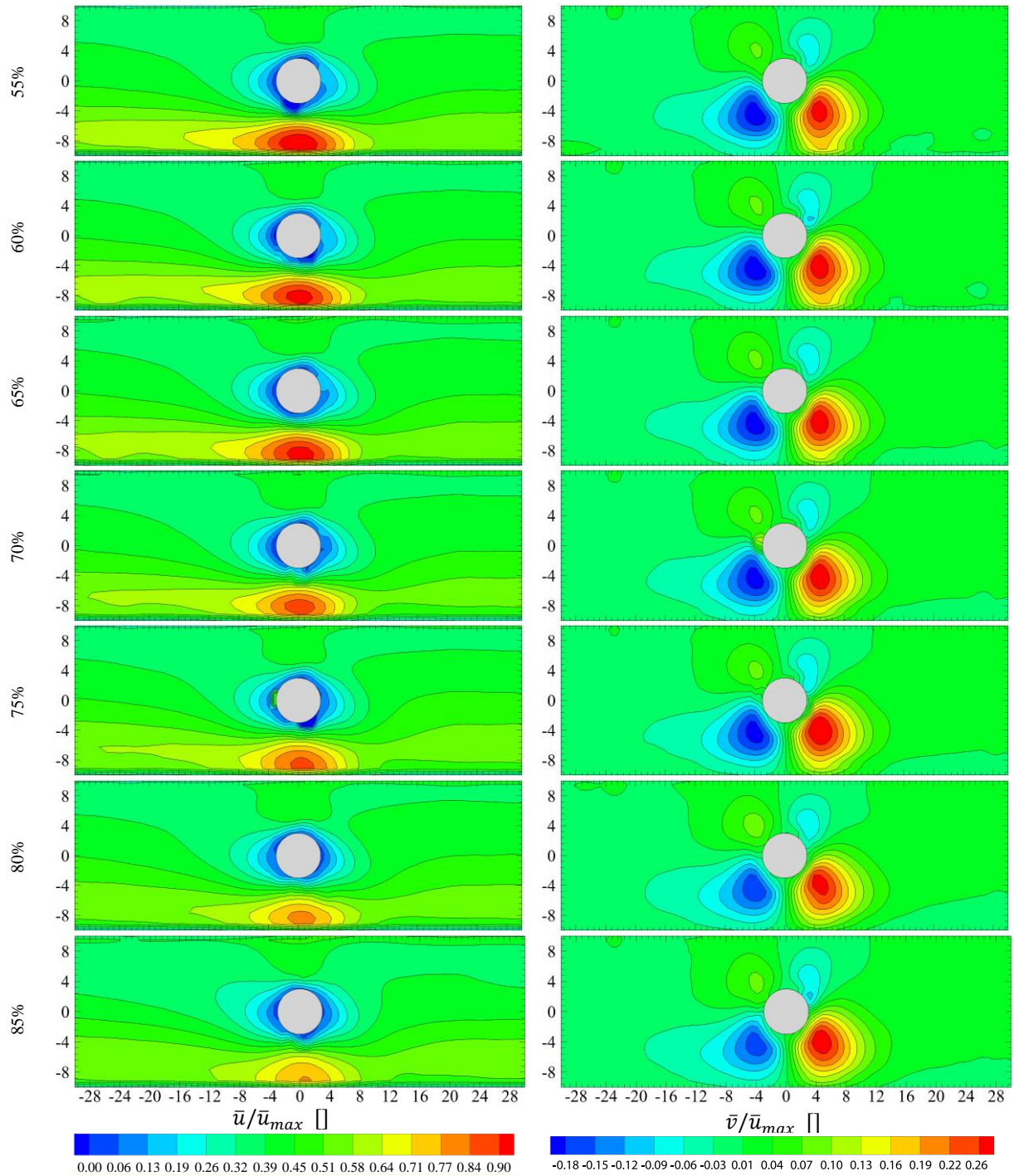


Figure 3.94 Averaged axial and vertical mean velocity fields for all qualities and the case III over the circle.

The average axial and vertical profiles as the foam flows across the cylinder from $x = -25 \text{ mm}$ to $x = 25 \text{ mm}$ are represented in Figures 3.95 to 3.97, that compare foam cases and qualities. The visco-elasto-plastic and mechanical properties of a fluid with particular properties confront this type of fdd, forcing the foam to compress, expand, divide and float at the same time.

As the foam moves closer to the obstacle, the average axial velocity profiles manifest acceleration on both sides of the cylinder, up and down, and a stagnation zone around it, where the velocities drop to zero. The acceleration at the bottom of the channel is higher than near the top. The maximum average axial velocities are 2.8 cm/s, 6.5 cm/s, and 9.2 cm/s near the lowest part of the channel; and 2.1 cm/s, 2.8 cm/s and 4.5 cm/s at the highest side for the cases I, II and III. This means that the largest velocity difference is 57% for the case II. This variance in the foam acceleration is due to the gravity force, the foam's density and the bottom liquid film. All these aspects affect the foam's behavior, and pattern, making it accelerate towards the bottom, and as it passes the cylinder, the slip-layer will increase even more its velocity. These results are consequence of the flow regimes and rheological properties. Case I presents a piston flow with a one-dimensional axial component. For cases II and III, the increment in the flow and liquid film layer movement originates a difference in velocities between the upper part of the channel and the liquid/foam interphase. This variance brings a shear along the axial velocity profile, making it dependent of the y values, as can be appreciated near the vicinity of the obstacle $x = -5 \text{ mm}$, $x = 0 \text{ mm}$ and $x = 5 \text{ mm}$. These graphs show the presence of the stagnation zone. All the velocities near the surface of the cylinder ($x = -3 \text{ mm}$ to $x = 3 \text{ mm}$) tend to a zero value.

The vertical velocity profiles are drawn along the same plane, near the lateral wall. They show the influence of the axial component in the horizontal foam flow. Most of the average vertical profiles tend to zero. The influence of the cylinder is most noticeable in the profiles over $x = -5 \text{ mm}$, $x = 0 \text{ mm}$ and $x = 5 \text{ mm}$. The gravity and inner bubble forces play an important role on the vertical displacement of the foam. As seen in the axial velocity component, the obstacle creates a change in the upstream profile pattern, and accelerates the foam flow over the two sides of its surface. One in the negative direction, under the cylinder, is due to gravitational forces. This force slows the other, in the positive vertical direction over the cylinder. Despite the influence of gravity, past the cylinder, the upper and downward acceleration present higher figures than their counterparts before the disruption. The expansion rate and density of the bubbles, due to the air inside them, overcome the gravity force increasing more the velocity than at the other side, which are also influenced by these parameters. The resultant average vertical velocity values are shown in Table 3.2.

Case	Upstream-Top [cm/s]	Upstream-Bottom [cm/s]	Downstream-Top [cm/s]	Downstream- Bottom [cm/s]
I	0.33	-0.67	-0.57	1.12
II	0.50	-1.07	-0.70	1.87
III	0.68	-1.67	-0.80	2.69

Table 3.2 Averaged vertical velocity values upstream and downstream, at the upper and lower part of the channel, near the cylinder in all cases ($x = -5 \text{ mm}$, $x = 0 \text{ mm}$ and $x = 5 \text{ mm}$).

The compression of the air inside the bubbles slows down the foam displacement upstream of the cylinder; as the foam comes out of the fdd the air in the bubbles expands and makes them accelerate. Accordingly, the velocity of the foam downstream is higher than upstream of the fdd. The foam quality affects its behavior near the bottom of the channel at higher velocities. Wetter foams develop faster movement near the liquid/foam interphase than the dryer ones, due to the thickness of the slip-layer and its liquid flow.

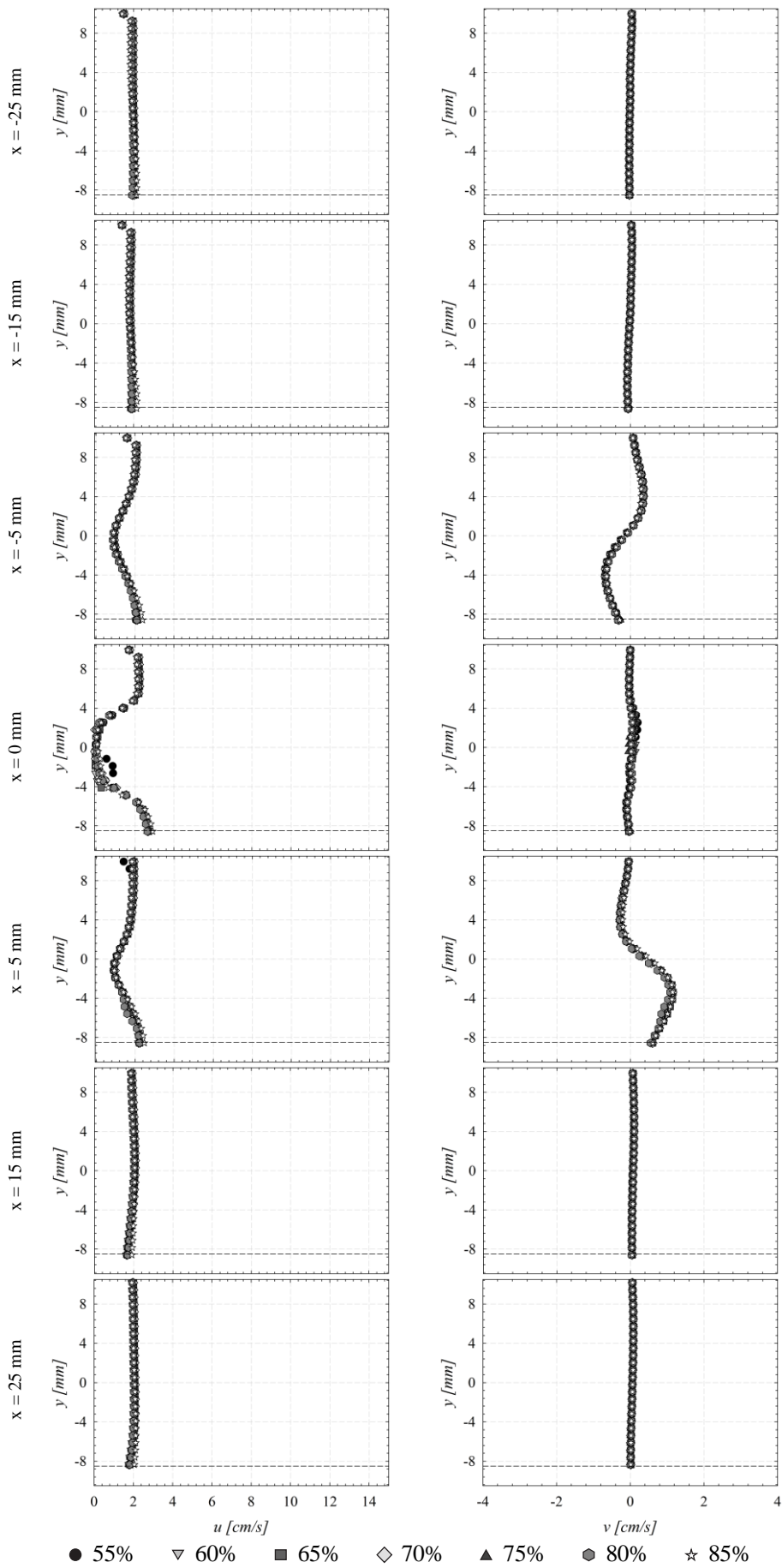


Figure 3.95 Averaged axial and vertical mean velocity profiles for all qualities, the case I and different distances over the circle.

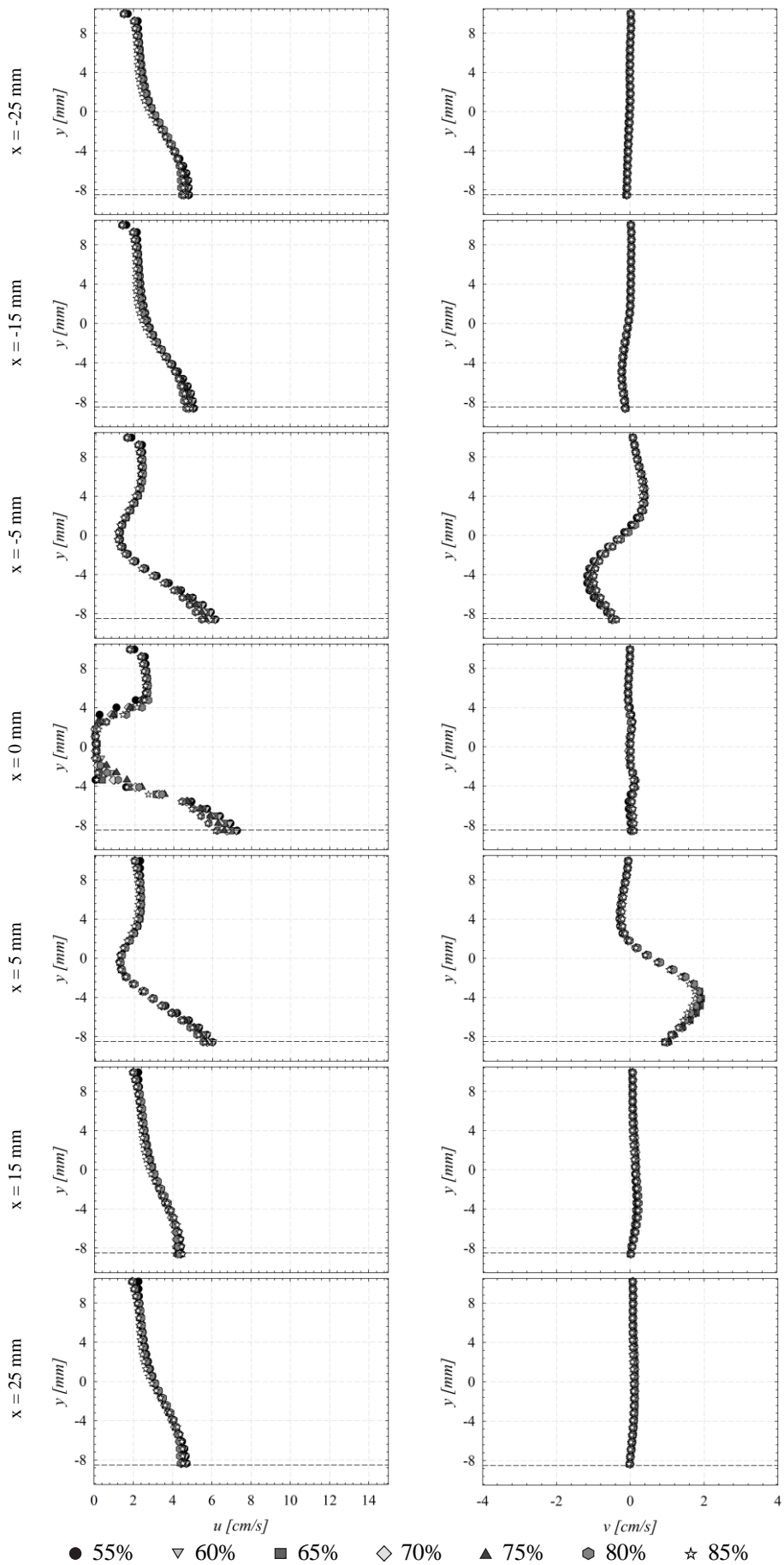


Figure 3.96 Averaged axial and vertical mean velocity profiles for all qualities, the case II and different distances over the circle.

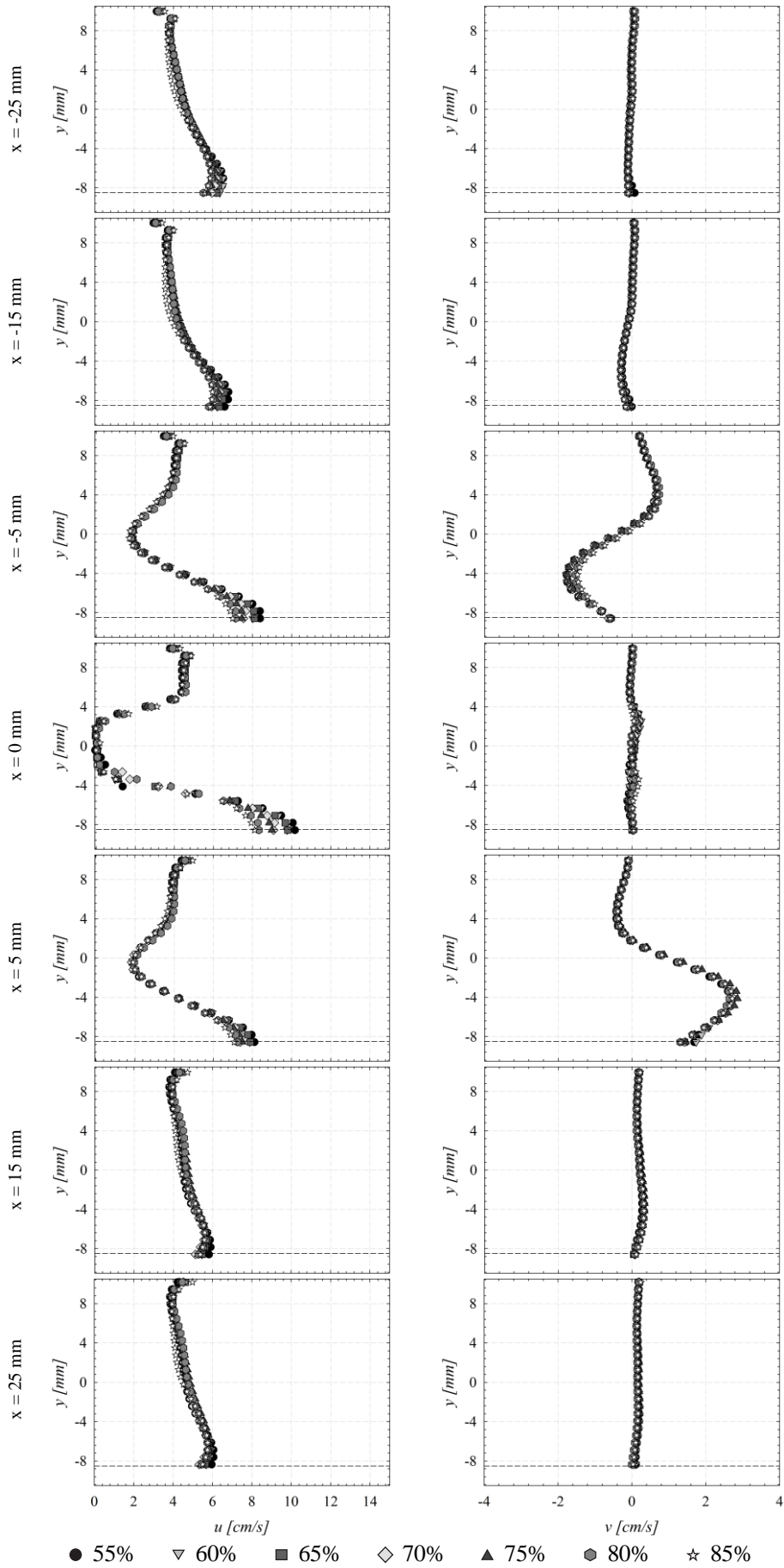


Figure 3.97 Averaged axial and vertical mean velocity profiles for all qualities, the case III and different distances over the fence.

2.4 Conclusions

The behavior of an aqueous foam flow through three flow disruption devices (fdd): half-sudden expansion, fence and cylinder, has been described and described for 7 foam qualities (55%, 60%, 65%, 70%, 75%, 80% and 85%) and three cases (2 cm/s, 4cm/s, 6 cm/s). The measurements of the static pressure losses, the pressure gradients, the velocity fields and profiles, allowed a better understanding of the hydrodynamics, physics and rheology of this complex type of fluid.

The static pressure losses vary linearly, upstream and downstream of the fdd with a transition zone at the obstacles. The pressure gradient is directly related to the channels cross-section, and to the foam flow regime. For the fence and the cylinder, the pressure gradients upstream and downstream of the fdd are similar for the three cases. The half-sudden expansion presents a pressure loss of about half of its value. There is no difference in pressure losses for the foam qualities studied.

By using the Particle Imaging Velocimetry (PIV) technique, we determined the average axial and vertical velocity fields and profiles in the vicinities of the fdd. The foam dynamics, when faced against three different obstacles, allowed a better understanding of the reorganization of the flow, its rheology and physics, and the existence of different regimes.

The PIV results for all foam qualities, cases and geometries recognized the visco-plasto-elastic properties of the foam. As long as it does not surpass a yield stress, it maintains a state of stagnation. Beyond that stress point, the foam flows like a viscous liquid, dissipating energy according to the deformation rate. When encountering a disruption device, two behaviors have been recognized. Either the foam stores up mechanical energy to later release it and return to its initial state, or the deformation will be irreversible, and the foam will acquire and adopt a new geometry. Despite the presence of important pattern change and flow disruptors, these properties also avoid the formation of turbulence zones, eddies or even recirculation. This is mainly due to the close packing that bubbles hold, allowing them to avoid overlaying.

These data results confirmed how sensitive and complex foam flow is. There are many aspects that influence its behaviors; it is known that temperature fluctuations may be other important element, altering its properties and behavior can alter its properties. The results confirm the importance of the liquid slip-layer, the foam flow regime and the gravitational forces in its rheology and physics. This information will facilitate future numerical studies and experimental research. In the following part, we will undertake some numerical CFD simulation studies using ANSYS-CFX.

3. Numerical CFD simulations of aqueous foam over different FDD

Rheological properties of foams, such as elasticity, plasticity, and viscosity, play a major role in foam applications and behavior. Defining the complexity of these interactions and processes, becomes a major challenge. Neighboring bubbles are squeezed against each other and separated by thin films and Plateau borders. Surfactant, proteins or solid particles stabilize the liquid/gas interphases. When foam is subjected to a small shear stress, it deforms like a soft solid. This response can be characterized by visco-elastic moduli. For applied stresses beyond a certain limit, foams behave like shear-thinning fluid; the effective viscosity decreases as a function of shear rate.

Due to the many different length and time scales, foam rheology is particularly difficult to model. From a macroscopic point of view (the phases, air and liquid, are considered as a continuous medium), the relation between stress, deformation and flow may be represented by a pseudo-fluid. To model the *steady flow* of materials that may behave as a solid or a liquid (depending on the applied stress) over a large range of strain values, we must consider viscous stresses. Aqueous foam flows are often described as “Bingham fluids”. The rheological behavior of this fluid can be expressed:

$$\begin{aligned} \gamma &= 0 && \text{if } \tau < \tau_c \\ \tau &= \tau_c + k \gamma && \text{if } \tau > \tau_c \end{aligned}$$

Bingham fluids will only yield if they are submitted to a stress superior to a yield point, but they can also slip along a solid wall. The velocity fields obtained in our measurements show a different yield behavior as the one describing this type of fluids. However, for small velocities (case I), a piston foam flow does relate to a Bingham fluid.

Computational Fluid Dynamics (CFD) allows the characterization of, almost, any given fluid. However, particular cases remain to be validated. In the case of non-Newtonian fluids, CFD allows defining important parameters like pressure losses, velocity fields and velocity profiles. These parameters directly affect the flow regime, fluid mobility and pressure profiles along the channel’s length. It is an appropriate method for obtaining a reasonable estimate of the foam flow behavior when going across different fdd (half-sudden expansion, fence and cylinder). The CFD results will be compared to the experimental ones under the same conditions.

3.1 Geometry and numerical parameters

The dimensions of the CFD geometry model coincided with the experimental ones. The length of the channel varies as a function of the flow disruption applied. For the half-sudden expansion, it is 3.87 m, for the fence 3.41 m and for the cylinder 3.38 m. The inlet of the channel presents a square section of 21 x 21 mm². The *measurement section* is located 1.3 m from the beginning of the duct. At this level, the three fdd were placed. The half-sudden expansion presents an upstream square section of 21 x 21 mm², and a section ratio of 0.5 to a downstream area of 21 x 42 mm². The fence has a height of 10 mm a width of 5 mm and an escape angle of 45°. Finally the cylinder has a diameter of 6 mm and is located in the middle of the channel’s height. To decrease the CPU time calculation and requirements, all three cases were assumed to have a 2D geometry. Accordingly, the depth of the numerical geometry was assumed infinite (*z coordinate*)

The coordinate systems for the half-sudden expansion and the fence were located at the fdd over the bottom of the channel. For the cylinder, it was located at the middle of the duct height over the flow disruption. Therefore, all measurements in its downstream will have a positive value in the *x-coordinate* and the measurements upstream a negative one.

Three meshes were adopted and tested. Each one presents a higher number of elements than the other, according to a grid refinement study. The cell numbers and the smallest cells size are represented in Table 3.3. The smallest cells are located near the FDD vicinities, enabling an accurate calculation of the velocity fields and profiles near this area.

Geometry	Coarse Mesh (Δx [mm])	Medium Mesh (Δx [mm])	Fine Mesh (Δx [mm])
Half-sudden expansion	133980 (2)	152438 (0.5)	221452 (0.25)
Fence	71615 (2)	84079 (0.5)	131074 (0.25)
Cylinder	68164 (2)	80584 (0.5)	124919 (0.25)

Table 3.3 Mesh characteristics (Cell numbers and smaller cell).

The process of accurately represent the perfect mesh, for a numerical simulation, is one of the most critical ones. A higher number of elements represent better results, however it also increases the CPU calculation time. Trying to limit the possible consumption of CPU resources, a so-called high-precision method was implemented for the spatial discretization. This last one is called GCI (Grid Convergence Index). It provides a confident estimated error band and can be used with a minimum of two meshes, but provides a better estimate error when applied to three different ones.

The basic idea is to approximately relate the results from a grid refinement using a second-order method. The GCI is based upon an error estimation derived from the theory of a generalized Richardson extrapolation. It is a measure of the percentage of the computed value, which is away from the value of the asymptotic numerical value. It indicates an error band on how far the solution is from the asymptotic value. It indicates how much the solution would change with further refinement of the grid. A small value of GCI indicates that the computation is within the asymptotic range.

Next, the procedure to estimate the discretization error [142]:

Firstly, we established a representative grid size:

$$h = \left[\frac{1}{N} \sum_{i=1}^N (\Delta A_i) \right]^{1/2} \quad (3.27)$$

where ΔA is an average “global” area of the cell and N the number of cells of the calculation domain. Select three significantly different set of grids and calculate the refinement factor r_e between the coarse, medium and fine grid:

$$r_{e32} = h_3/h_2 \rightarrow r_{e32} = h_{coarse}/h_{medium} \quad (3.28)$$

$$r_{e21} = h_2/h_1 \rightarrow r_{e21} = h_{medium}/h_{fine} \quad (3.29)$$

where $r_e > 1.3$ [142]. Then, we calculated the formal order of accuracy of the algorithm p , which is necessary to get the grid resolution into the asymptotic range for a grid convergence testing:

$$p = \frac{1}{\ln(r_{e21})} |\ln|\varepsilon_{32}/\varepsilon_{21}| + q(p)| \quad (3.30)$$

Where:

$$q(p) = \ln \left(\frac{r_{e21}^{p-s}}{r_{e32}^{p-s}} \right) \quad (3.31)$$

$$s = 1 \cdot \text{sign}(\varepsilon_{32}/\varepsilon_{21}) \quad (3.32)$$

$$\varepsilon_{32} = f_3 - f_2 \quad (3.33)$$

$$\varepsilon_{21} = f_2 - f_1 \quad (3.34)$$

f_1, f_2 and f_3 are the fine, medium and coarse grid solution variables of interest (for our study, the axial velocity u directly under each of the FDD), $\varepsilon_{32}/\varepsilon_{21} < 0$ is an indication of oscillatory convergence. After that, we calculated the extrapolated values f_{ext} :

$$f_{ext}^{32} = \frac{r_{e32}^p f_1 - f_2}{r_{e32}^p - 1} \quad (3.35)$$

$$f_{ext}^{21} = \frac{r_{e21}^p f_1 - f_2}{r_{e21}^p - 1} \quad (3.36)$$

The relative error e_a :

$$e_a^{32} = \frac{f_2 - f_3}{f_2} \quad (3.37)$$

$$e_a^{21} = \frac{f_1 - f_2}{f_1} \quad (3.38)$$

The extrapolated relative error e_{ext} :

$$e_{ext}^{32} = \frac{f_{ext}^{32} - f_2}{f_{ext}^{32}} \quad (3.39)$$

$$e_{ext}^{21} = \frac{f_{ext}^{21} - f_2}{f_{ext}^{21}} \quad (3.40)$$

and the GCI :

$$GCI_{medium}^{32} = \frac{1.25 e_a^{32}}{r_{32}^p - 1} \quad (3.41)$$

$$GCI_{fine}^{21} = \frac{1.25 e_a^{21}}{r_{21}^p - 1} \quad (3.42)$$

Table 3.4 expresses the results obtained for the GCI method. The variable evaluated was the axial velocity u near the vicinity for the case I and all the FDD.

Geometry	r_{e32}	r_{e21}	ε_{32}	ε_{21}	e_a^{32}	e_a^{21}	e_{ext}^{32}	e_{ext}^{21}	GCI_{32}	GCI_{21}
Half-sudden expansion	1.14	1.45	0.28	0.26	0.12	0.12	2.76	2.71	16.01%	2.71%
Fence	1.17	1.56	-0.09	-0.02	0.02	0.01	3.67	3.87	0.52%	0.01%
Cylinder	1.18	1.55	0.12	0.07	0.04	0.02	8.37	11.81	3.14%	0.29%

Table 3.4 GCI Results

Due to the absence of important fluctuations and transient data, a Steady-State analysis was undertaken, this one allows acquiring the mean static pressure losses, velocity fields and profiles, which will be compared against the experimental data already obtained.

To define the relevance of these considerations, the numerical simulations followed a regime similar to one-dimensional used by the experimental measurements. Before using the Bingham non-Newtonian model, simulations with the Eulerian-Eulerian multiphase model were undertaken. They considered all the important parameters of foam flow: a continuous phase, a disperse phase, diminution of the surface tension for the liquid phase, bubble size, drainage, wall lubrication forces, drag forces, velocity profiles and pressure losses. Despite all the data provided by the experimental study, the software (CFD code) was not able to accurately reproduce the rheological behavior of such a complex fluid. However, in a macroscopic review, the physical-chemical interactions between the bubbles can be related to some non-Newtonian models, Bingham, Power Law, etc. Therefore, an isothermal and laminar Bingham fluid will try to represent the behavior of aqueous foam with a quality of 70%, a bubble diameter of 0.5mm and a bulk velocity of 2 cm/s (piston flow) due to the linear rheological similarity between this fluid and the foam flow at small shears (Figure 1.12). Table 3.5 shows the rheological parameters that describe each Bingham fluid that better approaches each experimental case. This values where obtained by fixing the known pressure losses from the experimental results and assuming that the viscosity consistency is similar to the one of the liquid, one of the phases presented inside this kind of fluid.

Geometry	ρ (Kg/m^3)	τ (Pa)	k (Pa.s)
Half-sudden expansion	300.22	6.22	0.001
Fence	300.22	4.6	0.001
Cylinder	300.22	4.1	0.001

Table 3.5 Rheological properties of Bingham fluids for each FDD

Looking at the interaction between the foam and the liquid film that surrounds it, this presents an accurate description of the foam properties. A high yield stress represents the ability that foams have to oppose to change. Once it starts to flow, its viscosity is similar to that of the water ($\mu_l = 1.002 \times 10^{-3} Pa.s$ at $20^\circ C$), which is the fluid present around the bubbles. The density of the Bingham fluids was related to that of the foam flow, obtained through the equation (1.6):

$$\rho_f = (1 - \beta)\rho_l + \beta\rho_g$$

The results acquired from the comparison between the CFD simulations data and the experimental one are presented in form of pressure losses, velocity fields and velocity profiles.

3.2 Validation of the velocity profiles upstream of the fdd

In order to estimate the accuracy of our numerical CFD simulations, the boundary conditions should represent the real physics of the problem. It has been shown the properties of the three different Bingham fluids used, and that the numerical geometry agreed with the experimental one, with the difference that to decrease the CPU time calculation and requirements, all three cases were assumed to have a 2D geometry, infinite z coordinate. Despite knowing the bubbles slide over the channel's wall, a non-slip property was given to these walls and the ones forming the fdd surfaces. Slipping conditions alter the influence of the wall shear stress over the pressure losses and change completely the physical properties of the problem. Finally, depending on the fdd, a pressure difference was imposed between the inlet and outlet of the channel. To validate the boundary conditions, the similarity of a velocity profile was verified, before passing across the fdd at $x = -35$ mm. Figure 3.98 represents the velocity profiles upstream of the half-sudden expansion, the fence and the cylinder for an aqueous foam with a quality of 70% and a velocity of 2 cm/s for their respectively Bingham fluids.

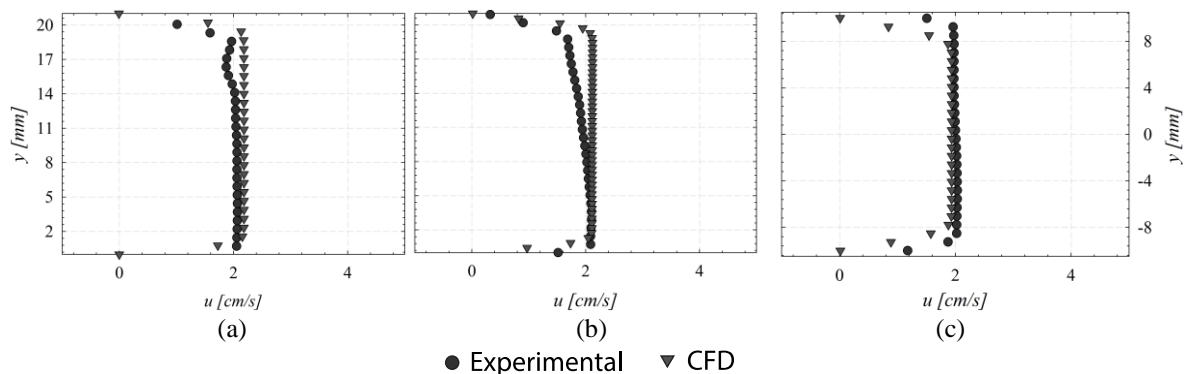


Figure 3.98 Averaged axial velocity profiles for an aqueous foam and a Bingham fluid upstream of the three fdd at $x = -35$ mm: (a) half-sudden expansion, (b) fence and (c) cylinder.

These figures validate the chosen boundary conditions, for all fdd the CFD results show a block flow with a bulk velocity of 2 cm/s. There is maximal deviation of 18% for the fence, near the top of the channel. The other two fdd present relatively close velocity profiles between the Bingham fluid, used in the numerical CFD simulation, and the aqueous foam flow. These results show the capacity of a given Bingham fluid to represent a one-dimensional flow with a component in the axial flow

direction. At the same time that the boundary conditions used in the numerical CFD simulations results represent accurately the initial physics of the foam, before entering the fdd.

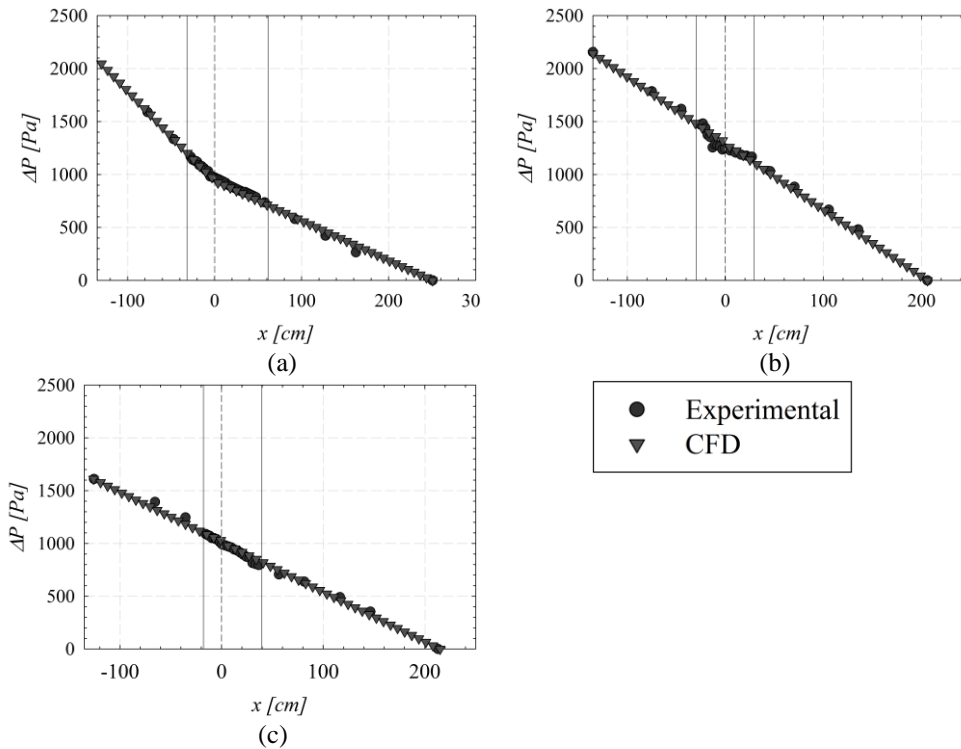


Figure 3.99 Evolution of the static pressure losses for an aqueous foam and a Bingham Fluid at 2 cm/s through three fdd: (a) half-sudden expansion, (b) fence and (c) cylinder

3.3 Static pressure losses

The pressure losses along the channel's length are one of the most significant parameters when trying to simulate and predict the rheological properties of any fluid. They are directly related to the wall shear stress. Therefore, it is important to define if the numerical CFD results, using a Bingham fluid, are close or similar to the experimental ones, for a horizontal aqueous foam flow. Figure 3.99 show the static pressure evolution lengthwise the duct near the vicinities of the three fdd, half-sudden expansion, fence and cylinder.

Both the CFD and experimental pressure losses show the same behavior along the channel. The biggest deviation between these two results is lesser than 10%. The static pressure varies linearly upstream and downstream of the fdd. As the foam approaches the obstacles, and enters their vicinities, the numerical CFD results accurately describe the transition from one side to the other. They even describe the energy degradation obtained at the half-sudden expansion where the channel's surface ratio makes the pressure gradient decrease half of its value.

3.4 Averaged axial and vertical velocity fields

To obtain an overall flow description of the two fluids used, a Bingham for the CFD simulation study, and aqueous foam for the experimental one, the axial and vertical velocity fields were obtained and analyzed. Despite doing a numerical analysis over the whole length of the channel, the velocity fields will only be considered in the region of interest near fdd. The velocity profiles remain constant

along the upstream of the channel until the exit of the generators and downstream of it, reaching the output to the recovery tank. They allow a first comparison between the two behaviors when faced against different obstacles and fdd. Figures 3.100 to 3.105 show the \bar{u}/\bar{u}_{max} and \bar{v}/\bar{u}_{max} velocity fields for our numerical simulations compared to the experimental results for the three fdd, half-sudden expansion, fence and cylinder.

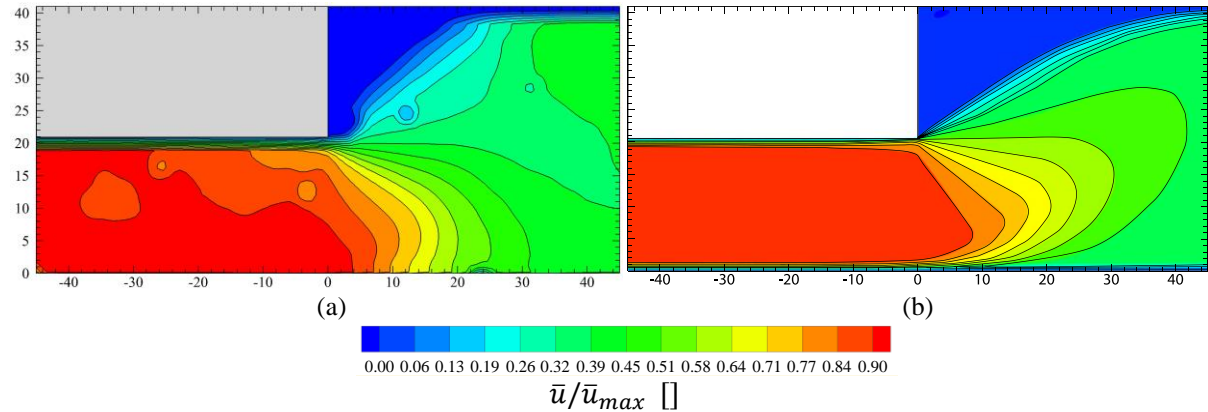


Figure 3.100 Average axial velocity field of an (a) experimental aqueous foam and a (b) CFD Bingham fluid flowing through a half-sudden expansion.

The axial average velocity fields over the half-sudden expansion show the similarities and differences between the Bingham (numerical CFD simulations) and the aqueous foam. Both fluids present an axial one-dimensional flow upstream of the fdd, and maintain it until the section changes. Due to the similarity in densities, they fill the channel creating a “stagnation zone” with non-negative values, at the upper part of the channel. Once they have occupied entirely the channel, their velocity diminishes, reaching an equilibrium state in which the axial component overtakes the vertical one and becomes predominant. The absence of negative axial velocity components over both stagnation region confirms there is no back flow, or vortices, in the opposite direction of the flow’s main stream. The length of this region shows a difference between the CFD and experimental results. The yield stress choose for the Bingham fluid, despite being the best fit from the point of view of the boundary conditions, doesn’t represent accurately the behavior of the foam flow inside this stagnation area.

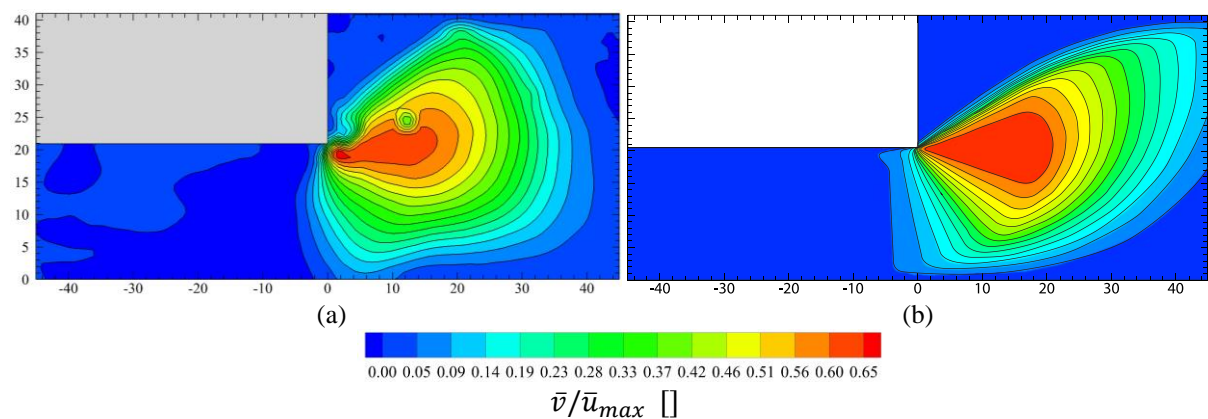


Figure 3.101 Averaged vertical velocity field of an (a) experimental aqueous foam and a (b) CFD Bingham fluid flowing through a half-sudden expansion.

As seen in the axial average velocity field, once the fluids go through the expansion, its axial component diminishes, as its vertical ones increase. This is a consequence of the low density that makes them rise towards the top of the channel. After a distance, they reach equilibrium where the axial movement sets in -and the vertical velocity approaches zero. These images show how the foam flow moves faster than the Bingham fluid towards the top of the channel, allowing the one-dimensional flow establish. This difference in raise velocity creates a larger stagnation zone for the

Bingham fluid than for the aqueous foam. Near the downstream of the half-sudden expansion, the mean vertical velocity values are more important in both cases, especially at $y = 21 \text{ mm}$. There is no presence of negative vertical velocities. This corroborates the previous assumption of absence of vortices and back flow in the opposite direction of the main flow.

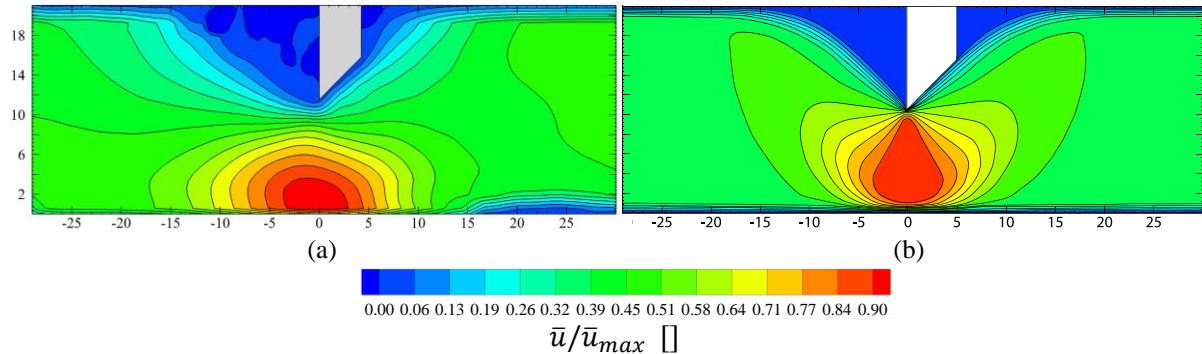


Figure 3.102 Averaged axial velocity field of an (a) experimental aqueous foam and a (b) CFD Bingham fluid flowing through a fence.

The axial average velocity fields -for the aqueous foam and the Bingham fluid over the fence- show the differences and similitudes of these two fluids. A one-dimensional flow occurs at the two cases, upstream and downstream of the fdd. As the fluids move closer to the fence, the obstacle prevents the passage through the top part of the channel, and creates an axial acceleration under it. Once the fluids have come out of the axial acceleration, they return to an equilibrium state close to its initial one, before the fdd, and stay this way until the end of the channel. They both show a stagnation zone upstream of the fdd, which is a consequence of the fluid encountering a barrier on its path, and another downstream, caused by the same buoyancy quality seen with the half-sudden expansion. The low density of the fluids will make them refill once again the channel's height completely. An important difference between both results is the behavior of the axial acceleration below the fence. The liquid slip-layer flowing at the bottom of the channel, for the foam flow, is one of the most difficult features to be numerically expressed. This film allows the sliding of bubbles along the channel's walls and doesn't slow down its axial acceleration at the bottom of the channel, giving the foam flow a larger acceleration surface than the Bingham fluid.

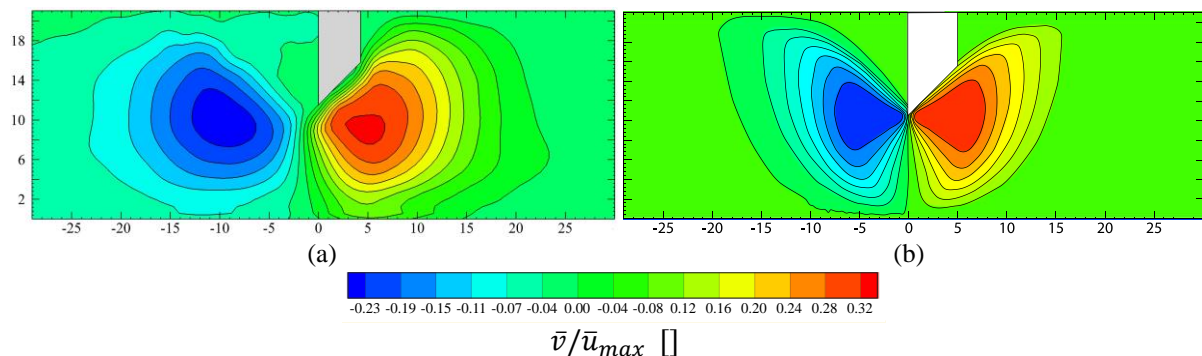


Figure 3.103 Averaged vertical velocity field of an (a) experimental aqueous foam and a (b) CFD Bingham fluid flowing through a fence.

The vertical velocity fields show the influence of the gravity forces and the difference that this one creates over the two studied fluids, foam flow and Bingham fluid. The presence of the fence at the upper part of the barrier forces the fluids to change their displacement pattern, and axially accelerate under the obstacle. As they approach the fdd, a negative acceleration is triggered, and the fluids flow downwards to the bottom of the channel. At this point under the fence, a state is reached where the

axial velocity is predominant and the vertical component becomes zero. Once the obstacle is surpassed, the lower density of the fluids drives them towards the upper part of the channel. Downstream from the fdd, they recover their initial behavior, with a one-dimensional flow and no influence of the vertical component. The main difference between the cases is the symmetry at both sides of the flow disruption. The foam flow is then influenced by the gravity and its internal properties, gas phase compressibility property, disjoining pressure, surfactants, and surface tension. In comparison, for the Bingham fluid the compression, the expansion and the gravity forces don't alter as much its behavior.

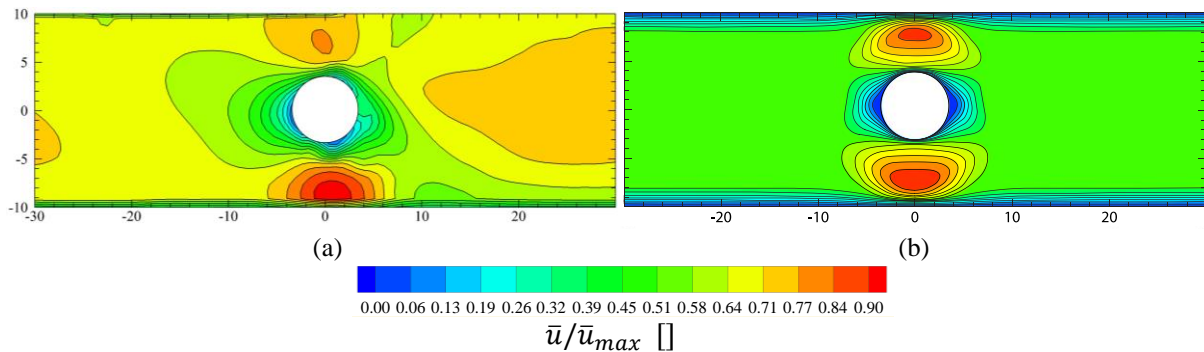


Figure 3.104 Averaged axial velocity field of an (a) experimental aqueous foam and a (b) CFD Bingham fluid flowing through a cylinder.

The axial average velocity fields of aqueous foam with a quality of 70%, and of the Bingham fluid show their different behavior when exposed against a cylinder. This type of fdd disrupts the pattern of the fluid by half, and makes its reorganization after it has gone through it. Both fluids exhibit a plug (one-dimensional) flow, upstream and downstream of the fdd. This shows the capacity that the Bingham fluid has to represent the visco-elastic properties of the foam. Getting near the cylinder a stagnation zone is formed. Any fluid close to the obstacle will scale down its velocity to a zero movement state at the direct contact with it. At the bottom of the channel, the axial velocity component shows a more significant value than at the top, mainly due to the influence of the gravity forces, although for the foam flow, the liquid slip-layer plays an important role over this axial acceleration. The Bingham fluid is less affected by the gravity than the real foam flow. Therefore, the axial velocity acceleration near the top part of the channel, directly over the cylinder, presents a higher mean value for the Bingham fluid than that of foam flow. The axial acceleration under the cylinder, presents a similar difference than that reported for the fence. The liquid slip-layer is not an easy phenomenon to represent numerically making a change in the acceleration surface.

The average axial velocity fields near the cylinder are highly influenced by the gravitational forces making some differences between the foam flow and Bingham fluid. Upstream and downstream of the obstacle, the presence of a flow regime with a predominant axial one-dimensional component is validated by the absence of vertical velocities. When approaching the fdd, two acceleration processes set off: an upward movement passing over the cylinder -near the top of the flow disruption-, and a downward one -accelerating under the obstacle. At $x = 0$, the fluids change their pattern with a transition at the middle of the obstacle, where the vertical component is null. Exiting the cylinder, the fluids recover their initial state, due to their visco-elastic properties, with an opposite behavior as the one upstream. The foam flow is highly affected by the gravity and its internal properties, seen in the presence of the fence. This creates an asymmetry in velocity magnitudes at both sides of the fdd. The Bingham fluid's density remains constant along the whole length of the channel. As for the foam flow, its density and vertical void fraction is constantly evolving, especially near the vicinities of the singularities. This is the main reason for the deviations between the CFD and experimental results.

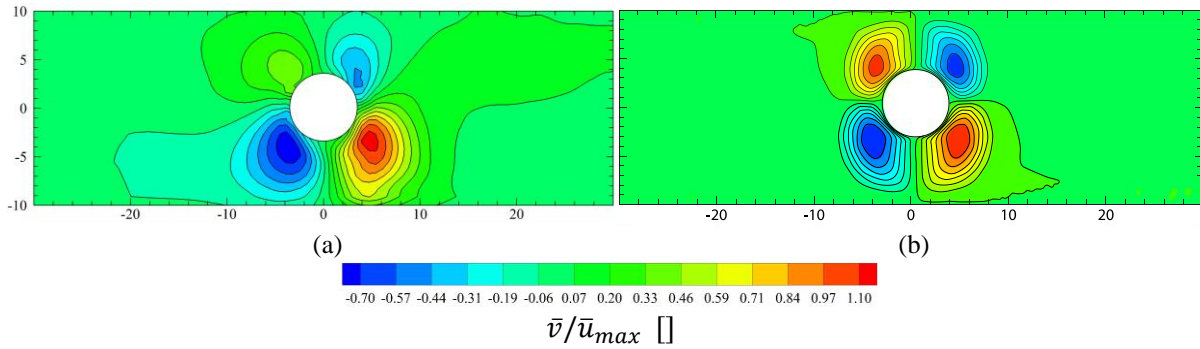


Figure 3.105 Averaged vertical velocity field of an (a) experimental aqueous foam and a (b) CFD Bingham fluid flowing through a cylinder.

3.5 Averaged axial and vertical velocity profiles

The velocity profiles allow a better comparison between the foam flow and the numerical simulations using a Bingham fluid. They were obtained near its influence zone, starting at $x = -25 \text{ mm}$ and finishing at $x = 25 \text{ mm}$. The average axial and vertical velocities profiles are represented in Figure 3.106 and Figure 3.108 for a foam flow with a void fraction of 70% and Bingham fluids trying to predict and represent its behavior. The velocity fields showed overall similarities and, differences, the profiles will allow their quantification.

The averaged axial velocity profiles for the half-sudden expansion prove that both, the foam and the Bingham fluid have a similar behavior when faced against this kind of fdd. They maintain their one-dimensional, piston, flow until the section change. Once it is reached, they both slow down, until reaching an equilibrium state where the vertical displacement disappears and, once again, an axial flow sets in. At this point, the bulk velocity for the foam flow is 1 cm/s and for the Bingham fluid 1.1 cm/s. This represents a difference of 10% between the two of them, the largest difference for all the velocity profiles surrounding the fdd. The axial velocity profiles also confirm the presence of a stagnation zone downstream of the fdd for both cases, where the mean value is zero. Once the fluids go through the expansion, they flow upward the upper wall of the channel, trapping some of it in the immediate neighborhood of the expansion. The stagnation zone has different surfaces, being bigger than that of the Bingham fluid, which is not formed by air and presents a slower expansion rate. The absence of negative velocity values, especially inside the stagnation region, indicates that there is no back flow, and no vortices formation.

The vertical velocity profiles over the half-sudden expansion, also confirm the absence of a block-flow upstream and downstream of the fdd, where their values are zero. In the downstream vicinity of the fdd, where the surface change occurs, the vertical velocity is more important for both the foam and the Bingham fluid. This behavior is directly related to the low density and expansion properties of both fluids. They present upward movement trying to occupy completely the height of the channel. The stagnation zone is also present in these results with a zero value near the top of the channel, once the fluids have gone through the expansion. The average vertical velocity profiles present a maximal deviation of 24% between the two cases, especially near the fdd where many factors influence the behavior.

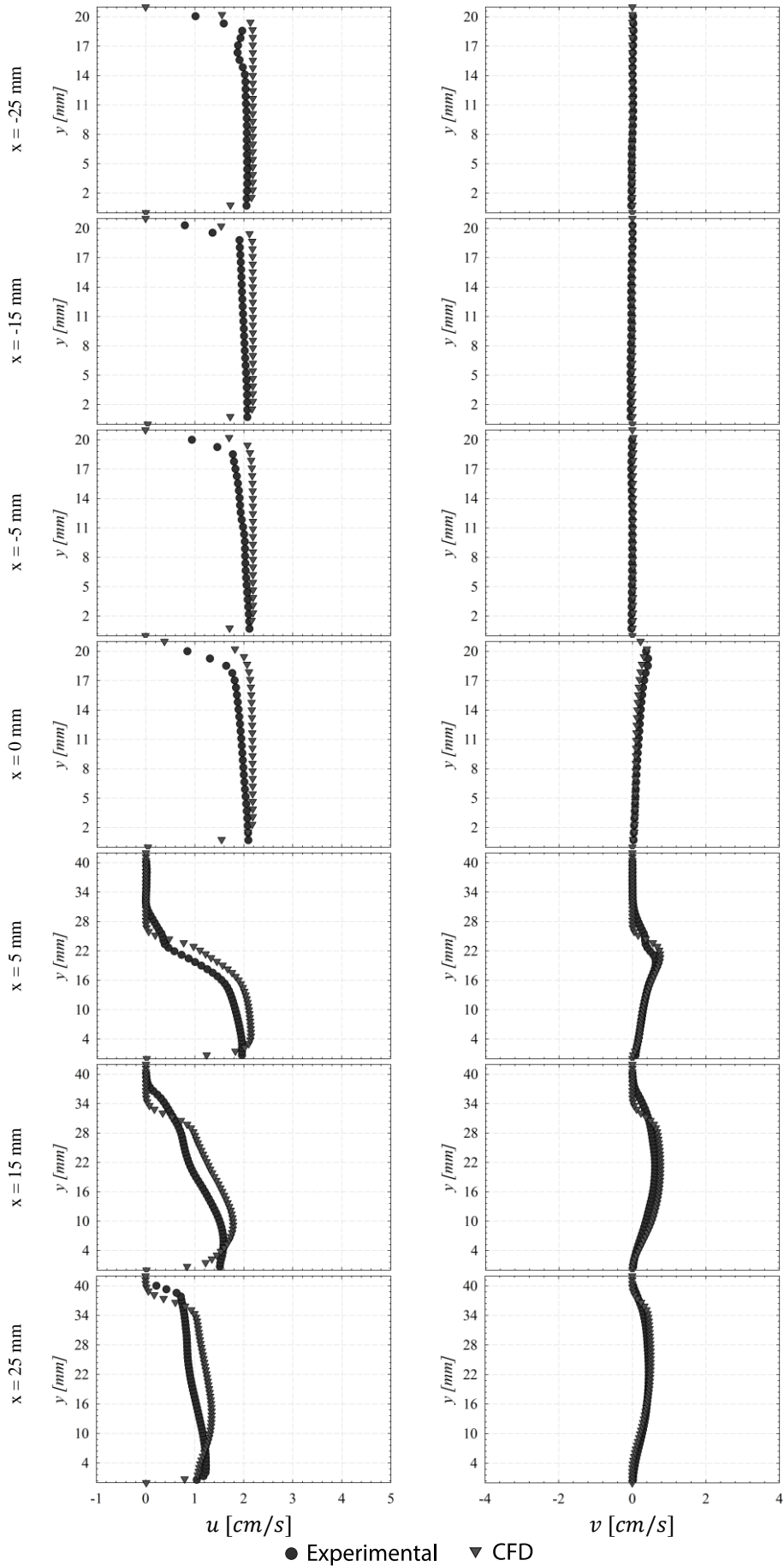


Figure 3.106 Averaged axial and vertical mean velocity profiles for aqueous foam and a Bingham fluid going through a half-sudden expansion.

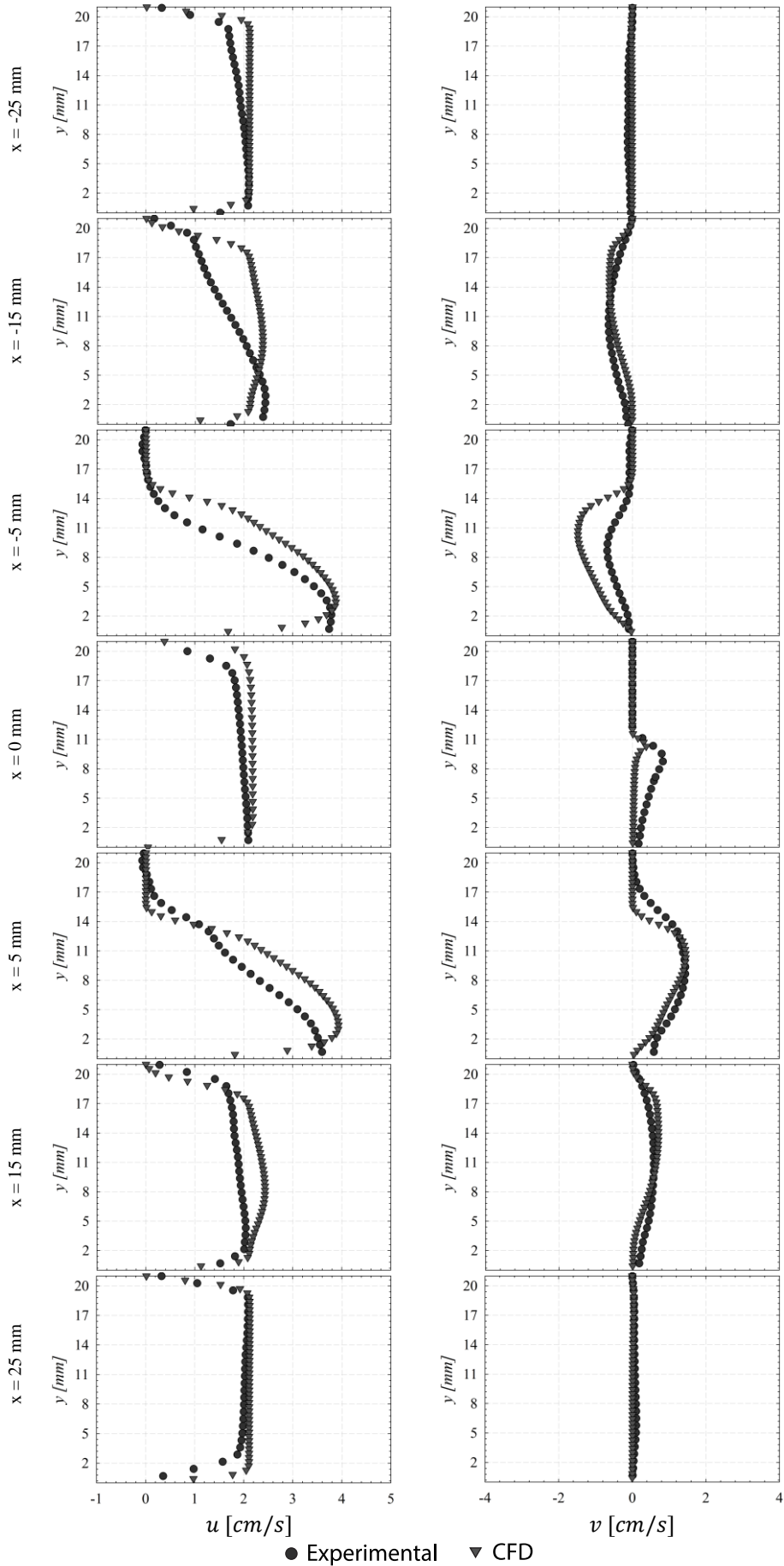


Figure 3.107 Averaged axial and vertical mean velocity profiles for aqueous foam and a Bingham fluid going through a fence.

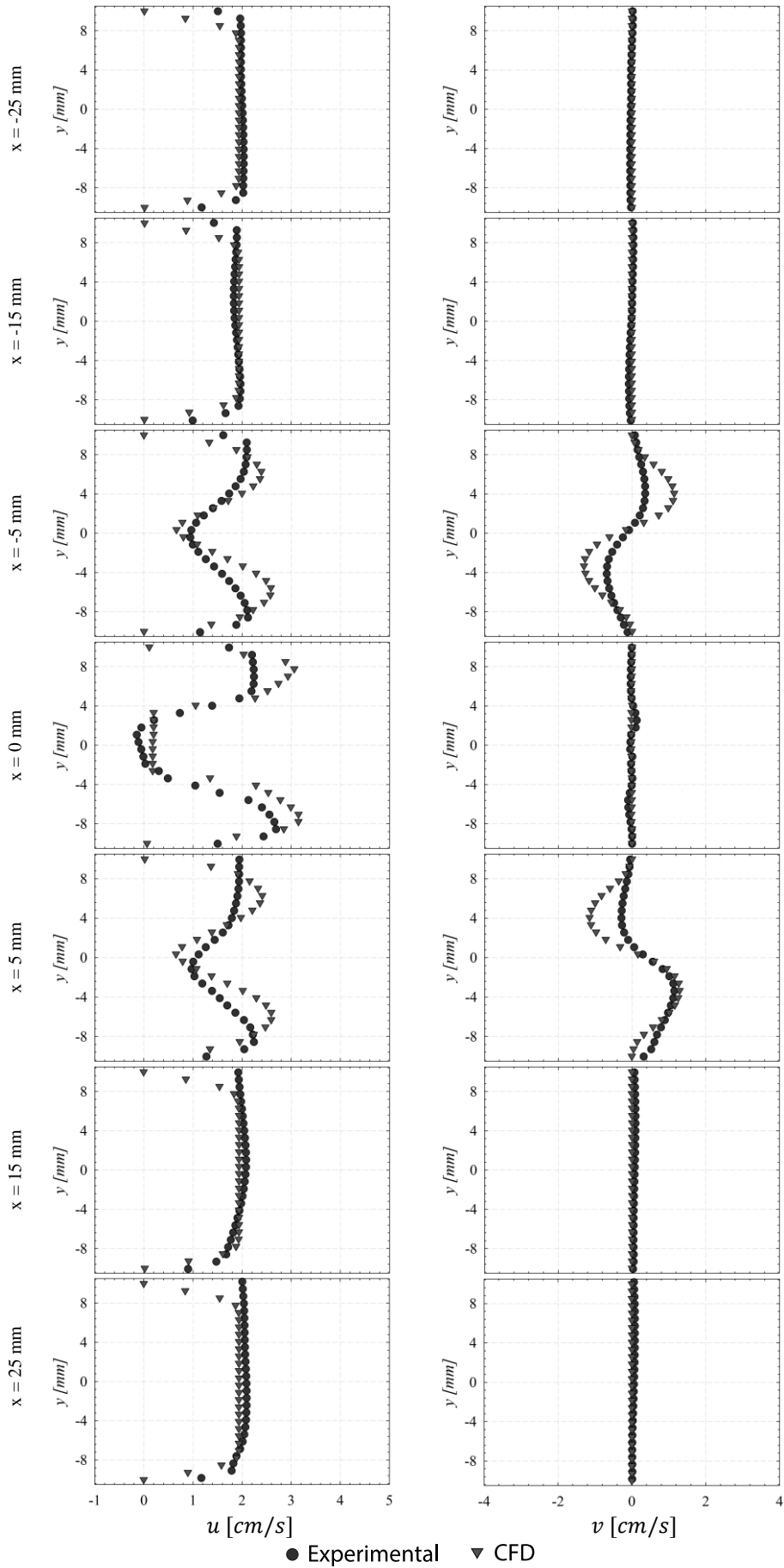


Figure 3.108 Averaged axial and vertical mean velocity profiles for aqueous foam and a Bingham fluid going through a cylinder.

The axial and vertical velocity profiles of foam and a Bingham fluid, over a fence, show that both are affected in the same way by the obstacle. They gradually reduce the axial velocity and increase the vertical one, towards the bottom of the channel, upstream of the fdd. At the top of the channel, upstream of the fence, the fluids stop completely, creating a stagnation zone, with similar dimension in both cases. Downstream of the fdd, the axial acceleration diminishes, and upward displacement sets in, as both fluids refill the whole height of the channel. This phenomenon creates a second stagnation region at the other side of the fence. A similar profile develops as the one seen upstream of the fence, with a bulk velocity of 2 cm/s. The largest deviation occurs directly under the fence ($x = 0$) with a percentage of 45%. This difference is mainly due to the influence of the liquid slip-layer, and to the viscous-plastic response of the foam.

The vertical velocity profiles show that the surface reduction creates a descending vertical movement towards the passage section, below the fdd. The transition zone under the fence presents a vertical velocity magnitude value of zero. Once the fluids leave the obstacle, and occupy the full channel's section, they present positive vertical displacement. Downstream, far from the fdd influence, the fluids recover their initial state. The biggest deviation between the two fluids is seen upstream of the fdd ($x = -5 \text{ mm}$) with a difference of 50%. This is mainly result from to the foam's gas phase resisting the surface change and compression, which opposes the downward displacement and slow down the fluid. It is impossible for the Bingham fluid to represent this phenomenon.

Reviewing average and vertical velocity profiles for the fluids going through a cylinder an axial velocity acceleration can be seen near the fdd. A maximum value of 2.8 cm/s is reached under the cylinder for the experimental results, and 3.2 cm/s for the CFD simulations. Once the flow passes across the obstacle, both cases return to the initial state, plug flow with a bulk velocity of 2cm/s. The flow in contact with the surface of the cylinder slows down, creating a stagnation zone near the upstream and downstream sides of the obstacle. The absence of negative values indicates that, despite the presence of an obstacle, there are no recirculation zones due to the rheological properties of these two fluids. The CFD simulation results show a good approach to the experimental measurements with a maximal difference of 28% near the upper side of the channel ($x = -5 \text{ mm}$).

For the same plane, over the channels lateral wall, the vertical velocity profiles between the Bingham fluid and the foam flow are evaluated. The influence of the fdd over the vertical component is most notable near its vicinity ($x = -5 \text{ mm}, 0 \text{ mm and } 5 \text{ mm}$). The gravity forces and internal properties play an important role on the vertical velocity foam behavior. The Bingham fluid does not contemplate as well this aspect. The cylinder creates a change in the upstream one-dimensional regime, and acceleration through both sides. The negative displacement, going under the cylinder, is helped by the gravitational forces. These forces slow the other movement, which goes in the positive vertical direction. When the fluid has gone through the fdd it returns, to its initial state, as showed in the axial component evolution. The CFD simulations and the experimental results provide the same behavior. However, there are some deviations on the velocity profiles, especially close to the fdd, up to 50%. This results from the Bingham fluid not being affected, as much as the foam, by the gravitational forces and internal properties.

3.6 Conclusions

CFD simulations of a Bingham fluid through a square channel, with three different fdd, half-sudden expansion, fence and cylinder, were compared with the experimental results of an aqueous foam flow under the same conditions. Pressure losses along the channels' length, the velocity fields and the velocity profiles near the fdd. The CFD simulations and the experimental results showed

similar evolution. Both fluids, foam flow and Bingham fluid, behave equally when faced against these three different fdd. For the pressure distribution along the channels length through the three flow disruptions, the CFD simulations and experimental measurements present the same behavior with a maximum deviation of 5%. As for the velocity fields and profiles, the slipping conditions of bubbles along the channels wall, the gas phase properties and other internal forces inside the foam flow play a major role in the results differences. Nevertheless, for a model as simple as the Bingham fluid, the approximation to the real physical aspect is relatively good. Most of the results present a deviation of 30% between the foam flow and the numerical simulations. Higher deviations are obtained when the complexity of the problem increases near the vicinity, of fdd, reaching values of 50%. This means that the numerical simulations are able to simulate the visco-elastic properties of the foam, but when a visco-plastic regime sets in, near the fdd, the CFD simulation doesn't represent properly the phenomenon. Accepting these limitations, these results show that a Bingham model is able to predict the main behavior of important parameters of the foam, for a one-dimensional plug flow against three different fdd, half-sudden expansion, fence and cylinder.

As seen along this whole study, an interesting aspect of the foam flow is its capacity to exert a high wall shear stress over a horizontal channel's wall. In order to be able to obtain this one it is of paramount importance to have an accurate value of the wall velocity gradient. From the CFD results we were able to obtain similar velocity fields to those ones seen over aqueous foam. However, for all foam flow cases and qualities, we assumed that the wall velocity gradient was linear inside the liquid film layer and that this one was related to the velocity value of the bubbles sliding over. These assumptions showed us a wall shear stress value far from the real ones. Therefore, repeating the same study with the CFD velocity fields will lead to similar results.

GENERAL CONCLUSIONS

This experimental and CFD numerical work is based on the study of rheological and physical properties of a horizontal aqueous foam flow.

This study is a continuation of the works of Blondin [3], Tisné [51] and Madani [113]. The main objective was to review information concerning aqueous foam flow related to: its physics, stability and hydrodynamics. Additionally, it intended creating a database to validate rheological models, looking to predict the behavior and reorganization of horizontal aqueous foam flow. The work would apply these studies and developments to compare a simple rheological model with the experimental results, and evaluate the similarities and differences.

The literature survey concerning the physics of foam allowed a solid foundation over which the experimental and numerical works were based. The main bibliographic investigation concerned the structure and stability of the foam, its rheology and other physical aspects. Foam has been a major subject of study for mathematicians and physicists. Empiric and semi-empiric models have been used to explain its behavior. These models were developed for dry foams with void fractions over 85% that has few industrial applications. An area not considered has been that of the horizontal aqueous foam, which is applied in all kind of industrial processes and agro alimentary products' manufacturing.

The results of Blondin [3] over an aqueous foam flow inside a channel showed that the ratio, between the pressure losses and the wet perimeter, generated inside two channels with the same height but different lengths. This means that the wall shear stress generated along the channels' length was not uniform. Tisné [51], tried to validate an innovative measurement technique: the "Polarographic Method". It measures the mass transfer between the fluid and some probes mounted over at the wall, and thereof the wall shear stress can be deduced. Madani [113], studied the velocity fields and profiles and the forced drainage obtained for a foam flow over a half-sudden expansion.

We selected these basic works, and others, to assist us at a preliminary spread database. Having at hand the experimental facility and measurement techniques used for these research works and modified it for our special study, we advanced to a more complete and organized database. The experimental study was focus on horizontal foam flow with a foam quality of 55%, 60%, 65%, 70%, 75%, 80% and 85%, three different velocities, 2 cm/s, 4 cm/s and 6 cm/s and three flow disruption devices (fdd): half-sudden expansion, fence, and cylinder.

In order to simplify the complexity of the study and control the variables related to foam flows, two scenarios were considered. A horizontal straight channel with no fdd was used to measure pressure losses, velocity profiles, liquid film thicknesses and wall shear stress using, pressure outlets, particle imaging velocimetry (PIV), conductimetry probes, and polarographic probes. To learn of the rheology of foam flows, a second set of experiments were made over a horizontal square straight channel with an exchangeable measure section that allowed us to obtain the pressure losses, velocity fields and velocity profiles of over the three fdd: half-sudden expansion, fence and cylinder.

For the first scenario, when there are no fdd, the static pressure varies linearly, along the channels length. It is a function of the foams velocity. Higher velocities will present bigger pressure losses. Despite the difference in foam quality, they showed a similar pressure behavior and value.

The velocity profiles, obtained at the lateral wall, the top wall of the channel, and liquid/foam interphase, with the PIV, exhibit three flow regimes:

- One-dimensional flow: the foam flows like a block sliding over the channel's walls,
- Two-dimensional flow: the foam is partially sheared. It slides over the channel's walls,
- Three-dimensional flow: The foam is completely sheared and it slides over the channel's walls.

The wall shear stress plays a major role in the rheology of foams, as shown by the pressure losses of foam flowing through a square channel, behavior of their velocity profiles, and bubble channel wall slippage. The polarographic method shows many advantages for measuring shear stresses of fluids over the wall. This method is based on the electrochemical reactions in micro-probes measuring electron exchange that relate to the wall shear stress. However, the walls must stay wet by the liquid film, being then important for its measurements.

Besides carrying out conductimetry and polarographic measurements, we theoretically reviewed the influence of liquid film thickness and wall shear stress over the convection-diffusion equation -and our polarographic probes ability- to measure this phenomenon. From the convection-diffusion general equation, a relationship was established between the current from the probes, the wall shear stress and the liquid film. It shows the conditions that are not optimal and where the diffusion limiting current is not achieved.

The conductimetry measurements' signals obtained at the top and lateral walls of the channel showed that the maximal and mean thicknesses, in the order of few micrometers were not significant. At the bottom of the channel, due to the gravitational drainage, the liquid film presents higher values. Therefore, attention was given to the top and sides of the channel, where the liquid thicknesses may condition the polarographic probes' response. It can be noted, that there is no influence of the quality and the velocity on the liquid film thicknesses.

The polarographic measurements were made at the top, bottom and one lateral wall of the channel. They presented a very high oscillating behavior, related to a wall shear stress reduction, as the bubbles crossed the probe. The mean wall shear stress values, obtained through this innovative method, were compared with the ones calculated by the pressure losses, which give an accurate mean value. As the velocity increases, the difference between the polarographic and the static pressure results diminish. The theoretical study showed a relationship between the probes response, and the wall shear stress measured. Larger stresses are related to higher velocities, which may reach easier the limit diffusion current. The observation that there is no difference between foam qualities and the local wall shear stresses, prove again the occurrence of different regimes.

Previous studies analyzed the causes of the oscillating signals, especially over the lateral and top walls of the channel on the conductimetry and polarographic measurements. The smaller oscillating thickness values are related to the bubbles passage over the measurement probes, and change in the thickness of the liquid film in contact with the probe. As for the polarographic signals measuring the wall shear stress, a theoretical study proved that the oscillating behavior was in fact originated by a reduction in the wall shear stress, not linked to the thickness oscillation by the bubbles passage. To characterize their behavior, all oscillating signals were subject to a probability analysis.

For the second case, of a straight channel in presence of fdd, the Particle Imaging Velocimetry (PIV) technique allowed to evaluate the axial and vertical velocity components of the foam, upstream, downstream and near the half-sudden expansion, the fence and the cylinder. These measurements confirmed the presence of three foam flow regimes, despite the existence of fdd in the channel. They also allowed understanding the reorganization that foam flow suffers, once its pattern has been changed including its visco-elasto-plastic properties.

The static pressure study verified the linear variation of the foam, which occurs in the upstream and downstream because of the influence of the fdd. There is a transition zone between the two side of the half-sudden expansion, the fence and the cylinder where the pressure losses reflect a change of state with no difference of foam qualities. However, faster velocities are associated to larger pressure gradients, at both sides of the fdd.

The transport characterization of foam flow brings to major areas of study: stability and rheology. Many parameters are involved, void fraction, bubbles packing and size, thickness of the liquid film, drainage and coalescence. Simplifying these variables allows predicting its behavior without so many constrains. The important aspects of any rheological model are shear stress, yield and yield stress. They are related to the velocity fields, velocity profiles and pressure losses. They were included in a CFD simulation trying to represent the behavior of the foam flow over the three different fdd, to validate the rheological model. When a Bingham fluid was used it did show similarities. However, there are some visco-elasto-plastic properties of the foam flow that this kind of fluid cannot simulate. Along with, some points near the fdd vicinities presented high deviations.

CFD provide an approximation on the way to see the behavior of certain fluids, without the need of experimental analysis. There are no usual rheological models that can predict the behavior of foam flow, once the one-dimensional flow has disappeared and axial velocity components depend on the y and z coordinate. For the cases II and III, the liquid slip-layer plays a major influence over the foam velocity fields and profiles. A fluid allowing prediction of this behavior, should be stratified in three zones, where this fluid can present the following characteristics:

- The first region, for the liquid slip-layer, will only present the liquid phase. This film spread all along the channels bottom will have a thickness of 1.5mm approximately.
- The second region is composed of flowing foam, or a rheological fluid capable of predicting its behavior even a Bingham fluid, with an imposed velocity profile.
- Finally, the third region is similar to the first one, but this one is located at the top of the channel. It presents only a liquid phase and a thickness of a few micrometers.

The perspective for future studies are still numerous, despite that this study took into consideration many foam characteristics, cases and qualities this subject has still many aspects to investigate. All the studies done in this work were focused on the surroundings of the foam flow, especially inside the liquid slip-layer. The characteristics in the foam core are unknown. There are two measurements techniques that are able to study the properties in this are: the optic probe and the ultrasound methods. Being the best one the ultrasound one. They do not influence the behavior of the foam and they should be put into use to obtain important characteristics inside the foam.

The same experiences should be done for faster foams, adding more generators will keep a foam structure constant, allowing the increment in flow. A detailed study over the liquid slip-layer hydrodynamics is important, its characteristics and scales make difficult the data acquisition in this region. At the same time, looking at the influence that the underlying liquid slip layer has over the

foam velocity fields, it can be interesting to study a foam flow that does not present this characteristic. In order to do so, a cavity at the bottom of the channel can be placed after the foam generators exit. It will recover the liquid inside the lower film and, with the proper measurements, calculate the topological and physical changes suffered by foam flow. To study the stability of the foam, a numerical image processing could be used to analyze the effect of the fdd over the coalescence bubbles rearrangement, and coarsening. Other fdd could be used to keep studying the foam rheology and behavior, like a half-sudden narrowing. The polarographic technique can also be applied over the fdd surfaces and analyze the wall shear stress that these ones suffer.

The upcoming CFD simulations for numerical studies should focus in closing the gap between the physical reality and the CFD simulations. Making a stratified flow could be a good alternative, varying the properties of the core fluid. Also, more complex rheological models might be able to better represent the visco-elasto-plastic properties of the foam. Obtaining the flow behavior index, for the power law fluid, is a good approach. This one will allow understanding if the flow is pseudoplastic or dilatant. In the case of the Bingham fluid, it is assumed to be one, with a yield stress. Also, understand if this one is a function of the foam quality or the bubbles diameter.

Future studies and models on this kind of flow can be as complex, inclusive and encompassing as their development and operations may justify them. The basic problem involving foam, and their flow, is its constant evolution in properties through space and time, as result of many factors, without forgetting, its composition. This study has allowed us to validate the use of several models and techniques to predict certain flow situations, and facilitate additional research in this intriguing and important field [143,144,145,146,147,148,149].

REFERENCES

- [1] Wearie D. and Hutzler S., *The Physics of Foams*. New York: Oxford University Press, 1999.
- [2] Stevenson P., *Foam Engineering: Fundamentals and Applications*. Auckland, New Zealand: John Wiley & Sons, 2012.
- [3] E. Blondin, *Etude experimentale d'une mousse humide en écoulement en conduite horizontale de section rectangulaire*, Ph.D. Thesis, Nantes, France, 1999.
- [4] Aloui F., Tisné P., Legrand J., and Doubriez L., "Limits of the electrochemical method for the determination of wall shear stresses in wet foam flows", in *Cost F2 2nd Workshop*, Aachen, Germany, 2002.
- [5] ANSYS Inc. ©, *ANSYS 14.0 Help Guide*. Canonsburg, 2011.
- [6] Herzhaft B., Kakadjian S., and Moan M., "Measurement and modeling of the flow behavior of aqueous foams using a recirculating pipe rheometer", in *Proc. of 5th European Conference on Foams, Emulsions and Applications*, France, 2005, pp. 263(1–3): 153–164.
- [7] Feitosa K. and Durian D.J., "Gas and liquid transport in steady-state aqueous foam", *European Physical Journal*, pp. 26(3): 309–316, 2008.
- [8] Ireland P.M., "Coalescence in a steady-state rising foam", *Chemical Engineering Science*, pp. 64(23): 4866–4874, 2009.
- [9] Gabrielaitiene I. and Gylys J., "Modelling of aqueous foam flow for developing energy-efficient heat exchanger applications", in *The 8th International Conference of Environmental Engineering*, Vilnius, Lithuania, 2011, pp. ISSN 2029-7106.
- [10] Thomson W., "On the division of space with minimum partitional area", *Phil. Mag.*, vol. 24, no. 151, p. 503, 1887.
- [11] Valko P. and Economides M.J., "Flow properties of foam with and without solid particles", *Ind. Eng. Chem. Process Des. Dev.*, vol. 24, pp. 748-753, 1992.
- [12] Ezendorfer C., Harris R.A., Valko P., and Economides M.J., "Pipe viscosimetry of foams", *J. Rheol.*, vol. 39, pp. 345-358, 1995.
- [13] Boissonnet G., Faury M., and Fournel B., "Decontamination of nuclear components through the use of foams", *Foams and Emulsions*, pp. 323-334, 1999.
- [14] Matzke E.B., "Volume-shape relationships in variant foams. A further study of the role of the surface forces in three-dimensional cell shape determination", *Am. J. Botany*, vol. 33, p. 58, 1946.
- [15] Saint-Jalmes A. and Durian D.J., "Vanishing elasticity for wet foams: Equivalence with emulsions and role of polydispersity", *J. Rheol.*, vol. 43, pp. 1411-1422, 1999.
- [16] Weaire D., Lanlgois V., Saadatfar M., and Hutzler S., "Foam as granular matter", *Granular and Complex Materials, World Scientific Lecture Notes in Complex Systems*, vol. 8, pp. 1-26, 2007.
- [17] Weaire D., Hutzler S., Verbist G., and Peters E., "A review of foam drainage", *Advances in Chemical Physics*, vol. 102, pp. 315-373, 1997.
- [18] Nakoryakov V.E., Pokusaev B.G., and Shreiber I.R., *Wave propagation in Gas-Liquid Media*. Boca Raton: CRC Press, 1993.

- [19] Mysels K.J. and Jones M.N., "Direct measurement of the variation of double-layer repulsion with distance", *Discuss. Faraday Soc.*, vol. 42, p. 42, 1966.
- [20] Claesson P.M., Ederth T., Bergeron V., and Rutland M.W., "Techniques for measuring surface forces", *Adv. Coll. Interface Sci.*, vol. 67, p. 119, 1996.
- [21] Plateau J.A.F., "On Foam Borders and Laws", *Mem. Acad. Roy. Sci. Belg.*, vol. 33, no. 5th and 6th, 1861.
- [22] Cohen-Addad S., Hoballah H., and Höhler R., "Viscoelastic response of a coarsening foam", *Phys. Rev.*, vol. 57, pp. 6897-6901, 1998.
- [23] Russell A., "Process innovation from research and development to production in a large company: development and commercialisation of a low temperature extrusion process.", in *Case Studies in Food Product Development*. Newbury: CPL Press, 2007.
- [24] Alavi S.H., Rizvi S.S.H., and Harriot P., "Process dynamics of starch-based microcellular foams produced by supercritical fluid extrusion", *Food Res. Int.*, vol. 36, pp. 309-319, 2003.
- [25] Martin P.J., Tasell A., Wiktorowicz R., Morratt C.J., and Campbell G.M., "Mixing bread doughs under highly soluble gas atmospheres and the effects on bread crumb texture: experimental results and theoretical interpretation.", in *In Bubbles in Food 2: Novelty, Health and Luxury*.: Eagan Press, 2008.
- [26] Ran L., Jones S.A., Embely B., Tong M.M.; Garret P.R., Cox S.J., Grassia P., and Neethling S.J., "Characterisation, modification and mathematically modelling of sudsing", *Coll. Surf. A: Physicochem. Eng. Aspects*, pp. doi:10.1016/j.colsurfa.2010.11.028, 2010.
- [27] Pichot R., Spyropoulos F., and Norton I.T., "Mixed-emulsifier stabilised emulsions: Investigation of the effect of monoolein and hydrophilic silica particle mixture on the stability against coalescence", *J. Coll. Int. Sci.*, vol. 329, pp. 284-291, 2009.
- [28] Myers D., *Surfactant Science and Technology*. New York: 3rd edn. Wiley, 2006.
- [29] Shafi M.A., Joshi K., and Fumerfelt R.W., "Bubble size distributions in freely expanded polymer foams", *Chem. Eng. Sci.*, vol. 52, pp. 635-644, 1997.
- [30] Niranjana K. and Silva S.F.J., "Bubbles in food: creating structures out of this air", in *Food Engineering: Integrated Approaches*. New York: Springer, 2008.
- [31] Gallart M., Tomás X., Suberbiola G., López-Tamames E., and Buxaderas S., "Relationship between foam parameters obtained by the gas-sparging method and sensory evaluation of sparkling wines", *J. Sci. Food Agric.*, vol. 84, pp. 127-133, 2004.
- [32] Egron P.E., *Étude Expérimentale d'une mousse en écoulement dans une conduite horizontale de section carrée: Influence de la variation de la proportion volumique de gaz*. Nantes, France: Master Sci. Report (DEA), 2003.
- [33] Lemlich R., "A theory for the limiting conductivity of polyhedral foam at low density", *J. Coll. Interface Sci.*, vol. 64, pp. 107-110, 1978.
- [34] Datye A.K. and Lemlich R., "Liquid distribution and electrical conductivity in foam", *Int. J. Multiphase Flow*, vol. 9, pp. 627-636, 1982.
- [35] Phelan R., Weaire D., Peters E., and Verbist G., "The conductivity of foam", *J. Phys.: Condens. Matter*, vol. 8, pp. 475-482, 1996.
- [36] Hutzler S., Verbist G., and Weaire D., "Measurement of a foam density profiles using AC capacitance", *Europhys. Letters*, vol. 31, pp. 497-502, 1995.
- [37] Barber C.D., Brown B.H., and Freeston I.L., "Imaging spatial distribution of resistivity using applied potential tomography", *Elec. Lett.*, vol. 19, pp. 933-935, 1983.

- [38] Dickin F.J. and Wang M., "Impedance sensors-conducting system", *Process Tomography*, pp. 63-84, 1995.
- [39] Koehler S.A., Hilgenfeldt S., and Stone H.A., "Liquid flow through aqueous foams: the node-dominated foam drainage equation", *Physical Review Letters*, vol. 82, pp. 4232-4235, 1999.
- [40] Magrabi S.A., Dlugogorski B.Z., and Jameson G.J., "Free drainage in aqueous foams : model and experimental study", *AIChE Journal*, vol. 47, pp. 314-327, 2001.
- [41] Wood A.B., *A textbook of sound*. London: Bell, 1941.
- [42] Durian D.J., Weitz D.A., and Pine D.J., "Multiple light scattering probes of foam structure and dynamics", *Science*, vol. 252, pp. 686-688, 1991.
- [43] Bispernik C.G.J., Ronteltap A.D., and Prins A., "Bubble size distribution in foams", *Advances in Colloid and Interface Science*, vol. 38, pp. 13-32, 1992.
- [44] Ronteltap A.D. and Prins A., "Food Colloids", *Royal Society of Chemistry Special Publication No. 75*, pp. 39-47, 1989.
- [45] Aloui F., *Etude des écoulements monophasiques et diphasiques dans les élargissements brusques axisymétrique et bidimensionnel*. Nancy, France: Ph.D. Thesis, 1994.
- [46] Galaup J.P., *Contribution à l'étude des méthodes de mesure en écoulement diphasique*. Grenoble, France: Ph.D. Thesis, 1975.
- [47] Fains A., Bertrand D., Baniel A., and Popineau Y., "Stability and texture of protein foams: a study by video analysis", *Food Hydrocolloids*, vol. 11, pp. 63-69, 1997.
- [48] Cheng H.C. and Lemlich R., "Errors in the measurements of bubble size distribution in foam", *Ind. Eng. Chem. Fundam.*, vol. 22, pp. 105-109, 1983.
- [49] De Vries A.J., "Morphology, coalescence and size distribution of foam bubbles", *Adsorptive Bubble Separation Techniques*, 1972.
- [50] Boissonnet G., *Étude de l'écoulement d'une mousse aqueuse de décontamination. Mécanismes de drainage et comportement hydrodynamique*. Montpellier, France: Ph.D. Thesis, 1998.
- [51] Tisné P., *Étude par la méthode polarographique des contraintes pariétales exercées par une mousse en écoulement*. Nantes, France: Ph.D. Thesis, 2003.
- [52] Di Meglio J.M. and Baglioni P., "Local dynamics of foam drainage investigated by ESR", *J. Phys.: Condens. Matter*, vol. 6, pp. 375-380, 1994.
- [53] Yamanaka T., Tano T., Kamegaya O., Exerowa D., and Cohen R.D., "Effects of meal-ions on the equilibrium thickness of foam films stabilized by lysophosphatidylcholine as studied by FT-IR spectroscopy", *Langmuir*, vol. 10, pp. 1871-1876, 1994.
- [54] Platikanov D., Graf H.A., Weiss A., and Clemens D., "X-ray scattering by black foam films-new data analysis", *Coll. Polymer Sci.*, vol. 271, pp. 106-107, 1993.
- [55] Mysels K.J., Shinoda K., and Frankels S., *Soap films: studies of their thinning, and a bibliography*. New York: Pergamon, 1959.
- [56] Weaire D., "The rheology of foam", *Curr. Opin. Coll. Interface Sci.*, vol. 13, p. 171, 2008.
- [57] Marze S., Langevin D., and Saint-Jalmes A., "Aqueous foam slip and shear regimes determined by rheometry and multiple light scattering", *J. Rheol.*, vol. 52, p. 1091, 2008.
- [58] Princen H.M., "Rheology of foams and highly concentrated emulsions: I. Elastic properties and yield stress of a cylindrical model system", *J. Coll. Interface Sci.*, vol. 91, p. 160, 1983.
- [59] Princen H.M., "The structure, mechanics, and rheology of concentrated emulsions and fluid foams", *Encyclopedia of Emulsion Technology*, 2001.
- [60] Van Hecke M., "Topical review: Jamming of soft particles: geometry, mechanics, scaling and

- isostaticity”, *J. Phys.: Condens. Matter*, vol. 22, 2010.
- [61] Edwards D.A., Wasan D.T., and Brenner H., *Interfacial Transport Processes and Rheology*. Boston: Butterworth-Heinemann, 1991.
- [62] Labiausse V., Hohler R., and Cohen-Addad S., "Shear induced normal stress differences in aqueous foams”, *J. Rheol.*, vol. 51, p. 2007, 2007.
- [63] Buzza D.M.A., Lu C.-Y.D., and Cates M.E., "Linear shear rheology of incompressible foams”, *J. Physique II France*, vol. 5, p. 37.
- [64] Larson R.G., *The Structure and Rheology of Complex Fluids*. New York: Oxford University Press, 1999.
- [65] Rouyer F., Cohen-Addad S., Vignes-Adler M., and Höhler R., "Dynamics of yielding observed in three-dimensional aqueous dry foams”, *Phys. Rev. E.*, vol. 67, pp. 021405-021407, 2003.
- [66] Picard G., Ajdari A., Lequeux F., and Bocquet L., "Elastic consequences of a single plastic event: A step towards the microscopic modeling of the flow of yield stress fluids”, *European Phys. J. E.*, vol. 15, p. 371, 2004.
- [67] Debregeas G., Tabuteau H., and Di Meglio J.-M., "Deformation and flow of a two dimensional foam under continuous shear”, *Phys. Rev. Lett.*, vol. 87, p. 178305, 2001.
- [68] Raufaste C., Cox S.J., Marmottant P., and Graner F., "Discrete rearranging disordered patterns: Prediction of elastic and plastic behaviour, and application to two-dimensional foams”, *Phys. Rev.*, vol. 81, p. 03404, 2010.
- [69] Weaire D. and Drenchan W., "Structure and dynamics of confined foams: A review of recent progress”, *Adv. Coll. Interface Sci.*, vol. 137, p. 20, 2008.
- [70] Hirasaki G.J. and Lawson J.B., "Mechanisms of foam flow in porous media: apparent viscosity in smooth capillaries”, *Soc. Petroleum Eng.*, vol. 25, p. 176, 1985.
- [71] Wong H., Radke C.J., and Morris S., "Motion of long bubbles in polygonal capillaries. Part 1. Thin films”, *J. Fluid Mech.*, vol. 292, p. 71, 1995.
- [72] Denkov N.D., Tcholakova S., Golemanov K., Subramanian V., and Lips A., "Foam-wall friction: Effect of air volume fraction for tangentially immobile bubble surface”, *Coll. Surf. A.*, vol. 282/283, p. 329, 2006.
- [73] Saugey A., Drenkhan W., and Weaire D., "Wall slip of bubbles in foams”, *Phys. Fluids*, vol. 18, p. 053101, 2006.
- [74] Heller J.P. and Kuntamukkula M.S., "Critical review of foam rheology literature”, *Ind. Eng. Chem. Res.*, vol. 26, pp. 318-325, 1987.
- [75] Miles G.D., Shedlovsky L., and Ross J., "Foam Drainage”, *J. Phys. Chem.*, vol. 49(2), pp. 93-107, 1945.
- [76] Durian D.J., Weitz D.A., and Pine D.J., "Dynamics and coarsening in three-dimensional foams”, *J. Phys.: Condensed Matter*, vol. 2, pp. SA433-6, 1990.
- [77] Bikerman J.J., *Foams*. New York: Springer, 1973.
- [78] Guillaume C., Loisel W., Bertrand D., and Popineau Y., "Study of foam stability by video image analysis: relationship with the quantity of liquid in the foam”, *Journal of Texture Studies*, vol. 24, pp. 287-302, 1993.
- [79] Desai D. and Kumar R., "Liquid hold-up in semi-batch cellular foams”, *Chem. Eng. Science*, vol. 38, pp. 1525-1534, 1983.
- [80] Gol'dfarb I.I., Kann K.B., and Shreiber I.R., "Liquid flow in foams”, *Fluid Dynamics*, vol. 23, pp. 244-249, 1988.

- [81] Lorenceau E., Louvet N., Rouyer F., and Pitiois O., "Permeability of aqueous foams", *Eur. Phys. J. E.*, vol. 28(3), pp. 293-304, 2009.
- [82] Stevenson P., "On forced drainage of foam", *Coll. Surf. A: Physicochem. Eng. Aspects*, vol. 305, pp. 1-9, 2007.
- [83] Von Neumann J., "Discussion - shape of metal grains", *Metal Interfaces*, 1952.
- [84] Ivanov I. and Dimitrov D.S., "Thin liquid films", *Surfactant Science Series*, vol. 29, p. 323, 1988.
- [85] Manev E. and Pugh R.J., *J. Colloid Interface Sci.*, vol. 186, p. 493, 1997.
- [86] Vrij A. and Overbeek J.T.G., "Rupture of thin liquid films due to spontaneous fluctuations in thickness", *J. Am. Chem. Soc.*, vol. 90, p. 3074, 1968.
- [87] Burnett G.D., Chae J.J., Tam W.Y., de Almeida M.C., and Tabor M., "Structure and dynamics of breaking foams", *Phys. Rev. E.*, vol. 51, p. 6, 1995.
- [88] Ritacco H., Kiefer F., and Langevin D., "Lifetime of bubble rafts: cooperativity and avalanches", *Phys. Rev. Lett.*, vol. 98, p. 244501, 2007.
- [89] Vandewalle N., Lentz J.F., Dorbolo S., and Brisbois F., "Avalanche of draining foams", *Phys. Rev. Lett.*, vol. 86, pp. 179-182, 2001.
- [90] Carrier V. and Colin A., "Coalescence in draining foams", *Langmuir*, vol. 19(11), pp. 4535-4538, 2003.
- [91] Hutzler S., Saadatfar M., van der Net A., Weaire D., and Cox S.J., "The dynamics of a topological change in a system of soap films", *Coll. Surf. A.*, vol. 323, pp. 123-31, 2008.
- [92] Mooney M., "Explicit formulas for slip and fluidity", *J. Rheol.*, vol. 2, pp. 210-222, 1931.
- [93] Hatschek E., "Die viskosität der dispersoide", *Kolloid-Z.*, vol. 8, pp. 34-39, 1911.
- [94] Wu M.S., Sullivan M.E., and Yee D.J., "The viscosity of a foam (air in water emulsion)", *Colloids and Surface*, vol. 12, pp. 375-380, 1984.
- [95] Khan S.A. and Armstrong R.C., "Rheology of foams: II. Effects of polydispersity and liquid viscosity for foams having gas fraction approaching unity", *J. Non-Newtonian Fluid Mech.*, vol. 25, pp. 61-92, 1988.
- [96] Tcholakova S., N.D. Denkov, Golemanov K., Ananthapadmanabhan H.P., and Lips A., "Theoretical model of viscous friction inside steadily sheared foams and concentrated emulsions", *Phys. Rev. E.*, vol. 78, p. 011405, 2008.
- [97] Harris P.C., "Effects of texture on rheology of foam fracturing fluids", *SPE production Engineering*, pp. 249-257, 1989.
- [98] Reindenbach V.G., Harris P.C., Lee Y.N., and Lord D.L., "Rheological study of foam fracturing fluids using nitrogen and carbon dioxide", *SPE Production Engineering*, pp. 31-41, 1986.
- [99] Wenzel H.G., Stelson T.E., and Brungraber R.J., "Flow of high expansion foams in pipes", *J. Eng. Mech.*, vol. 6, pp. 153-165, 1967.
- [100] Thondavadi N.N. and Lemlich R., "Flow properties of foam with and without particles", *Indus. Eng. Chem. Process Design Devel.*, vol. 24, pp. 748-53, 1985.
- [101] Briceño M.I. and Joseph D.D., "Self-lubricated transport of aqueous foams in horizontal conduits", *Int. J. Multiphase Flow*, vol. 29, pp. 1817-1831, 2003.
- [102] Camp M.A., *The rheology of high gas volume fraction aqueous foam*. Southampton, England, 1988.
- [103] Wenzel H.G., Brungraber R.J., and Stelson T.E., "The viscosity of high expansion foam in pipes", *Journal of Materials JMLSA*, vol. 5, pp. 396-412, 1970.

- [104] Fairbrother R. and Stubbs A.E., "Studies in electroendosmosis. Part IV. The bubble-tube method of measurement", *Journal of the chemical society*, p. 527, 1935.
- [105] Jastrzebski Z.D., "Entrance effects and wall effects in an extrusion rheometer during the flow of concentrated suspensions", *Indus. Eng. Chem. Fundament.*, vol. 6, pp. 445-454, 1967.
- [106] Yeow Y.L., Lee H.L., Melvani A.R., and Mifsud G.C., "A new method of processing capillary viscometry data in the presence of wall slip", *J. Rheol.*, vol. 47, pp. 337-348, 2003.
- [107] Tychonoff A.N. and Arsenin V.Y., *Solution of Ill-Posed Problems*. Washington D.C: Winston & Sons.
- [108] Calvert J.R. and Nezhati K., "A rheological model for a liquid-gas foam", *Int. J. of heat and fluid flow*, vol. 7, pp. 164-168, 1986.
- [109] Calvert J.R., "Pressure drop for foam flow through pipes", *Int. J. of heat and fluid flow*, vol. 11, pp. 236-241, 1990.
- [110] Blauer R.E., Mitchell B.J., and Kohlaas C.A., "Determination of laminar, turbulent and transitional foam flow losses in pipes", in *44th Annual California Regional Meeting*, California, 1974.
- [111] Gotovtsev V.M., "Viscoelastic model for the plug flow of a foam in a cylindrical channel", *Theoretical foundations of Chemical Engineering*, vol. 30, pp. 523-529, 1996.
- [112] Versteeg H.K. and Malalasekera W., *An Introduction to Computational Fluid Dynamics, The Finite Volume Method.*: Longman, 1995.
- [113] Madani S.S., *Écoulement de Mousse Humide dans une Conduite Horizontale en Présence d'un Demi Élargissement Brusque, puis d'une Chicane*, Master Sci. Report (DEA), Ed. Saint Nazaire, France, 2006.
- [114] Belikov V.I. and Feklistov V.N., "Viscosimeter for study of rheology of two- and three-phase foams", *Russian Academy of Sciences*, pp. 193-196, 1992.
- [115] Gori F., Petracci I., and Angelino M., "Flow evolution of a turbulent submerged two-dimensional rectangular free jet air. Average Particle Image Velocimetry (PIV) visualizations and measurements.", *Int. J. Heat Fluid Fl.*, vol. 44, pp. 764-775, 2013.
- [116] Bryanston-Cross P.J. and Epstein A., "The application of sub-micron particle visualisation for PIV (Particle Image Velocimetry) at transonic and supersonic speeds", *Progress in Aerospace Science*, vol. 27, pp. 237-265, 1990.
- [117] Nernst W., "A One-Dimensional Reaction/Diffusion System with a Fast Reaction", *Z. Physik Chem.*, vol. 47, p. 52, 1904.
- [118] Lin C.S., Denton E.B., Gaskhill H.S., and Putnam G.L., "Diffusion-controlled electrode reactions", *Ind. Eng. Chem.*, vol. 43, pp. 2136-2143, 1951.
- [119] Magaud F., Souhar M., Wild G., and Boisson N., "Experimental study of bubble column hydrodynamics", *Chem. Eng. Sci.*, vol. 56, pp. 4597-4607, 2001.
- [120] Mitchell J.E. and Hanratty T.J., "A study of turbulence at a wall using an electrochemical wall shear stress method", *J. Fluid Mech.*, vol. 26, pp. 199-221, 1966.
- [121] Lévêque M.A., "Les lois de la transmission de la chaleur par convection", *Ann. Mines Carbur.*, vol. 13, pp. 201-239, 1928.
- [122] Mao Z.X. and Hanratty T.J., "Analysis of wall shear stress probes in large amplitude unsteady flows", *Int. J. Mass Transfer*, vol. 34, pp. 281-290, 1991.
- [123] Lebouché M., *Contribution à l'étude des mouvements turbulents des liquides par la méthode polarographique*, State Ph.D. es Sciences, Nancy, France, 1968.

- [124] Fortuna G. and Hanratty T.J., "Frequency response of the boundary layer on wall transfer probes", *Int. J. Heat Mass Transfer*, vol. 14, pp. 1499-1507, 1971.
- [125] Mao Z.X. and Hanratty T.J., "The use of scalar transport probes to measure wall shear stress in a flow with imposed oscillations", *Expt Fluids*, vol. 3, p. 129, 1985.
- [126] Kaiping P., "Unsteady forced convective heat transfer from a hot film in non-reversing and reversing shear flow", *Int. J. Heat Mass Transfer*, vol. 26, pp. 545-557, 1983.
- [127] Mao Z.X. and Hanratty T.J., "Numerical analysis of higher order harmonics in the response of a mass transfer probe", *Expt Fluids*, vol. 11, pp. 65-73, 1991.
- [128] Funfschilling P., *Investigation par un écoulement de Couette de la réponse fréquentielle des sondes électrochimiques et de la floculation de particules en suspension*. Nancy: Thèse, 2001.
- [129] Sobolik V., Wein O., and Cermák J., "Simultaneous measurement of film thickness and wall shear stress in a wavy flow of non-Newtonian liquids", *Collection of Czechoslovak chemical communications*, vol. 52, pp. 913-928, 1987.
- [130] Tihon J. and Sobolik V., "Dynamics of electrodiffusion in wavy films", *Proceedings of the 3rd International Workshop on Electrodiffusion Diagnostic of Flows*, pp. 397-404, 1993.
- [131] Sekogushi K. and Takeishi M., "Interfacial structure in upward huge wave flow annular flow regimes", *Int. J. Multiphase Flow*, vol. 15, pp. 295-305, 1989.
- [132] Coney M.W.E., "The theory and application of conductance probes for measurement of liquid film thickness in two-phase flow", *J. of physics E: Scientific Instruments*, vol. 6, pp. 903-910, 1973.
- [133] Sobolik V., Pauli J., and Onken U., "Three-segment electrodiffusion probe for velocity measurement", *Experiments in Fluids*, vol. 11, pp. 186-190, 1991.
- [134] L.P. Reiss and T.J. Hanratty, "An experimental study of the unsteady nature of the viscous sublayer", *AIChE Journal*, vol. 8, pp. 154-160, 1963.
- [135] T.S. Lundgren, E.M. Sparrow, and J.B. Starr, "Pressure drop due to the entrance region in ducts of arbitrary cross section", *J. Basic Eng*, vol. 86, pp. 620-626, 1964.
- [136] H. Darcy, *Recherches Experimentales Relatives au Mouvement de L'Eau dans les Tuyaux*. Paris: Mallet-Bachelier, 1857.
- [137] J.L. Poiseuille, "Recherches expérimentales sur le mouvement des liquides dans les tubes de très-petits diamètres", Paris, 1841.
- [138] M.A. Latifi, N. Midoux, and A. Stork, "The use of micro-electrodes in the study of flow regimes in a packed bed reactor with single phase liquid flow", *Chem. Eng. Sci.*, vol. 21, pp. 1185-1190, 1989.
- [139] Naderifar A., *Etude expérimentale locale et globale du transfert de matière liquide-solide à la paroi d'un réacteur à lit fixe*, Ph.D. Thesis, Nancy, France, 1995.
- [140] Seguin D., *Contribution à l'étude du transfert de matière et des régimes d'écoulement dans des milieux poreux de structures variées*, Ph.D. Thesis, Saint-Nazaire, France, 1997.
- [141] G.I. Taylor, "Production and Dissipation of Vorticity in a Turbulent Fluid", *Proceedings of the Royal Society of London, Series A, Mathematical and Physical Sciences*, vol. 164, pp. 15-23, 1938.
- [142] Celik I., Urmila G., Roache P., Freitas C., Coleman H., and Raad P., "Procedure for estimation and reporting uncertainty due to discretization in CFD applications", *J. Fluids Eng.*, vol. 130, no. 7, p. 078001, July 2008.
- [143] Fadla. F., Chovet R., Cornu D., Lippert M., Aloui F., and Keirsbulck L., "Spatial resolution

- correction for electrochemical wall-shear stress measurements using rectangular sensors”, *Journal of Applied Fluid Mech.*, vol. 9, no. 4, 2016.
- [144] Chovet R. and Aloui F., "Liquid Film Thickness: Study and Influence over Aqueous Foam Flow”, in *7th International Exergy, Energy and Environment Symposium*, Valenciennes, France, 2015, p. V263.
- [145] Chovet R., Aloui F., and Keirsbulck L., "Wall shear stress generated by aqueous foam flow”, in *Proceedings of the ASME-JSME-KSME Joint Fluids Engineering Conference*, Seoul, Korea, 2015, pp. AJK2015-14039.
- [146] Chovet R. and Aloui F., "Void fraction influence over aqueous foam flow: wall shear stress and core shear evolution”, in *International Conference on Clean Energy*, Istanbul, Turkey, 2014, p. #1604.
- [147] Chovet R., Aloui F., and Keirsbulck L., "Behaviour of a non-newtonian wet foam flow downstream an obstacle”, in *10th European Conference on Coal Research and its Applications*, Hull, England, 2014.
- [148] Chovet R. and Aloui F., "Gas-liquid foam through a straight duct and singularities: CFD simulations and experiments”, in *ASME 2014, 4th US-European Fluids Engineering Division Summer Meeting*, Chicago, USA, 2014, pp. FEDSM2014-21190.
- [149] Chovet R., Aloui F., and Labraga L., "Wet foam flow in horizontal square duct and through singularities”, in *ASME 2013, Fluids Engineering Division Summer Meeting*, Nevada, USA, 2013, pp. FEDSM2013-16307.
- [150] Soller R. and Koehler S.A., "Rheology of steady-state draining foams”, *Phys. Rev. Lett.*, pp. 100: 208301, 2008.
- [151] Wearie D. and Phelan R., "A counter-example to Kelvin’s conjecture on minimal surfaces”, *Philosophical Magazine Letters*, vol. 69, pp. 107-110, 1994.
- [152] Rossen W.R., "Foams in enhanced oil recovery”, *Foams, Theory, Measurements and Applications*, vol. 57, pp. 413-464, 1996.
- [153] Drenckhan W., Ritacco H., Saint-Jalmes A., Saugey A., McGuinness P., van der Net A., Langevin D., Wearie D., "Fluid dynamics of rivulet flow between plates”, *Phys. Fluids*, p. 19(10), 2007.

Titre : Caractérisation Expérimentale et Numérique du Comportement Rhéologique d'un Fluide Complexe : Application à une Mousse en Écoulement dans un Canal Horizontal Droit avec et sans Singularités

Résumé :

Ce travail porte sur l'étude expérimentale et numérique de l'écoulement des mousses humides dans un canal horizontal droit de section carrée avec ou sans singularités. Il est consacré tout particulièrement à déterminer les paramètres pertinents de l'écoulement dont la chute de pression longitudinale, les champs de vitesse de l'écoulement de mousse en proche parois, les épaisseurs de films liquides minces et épais en paroi et l'évolution de la contrainte pariétale pour une mousse humide dont la fraction gazeuse varie de 55 à 85% et la vitesse débitante de la mousse est 2, 4 puis 6 cm/s. Une fois ces paramètres déterminés en conduite horizontale droite, nous avons ensuite effectué des mesures sur différentes géométries représentant un élargissement brusque, une chicane verticale et écoulement de mousse autour d'un cylindre, dont le but est d'étudier la réorganisation de l'écoulement en vue de déterminer le comportement rhéologique des mousses en écoulement à l'aval et à l'amont des singularités. Finalement, une étude de simulation numérique (CFD) en utilisant les lois de comportement de type Bingham, pour fluides non newtoniens, a été effectuée afin de tester sa capacité de représenter des écoulements type mousse humide dans une conduite horizontale avec ou sans singularités. Nous avons vérifié tout d'abord l'évolution longitudinale de la pression statique qui est linéaire à l'amont comme à l'aval loin des zones influencées par les singularités. La chute de pression singulière reste à peu près constante pour une vitesse débitante donnée de la mousse. À partir de la technique de Vélocimétrie par Image de Particule (PIV), nous avons déterminé les composantes de vitesse au voisinage immédiat des singularités. Ces mesures nous ont permis de mettre en évidence l'existence de différents régimes d'écoulement, et de déterminer la réorganisation et le comportement rhéologique de l'écoulement de mousse autour des géométries étudiées. L'analyse des mesures d'épaisseur de films liquides, obtenues par la méthode conductimétrique, indique que la paroi reste mouillée par un film liquide suffisamment épais pour qu'on puisse appliquer la méthode électrochimique. Les signaux polarographiques obtenus avec la mousse présentent alors de fortes fluctuations. La comparaison de celles-ci avec les contraintes pariétales déduites à partir des mesures de la chute de pression montre bien une bonne concordance. L'étude numérique (CFD), effectuée pour une fraction volumique de gaz égale à 70% et qui s'écoule avec une vitesse débitante de 2 cm/s, montre que le modèle rhéologique de Bingham pourrait être bien adapté à ce genre de mousse humide évoluant en écoulement en bloc.

Mots clés : Mousse humide, écoulement, rhéologie, conduite horizontale, section carrée, singularités, Vélocimétrie par Image de Particules (VIP), méthode polarographique, contrainte pariétale, méthode conductimétrique, film liquide, taux de vide, CFD, Modèle de Bingham.

Title: Experimental and Numerical Characterization of the Rheological Behavior of a Complex Fluid: Application to a Wet Foam Flow Through a Horizontal Straight Duct with and without Flow Disruption Devices (FDD)

Abstract:

This work is an experimental and numerical study of aqueous foam flow inside a horizontal square duct, with and without flow disruption devices (fdd). It is especially devoted to determine the pertinent parameters of the flow: longitudinal pressure losses, velocity fields of foam flow near the walls, liquid film thickness (thick and thin), and the wall shear stress evolution, for an aqueous foam with a void fraction range between 55 and 85%, for a mean foam flow velocity of 2, 4 and 6 cm/s. Once they were determined, inside the horizontal channel, we carried out measurements over different geometries: half-sudden expansion, vertical fence and foam flow around a cylinder. The goal was to study the foam flow reorganization to well understand the rheological behavior of aqueous foam flow in the vicinities of different fdd. Finally, a numerical simulation (CFD), using the Bingham behavior model of non-Newtonian fluid, was undertaken to test its capacity to represent the aqueous foam flow inside the horizontal duct with flow disruption devices. First of all, we verified the static longitudinal pressure evolution, which varies linearly upstream and downstream far from the fdd. The singular pressure loss remains constant for a given mean foam velocity and a foam quality (void fraction). From the Particle Imaging Velocimetry (PIV) technique (2D), we determined the two velocity components in the immediate vicinities of the disruption devices. They allowed us to put into evidence the different foam flow regimes and to observe the foam flow reorganization and rheological behavior through the studied fdd. The slip-layer thickness analysis, obtained using the conductimetry method, shows that the wall presents a liquid film thick enough to apply an electrochemical technique (polarography). Thus, the polarographic signals, obtained for the foam flow, present important fluctuations. They were compared to the wall shear stress deduced from the measurement of pressure losses, showing a good similarity between them. The numerical study (CFD), carried out for aqueous foam flow with a void fraction of 70% and a mean foam flow velocity of 2 cm/s, shows that the Bingham rheological model can be adapted to this kind of aqueous foam flow which is flowing like a block.

Keywords: Aqueous foam, flow, rheology, horizontal duct, square section, flow disruption devices, Particle Imaging Velocimetry (PIV), polarographic method, wall shear stress, conductimetric method, liquid-slip layer, void fraction, CFD, Bingham model.